DIRECT AERIAL IMAGE MONITORING FOR EXTREME ULTRAVIOLET LITHOGRAPHY SYSTEMS

by

Charles Henry Fields

Memorandum No. UCB/ERL M97/16

14 March 1997

DIRECT AERIAL IMAGE MONITORING FOR EXTREME ULTRAVIOLET LITHOGRAPHY SYSTEMS

by

Charles Henry Fields

Memorandum No. UCB/ERL M97/16

14 March 1997

ELECTRONICS RESEARCH LABORATORY

College of Engineering
University of California, Berkeley
94720

Direct Aerial Image Monitoring for Extreme Ultraviolet Lithography Systems

by

Charles Henry Fields

Doctor of Philosophy in Engineering -
Electrical Engineering and Computer Sciences

University of California at Berkeley
Professor William G. Oldham, Chair

Abstract

An aerial image monitor (AIM) for operation in the extreme ultraviolet (EUV) is constructed to characterize the performance of a prototype EUV projection lithography system (10X-I at Sandia National Laboratories in Livermore, CA). The AIM is also used to rapidly align the optical system and to find the plane of best focus.

Two patterning techniques are developed for EUV AIM aperture fabrication using electron-beam lithography. The fabrication of the final artifacts uses focused ion beam lithography and thermal evaporation to produce aperture slits with widths less than 100nm that are used for AIM as well as two other interferometry experiments carried out in the EUV.

AIM is used to quantify EUV lithographic system vibration which is reduced from an initial value of 350nm to 17±3nm. This level of vibration suppression is reproducible

after mask changes that involve the complete removal of both mask and wafer stages as well as the camera.

Three distinct methods of aerial image monitoring are implemented on the 10X-I EUVL system. The first scans a knife-edge at the image plane across the aerial image of a 2.5μm slit source. The results are in qualitative agreement with theory and simulation, but the accuracy of the measurements is limited because the slit mask has a peak-to-peak edge roughness of 0.9μm, distorting the image. In the second experiment a single narrow slit artifact is scanned over a step function aerial image. The resulting edge spread function is used to calculate the modulation transfer function (MTF) of the camera. The spatial frequency dependence of the MTF(f) is used together with simulation to estimate the effective imaging system multi-layer surface roughness variance σ^2_{rms} following theoretical calculations. The measured value of σ_{rms} is between 0.4nm and 1.3nm for the spatial frequencies between $0.1\mu m^{-1}$ and $10\mu m^{-1}$ respectively.

The final set of image monitoring experiments is a depth of focus study that involves scanning a single narrow slit artifact across the aerial image of 0.5μm equal lines and spaces. The measured peak contrast of the aerial image is 57% which is in agreement with simulation and photoresist exposures. The measured depth of focus is ±5μm based on 80% of the peak contrast.

W G Oldham 3/13/97

Prof. W.G. Oldham
Committee Chairman

Dedicated to my wife Vanessa, and to my family: James, Mary, and Violet.

Table of Contents

Acknowledgments

At the completion of this work, I can attempt to thank all those who have made this work possible. I would like foremost to thank Prof. William Oldham for allowing me to be member of his research group and for his guidance and support throughout my graduate school experience. He always challenged me to look deeper into problems and to develop my curiosity. Thanks for always having faith in me. Thanks for all the great golf and also for the many winters at the Heidelmann.

Prof. Jeff Bokor for his encouragement to always do more and think harder. His critical thinking on several issues greatly improved the overall quality of my work and dissertation.

Thanks to Prof. Paul McEuen and Prof. Bruce Hasegawa for sitting on my qualifying examination committee. It was quite a drive for Prof. Hasegawa. I would also like to than Prof. McEuen for reading my dissertation and serving on my qualifying exam committee.

Thanks to Dr. Rick Stulen and Dr. Dan Tichenor for allowing me the opportunity to work in the 10X-I EUVL laboratory at Sandia. Thanks for trusting in us and an idea that, at the time, seemed pretty far-fetched.

Dr. Avi Ray-Chaudhuri and Mr. Kevin Krenz who accepted me into their lab to conduct my experiments. After a short time working together they soon thought of me as one of the team. I am forever indebted to Kevin for all his help during the experiments and for his ingenious mechanical design ideas for the 10X-I stages. We also enjoyed much good golf together in the mornings before work. The discussions that I had with Avi were

invaluable in the understanding of the 10X-I system and the requirements for our mutual experiments. I thank him also for working nearly as hard as I did to get data out for a couple of conference papers; even to the point of working 7 days a week for a month straight.

A special thanks to Kim Chan. Kim's help in several of the fabrication tasks was invaluable. Kim did not hesitate to stay late for some of the special processes. She also trained me on several pieces of equipment in the microlab. Without Kim's help, I would still be at Cal.

Thanks to Dr. John Hutchinson for his help in opening the door to allow us access to the FIB facilities at Intel, Santa Clara. The FIB group at Intel were extremely helpful with the most crucial step in the fabrication process. Thanks to the FIB group manager Bob Rao for buying onto this idea when the connection to Intel was not perfectly clear. The group leader, Rick Livengood, went out of his way to make time out of their busy schedule for our work. On a couple of occasions he and I even drove up to Folsom to use another FIB at another Intel site. Thanks also to Theresa Rinni, the technician with whom I spent many hours in front of Micrion FIB machines. Theresa even worked on her days off to meet the scheduling demands of the group's work load.

Thanks to Rod Nissen and Steve Haney for their fantastic design work modifying the 10X-I test bed for both our AIM experiments and also for Avi's interferometry measurements. They were also helpful in discussions on ways to decrease stage vibration.

I am very grateful to several of the graduate students in our department. Thanks to Bob Socha and Tom Pistor for their help in getting the TEMPEST simulation to work

correctly and in properly interpreting the data. Thanks also to Edita Tejnil for her enlightening conversations on optics and EUV lithography.

Thanks to Jeff Markakis for his friendship and helpful suggestions concerning detector noise. Henry Chapman and Dave Gaines from LLNL were extremely helpful in measurements of our test optics and in calculating the PSDs from the data. Thanks also to Obert Wood of Lucent Technologies who provided the optics for test.

A special thanks to my wife Vanessa who supported me through the many ups and downs of my graduate career. She delayed having a real house, job, car, and life for nearly five years while I satisfied my desire to be all that I could be. I am truly blessed with such a considerate and understanding wife as Vanessa.

Thanks to the Semiconductor Research Corp. (SRC) for their financial support of my graduate school work. Additional thanks to Prof. David Attwood and the Advanced Research Projects Agency (ARPA) for funding support during the middle couple of years of my graduate career.

Chapter 1

Introduction to Aerial Image Measurements

1.1 Introduction

The precise measurement of the aerial image of a lithography system is the key to the characterization of stepper performance. An image monitor that directly measures the aerial image incident on the wafer would allow the real time evaluation of the projection photolithography system without the costly and time consuming steps involved in evaluating images developed in resist. Direct image monitoring improves accuracy by removing the resist stage entirely. The improved characterization speed and accuracy possible with AIM will therefore improve the efficiency and overall quality of sub-micron lithography.

A fully assembled microlithography lens is traditionally tested in two ways. The first method is to measure the wave front aberrations using a transmissive interferometer. Transmission interferometry is critical to adjusting the spacing and positioning of each lens element and subgroup. The method used to quantify the final lens performance involves producing exposures in photoresist and measuring the developed resist profiles in a scanning electron microscope (SEM). These SEM-verified exposures have several drawbacks. First, the time needed to make the required SEM measurements is long, approximately two days. The photoresist exposure measurement method is also subject to changes in the photoresist process and differences in SEM and SEM operator performance. Variations due to the photoresist process and SEM linewidth measurements are eliminated by measuring the aerial image directly.

Furthermore, many new problems arise when the lens is mounted onto a stepper system, including mechanical deformations of the lens assembly, condenser optics aberrations, mechanical vibrations, reticle or wafer non-planarity, temperature variations, barometric pressure variations, and others. Thus it is necessary to test full stepper systems even though previous measurements of the projection lens itself have been done.

In previous publications, an image monitor was developed and used to rapidly characterize a stepper lens *in-situ* [17, 19]. Previous image monitors used a one-dimensional scanning routine to monitor the intensity profile. This process involves scanning a photodiode with a line grating pattern mask cover at the wafer under aerial images of the same pattern from the stepper reticle. This research explores a method of characterizing EUV microlithographic stepper performance by direct measurement of the aerial images produced by the system. An image monitor is constructed which uses arrays of scanning slits and pinholes in the mask to produce arrays of line and point light sources, respectively, at the wafer plane. These patterns are monitored by scanning the corresponding pinhole or slit array in the image plane in front of a photodiode detector. From the resulting intensity profile we can determine information concerning the characteristics of the stepper lens optics including focus, scattered light, and lens aberrations such as distortion, coma, and astigmatism.

The concept of measuring the aerial images produced from lithographic system is not new to the field, only the technique, and results. Several researchers have invented ingenious methods of estimating the aerial images by indirect measurement [1-5]. The simplest method is measure the result of the projected aerial image by printing in photoresist. Other methods make inferences about image quality based upon indirect

measurements of the aerial image intensity. This chapter explores the major early techniques and lists the advantages and disadvantages of each. The later sections explore the issue and application of direct aerial image measurements both at deep ultraviolet and extreme ultraviolet wavelengths.

1.2 Previous Work

1.2.1 Stepper Image Monitor

An early attempt to measure of the aerial images produced from a complete microlithography stepper system developed by Brunner et. al. [1] lead to the Stepper Vision Stepper Image Monitor (SIM). The general approach of the SIM is shown in Figure 1.1 where a special test reticle forms an aerial image over a special test wafer with narrow lines which scatter light into a detector. The detector signal is then observed as the narrow lines move in tiny steps, 0.25μm in this case. In the limit of very narrow lines on the test wafer, the detector signal versus wafer stage position forms an accurate representation of the actual aerial image profile.

Two methods were implemented by Brunner et. al. the first of which used narrow lines made of heavily dyed photoresist which fluoresced in the green when excited by the blue light in the aerial image. This was accomplished with a Portable Conformable Mask [7,8] utilizing a PMMA bottom layer that has been heavily doped with Coumarin dye. Although this method proved effective and usable results were obtained with the fluorescence approach, the signal decayed with time due to the photo-chemical degradation of the dye. Another limitation of this technique is the fact that the relatively

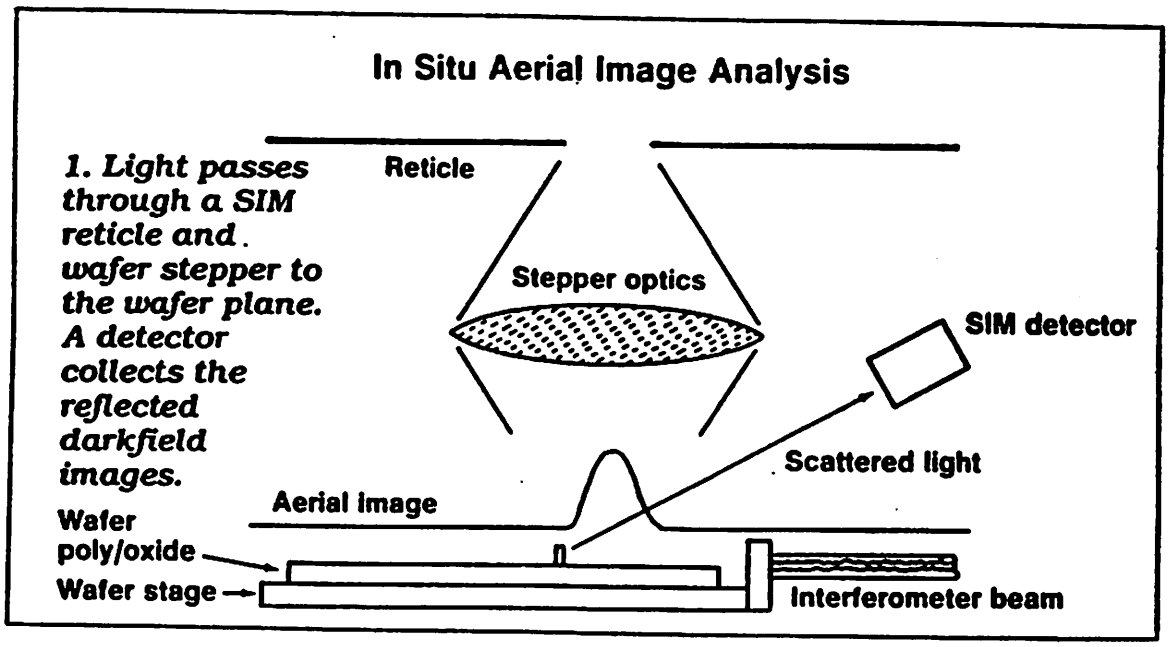

Figure 1.1 Illustration of the concept of the stepper image monitor by Brunner et. al. Reference [1]

soft photoresist material was not well suited for a permanent *in-situ* artifact wafer and the heavily dyed photoresist process is not standard in most IC houses [1].

The problems associated with the use of photoresist were solved by the use of narrow poly lines on oxide wafers. In the new version of the SIM, instead of monitoring the green fluorescence from the photoresist, the blue light scattered from the poly line was the measured signal. The smooth oxide beneath the poly line will not scatter light while the relatively rough poly lines scatter light into the detector. Further improvements involved a quick etch of the poly line to add further roughness and therefore better reflection. The width of the poly lines were 0.4±0.1μm as measured on a CWIKSCAN IIE SEM. The lines were printed using a G-line lens with a numerical aperture (NA) of 0.3 [1].

The detected signal is then measured as a function of slit position (X_o) for a slit width of W as shown in Fig. 1. Then an expression for the observed signal is:

$$\text{Signal}(X_o,W) \propto \sigma I(x)dx \tag{1}$$

and in the limit of sufficiently narrow linewidth W (as $W \Rightarrow 0$) the measured signal becomes a better representation of the image, i.e.:

$$\text{Signal}(X_o,W \Rightarrow 0) \propto I(x) \tag{2}$$

The relatively large linewidths used for the SIM limit its ability to provide an accurate measure of the aerial image itself. While it is theoretically possible to deconvolve the measured signal by the response of the scanning line, this response is a complicated function of the specular reflection from the rough poly line. All data presented from the SIM work done to date has been presented raw where background subtraction and re-normalization are the only manipulations done to the data. It should be noted that for most applications of the SIM, such as determination of best focus or determination of overlay error or vibration measurements, the relatively large linewidths used are perfectly adequate [2].

Current production steppers are extending the limits of refractive optical lithography far beyond what early lithographers predicted with the use of high NA [4]. But this high resolution comes at the cost of a reduced depth of focus. The SIM technique described in this section finds its most common use in finding the plane of best focus of the stepper.

1.2.2 Microlithography Simulation Microscope

There exist several computer programs for simulating the aerial images produced from lithography systems with defined parameters such as NA, wavelength, and illumination coherence. However, actual production masks used to produce the desired aerial images are often imperfect and contain small errors that may not be recognized or may be difficult to model. For this reason researchers at IBM have developed a technique called Aerial Image Measurement System (AIMS) which later evolved into a commercial product labeled the Microlithography Simulation Microscope (MSM). The MSM is a UV microscope based imaging system that may be used to measure actual masks under conditions which mimic the stepper of interest. This MSM has been used successfully in a variety of applications including mask etch process optimization, determination of defect printability in resist, and studies of alternate illumination schemes.

Figure 1.2 illustrates the system layout of the MSM-100. The MSM provides a magnified stepper equivalent image that is captured by a DUV sensitive CCD camera. The system is controlled by the AIMS software package that also provides aerial image recording and analysis capabilities. Proper operation of the system is verified by comparing measurements through focus with computer simulations.

The system is based on the Zeiss Axiotron DUV microscope [9] and contains two illumination sources, a high-pressure mercury arc lamp for data recording and halogen lamp for visual preview. Bandpass dichroic filters can be electro-mechanically actuated to select either 365 or 248nm wavelengths for image measurements. Interchangeable

apertures are used to define the sigma (pupil filling factor) of the system and also to define the objective lens NA.

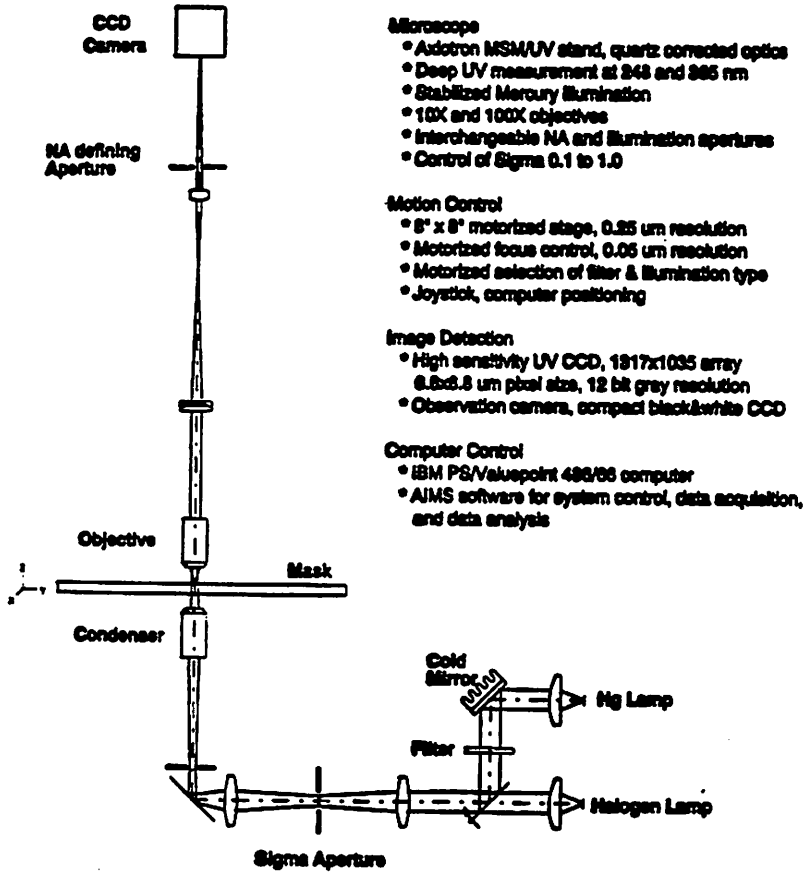

Figure 1.2 Layout and system description of the MSM-100 from Zeiss, Reference [3]

There are three common uses for the MSM: (1) To compare the image produced from the mask with computer simulation to verify that the mask has been fabricated free of basic phase and other errors, (2) To predict resist feature size for a given exposure or threshold, and (3) To predict the magnitude of resist CD perturbations due to mask defects. These applications are important in providing an early preview of the printing characteristics of a given reticle and stepper combination without undertaking time consuming SEM resist studies on an actual stepper.

1.2.3 Latent Image Measurements

Another technique known as Latent Image Metrology (LIM) [10-11], collects a "snapshot" of a test image in a thin layer of photoresist. Next, measurements are done of the quality of the test image in the photoresist before the resist is developed. This eliminates the contrast enhancement effect of the develop chemistry, in theory allowing observation of subtle variations in the printed pattern.

Figure 1.3 illustrates the experimental technique for LIM. The figure considers a grating projected by a stepper onto a photoresist-covered wafer. A photo-chemical reaction occurs in the light regions of the grating, causing the resist there to change its index of refraction slightly whereas there is no change in the dark regions. The sharpness of the transition region between the light and dark regions is an indication of the contrast of the aerial image. The second step in LIM is a post-exposure bake which elicits the latent image in the chemically-amplified resist (XP-89-131 0.5μm thickness). The third and final step of LIM requires probing the resulting pattern in the photoresist. This step is accomplished with the AT&T Lithographic Analysis Workstation (LAWS). LAWS consists of a dark-field microscope with a photomultiplier tube to integrate the weak dark-field scattering signal. By probing the resist patterns, it has been shown that the peak signal in the first-order of the non-specular scatter occurs when the resist pattern is exposed at best stepper focus [10,11]. "Ultra-flat" wafers were used for these experiments to minimize variations in imaging surface that cause inaccurate measurements of the optimum focal plane.

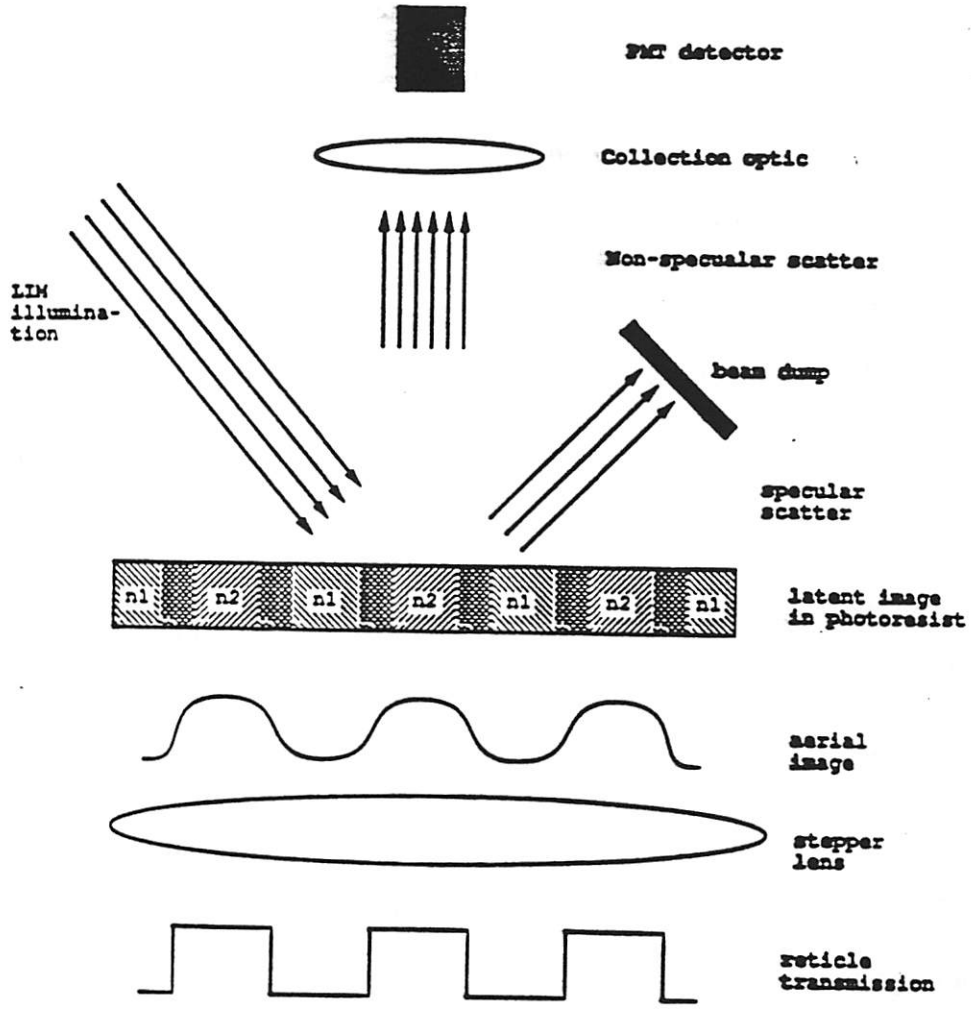

Figure 1.3 Illustration of the principle of LIM, Reference [10]

1.2.4 Aerial Image Measurements in the Deep UV

1.2.4.1 U.C. Berkeley Micro-Stepper

The previous sections describes methods of indirectly measuring the image quality produced by high-resolution stepper systems. This section presents a technique to directly measure image quality. The ideas introduced by Brunner with his SIM were improved upon by Pfau et. al. [15]. The technique for the direct measurement of the aerial images

intensity is to scan the stepper stage containing the image monitor through the image plane. The main components of the aerial image intensity sensor are a photodiode which is integrated in the wafer chuck and a chromium coated quartz wafer with a 10x10 array of 200nm pinholes. The imaged light intensity is spatially filtered by the pinholes pattern before reaching the underlying photodetector. The diode signal is proportional to the light intensity at the location of the sensor and integrated over its area. Therefore, the measured two-dimensional intensity distribution is the convolution of the sensor with the intensity profile. For a sufficiently small sensor, the blurring caused by the convolution is negligible and the obtained contour represents the true image intensity. The effect of sensor size on the measured images is covered in greater detail in a later section.

This image monitor was implemented on the Berkeley microstepper [15]. The same stepper was used to pattern the sampling pinholes in chromium. The metal was removed in a wet etch process with standard Cr-4 etchant. The isotropic etch caused highly sloping sidewall angles which degraded the resultant sampled aerial images. With the aid of frequency filtering the photodiode signal to improve the signal to noise ratio, the image monitor was tested and applied in a variety of experiments including determination of best focus and two-dimensional scans of elbow and contact patterns with reasonable correlation to simulations done using SPLAT [15].

These image measurements depend critically on precise stage position measurement and system stability during the integration time of the lock-in amplifier. Slow stage or interferometer drift degraded the integrity of the measured aerial images and imposed limitations as to the minimum feature size measurable with this stepper. Despite the limitations imposed by the patterning of the sampling pinholes and stepper motion,

these experiments represented the first direct measurement of aerial images produced from a microlithographic stepper.

1.2.4.2 AIM on a Commercial Stepper (GCA)

GCA steppers were equipped with a version of the image monitor described in the previous section. The standard *in-situ* system was used to find best focus, perform reticle to reticle alignment, and measure intrafield image placement errors. The ability of the standard *in-situ* system to measure small features was limited by the 0.8μm slit width on the artifact. To scan features as small as 0.35μm with high fidelity, the slit width must be less than 0.35μm. For energy throughput and patterning reasons, an 0.2μm slit width was chosen.

The thickness of the chrome absorber on the standard GCA in-situ artifact is 200nm. An absorber thickness comparable to the slit width is undesirable since the artifact would no longer approximate an infinitely thin intensity sampler. The modified artifact with 200nm features was patterned in amorphous silicon instead of chrome. Amorphous Silicon has a higher optical density than chrome in the deep-UV [17-18] and thus a thinner layer can be used. An absorber thickness of 80nm was used, giving an aspect ratio of 1 to 2.5 (height to width). An additional advantage is the ability to plasma etch amorphous silicon instead of using a wet etch similar to that used from the chrome. The vertical sidewalls produced by plasma etching the amorphous silicon ensure that the 200nm slits have optically sharp edges [18].

The modified artifact was designed such that the pitch of the 0.2μm slits matched that of the previous artifact so that all the existing in-situ software and hardware of the

GCA XLS stepper function without modification. Thus the modified artifact maintains the ability to measure lens distortion, find best focus, and perform wafer to reticle alignment.

Figure 1.4a shows the contrast versus focus for 0.35μm dense line/space (L/S) patterns measured with the modified *in-situ* artifact. Two partial coherence values are shown - 0.44 and 0.74. Figure 1.4b shows simulated contrast versus focus using the aberrations measured with a transmission interferometer. The measured aberrations are expressed using the Zernike polynomials. All the terms corresponding to the third and fifth order aberrations are used in the simulation.

The peak contrast values in Figure 1.4a are slightly less than the simulated values. For example, the peak measured contrast with 0.44 partial coherence is 84% while the simulated peak contrast is 94%. Most of this reduction in measured contrast can be attributed to the finite width of the scanning slits used on the artifact. Convolving a 0.2μm slit with the simulated 0.35μm aerial image reduces the peak contrast to 88%. The remaining 4% difference between measured and simulated is likely due to the finite bandwidth of the laser source (1.4 pm). The lens in this stepper is an all fused silica design and thus has no color correction.

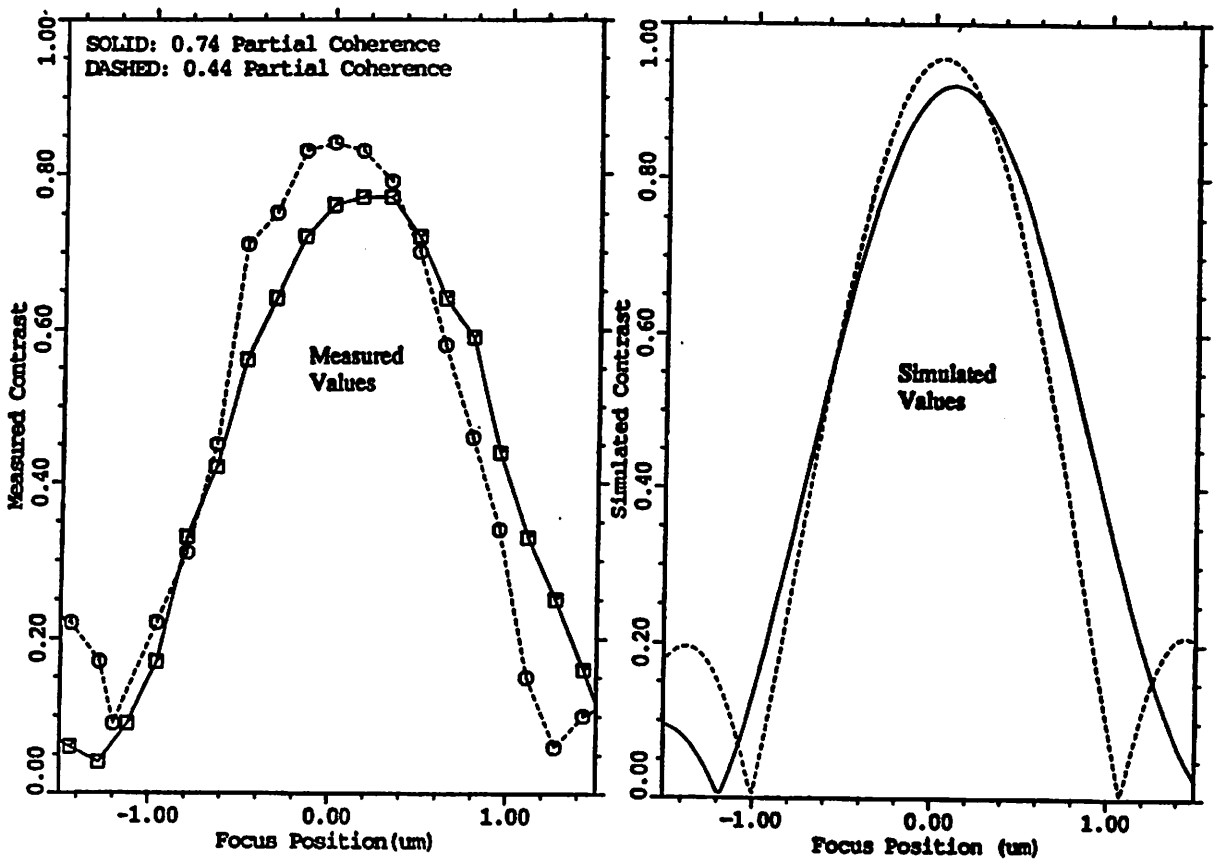

a. Measured contrast vs. focus position

b. Simulated contrast vs. focus position

Figure 1.4 Measured and simulated contrast of 0.35μm dense L/S patterns for two values of partial coherence, $\sigma = 0.44$ and $\sigma = 0.74$. The simulations are carried out using the polynomial terms from visible light interferometry measurements, Reference [3].

Changing partial coherence from 0.44 to 0.74 causes a reduction in contrast at best focus, but improves contrast for defocus values greater than approximately 0.75μm. This effect is expected due to the different energy weighting of two beam and three beam interference. The shift in best focus when changing from 0.44 to 0.74 partial coherence is due to spherical aberrations. This is demonstrated by Figure 1.4a which shows simulated contrast versus focus with only the third and fifth order spherical aberrations set to their measured values, all other Zernike terms are set to zero. Imaging with a larger partial

coherence places more energy at the edges of the pupil where the optical path difference (OPD) is larger, leading to a shift in best focus (positive defocus is toward the lens).

The increase in DOF and the shift in best focus due to changes in partial coherence are also found in photoresist exposures. Figure 1.5 shows the measured critical dimension (CD) versus focus for 0.35μm dense L/S features for both 0.44 and 0.74 partial coherence. In this figure, the measured CD curves terminate where scumming of the photoresist in the space region occurred. The increased DOF with 0.74 partial coherence is evidenced by the extension of the CD curve on the positive side of focus. Before aerial image measurements were made, this asymmetric increase in DOF when changing partial coherence was thought to be due to the volume imaging nature of the photoresist.

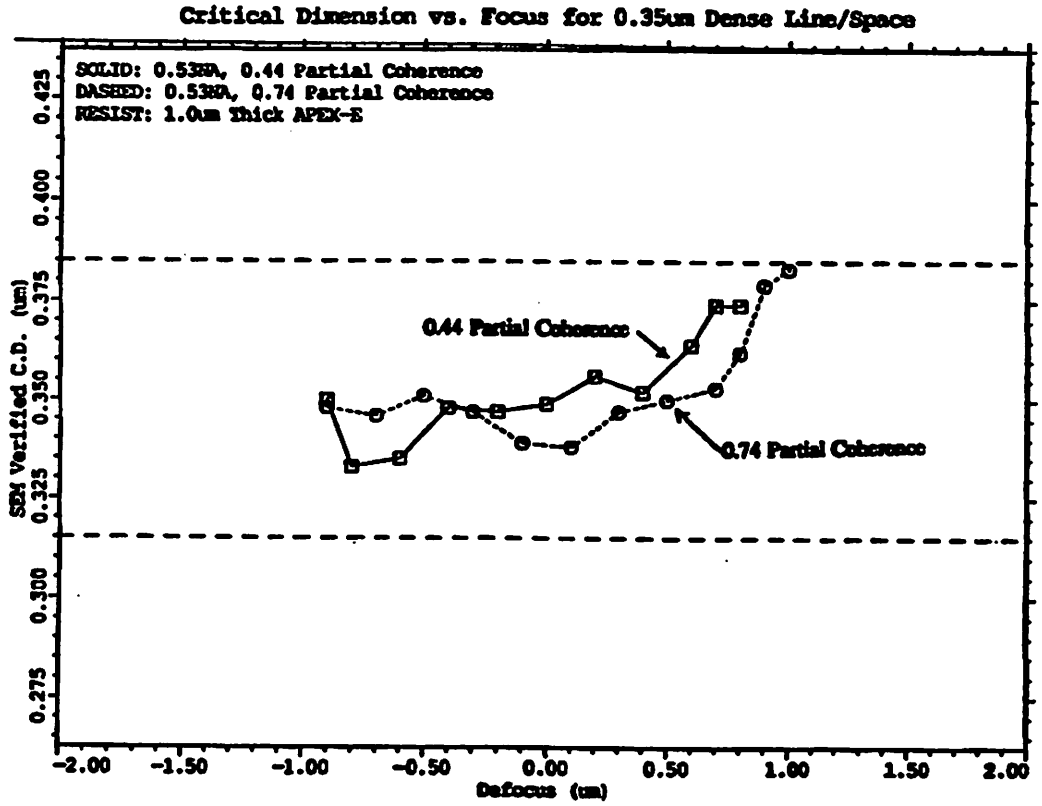

Figure 1.5 Critical dimension versus focus for 0.35μm dense L/S patterns, Reference [19].

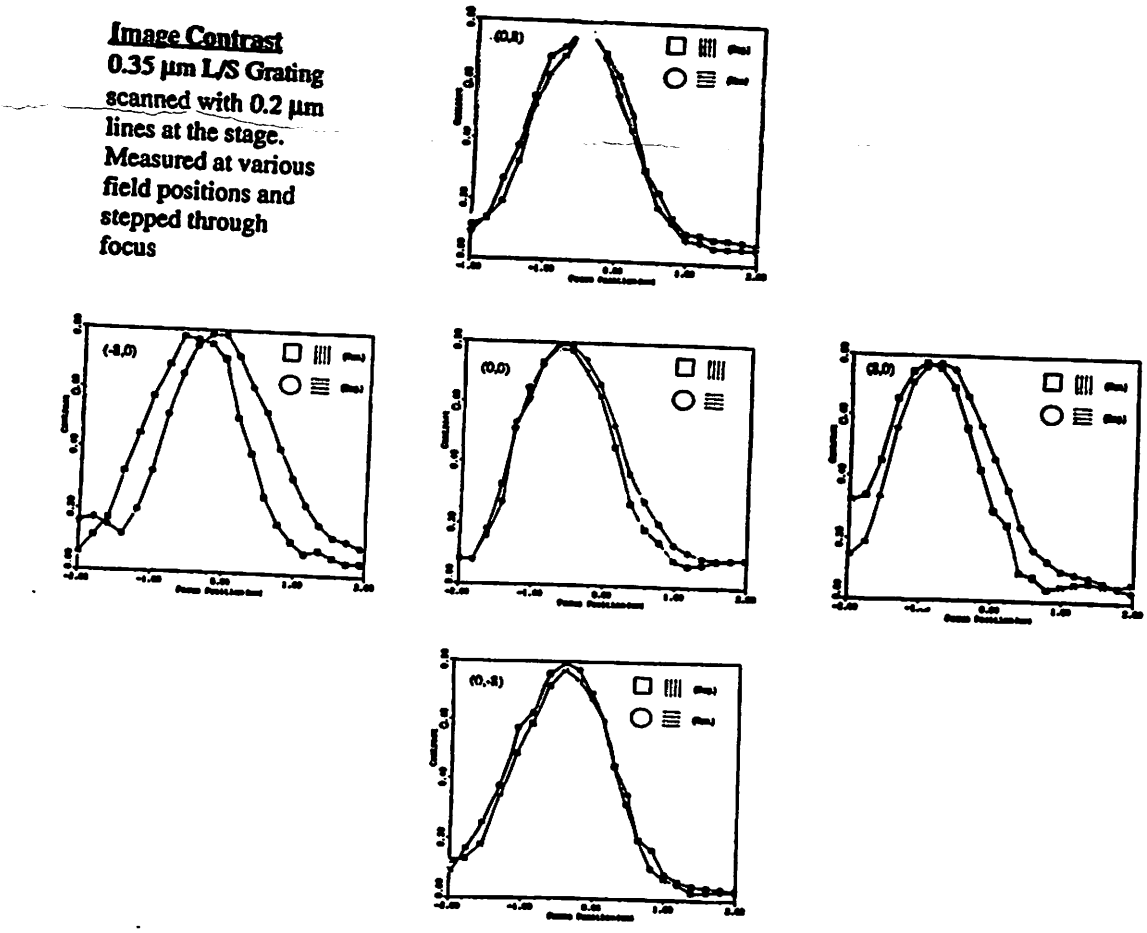

Figure 1.6 Measured contrast of 0.35µm dense L/S patterns for both orientations, sagittal and tangential, measured in the center of the image field and at four locations along the periphery, Reference [19].

It has been shown that AIM can be used to quantify the effects of spherical aberration and these effects have reasonable agreement with simulation. For well balanced lenses, all of the other primary aberrations are nearly zero on axis. Off axis, however, other aberrations become important and can limit imaging performance. The magnitude of

astigmatism can be found by measuring the difference in best focus between sagittal and tangential L/S features. Figure 1.6 shows the contrast versus focus for both orientations measured in the center of the lens and four locations along the periphery. Figure 1.7 is an expanded plot of the 10mm radius point which exhibits the greatest amount of astigmatism. The focus shift shown in this figure compares well with the value of astigmatism measured by the interferometer. Figure 1.7b shows simulated contrast versus focus with the pupil aberrations set to the third and fifth order astigmatism values measured by interferometry.

To determine the amount of astigmatism for each point in the field, a third order polynomial was fit to the measured contrast curves at each point in the field. The difference between the peak values for the sagittal and tangential features gives the amount of astigmatism. Figure 1.8 shows the results for the left-right meridian and the top-bottom meridian. The maximum amount of astigmatism can be reduced by shifting lens groups so that the measured astigmatism is symmetric about the axis along each meridian. For this lens, the astigmatism values in the top and right portions of the lens can be reduced while increasing the values in the bottom and left portions. This balancing will produce a net increase in the usable DOF.

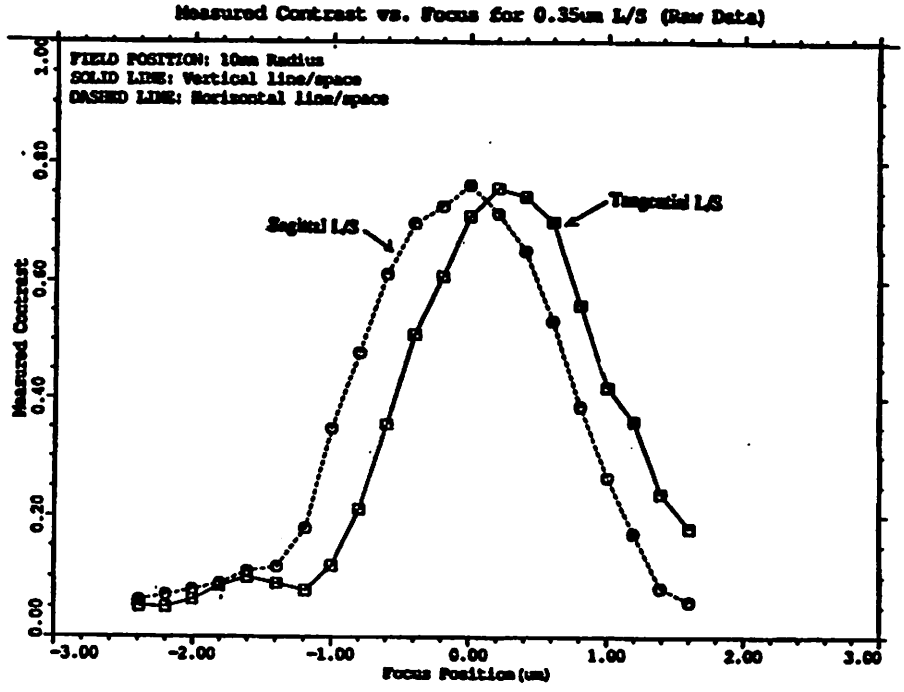

Figure 1.7 Measured image contrast versus focus for 0.35μm dense L/S patterns at the location of worst astigmatism (10mm radius location), Reference [19].

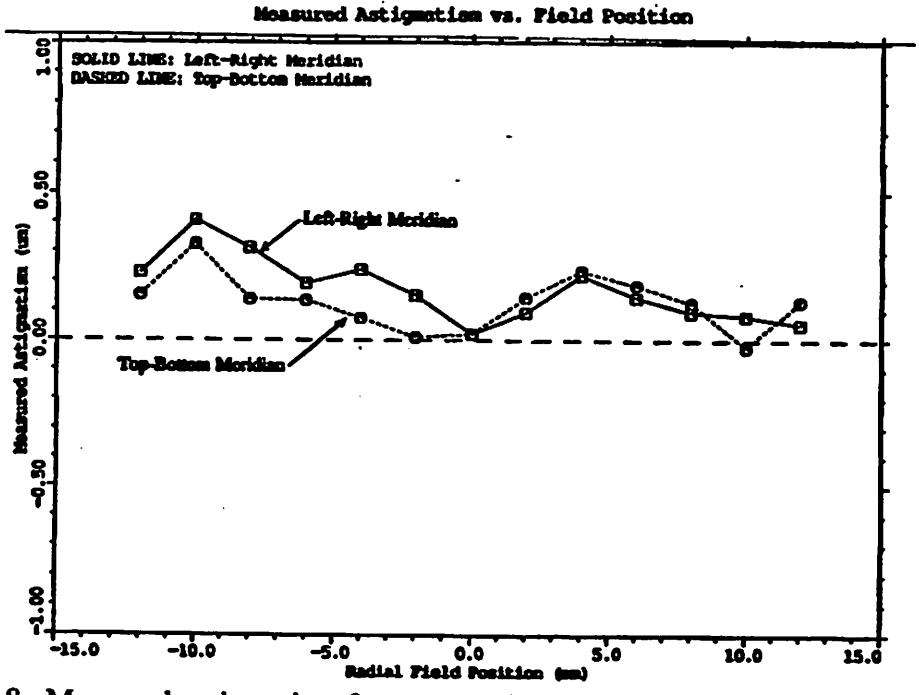

Figure 1.8 Measured astigmatism for two meridians, horizontal and vertical, Reference [19].

Field curvature can also be measured by plotting the average best focus position for the curves shown in Figure 1.6. Figure 1.9 shows the measured best focus across the field for two meridians. Field curvature has a best focus position that varies as the square of the field radius. Little of this type of field curvature is evident in Figure 1.9. Similar to astigmatism, overall lens performance could be improved by making Figure 1.9 more symmetric about the axis, leading again to an increase in the useable DOF.

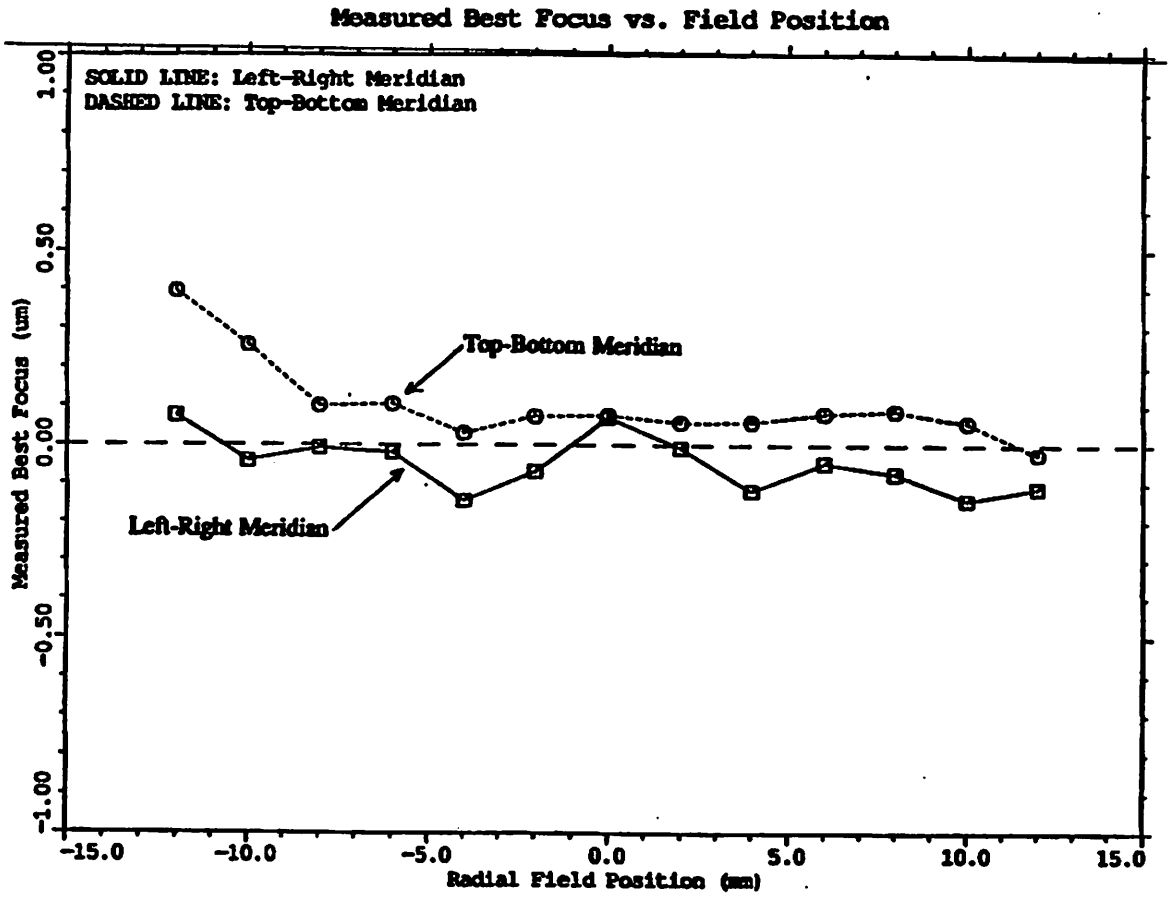

Figure 1.9 Measured best focus across the image field for two meridians. This plot shows a measured best focus that varies which is a measure of field curvature where the best focus varies as the square of the field radius.

The ability to quantify four of the five primary Seidel aberrations using direct aerial image measurements has been demonstrated in this section. Reasonable agreement has been found between interferometric measurements and the AIM results. The fifth and last Seidel aberration, coma, causes suppressed contrast for tangential features. Little or no evidence of this suppression has been found in these measurements. The Zernike terms for coma in the interferometer measurements are small and thus little effect is expected.

1.3. AIM in the Extreme Ultraviolet

Since the utility of AIM is proven in the DUV, the next logical evolution of image monitoring is to the next generation of projection lithography steppers. The adaptation of the AIM hardware to this new shorter wavelength is not as simple as merely scaling the dimensions of the aperture. Several issues complicate attempts to perform AIM at EUV wavelengths. In this section we will cover the major issues separately. Figure 1.10 illustrates the basic concept of AIM in the EUV.

1.3.1 Sampling Aperture

As mentioned previously, the signal measured by the direct aerial image measurement technique is the convolution of the aerial image under test with the response function of the scanning aperture, the Line Spread Function (LSF) for one-dimensional scanning slits and the Point Spread Function (PSF) for two-dimensional scanning pinholes. Therefore, the ideal intensity sampler would consist of an infinitesimally narrow scanning aperture but such an aperture would be impossible to fabricate and would also provide no

light signal for measurement. An aperture of finite width would act to widen the Full-Width-Half-Maximum (FWHM) value of the measured aerial image for isolated features and would act to decrease the contrast of equal L/S images. Clearly a compromise of measured signal fidelity and signal to noise must be reached.

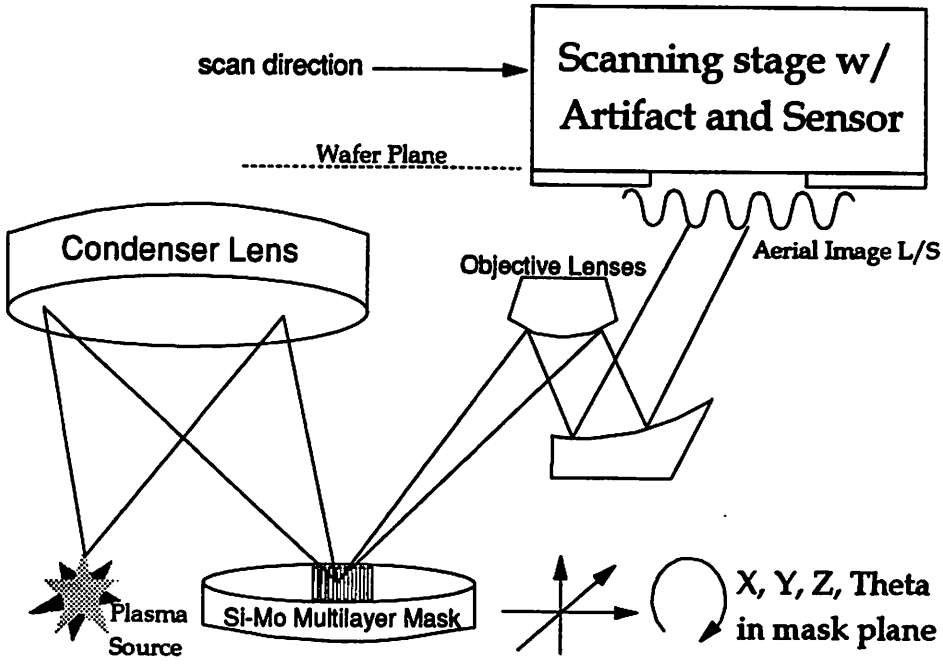

Figure 1.10 Illustration of the concept of AIM in the EUV where photons are collected from a laser plasma source with the aid of a multi-layer reflective mirror (R ~ 0.7). The artifact and photodiode are placed at the image plane to monitor the aerial image produced from the all reflective lithography system.

Theoretical simulations are carried out to more quantitatively evaluate the trade-offs in this case. Simulated aerial images of 0.5μm equal L/S patterns are convolved with detectors of various sizes to evaluate the degradation in peak L/S image contrast as a function of detector size. The simulations are done assuming a EUV wavelength of 13.4nm, a numerical aperture (NA) of 0.08, and a partial coherence value of 0.5. The simulated experiment is done for one-dimensional image scans. The response function of the detector is assumed to be an ideal top-hat function. The results of the experiment

shown in Figure 1.11 plot the peak measured image contrast versus the detector width normalized to the feature size (line or space width). The data in Figure 1.11 is normalized to the peak simulated contrast of 96%.

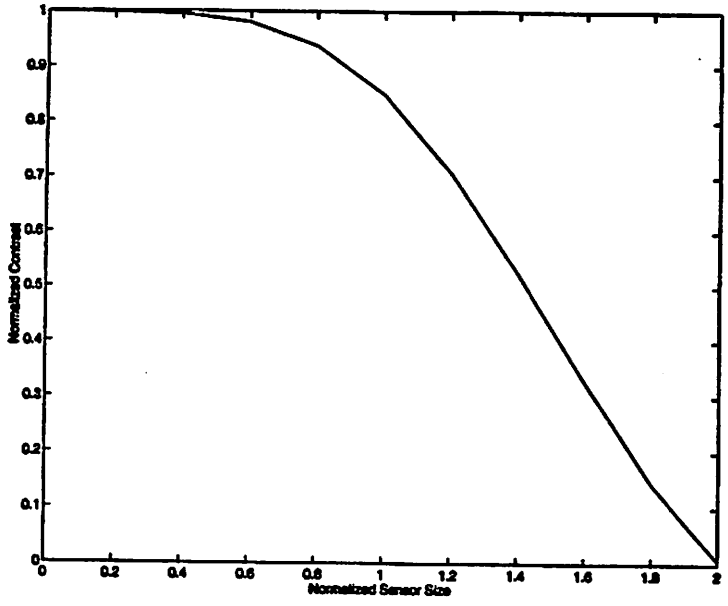

Figure 1.11 Simulated contrast of 0.5μm L/S patterns after convolution with an ideal top-hat sampling function versus width of the sampling function.

As expected, for an aperture equal to twice the minimum line width, the measured image contrast equals zero. This figure also shows that there is minimal loss in measured contrast for aperture sizes up 0.6 times minimum line width; after which significant reduction in the contrast is noted. There is a loss in image contrast of 15% for a scanning aperture equal in size to the scanned feature and falls off rapidly for larger aperture sizes. Image monitoring experiments at EUV wavelengths to measure 100nm L/S patterns, require apertures with widths ≤ 100nm. The lower limit on the width will be imposed by the minimum measurable signal determined by photon flux and noise in the collection electronics.

1.3.2 Scanning Stage

Limits on the minimum step size of the scanning stage for AIM at EUV wavelengths present a formidable obstacle. For spatial frequency band-limited signals with maximum spatial frequency f_s, the Nyquist criterion dictates that the minimum sampling frequency must be greater than or equal to $2*f_s$. For the case of the 0.1μm L/S patterns, this requirement equates to a minimum step size of 50nm. For high fidelity measurements where an oversampling rate of 10 might be desired, a minimum step size of 5nm would be required.

For scanning stages utilizing HeNe laser interferometry for positioning, the requirement of 5nm positioning accuracy would equate to $\lambda/127$. However, the vacuum enclosure of the available EUVL system (10X-I at Sandia) precludes the use of such large interferometric based stages. Several brands of pico-motors (also known as "inch-worm" motors) are available which claim resolution on this order. They accomplish this fine motion by placing two piezoelectric slabs on either side of a threaded screw. The two slabs are then pulsed in opposite directions to turn the screw similar to the motion of "fingers" turning the screw. Pico-motors are used extensively in conjunction with a feedback system to position optical elements. Their motion is deterministic over relatively large range motions (>10μm) but are less reliable for the fine motion scans required for EUVL AIM scans. Therefore, these motors were employed for large scale stage motions such as aperture-image alignment, coarse scans over several hundred microns, and PR exposures. Specifics of the performance of these pico motors will be described in subsequent sections.

For the fine step size scans in the actual image sampling, a piezo-electric stack with capacitive position measurement feedback was chosen. There are currently two vendors which market commercial stacks with capacitive feedback in a closed loop configuration. These stacks are easily capable of 5nm minimum controllable step size. The system chosen which was manufactured by Queens Gate Inc., U.K., quotes a minimum step size of less than 1nm. In practice, the minimum controllable step size was found to 3nm. Subsequent chapters report the performance of the scanning stage.

1.3.3 Signal Acquisition Electronics

1.3.3.1 Detector Quantum Efficiency in the Extreme Ultraviolet

AIM in the EUV requires a detector with the highest possible quantum efficiency and stability in the EUV regions. Furthermore, since EUV photons are absorbed by air, the detector must be compatible with vacuum operation. Several types of detectors are available for these applications including: Photomultiplier Tubes (PMTs), Streak Tubes, Multi-Channel Plates (MCPs), solid-state detectors (silicon).

There are advantages to using silicon for detecting EUV photons. Foremost is the fact that solid-state silicon detectors have been shown [20] to have the highest quantum efficiency of all the EUV detectors suitable for use as radiometric standards. Silicon detectors are also vacuum compatible and have very low noise, which make them attractive for low flux photolithography applications. Unlike PMTs and MCPs, silicon photodiodes do not need high voltages for their normal operation and can perform in vacuum environments. Electron mobilities in silicon are high ensuring fast charge collection time and high photon counting rates.

Quantum efficiency (QE) is the ratio of number of generated electron-hole pairs (EHP) per incident photon. For detecting radiation within the wavelength range of 400 to 700nm the QE of silicon is always less than unity and varies as a function of wavelength. For the shorter EUV wavelengths less than about 150nm, the quantum efficiency can be greater than one since each individual photon is greater than the ionization energy for silicon and therefore capable of producing multiple EHP.

$$QE_I = GE * CE \tag{3}$$

I define an interacting quantum efficiency QE_I in equation (3) that is the product of the generation efficiency GE and the collection efficiency CE. The GE is the fraction of incident photons that produce EHP in Silicon and suffers primarily from absorption in the oxide layer and loss to blocked areas (eg. by wires). The CE is the fraction of generated EHP that are collected by the diode and suffers primarily from surface and near-surface recombination of EHP.

Only the pairs that are separated by the internal electric field give rise to an external photocurrent. This occurs for the pairs that are generated in the depletion region or pairs that diffuse into the space charge region. For photons with energy E, incident on a silicon detector, the quantum efficiency QE then is given by:

$$QE = QE_I * \eta \qquad \text{where } \eta = E\,(eV) / 3.61 \quad [21] \tag{4}$$

The term QE is the number of EHP per incident photon seen at the output terminals of the detector. The photons used in EUV photolithography have a wavelength

of around 13.4nm or about 92.5eV in energy. Thus at 13.4nm, the ideal Si detector has a responsivitiy of 1/3.61 A/W.

The current state of semiconductor process technology allows the purchase of silicon radiation detectors with interacting quantum efficiencies in excess of 90% in the EUV region. High quantum efficiency in the EUV range for these photodetectors is required for the low photon flux measurements in EUV AIM. These diodes are manufactured using a proprietary arsenic implant followed by a laser annealing step. The top surface of the photodiode is an 8nm thermal oxide layer [20]. The specifications of the EUV diode are listed in table 1.

Active Area		$0.05mm^2$
C_D at 0V bias		6pF
Shunt Resistance (R_{sh})		1GΩ
Responsivity		0.255 A/W
NEP at 10eV		$5.6 \cdot 10^{-14}$ W/√Hz

Table 1. Specifications of EUV Photodiode (XUV-100) from International Radiation Detector, reference [20].

As an example we may wish to investigate the possibility of detecting a single EUV photon. For photon counting measurements the photodetectors are often operated in the Photoamperic mode which involves integrating the collected charge current onto a capacitor in order to obtain a measurable output voltage. One 92eV photon will generate about 23 EHP or the equivalent of $3.7 \cdot 10^{-18}$ Coulombs of charge for a $QE_I = 90\%$. If this charge were integrated on a 10pF capacitor it would produce a voltage of 0.37μV. This is not much of a signal when compared with the integrated background noise (shot noise and detector dark current) or detector noise (thermal noise of the input stage of the integrating op-amp) [54].

Typical laser plasma sources are capable of producing ~0.3mJ/cm^2 per pulse. If radiation of this intensity is incident on a 100nm diameter circular aperture there would be 2027 photons per pulse passing through the pinhole aperture. With a $QE_I = 0.9$ this equates to $4.2 \cdot 10^4$ EHP/pulse collected by the detector. This quantity of charge integrated onto a 10pF capacitor equates to 672μV. Signals on this order are above the background and detector noise floors, so they can provide meaningful information.

1.3.3.2 Signal-to-Noise Estimate for a Real EUVL System

We have estimated the signal-to-noise ratio (SNR) in the photo detector-electronics system, including thermal, flicker, diode leakage current, and shot noise sources. The signal is estimated as a function of the sampling aperture by using the known resist sensitivity of PMMA as a dosimeter. Then using the quantum efficiency model developed in the 1.3.3.1, we can estimate the number of signal quanta available for collection.

The signal-to-noise ratio of the imaging system is measured at the photodiode; where the number of photons per laser shot impinging on the surface of the photodiode is the signal quanta. The effective noise for all noise sources is referred to an equivalent number of photons (ENP) at the surface of the photodiode. The SNR can be expressed as:

$$SNR = \frac{ENP_{signal}}{\sqrt{ENP^2_{thermal} + ENP^2_{shot} + ENP^2_{leakage}}} \qquad (6)$$

Where the $ENP_{thermal}$ is the equivalent noise photon term generated from thermal noise contribution of the preamplifier input FET. This noise source is dependent upon the detector capacitance (4pF for the detector used in this experiment). Reduction of the detector capacitance is accomplished by choice of a small active area diode and by applying a reverse bias to the detector through a filtered bias network. The thermal noise from the pre-amp/FET combination is quoted as 100 electrons RMS for this value of detector capacitance. To convert this to an equivalent number of "noise photons" we use the measured quantum efficiency of the photodiode: η=20 EHP/photon [21], which yields $ENP_{thermal}$~5 photons. The signal collection electronics will be discussed in section 3.3. Only the pertinent details for estimation of the SNR are given here.

The noise term, $ENP^2_{leakage}$, stems from the leakage current of the photodiode. The effect of this dark current is minimized by using a diode with a small active area. The diodes used for these experiments have an active area of 0.05mm^2. The leakage current for the diode is 4pA. The signal pulse from the preamplifier is input to a pulse shaper with a shaping time constant of 2μsec. The filtered pulse was sampled at its peak. Silicon requires 3.63eV for the generation of an electron hole pair. Therefore the estimated contribution of the leakage current for such a diode can be estimated to be: $ENP_{leakage}$ ~ 14 photons.

The final term, ENP_{shot}, stems from shot noise. Since the emission of photons from our source follows a Poisson distribution, for N photons the ENP^2_{shot} is equal to the variance σ^2=N; hence $ENP_{shot}=\sqrt{ENP_{signal}}$. The flicker noise contribution to equation (6) is negligible for our junction field effect (JFET) input stage. The ENP_{signal} is calculated from the total slit area and a large area calibration. The estimated dose/shot is 30μC/cm^2/shot

or approximately 1000 (92.4eV) photons. Thus $ENP_{shot}=\sqrt{1000}$. Combining according to eq. 3, we obtain an estimate of the SNR equal to 29 for a slit array of 10 slits and 13 for the single slit.

1.4 Conclusion

Several methods of evaluating the aerial image produced from projection lithographic steppers are explored. Each have their respective merits. Many have the advantage of simplicity and some have *in-situ* capabilities. Many of the techniques do not remove the photoresist from the evaluation process. In some cases it is desirable to evaluate the final resist profile. Direct aerial image monitoring is presented as a technique which completely removes the photoresist step from the image evaluation.

Direct measurement of the projected aerial image of a stepper is successfully demonstrated at deep UV wavelengths on several systems [15, 17-19]. Extending this method to projection lithography at extreme ultraviolet wavelengths presents many challenges including flux, vibration, the availability and reliability of suitable scanning stages, and the fabrication of sub-100nm AIM apertures.

A silicon p-n junction photodiode is selected based upon high QE and vacuum compatability. The interacting quantuum efficiency is quoted by the manufacturer as 90% for 13.4nm photons leading to a calculated SNR of 13 for the case of a single 50μm long slit based upon dose estimations from PR experiments. Experimental results in chapters 3-5 show a signal to noise ratio of 12 for single-shot operation.

References

[1] T.A. Brunner and R.R. Allen, "*In-Situ* measurement of an Image during Lithographic Exposure", Electron Device Letters, EDL-6, p.329, July 1985.

[2] T.A. Brunner and R.R. Allen, "*In-Situ* Resolution and Overlay Measurement on a Stepper", Proc. of SPIE Vol. 565, pp. 6-13, August 1985.

[3] T.A. Brunner and S.M. Stuber, "Characterization and Setup techniques for a 5X Stepper", Proc. of SPIE, Vol. 633, p.106, 1986.

[4] W.H. Arnold and H.J. Levinson, "Focus: the critical parameter for submicron optical lithography: Part 2", Proc. of SPIE, Vol. 772, 1986.

[5] J.E. Webb, "Measurement of Optical Performance of Photolithographic Lenses", Proc. of SPIE, Vol. 480, p.133, 1984.

[6] F. Spron-Fielder and J. Williams, "Atmospheric pressure induced Reduction errors in Reduction Stepper Lenses", Proc. of SPIE Vol. 538, pp.86-90, March 1985.

[7] B.J. Lin, "Portable Conformal Mask - A Hybrid Near-UV and Deep-UV Patterning Technique", Proc. of SPIE Vol. 174, p. 114, 1979.

[8] K. Bartlett et al., "A Two layer Photoresist Process in a Production Environment", Proc. of SPIE, Vol. 394, pp. 49-56, 1983.

[9] R.A. Budd, D.B. Dove, J.L. Staples, H. Nasse, and W. Ulrich, "A New Mask Evaluation Tool, the Microlithography Simulation Microscope Aerial Image Measurement System", Proc. of SPIE, Vol. 2197, pp530-540, 1994.

[10] T.E. Adams, "Application of Latent Image Metrology in Microlithography", Proc. of SPIE, Vol. 1464, p.294, 1991.

[11] J. Milner et. al., "Latent Image Exposure Monitor Using Scatterometry", Proc. of SPIE, Vol. 1673, pp.274-283, 1992.

[12] T.A. Brunner, J.M. Lewis, M.P. Manny, "Stepper Self-Metrology using Automated Techniques", Proc. SPIE IC Metrology, Inspection, and Process Control IV, Vol. 1261, pp286-297, 1990.

[13] K.K.H. Toh, "Two Dimensional Images with Effect of Lens Aberrations in Optical Lithography", M.S. Thesis, University of California, Berkeley, May, 1988.

[14] N. Bobroff, P. Fadi, A.E. Rosenbluth, D.S. Goodman, " Bench Evaluation of Lithographic Lenses from Measurements of the Point Spread Function", Proc. SPIE Optical/Laser Microlithography I, Vol. 922, pp.376-386, 1988.

[15] A.K. Pfau, Richard Hsu, W.G. Oldham, "A two-dimensional High-Resolution Stepper Image Monitor", U.C. Berkeley, 1990.

[16] C.A. Spence, W.G. Oldham, W.N. Partlo, J.H. Brining, D. Markle, and R. Hsu, "Deep-UV Lithography with Small-Field 0.6NA 'Microstepper'", Proc. SPIE Optical/Laser Microlithography II, Vol. 1088, pp.471-482, 1989.

[17] C.H. Fields, "Direct Aerial Image Measurements", M.S. Thesis, University of California, Berkeley, December, 1993.

[18] C.H. Fields, R.J. Bojko, and W.G. Oldham, "The Use of Amorphous Silicon as a Mask Material for Deep-UV Lithography", Proc. SPIE Optical/Laser Microlithography II, Vol. 1088, pp.471-482, 1993.

[19] W. Partlo, C. Fields, and W. Oldham, "Direct Aerial Image Measurement as a Method of Testing High Numerical Aperture Microlithographic Lenses," J. Vac. Sci. Technol. B 11(6), Nov/Dec 1993, pp. 2686-2691.

[20] R. Korde, L.R. Canfield, "Silicon photodiodes with stable, near-theoretical quantum efficiency in the soft x-ray region", SPIE X-Ray Instrumentation, Vol. 1140, pp. 126 - 132, 1989.

[21] E. Sakai, Nuclear Instruments and Methods, Vol. 196, p. 121, 1982.

[22] C. Tassin, Y. Thenoz, R Lemaitre, J. Chabbal, "Thinned backside illuminated CCDs for ultraviolet, soft X-Ray, and electron-beam imaging", SPIE X-Ray Instrumentation, Vol. 1140(1989), pp. 139-149.

[23] M. Blouke, W.A. Delamere, G. Womack, "A simplified model of the back surface of a charge-coupled device", SPIE Charge-coupled Devices and Solid State Optical Sensors II, Vol. 1447, pp. 142-155, 1991.

[24] C.M. Huang, B.B. Kosicki, J.R. Theriault, J.A. Gregory, B.E. Burke, B.W. Johnson, and E.T. Hurley, "Quantum efficiency model for p+-doped back-illuminated CCD imager", SPIE Charge-coupled Devices and Solid State Optical Sensors II, Vol. 1447, pp. 156-164, 1991.

[25] H. Fiedorowics, P. Parys, and L. Ryc, "Measurements of the soft X-Ray emission from laser plasma using silicon photodiodes", SPIE X-Ray Instrumentation, Vol. 1140, pp. 518-521, 1989.

[26] E. Tegeler, M. Krumrey, "Semiconductor photodiodes as detectors in the VUV and soft X-Ray range", reprinted from Hamamatsu Technical Services.

[27] J. Barch, W. Jark, R. Wolf, and E. Tegeler, "Quantum efficiency of a GaAsP Schottky diode in the spectral range from 5eV to 1000eV", reprinted from Hamamatsu Technical Services.

[28] K.H. Brown, "Lithography: Today's Performance, Tomorrow's Challenges", OSA Optical Society of America Conference Proceedings on Extreme Ultraviolet Lithography, Vol. 35, pp. 2-9, Monterey, CA, 1994.

[29] D.L. White, J.E. Bjorkholm, J. Bokor, L. Eichner, R.R. Freeman, T.E. Jewell, W. M. Mansfield, A.A. MacDowell, L.H. Szeto, D.W. Taylor, D.M. Tennant, W.K. Waskiewics, D.L. Windt, O.R. Wood, II, "Soft X-ray Projection Lithography", Solid State Technology, pp.37-42, July 1991.

[30] R.F. Pease, "Limits of Ultraviolet Lithography", OSA Optical Society of America Conference Proceedings on Soft X-Ray Projection Lithography, Vol. 18, pp. 6-9, Monterey, CA, 1993.

[31] Hisataka Takenaka, Tomoaki Kawamura, Yoshikazu Ishii, Tsuneyuki Haga, and Hiroo Kinoshita, "Evaluation of Mo-Based Multilayer EUV Mirrors", OSA Optical Society of America Conference Proceedings on Extreme Ultraviolet Lithography, Vol. 35, pp. 26-32 , Monterey, CA, 1994.

[32] D.P. Gaines, S.P. Vernon, G.E. Sommargren, and D.R. Kania, "Coating Strategy for Enhancing Illumination Uniformity in a Lithographic Condenser", D.P. Gaines, S.P. Vernon, G.E. Sommargren, and D.R. Kania, OSA Optical Society of America Conference Proceedings on Extreme Ultraviolet Lithography, Vol. 35, pp. 41-46, Monterey, CA, 1994.

[33] S.P. Vernon, M.J. Carey, D.P. Gaines, and F.J. Weber, "Multilayer Coating for the EUV Lithograph front-end Test Bed", OSA Optical Society of America Conference Proceedings on Extreme Ultraviolet Lithography, Vol. 35, pp. 33-40 , Monterey, CA, 1994.

[34] T.D. Ngyuen, C. Kan-Malek, and J.H. Underwood, "Achievement of Low Stress in Mo/Si Multilayer Mirrors", OSA Optical Society of America Conference Proceedings on Extreme Ultraviolet Lithography, Vol. 35, pp. 56-60 , Monterey, CA, 1994.

[35] J.H. Underwood, E.M. Gullikson, W. Ng, A. Ray-Chaudhuri, and F. Cerrina, "Effect of contamination and Oxide Layers on Scattering and Reflectivity of Multilayer Mirrors", OSA Optical Society of America Conference Proceedings on Extreme Ultraviolet Lithography, Vol. 35, pp. 61-67, Monterey, CA, 1994.

[36] E.L. Church and P.Z. Takacs, "Specifying the Surface Finish of X-Ray Mirrors", OSA Optical Society of America Conference Proceedings on Soft X-Ray Projection Lithography, Vol. 18, pp. 105-107 1993.

[37] K.B. Nyugen, D.T. Attwood, T. Mizota, T. Haga, and H. Kinoshita, "Imaging of EUV Lithographic Masks with Programmed Substrate Defects", OSA Optical Society of America Conference Proceedings on Extreme Ultraviolet Lithography, Vol. 35, pp. 193-203, Monterey, CA, 1994.

[38] D.R. Kania, F.J. Weber, S.P. Vernon, A. Hawryluk, S.L. Baker, A. M. Bolub, A. Shikata, and E.C. Grady, "Quartz Substrates for EUV Lithography Reticles", OSA Optical Society of America Conference Proceedings on Extreme Ultraviolet Lithography, Vol. 35, pp. 217-221, Monterey, CA, 1994.

[39] S.P. Vernon and S.L. Baker, "Recovery of EUV Lithography Substrates", OSA Optical Society of America Conference Proceedings on Extreme Ultraviolet Lithography, Vol. 35, pp. 222-226, Monterey, CA, 1994.

[40] Yasuyuki Saito, "Discussion of Mask Alignment Accuracy for EUV Lithography", OSA Optical Society of America Conference Proceedings on Extreme Ultraviolet Lithography, Vol. 35, pp. 227-233, Monterey, CA, 1994.

[41] D.R. Kania, D.P. Gaines, M. Hermann, J. Honig, R. Hostetler, R. Levesque, G.E. Sommargren, R. C. Spitzer, and S.P. Vernon, "High Average Power Laser for EUV Lithography", OSA Optical Society of America Conference Proceedings on Extreme Ultraviolet Lithography, Vol. 35, pp. 234-237, Monterey, CA, 1994.

[42] R.C. Spitzer and D.P. Gaines, "Advanced Source Studies on Laser Produced Plasmas for EUV Lithography", OSA Optical Society of America Conference Proceedings on Extreme Ultraviolet Lithography, Vol. 35, pp. 243-247, Monterey, CA, 1994.

[43] G.D. Kubiak, K.D. Krenz, K.W. Berger, T.G. Trucano, P.W. Fisher, and M.J. Gouge, "Cryogenic Pellet Laser Plasma Source Targets", OSA Optical Society of America Conference Proceedings on Extreme Ultraviolet Lithography, Vol. 35, pp. 248-254 , Monterey, CA, 1994.

[44] P.D. Rockett, J.A. Hunter, G.D. Kubiak, K.D. Krenz, H. Shields, and M. Powers, "Detailed EUV Characterization of Laser-Plasma Sources for EUV Lithography", OSA Optical Society of America Conference Proceedings on Extreme Ultraviolet Lithography, Vol. 35, pp. 255-259, Monterey, CA, 1994.

[45] D.A. Tichenor, A.K. Ray-Chaudhuri, G. D. Kubiak, S. J. Haney, K. W. Berger, R.P. Nissen, G.A Wilkerson, R.H. Stulen, P.H. Paul, R.W. Arling, T.E. Jewell,

Edita Tejnil, et. al., "10X Reduction Imaging at 13.4nm", OSA Optical Society of America Conference Proceedings on Extreme Ultraviolet Lithography, Vol. 35, pp. 89-97, Monterey, CA, 1994.

[46] O.R. Wood, II, J.E. Bjorkholm, K.F. Dreyer, L. Fetter, M.D. Himel, R.R. Freeman, D.M. Tennant, J.E. Griffith, G.N. Taylor, W. K. Waskiewicz, D.L. White, D.L. Windt, A. A. MacDowell, B. La Fontaine, B.M. Lum, A.R. Neureuther, J.B. Kortright, E.M. Gullikson, and K.D. Nguyen, "Experiments and Simulation of EUV Lithographic resist Patterning at Wavelengths from 7 to 40nm", OSA Optical Society of America Conference Proceedings on Extreme Ultraviolet Lithography, Vol. 35, pp. , Monterey, CA, 1994.

[47] D.A. Tichenor, G. D. Kubiak, M.E. Malinowski, S. J. Haney, K. W. Berger, R.H. Stulen, L.A. Brown, O.R. Wood, II, J.E. Bjorkholm, D.M. Tennant, R.R. Freeman, T.E. Jewell, W. K. Waskiewicz, D.L. White, and D.L. Windt, "Soft X-Ray Projection Imaging Using a Laser Plasma Source", OSA Optical Society of America Conference Proceedings on Soft X-Ray Projection Lithography, Vol. 12, pp. 54-57, 1991.

[48] Z. Tan, A. A. MacDowell, B. La Fontaine, J. Russo, J.E. Bjorkholm, D. Tennant, D. Taylor, M. Himel, O.R. Wood, II, R.R. Freeman, W.K. Waskiewicz, D.L. Windt, D. White, S. Spector, A.K. Ray-Chaudhuri, and R.H. Stulen, "At-Wavelength Metrology of EUV Cameras using Lateral-Shearing Interferometry", OSA Optical Society of America Conference Proceedings on Extreme Ultraviolet Lithography, Vol. 35, pp. 151-160, Monterey, CA, 1994.

[49] A.K. Ray-Chaudhuri, R.H. Stulen, W. Ng, F. Cerrina, S. Spector, Z. Tan, J. Bjorkholm, and D. Tennant, "EUV Metrology of Multilayer Optics", OSA Optical Society of America Conference Proceedings on Extreme Ultraviolet Lithography, Vol. 35, pp. 161-166, Monterey, CA, 1994.

[50] B. La Fontaine, D.L. White, A.A. MacDowell, Z. Tan, D.M. Tennant, and O.R. Wood, II, "Extreme Ultraviolet Moiré Interferometry", OSA Optical Society of America Conference Proceedings on Extreme Ultraviolet Lithography, Vol. 35, pp. 167-170, Monterey, CA, 1994.

[51] B. La Fontaine, A.A. MacDowell, Z. Tan, G.N. Taylor, D.L. White, D.M. Tennant, and O.R. Wood, II, "Real-Time, Sub-Micron Fluorescence Imaging of Extreme Ultraviolet Aerial Images", OSA Optical Society of America Conference Proceedings on Extreme Ultraviolet Lithography, Vol. 35, pp. 177-181, Monterey, CA, 1994.

[52] K.A. Goldberg, R. Beguiristain, J. Bokor, H. Medecki, K. Jackson, D.T. Attwood, G.E. Sommargren, J.P. Spallas, and R. Hostetler, "Point-Diffraction Interferometry at EUV Wavelengths", OSA Optical Society of America

Conference Proceedings on Extreme Ultraviolet Lithography, Vol. 35, pp. 134-141, Monterey, CA, 1994.

[53] A.K. Ray-Chaudhuri, W. Ng, F. Cerrina, S. Spector, Z. Tan, J. Bjorkholm, D. Tennant, and R.H. Stulen, "EUV Metrology of Multi-layer Optics", OSA Optical Society of America Conference Proceedings on Soft X-Ray Projection Lithography, Vol. 18, 1993.

Chapter 2

Sampling Aperture Fabrication and Characterization

2.1 Introduction

Image monitoring in the EUV requires narrow scanning apertures of width 100nm or less compared to the apertures in the image monitoring artifacts for DUV AIM that are twice this width. Several issues complicate the fabrication but the patterning approach and the absorber material are the two key factors in our control which determine practical slit/pinhole size and performance.

2.2 Absorber Materials

The sampling artifacts in our image monitoring experiments on DUV steppers utilized a thin layer of amorphous silicon (80nm) as the absorber, deposited on a 500μm thick quartz blank wafer. Current EUV lithography systems operate at a wavelength of 13.4nm. The short absorption depth of 13.4nm radiation in all materials precludes use of blanks for the support of the absorber. The absorption coefficient of SiO_2 at 13.4nm is: $\mu_{SiO2}=8.1\mu m^{-1}$ requiring either submicron membranes for support or the use of "stencil" patterns. Other materials of choice are Silicon ($\mu_{Si}=1.71\mu m^{-1}$) and Silicon Nitride ($\mu_{Si3N4}=8.6\mu m^{-1}$). Clearly no matter what material is chosen, very thin membranes are required.

Silicon nitride membranes are chosen as the support membrane over silicon membranes owing to their higher tensile strength and toughness as well as ease of fabrication. Pure silicon membranes are especially susceptible to damage when the vacuum chamber is both opened to atmosphere or pumped to vacuum.

The choice of absorber material used for the aperture is affected by two major concerns. First, it must be compatible with available processing techniques. Second, the absorber chosen should have the highest possible extinction coefficient for 13.4nm radiation. Figure 2.1 is a plot of mass absorption coefficient (cm^2/g) versus atomic number (Z) for 13.4nm radiation. Several materials initially appear to meet both of the requirements with mass absorption coefficients around 10^5 cm^2/g and process compatibility. Table 1 lists several potential absorber materials, with their mass absorption coefficients, standard pressure and temperature (STP) densities, absorption coefficients, and film thickness required to achieve 1% transmission. For reference comparison, silicon and silicon-nitride are also included in the table.

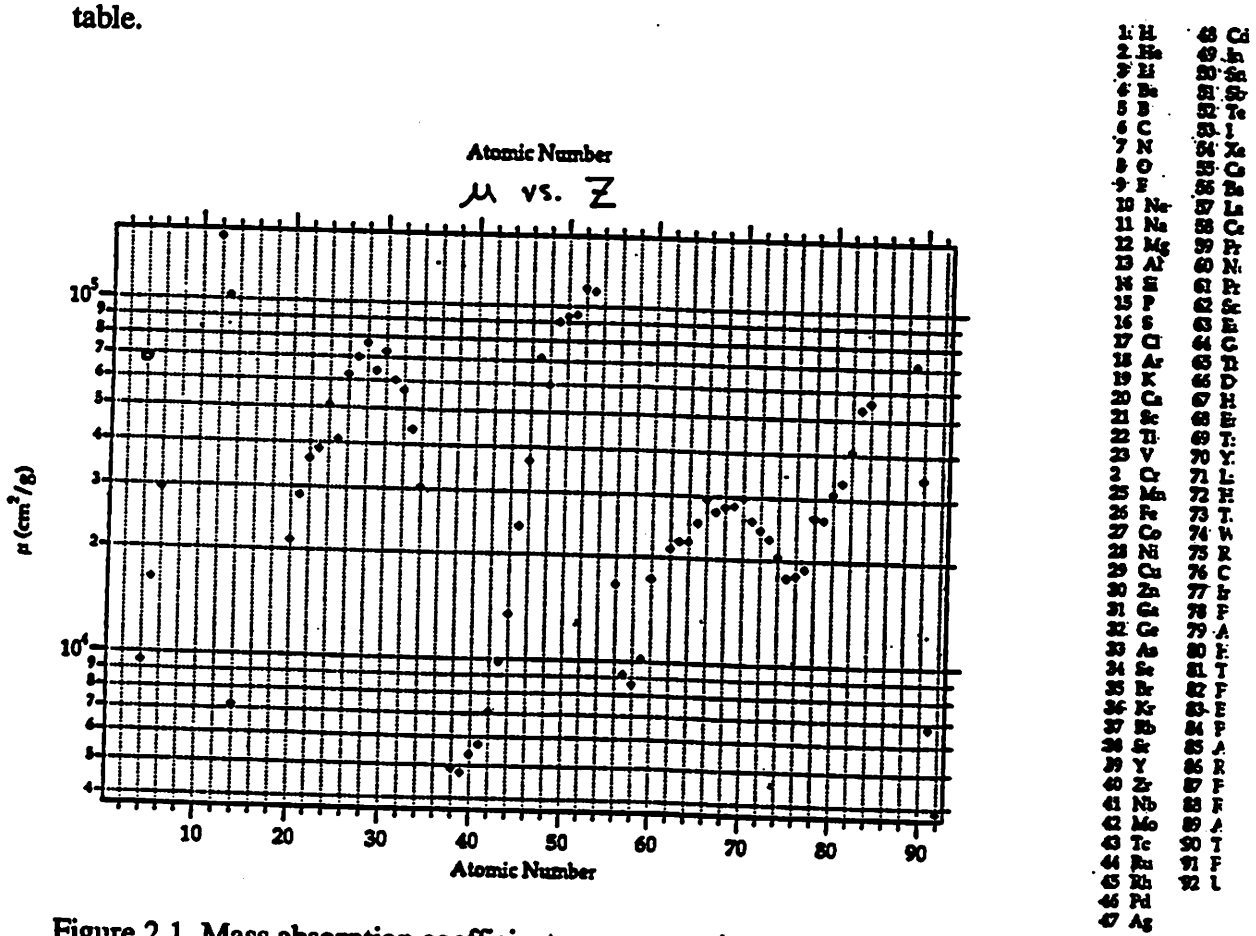

Figure 2.1 Mass absorption coefficient versus atomic number for 13.4nm radiation, Reference Center for X-ray Optics Home page: http://www-cxro.lbl/gov/optical_constants.

Material	Z	μ/ρ [cm^2/g]	ρ [g/cm^3]	μ [μm^{-1}]	$t_{1\%}$ [nm]
Al	13	10^5	2.69	26.90	171
Cr	24	$5 \cdot 10^4$	7.18	35.90	128
Cu	29	$6.5 \cdot 10^4$	8.94	58.11	79
Ge	32	$5.7 \cdot 10^4$	5.31	30.25	152
Ag	47	$7 \cdot 10^4$	10.48	73.36	63
W	74	$2 \cdot 10^4$	19.30	38.60	119
Au	79	$2.6 \cdot 10^4$	18.85	49.01	94
Co	27	$7.0 \cdot 10^4$	8.90	62.3	74
Ni	28	$7.8 \cdot 10^4$	8.90	69.42	66
In	49	$8.8 \cdot 10^4$	7.30	64.24	72
Sb	51	$9.5 \cdot 10^4$	6.69	63.56	73
InSb	N/A	$9.02 \cdot 10^4$	7.31	65.96	70
Si_3N_4	N/A	$2.5 \cdot 10^4$	3.44	8.60	536
Si	14	$7.34 \cdot 10^3$	2.33	1.71	2693

Table 1. EUV (13.4nm) absorbance specifications for several potential absorber materials.

Based solely on absorption coefficient, the optimum choice of material would be Silver with μ=73.36μm^{-1}. However, several materials show extinction coefficients of comparable magnitude. For instance, the absorption coefficient of Nickel is 1.4% lower than Silver. The elements and compounds of Indium and Antimony possess an extinction coefficient only about 10.5% lower than Silver. Similar to these is Cobalt with an EUV attenuation coefficient 15.1% higher than Ag. Copper also exhibits high attenuation to EUV photons with 20.8% less attenuation than Silver.

Compatibility with existing deposition and patterning techniques explains the widespread use of Germanium as an absorber material for many EUV experiments. Although

Ge requires 2.42 times the thickness of Ag to achieve the same magnitude of attenuation, Ge has a well defined etch using Fluorine-based plasmas. Cobalt deposited using electron-beam evaporation has also been used for such applications [5].

The elements Indium and Antimony are interesting for this application since they both exhibit high attenuation to EUV. Indium has a very high vapor pressure and can be easily deposited using thermal evaporation but exhibits poor film-forming properties. Several methods were used in an attempt to preserve/repair the quality of In films including annealing, flash evaporation, and low temperature evaporation, without success.

These problems are overcome by the use of the compound Indium Antimonide which is also easily deposited by means of thermal evaporation. The addition of Antimony to Indium results in uniform as-deposited films. The final process sequence chosen did not require etching of InSb films.

2.3 Lithographic Patterning Options

2.3.1 Electron-beam Lithography Approaches

Electron Beam Lithography offers the capability of patterning sub-quarter-micron features. In fact features as small as 10 nanometers have been patterned with the use of e-beam lithography using lift-off and special pattern transfer techniques [11-17]. This form of lithography has many interesting possibilities for the fabrication of the scanning apertures required for EUV AIM.

Electron beam lithography differs from conventional optical lithography in many areas. One difference is the photoresist used in e-beam lithography: Poly(methyl-methacrylate)

(PMMA). While PMMA is capable of good resolution (on the order of 5nm [10]), it suffers from poor plasma etch resistance which limits its effectiveness in pattern transfer. Another factor affecting e-beam lithography is proximity effects.

2.3.1.1 E-beam Factorial Experiment Results

Appendix A contains the results of a 3^5 full factorial experiment to analyze the factors that affect the ultimate resolution achievable through electron-beam (e-beam) lithography. The exposure tool in this experiment was a Jeol 6400 Scanning Electron Microscope (SEM) modified to perform e-beam lithography. The five variables investigated are electron energy expressed in kV, exposure dose in $\mu C/cm^2$, photoresist thickness, line spacing pitch, and drawn linewidth. The results of the experiment are analyzed using regression. The significance of each parameter and cross-interactions is analyzed and a model fit to significant terms.

The main factors affecting the resulting linewidths in electron-beam lithography are analyzed using linear regression. Regression was used to fit a model to measured linewidth data from the 3^5 factorial experiment. The model contains the five variables of exposure dose, electron energy, line pitch, resist thickness and drawn linewidth. The results of the analysis point to exposure dose as the most important factor, after drawn linewidth, in determining the developed CD.

From the analysis, we obtain a measure of both the inter and intra-proximity effects. Electron beam writing energy is found to be nearly as significant as dose and plays the major role in reducing proximity effects by reducing the forward-scattered distribution width of the beam. Although line pitch plays an important role in determining the magnitude of the inter-

proximity effects, it was found that it is possible to overcome this effect by the proper choice of exposure dose. These models are used to guide the choice of operating parameters for the e-beam lithography in the following sections.

2.3.1.2 Patterning Techniques

(a) Single-layer Photoresist

As mentioned in the previous section, the highest resolution resist, PMMA, has poor plasma etch resistance. Our experiments demonstrated a PMMA etch rate of ~90nm/min. in Chlorine-based plasmas and an etch rate of ~100nm/min. in Fluorine-based plasmas. These rates are too high to permit pattern transfer into the relatively thick absorber layer required for say Germanium (300nm for 1% EUV photon transmission).

(b) Hard Mask Pattern Transfer

Since a single layer of photoresist alone is insufficient for the transfer of the e-beam pattern into the absorber material, another technique is attempted. A hard mask is investigated for the case of a Germanium absorber layer with a layer of Aluminum as the hard mask, as depicted in Figure 2.2 The substrate is coated with the absorber (Ge - 300nm), then a thin layer of Al (50nm) is evaporated and finally coated with layer of PMMA. Electron beam lithography is used to define the patterns in the top layer of PR. After developing the PR, the pattern is transferred to the Al through an anisotropic dry etch in a chlorinated plasma.

The final step in the process is to transfer the pattern into the bulk Ge. This step is accomplished through an anisotropic dry etch in a fluorinated plasma. The thin aluminum

layer is not etched by the fluorine in the plasma and is only removed by ion bombardment which acting on its own is a very slow process (~1nm/min.). The Al layer therefore serves as an efficient hard mask for transfer of the pattern into the Ge absorber layer. Figure 2.2 illustrates the final results. The exact steps and parameters of the process are detailed in appendix B5.

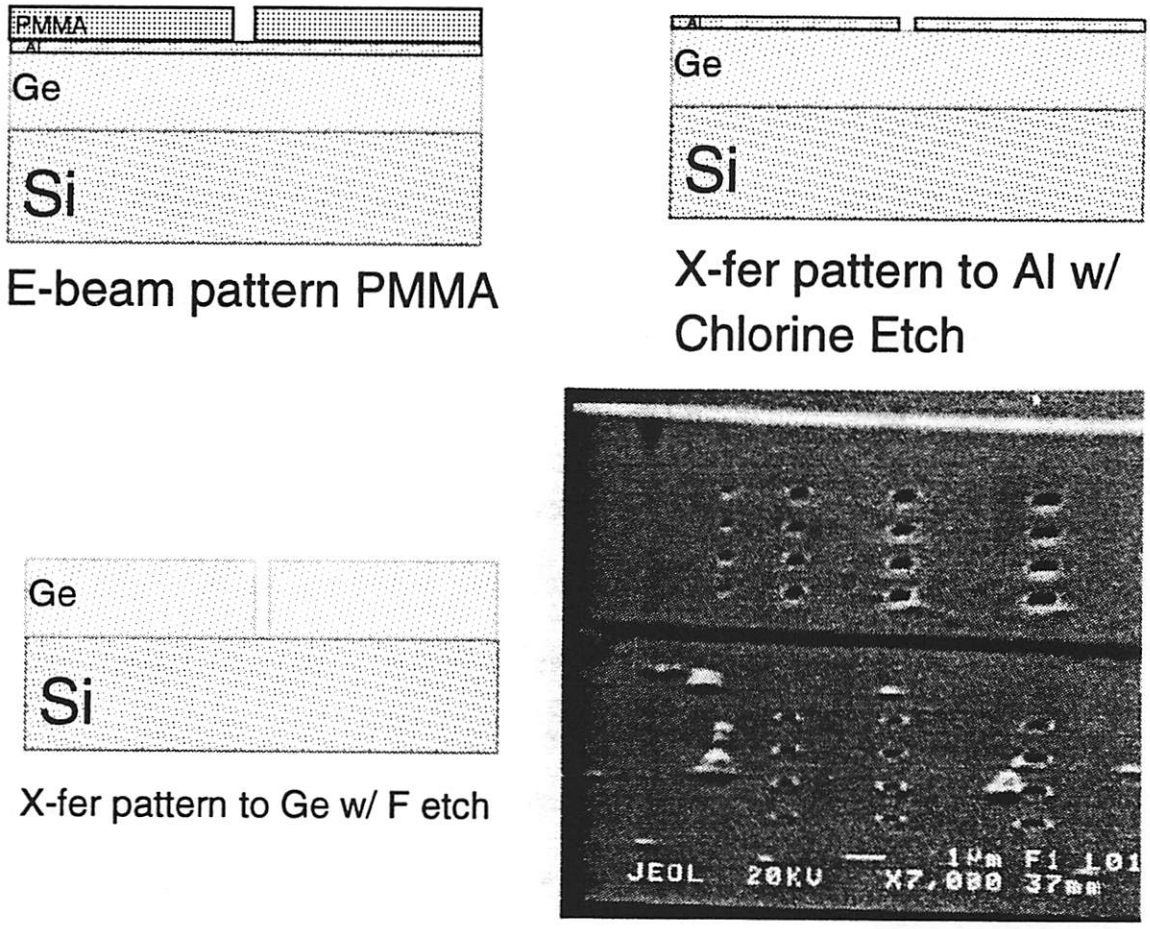

Figure 2.2 Hard mask pattern transfer technique developed to pattern a thick Germanium layer using electron-beam lithography. The e-beam pattern is defined in the top layer of PMMA PR then transferred to the thin Aluminum layer by a brief Chlorine RIE, this thin Aluminum is then used as a hard-mask to etch the thick Ge film in a Flourine-based RIE.

(c) Double Lift-off Technique

Another approach explored in this work for patterning of sub-100nm features employs two lift-off steps to form the final pattern. The substrate is coated with a thick (250nm) layer of super-hard baked photoresist (SHBPR) with a layer of PMMA (100nm) as the initial image formation layer.

After PMMA exposure and development, a thin Aluminum layer is evaporated onto the chip. The first lift-off is then performed in a bath of acetone heated to 90deg. C. The lift-off leaves small dots or lines on the chip as shown in Figure 2.3. These small metal formations are then used as a hard mask to transfer the patterns into the bulk SHBPR. A dry etch is performed in a parallel plate reactive ion etcher (RIE) with an oxygen plasma operating at low power to insure an anisotropic etch. Over-etching the chip further reduces the width of the features. The resulting pillars of SHBPR for the fabrication of pinhole apertures can be seen in Figure 2.4. The absorber material is then evaporated onto the pillars and chip. The second lift off, which is a two step process first placing the chip in a heated bath of acetone that is also ultrasonically agitated. This bath removes the top caps of aluminum but does not remove all of the photoresist (PR) from the bottom corners of the features. This residual PR is removed from the trenches by a standard descum etch which is a non-directional etch performed in a high-powered oxygen-based plasma. An array of pinholes fabricated with this technique is shown in Figure 2.5.

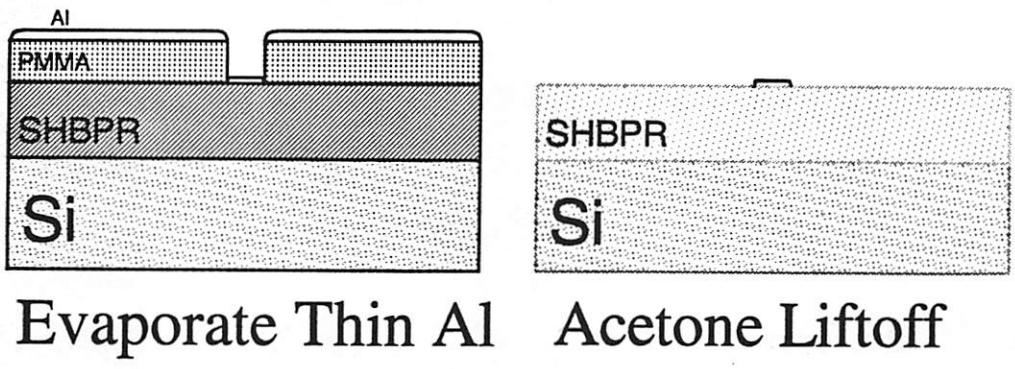

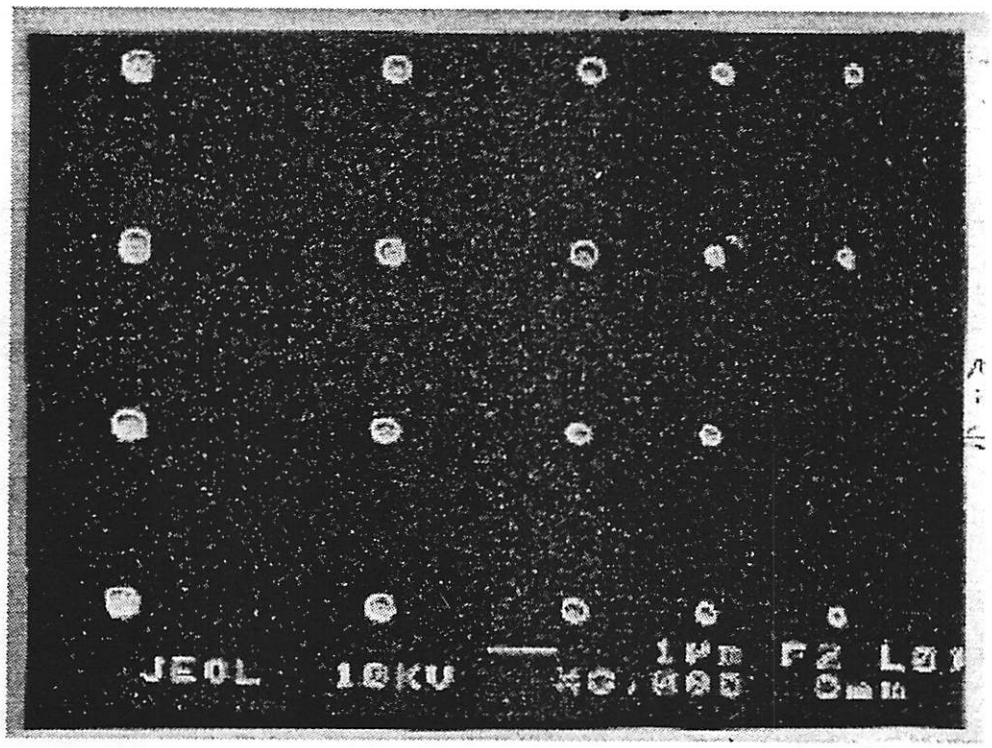

Figure 2.3 Aluminum features on a 0.25μm layer of PR defined by lift-off using e-beam lithography and thermal evaporation of 30nm of Aluminum.

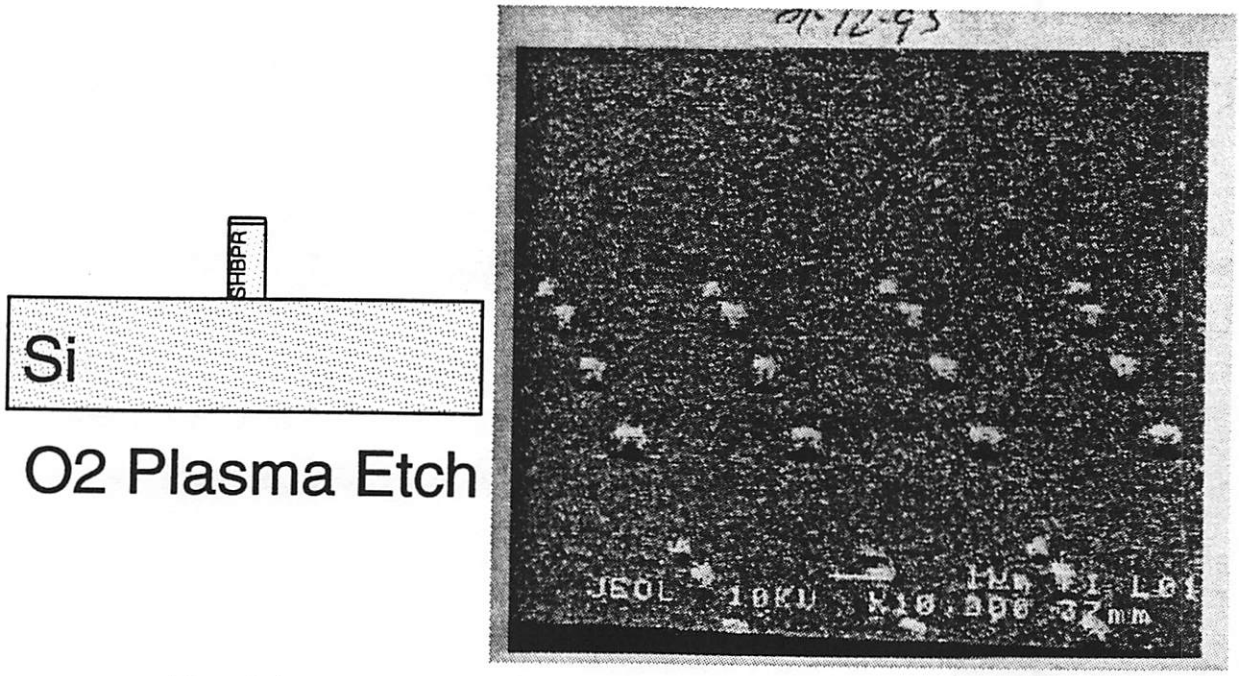

Figre 2.4a Pillars of SHBPR; cross-section illustration and SEM micrograph

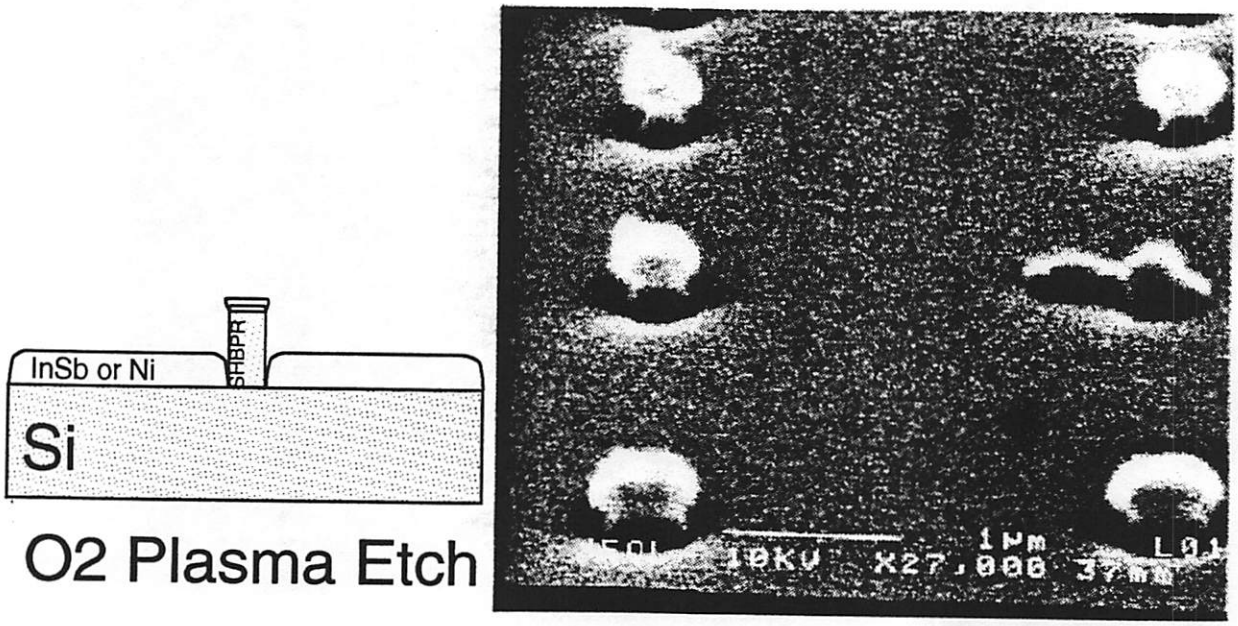

Figre 2.4b Double lift-off process prior tofinal lift-off; cross-section illustration and SEM micrograph

Figure 2.4 Pillars of SHBPR defined using an Oxygen-based RIE with the Al hard mask from Figure 2.3.

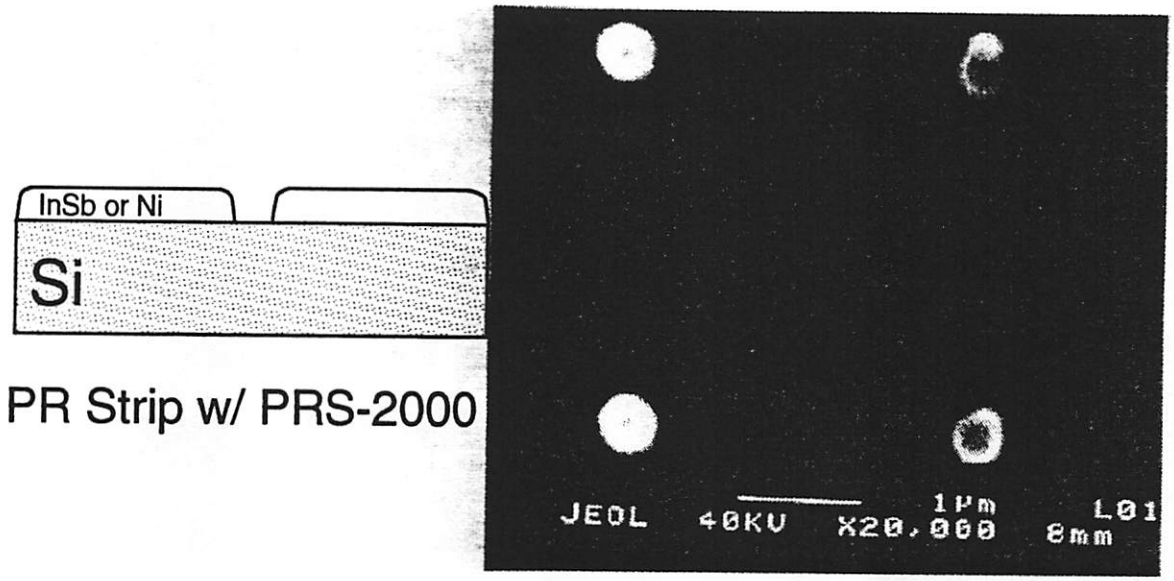

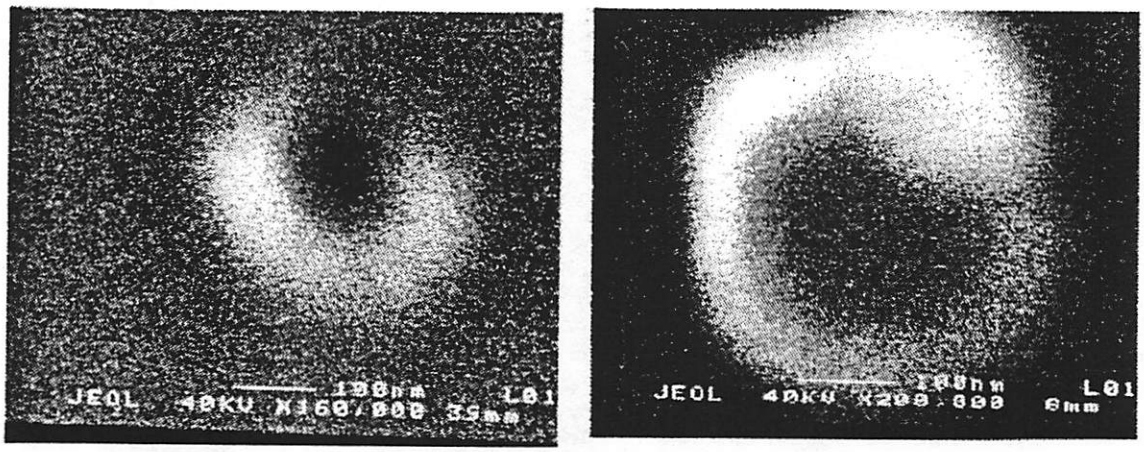

Figure 2.5 SEM micrograph of pinholes defined in 80nm of InSb using the double lift-off technique.

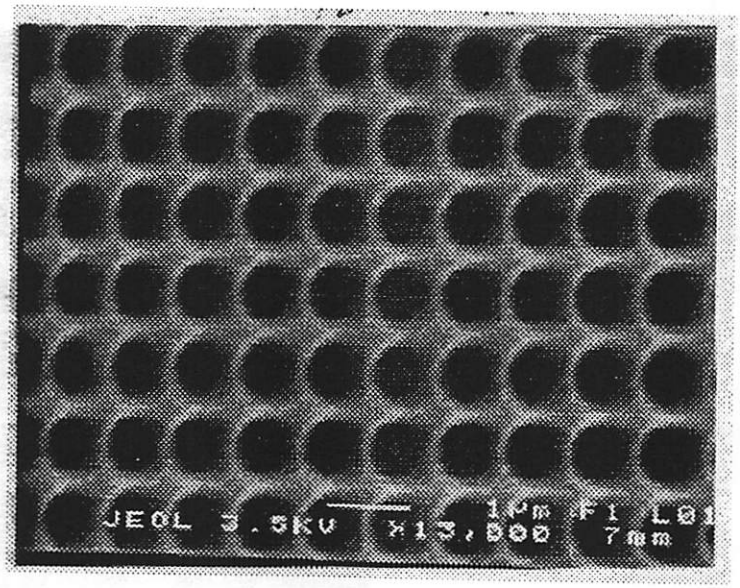

Figure 2.6a Array of pinholes in a silicon nitride membrane.

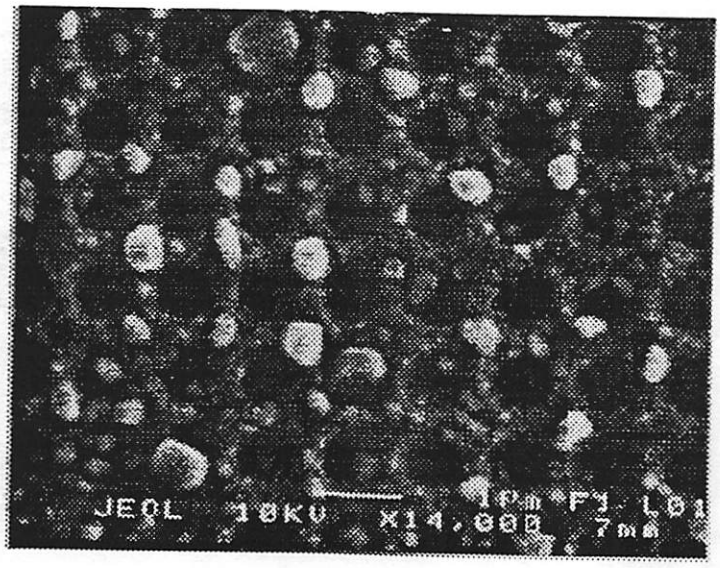

Figure 2.6b Pinhole array after absorber deposition.

Figure 2.6 Pinholes defined on a 120nm silicon nitride membrane by using a DUV stepper and a Flourine-based RIE to pattern circa 0.25μm features in the nitride film. The final pinholes are produced by thermal evaporation of an EUV absorber material, InSb in this test.

2.3.2 Focused Ion Beam Lithography Approach

2.3.2.1 Fabrication

The double lift-off technique was successful in fabricating very small features on top of a substrate, but the use of InSb as the absorber precludes plasma processing to etch these patterns completely through the substrate membrane itself. Even with a nitride layer as thin as 700A, 45% of the signal is lost in the membrane.

An artifact fabrication process is developed where the apertures are first patterned in a thin free-standing silicon nitride membrane by either optical, e-beam, or focus ion-beam (FIB) lithography followed by absorber evaporation which determines the final width of the aperture. Initial tests of this technique using optical lithography to define pinholes in the nitride layer (Appendix B6) were successful in fabricating 100nm pinholes (see Figure 2.6).

Silicon nitride membranes are patterned on 4 inch silicon wafers by optical lithography and an anisotropic etch of the silicon following the steps outlined in appendix B2. The nitride membranes used for these experiments have side length of 100μm to reduce background transmission of EUV photons through the bulk area of the membrane. A thick absorber layer (100nm of InSb) is then evaporated onto the backside of the membrane. This layer serves three purposes: (1) to further reduce the background transmission of the membrane, (2) fill in membrane defects, and (3) to absorb the "tails" of the FIB distribution leaving only the central portion of the beam to define the opening in the nitride layer.

The initial slit is cut directly into the nitride membrane from the backside using the FIB eliminating the complicated front-to-back alignment necessary with previous techniques. The wide tails of the FIB profile approximate a Lorentzian distribution resulting in narrow slit with steep sidewalls in the nitride but a wider profile in the bottom absorber. A FIB aperture

size of 100μm is used resulting in a beam size of 30nm. The total dose required to mill completely through the membrane/absorber stack is 0.6 Coulombs.

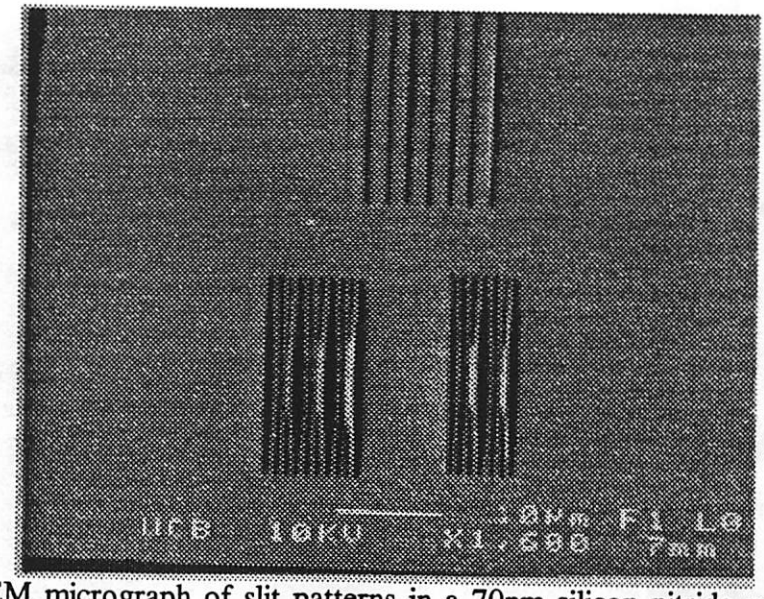

Figure 2.7 SEM micrograph of slit patterns in a 70nm silicon nitride membrane. The Three sets of slits shown vary in slit number and pitch. Stress in the nitride film results in distortion of the patterns at all pitches tested.

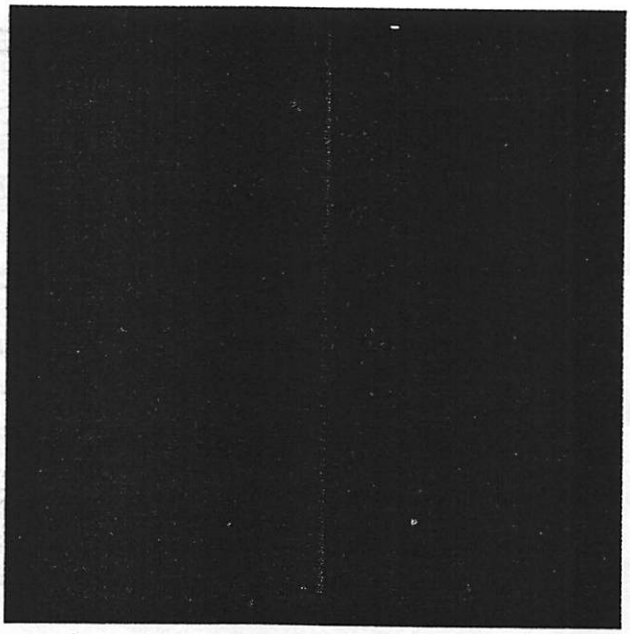

Figure 2.8 A FIB image of a 100μm slit milled using the same FIB with a beam diameter of 30nm. The patterning of the single slit using 4μm slit segments with 1μm spacers, prevents nitride film stress from distorting the resulting slit width. Imaging with the FIB also removes a portion of the backside InSb absorber which must be replaced by subsequent deposition to restore the background attenuation.

Initial apertures where a single continuous FIB cut defines the aperture, are distorted owing to stress in the Si_3N_4 layer as seen in Figure 2.7. This problem is overcome by patterning the single long slit as a series of smaller, collinear, lines. Figure 2.8 shows a FIB image of a 50μm AIM slit aperture consisting of 20 4μm segments spaced 5μm apart. The new milling strategy allows 1μm strips of Si_3N_4 between the slit segments to hold the two edge together and minimize the impact of nitride film stress.

The final step of the process is the deposition of additional absorber layers onto the front and backside of the membrane to define the final aperture width and profile. Signal to noise requirements and the need to repair nitride defects determine the absorber thickness deposited. Radiation that passes, attenuated, through the bulk of the membrane reduces the signal to noise ratio of the measurement. The ratio of the number of EUV photons passing through the AIM aperture to the number of photons that pass through the membrane and absorber film is defined as the alpha ratio (α):

$$\alpha \equiv \frac{\gamma_{AIM}}{\gamma_{Back}} \cong \frac{N \cdot A_{slit} \cdot T_{slit}}{(A_{back} - N \cdot A_{slit}) \cdot T_{back}} \tag{1}$$

Where γ_{AIM} and γ_{back} represent the respective number of photons passing through the AIM aperture and the background. For an artifact with N apertures, α is a function of the ratio of their respective areas (A) times the transmission (T) of that region. Assuming that the transmission through the slit is equal to 1, equation 1 simplifies to:

$$\alpha \cong \frac{N \cdot l_{slit} \cdot w_{slit}}{(l^2_{back} - N \cdot l_{slit} \cdot w_{slit}) \cdot T_{back}} \tag{2}$$

Where l_{AIM} is the w_{AIM} are the length and width, respectively, of the aperture and l_{back} the side-length of the square membrane.

Then for a single slit (N=1) of length 50μm and width 0.1μm and assuming a support membrane that is square with length 100μm, the background transmission required to achieve a 1% reduction in SNR (α = 100) would be $T_{back} = 5 \cdot 10^{-6}$ which would require a total of 185nm of InSb. If a slit array of 10 slits, each 50μm in length, were employed, the background transmission requirements drop to $5 \cdot 10^{-5}$ or 150nm of InSb absorber film.

Although the total absorber thickness requirement is now defined, equation 2 does not specify the sequence of absorber deposition (i.e. how much absorber to apply individually to the back and front sides of the membrane apertures). Simulations are conducted to evaluate the impact of various physical profiles resulting from different evaporation sequences, on the response of the final aperture.

2.3.2.2 Optimization of Aperture Response through Simulation

The Huygens-Fresnel (H-F) integral is useful in calculating the electrical field incident on a plane at some distance after passing through an aperture [4]. The H-F equation assumes an absorber screen of negligible thickness and neglects the effect of finite screen thickness and aperture taper on the response of the aperture. The classical Huygen-Fresnel integral for the observed field strength (U(x,y)) in two dimensions is expressed by the following equation [4]:

$$U(x,y) = \frac{z}{j \cdot \lambda} \cdot \int_{\Sigma} \int U(\xi,\eta) \cdot \frac{e^{-jk(x \cdot \xi + y \cdot \eta)}}{r^2} d\xi \cdot d\eta \qquad (3)$$

were: $r = \text{sqrt}[z^2+(x-\xi)^2+(y-\eta)^2]$

If the aperture is assumed to be a circularly symmetric pinhole aperture, then the distribution function $U(\xi,\eta)$ can be expressed by the transmittance function:

$$t_A(q) = \text{circ}(q/w) \quad \text{(for a circular pinhole aperture)} \tag{4}$$

Where w is the half-width of the aperture and q is the radius variable. A first order model is constructed assuming that the taper and profile of the aperture are also circularly symmetric. This can be modeled as a variation in the effective radius through the thickness of the aperture screen: t_0. The aperture distribution function now becomes a function of z as well as the radial coordinates: $U(\zeta,\eta,z)$ and equations 3 becomes:

$$U(x,y) = \frac{z}{j\cdot\lambda}\cdot\int_{\Sigma}\int_{0}^{t}\cdot U(\xi,\eta,z)\cdot\frac{e^{-jk(x\cdot\xi+y\cdot\eta)}}{r^2}dz\cdot d\xi\cdot d\eta \tag{5}$$

where previously the aperture transmittance was a function only of the radius (for circular apertures), the transmittance is now expressed as a function of z.

$$t_A(z) = \text{circ}(q(z)/w) \tag{6}$$

The following sections address the effects of finite thickness on the transmitted wave and the question of required absorber thickness to neglect any further absorption from the aperture. There are two cases for small apertures which each have their own special concerns.

2-D Case

For Extreme Ultraviolet (EUV) interferometry utilizing a Point Diffraction Interferometer (PDI), it is necessary to produce a spherical reference wave [5-6]. This reference wave is produced from a pinhole aperture. Producing a spherical reference wave with good quality and coherence at 13.4nm requires fabrication of pinholes on the order of 100nm. The pinhole must be circularly symmetric and have nearly unity transmittance. Furthermore, the desired background transmittance of the screen is on the order of e^{-2}. Goldberg has used TEMPEST to study, in three dimensions, the propagation of waves through circularly symmetric pinhole apertures at EUV wavelengths [6]. He considered apertures consisting of a thin layer of cobalt as an absorber, with varying sidewall slope.

1-D Case

For the case of the narrow apertures for EUVL AIM, a thin scanning slit ~90nm wide and 50μm in length is placed in front of a photodetector. The two are then scanned together across an image of equal lines and spaces to measure the contrast in the aerial images produced by a lens as described in chapter 1. In this case, the measured signal is the convolution of the aerial image with the response function of the scanning slit. It is possible to deconvolve the measured signal to arrive at a more accurate measure of the aerial image if the response function of the scanning slit is well known.

It is necessary to define some objective criterion on which to base the analysis of the response of the apertures. The ideal scanning aperture would be a delta function in order to remove the requirements for signal deconvolution [18-21, 27-30]. Therefore, the first criteria for the optimization is to minimize the half width of the aperture response function.

Furthermore, since the light transmitted through the aperture must be detected, the second criteria is to maximize the amplitude of the zero order wave through the aperture (the peak value of the central lobe).

TEMPEST Simulations

TEMPEST calculates a rigorous solution to Maxwell's equations [7]. TEMPEST simulations are done to evaluate the response of these one-dimensional slit apertures assuming no variation in aperture profile in the transverse (Y) direction. The domain of the 2-D simulations have 250 nodes in X and at most 2000 in Z. The relatively small number of total nodes enable the simulations to be carried out using a local server (Litho). The simulation conditions are listed in table 2.

Wavelength		13.4nm
Nodes (X, Y, Z)		257, 1, 512
Boundary Conditions		Mirror Symmetry
n_{InSb} (n, k)		0.93531, 0.07002
n_{Si3N4} (n, k)		0.97304, 0.00914

Table 2.2 List of TEMPEST aperture simulation conditions.

All simulations are done using a plane wave striking the screen at normal incidence. Although this is not always the case in actual experiments, it is possible to orient the absorber screen such that the incident wave is perpendicular. Another assumption is that the EUVL camera produces a plane wave. Actual systems, such as typical EUV lithography systems utilizing Schwarzchild optics, produce "light" that is neither a plane wave nor at normal incidence [8]. The optics have a numerical aperture of 0.08 which mean that the incoming fields can be thought of as a series of plane waves varying 4.59 degrees in angle of incidence.

Furthermore, the central ray of the beam arrives with a non-telecentric angle of 12.1 degrees to the normal. A more accurate simulation of the 10X-I camera can be accomplished by plane wave decomposition using the Abbe formulation [31] which involves simulating many discrete plane waves at angles corresponding to the angles within the NA of the camera. The simplification of using a single plane wave, makes the problem more tractable while still providing a qualitative comparison of responses of the various aperture geometries.

TEMPEST produces a variety of outputs. Figure 2.9 shows an intensity plot of the wave as it propagates through an aperture with a top InSb absorber film (80nm) with transmittance of 0.5%. The output from TEMPEST is the electric field and the intensity in Figure 2.9 is calculated as the modulus squared of this field. TEMPEST uses polygons to distinguish regions of differing (complex) refractive index which are outline in white and labeled in the figure. Standing waves are produced as the wave is reflected from the top surface. This plot also illustrates the reflection from the side of the aperture wall which is seen as fringing of the field near the corner of the aperture. While this output is visually appealing, a more quantitative measure of the aperture response to the plane wave input, is obtained from a line plot of the intensity at the bottom of the simulation domain shown in Figure 2.10.

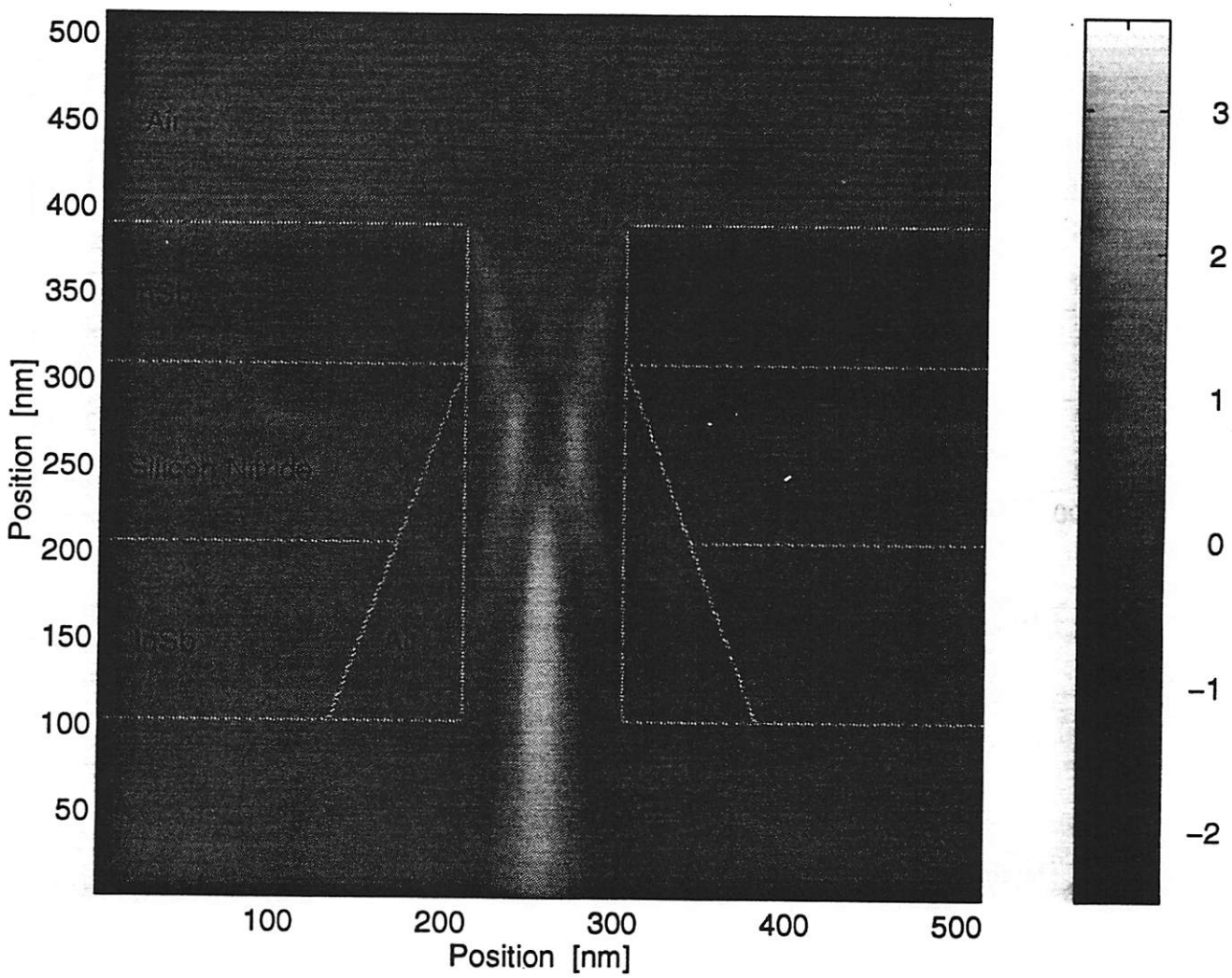

Figure 2.9 Simulated EUV image intensity passing through a 90nm AIM aperture. Intensity is displayed in the plot as brightness (scale on right). TEMPEST uses simple polygons to distinguish regions of differing (complex) refractive index. The polygons used in this simulation are outlined in white.

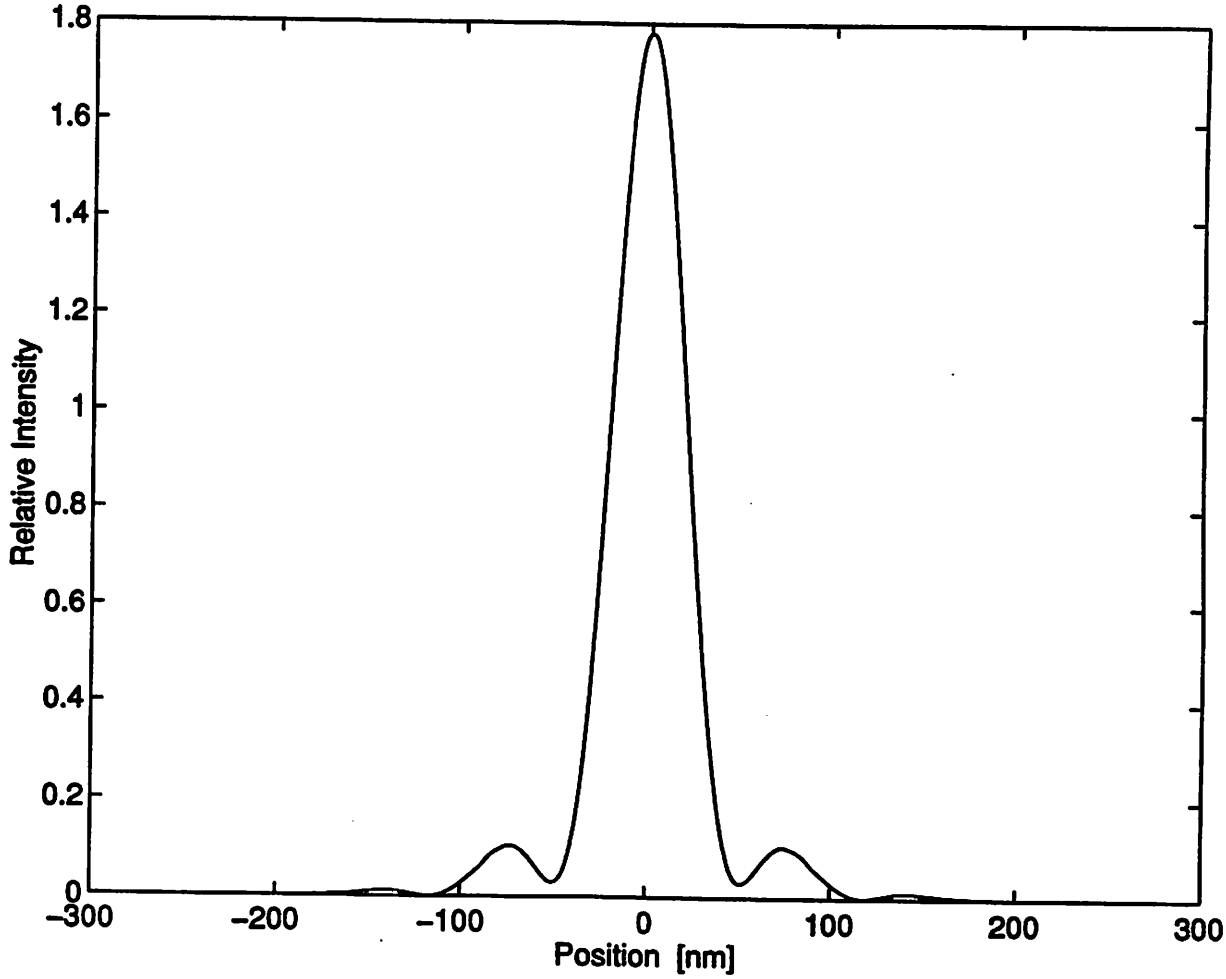

Figure 2.10 A line plot of the intensity at the bottom of the simulation domain of Figure 2.9. These plots are used to define the criteria of aperture response optimization.

(a) Absorber Film Alone

The first series of TEMPEST simulations assumes a thin absorber screen suspended in free space with 500nm of air above and below the absorber film. Although this situation is oversimplified, it provides insight into the interaction of EUV light with matter.

Figure 2.11 show responses for several absorber thicknesses ranging from 10nm to 100nm. Several features are noted from these simulations. The 10nm thickness layer produces the largest background transmission and also the lowest peak value. The response

to a 60nm thick absorber produces both the minimum width of the central lobe and the maximum peak intensity of all the thicknesses simulated. The toe intensity for the 60nm absorber is slightly higher around 75nm from the center and slightly lower than the 80nm or 100nm.

A widening of the central lobe occurs near the edge of the aperture at approximately 45nm from the center, seen in this figure. This is a result of reflection of the incident wave from the absorber sidewall, and can be seen in Figure 2.9 in the fringing of the field near the edges and top corner of the aperture. Increasing absorber thickness has the dual effect of narrowing the width of these extensions while increasing the magnitude of the field in these locations reaching a maximum around 60nm thickness.

To meet the first criteria of maximizing the central lobe, an absorber film as thick as possible should be chosen. The limitations on the maximum film thickness is imposed by aspect ratio issues in the fabrication. However, there is little improvement in both regards for films thicker than 100nm.

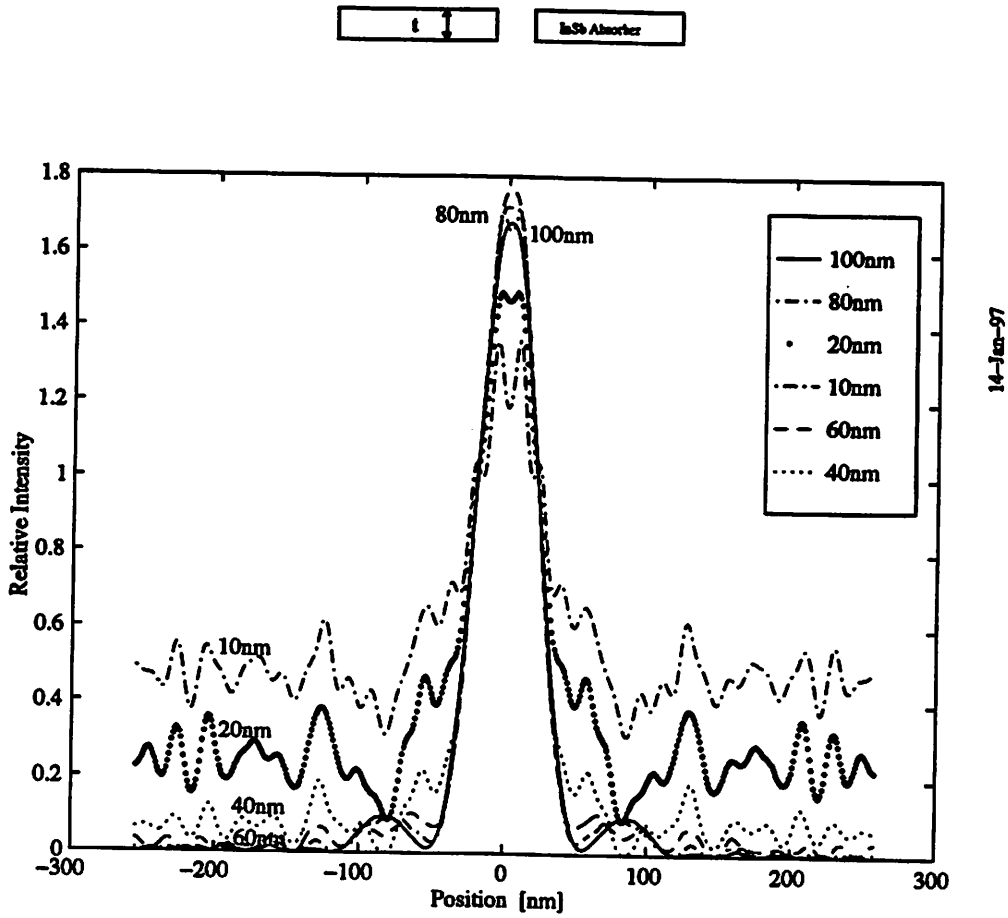

Figure 2.11 Line plots of the intensity at the bottom of the TEMPEST simulation domain for an aperture patterned in a free-standing absorber layer of varying thickness.

(b) Absorber w/ Si_3N_4 membrane

The aperture simulations in the previous section indicate that a thicker absorber will minimize the impact of the glancing incidence reflections on the width of the aperture response to the plane wave input as well as reduce the background signal level. However, apertures consisting of a free-standing absorber films are impossible to fabricate and it is necessary to consider the impact of the underlying support structure, namely the Si_3N_4 membrane, on the EUV aperture response. For the purposes of these simulations a nitride

layer of 100nm was assumed. Although it is possible to utilize thinner membranes to reduce the aspect ratio, thinner membranes are more susceptible to breakage. For this reason, 100nm is used as compromise.

Figure 2.12 illustrates the initial membrane stack before and after FIB mill. Adjusting the focus of the FIB system prior to milling removes a portion of the backside absorber layer to around 30-50nm as illustrated in the figure. Additional InSb is deposited by thermal evaporation to replace the lost absorber.

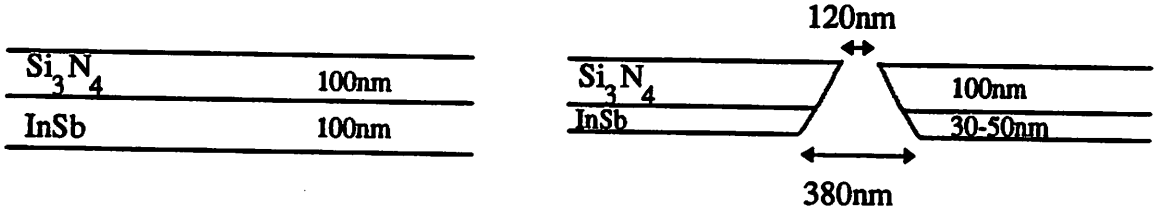

Membrane stack profile prior to FIB mill. a.

Membrane stack profile after FIB mill. b.

Figure 2.12. Illustration of the FIB aperture fabrication showing the membrane stack before and after the FIB mill step. A portion of the InSb absorber thickness is removed by the FIB during focus adjustment.

This section investigates the effect of the backside absorber deposition on the aperture response. Thermal evaporation of the absorber onto the backside of the artifact reduces the sidewall angle of the aperture. To evaluate the effect this has on the aperture response, simulations are done at five side wall angles ranging from 21 to 36 degrees to the normal. The FIB processing produces an aperture with a sidewall angle of approximately 36 degrees.

Figure 2.13 shows the intensity at the bottom of the simulation domain for each case simulated from the initial backside angle of 36 degrees to an angle of 21, which corresponds to a backside evaporation of around 90nm of absorber film. The widths of the responses are

2.5 times the widths of the responses of the metal film alone in the previous section. The width of the response is narrowed by increasing the absorber film thickness deposited.

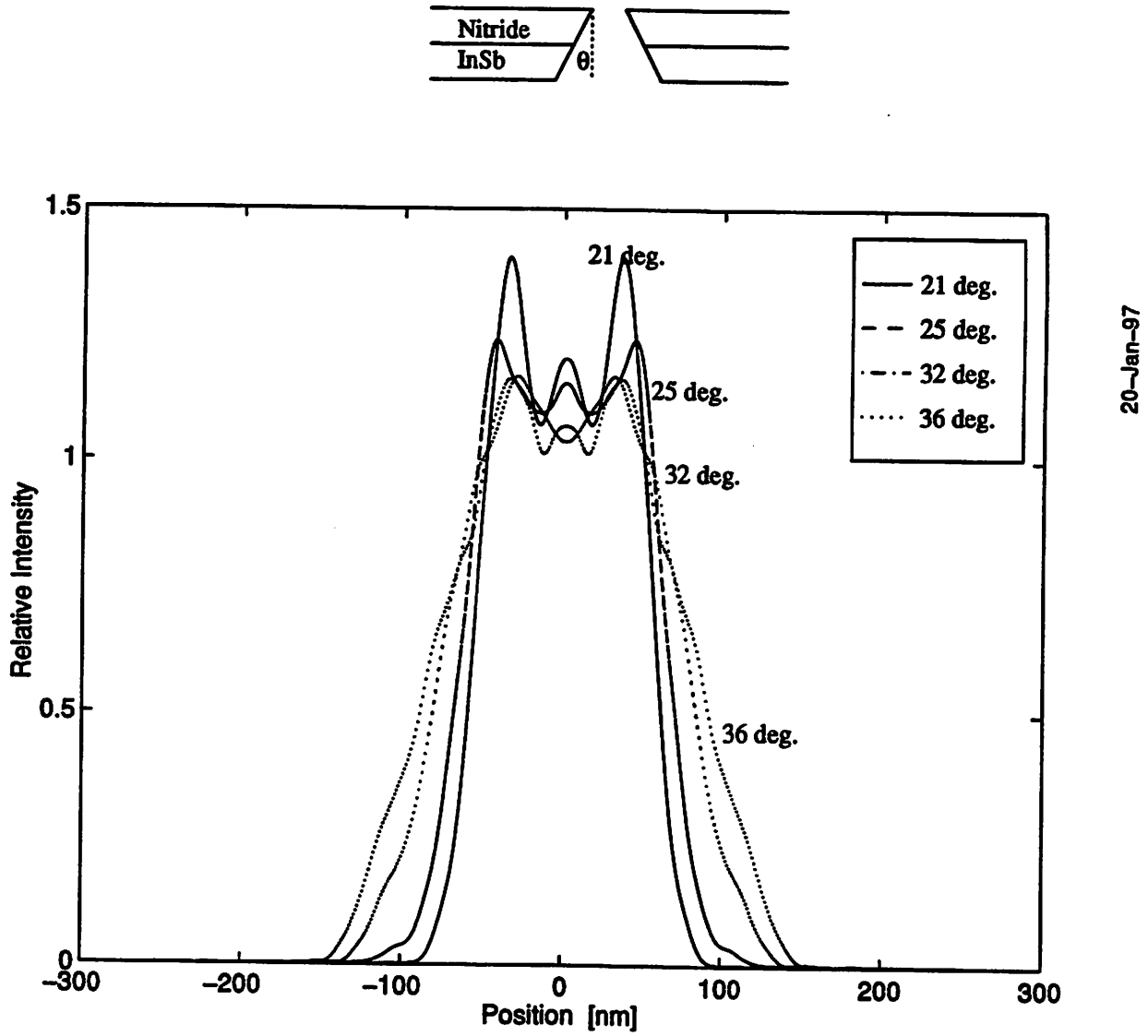

Figure 2.13 Intensity line plots resulting from TEMPEST simulations where the angle of the material on the bottom side of the aperture in Figure 2.12b is varied. The aperture profile is shown in the inset.

The next set of simulations investigates the effect of a top surface absorber layer on the aperture response. With this structure, the output intensity, shown in Figure 2.14, is

essentially independent of angle over the range 21-36 degrees. The sidelobe peaks that resulted in the widening of the response width in the previous simulations are not present in these responses.

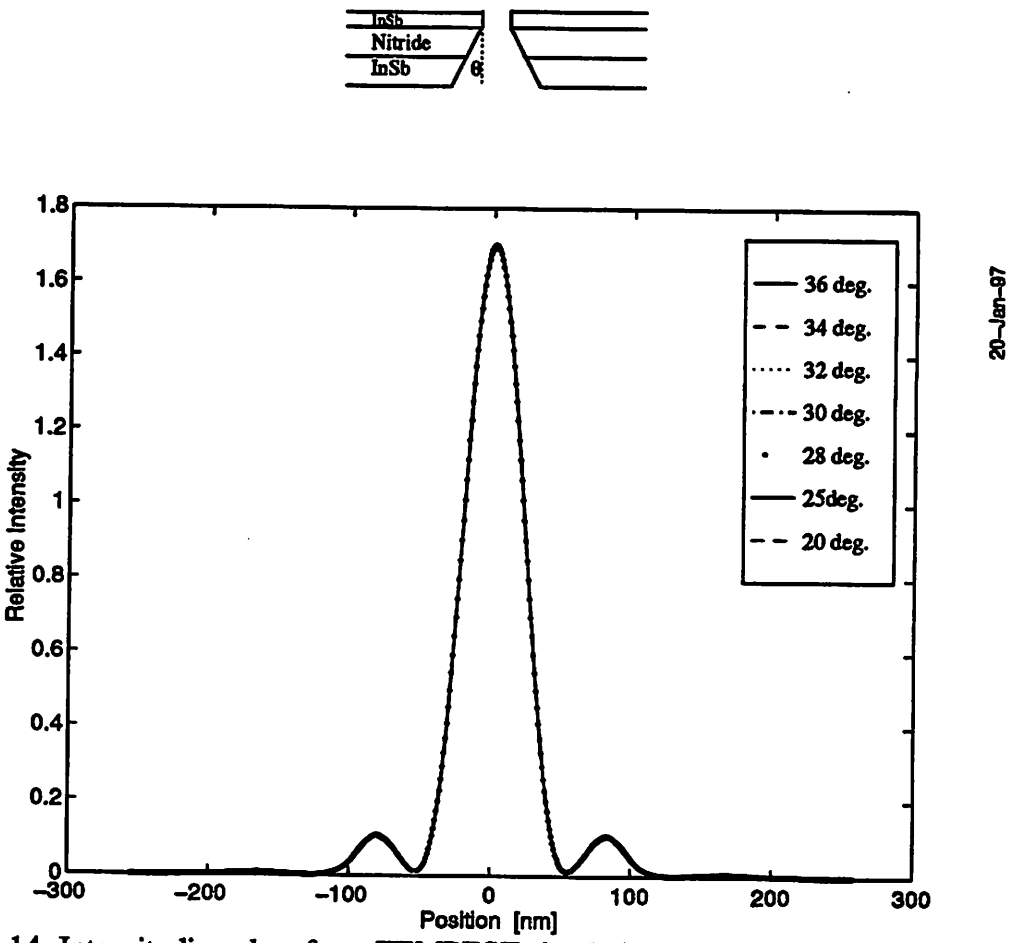

Figure 2.14 Intensity line plots from TEMPEST simulations of the aperture from Figure 2.13 with a top InSb absorber layer with 1% transmission. The aperture cross-section used in the simulation is shown in the inset.

(c) Top Absorber Layer Thickness

For the next set of simulations, an aperture is considered consisting of the nitride membrane along with the front and backside absorber layers as in Figure 2.14. For these simulations, the thickness of the top absorber layer is varied as shown in the inset of Figure 2.15. Since the results from section 2.4.2.2 point to the fact that the angle of the support

films has little effect on the response of these apertures, these simulations used a backside sidewall angle of 36 degrees consistent with a known ion beam process [9].

Figure 2.15 plots the results of the simulations in which the thickness of the top layer is varied from 10 - 100nm. The plot shows that very thin films produce a slightly higher peak intensity but at the expense of width. Equally, thick films produce peak intensity loss as well as broaden the width of the response. There exists a tradeoff here once again between maximizing the two criteria for response optimization. A subjective choice of both minimizing the lobe width and at the same time maximizing the peak intensity is a film thickness of 80nm.

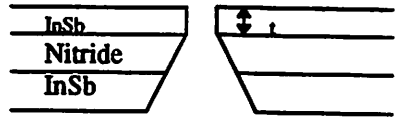

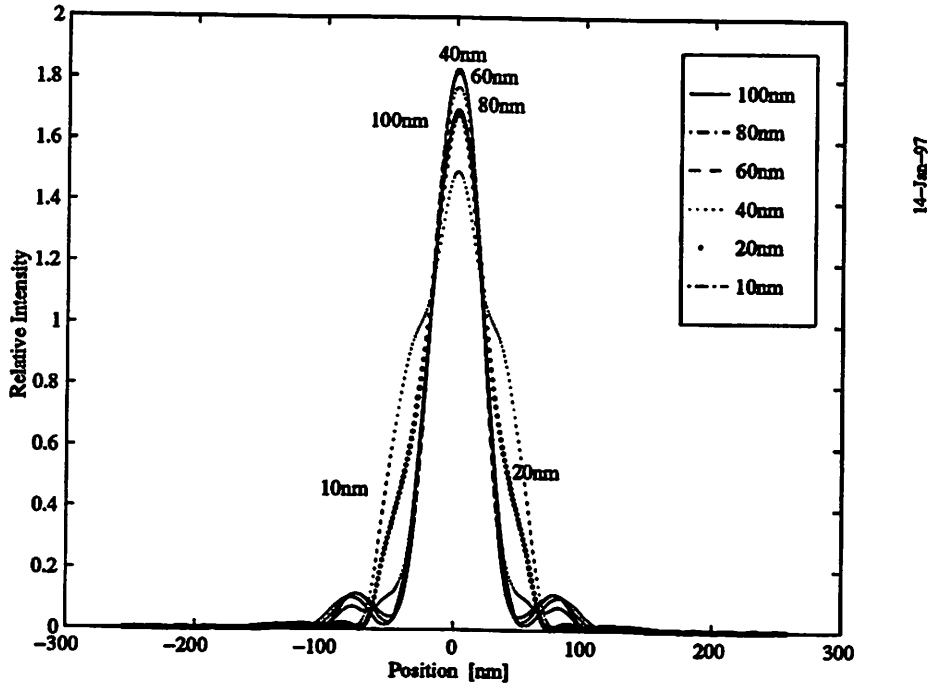

Figure 2.15 Intensity versus position at the bottom of the TEMPEST simulation domain where the thickness of the top absorber layer is varied from 10 - 100nm.

(d) Top Absorber Layer Angle

The physical profile of the aperture edge resulting from the thermal evaporation of the InSb is unclear without evaluation with the aid of SEM or TEM. It is of interest to investigate how variations in the edge profile of the top absorber layer will affect the aperture response function. The final set of simulations are carried out once again using the entire aperture structure from the previous section with a 80nm top absorber layer. This time the angle of a top InSb absorber film near the edge was varied from 90 to 75 degrees. Figure 2.16 shows the aperture response functions that resulted from the simulations as well as the aperture profile used for the simulations. From the figure we see that the aperture response function is a sensitive function of the angle of the top absorber layer producing wings on the response function similar to the case of an absorber layer alone at the large angles.

At three angles (75, 60 & 43) the amplitude of the central lobe is greater than the that for the case of a 90 degree top corner. The intensity gained is due to the summation of the reflected and diffracted waves. While the FWHM values of these four responses are nearly identical, the 90 degree top layer results in the minimum response width measured at the first null of the response.

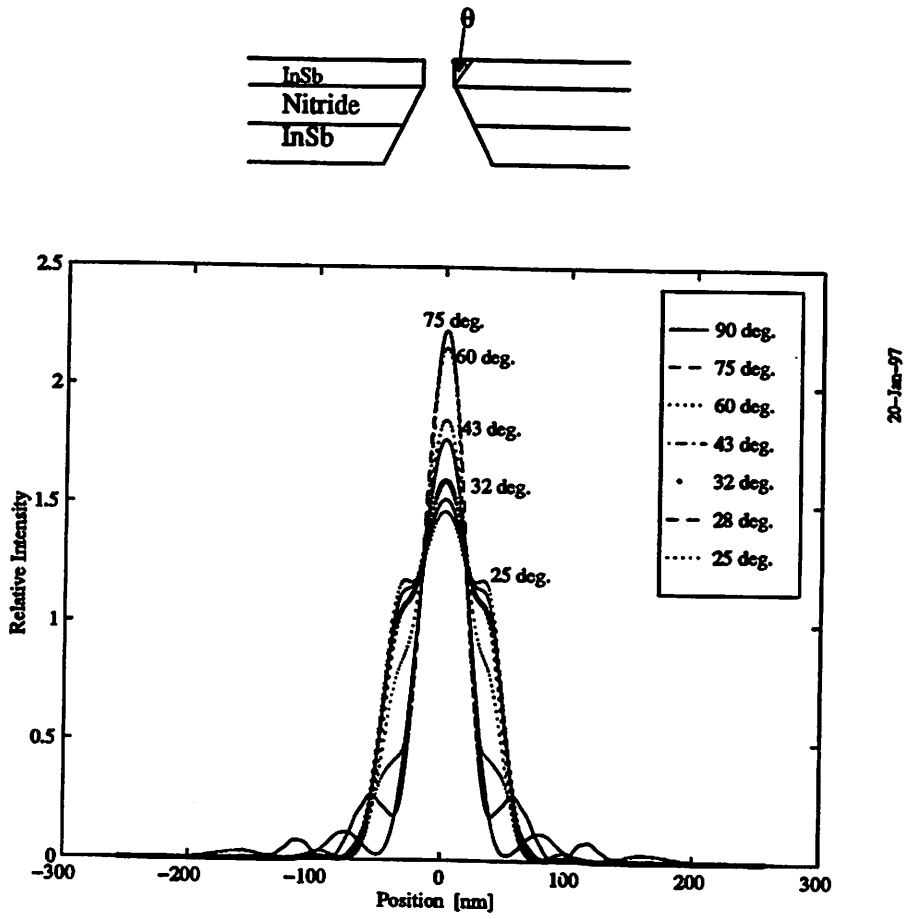

Figure 2.16 Simulated intensity versus position for the aperture defined in Figure 2.14 where the angle of the top absorber film near the aperture edge is varied. The thickness of the top absorber layer used in the simulations is 80nm.

Simulation Results

These simulations provide an initial guide in the fabrication process. Several apertures are manufactured using the specifications above. Analysis of the response of the actual AIM apertures involves SEM cross-section analysis to provide the detailed physical profile of the aperture. The actual geometry of the aperture is then used in further TEMPEST simulations to measure its response.

2.4 Aperture Physical Profile Characterization

2.4.1 Scanning Electron Microscopy

Top-down SEM was performed on several of the slit apertures. This form of inspection will only reveal the width of the aperture. SEM micrographs taken on two microscopes (Jeol-6400 at U.C. Berkeley and Hitachi-800 at Sandia) revealed the width of the final apertures to be 90 ± 5nm. A cross-section type inspection is required to view the physical profile of the apertures.

2.4.2 Process Simulation using SAMPLE

The U.C. Berkeley process simulation tool SAMPLE is used to predict the profile of the AIM aperture following the fabrication steps in section 2.3.2. The simulations assume a hemishperical deposition source. Figure 2.17 shows the initial structure used in the simulations and the resulting profile after the deposition of a 90nm InSb layer where the separate curves represent profiles at 10 second time steps during the simulation.

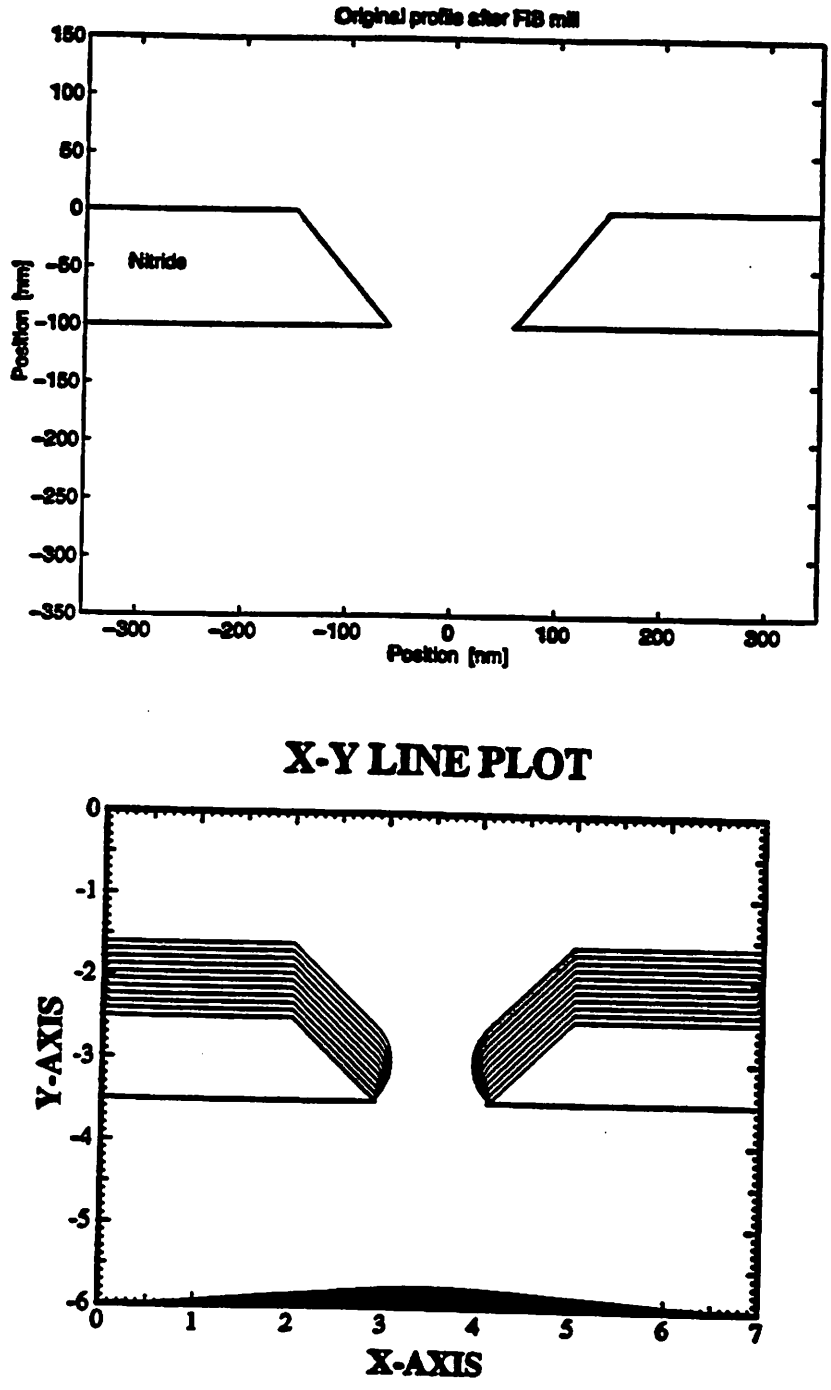

Figure 2.17 Simulated cross-sectional profiles from SAMPLE after the deposition of 90nm of InSb from a hemispherical source onto the backside of the AIM aperture. The aperture profile after FIB mill is depicted in (a). The profiles at 10 second simulation steps during the deposition are plotted in (b).

The half-angle of the hemispherical deposition source in these simulations is 45 degrees. To investigate the effect of source angle on the profile, several simulations are conducted where the source angle is varied. The resulting profiles, shown in Figure 2.18, shown little variation when the source angle is varied from 5 to 90 degrees.

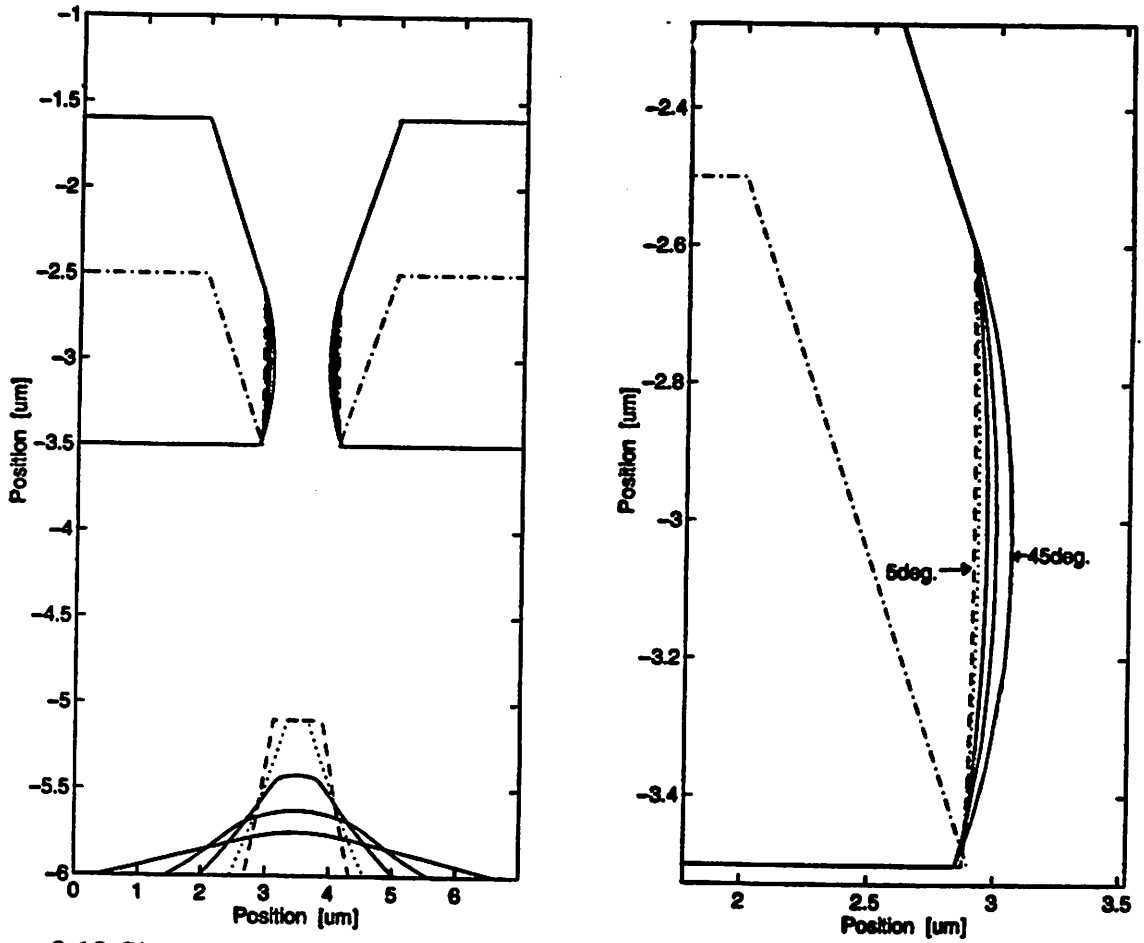

Figure 2.18 Simulated profiles from SAMPLE after the deposition of 90nm of InSb from a hemispherical source with varying half-angle, onto the backside of the AIM aperture.

To simulate the second (front-side) absorber deposition, the final profile from Figure 2.17a is inverted and used as the starting profile for the deposition of another 90nm InSb absorber layer. Figure 2.19 shows the aperture profile at 10 second time steps during the simulation of the deposition and the final profile together with the starting profile and the

profile following the first back-side deposition. Again the effect of hemispherical source angle are investigated using SAMPLE simulation. The resulting aperture profiles plotted in Figure 2.20 show a variation in thickness near the aperture tip of 15nm between the 5 and 90 degree curves.

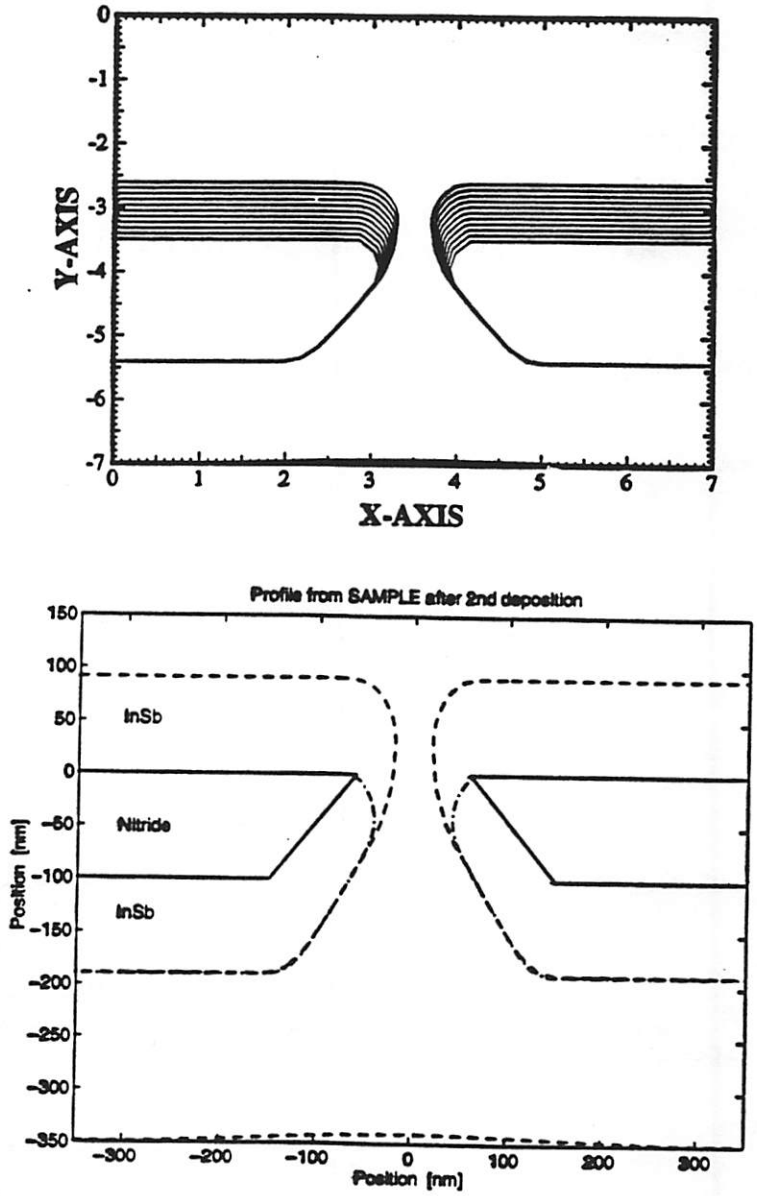

Figure 2.19 Simulated cross-sectional profiles from SAMPLE after the deposition of 90nm of InSb onto the frontside of the AIM aperture. The starting profile for the simulations is the inverted final profile from Figure 2.18. The curves represent profiles at 10 second simulation steps.

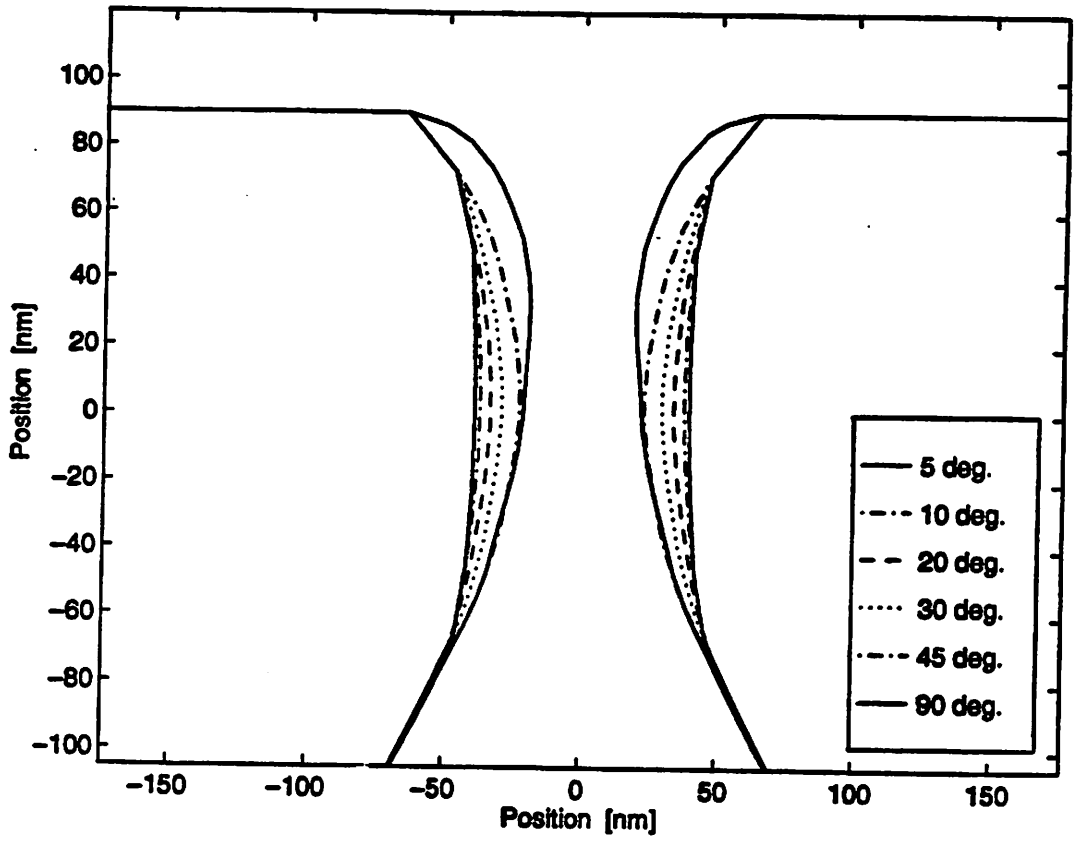

Figure 2.20 Simulated profiles from SAMPLE after the deposition of 90nm of InSb from a hemispherical source with varying half-angle, onto the frontside of the AIM aperture.

2.4.3 Focused Ion Beam Cross-section

The technique of using a FIB to perform the cross-sectioning is a common procedure in micro-electronics. The FIB mills away a portion of the structure then SEM inspection is performed to analyze the sidewall profile or device structure. This technique is applied to the evaluation of the physical profile of the EUVL AIM apertures.

A material is deposited into the aperture to preserve the sidewall features during the milling process. This process is referred to as "fossilization". The choice of material for the

fossilization is based upon SEM imaging concerns. It is desirable to produce a high contrast between the fossilization material, the InSb absorber, and the nitride membrane layers. Aluminum is selected as the fossilization material since it has an atomic number of 13 compared to 49 for In and 51 for Sb. To completely enclose the aperture, 300nm of Al is deposited onto the backside of the membrane by thermal evaporation. This is followed by an identical evaporation of another 100nm onto the front side of the membrane.

The next step in the cross-sectioning process is to mill completely through the aperture membrane with the Al metalization. Figure 2.21 shows a FIB image of a test aperture complete to this step which shows two FIB mills in the membrane. One is across a set of 10 aperture slits while the other is a mill through a longer single slit. This membrane can now be viewed in cross-section with a SEM to analyze the details of the slit. Figure 2.22 is a SEM image of the same membrane sample after a second FIB mill process to relieve stress.

Figure 2.23 shows a SEM micrograph of one such slit. There exists good contrast between the Al fossilization metal and the InSb absorber layers as well as delineation of the Si_3N_4 support membrane layer. This cross-section profile from the SEM micrograph is compared to the simulated profile in Figure 2.19.

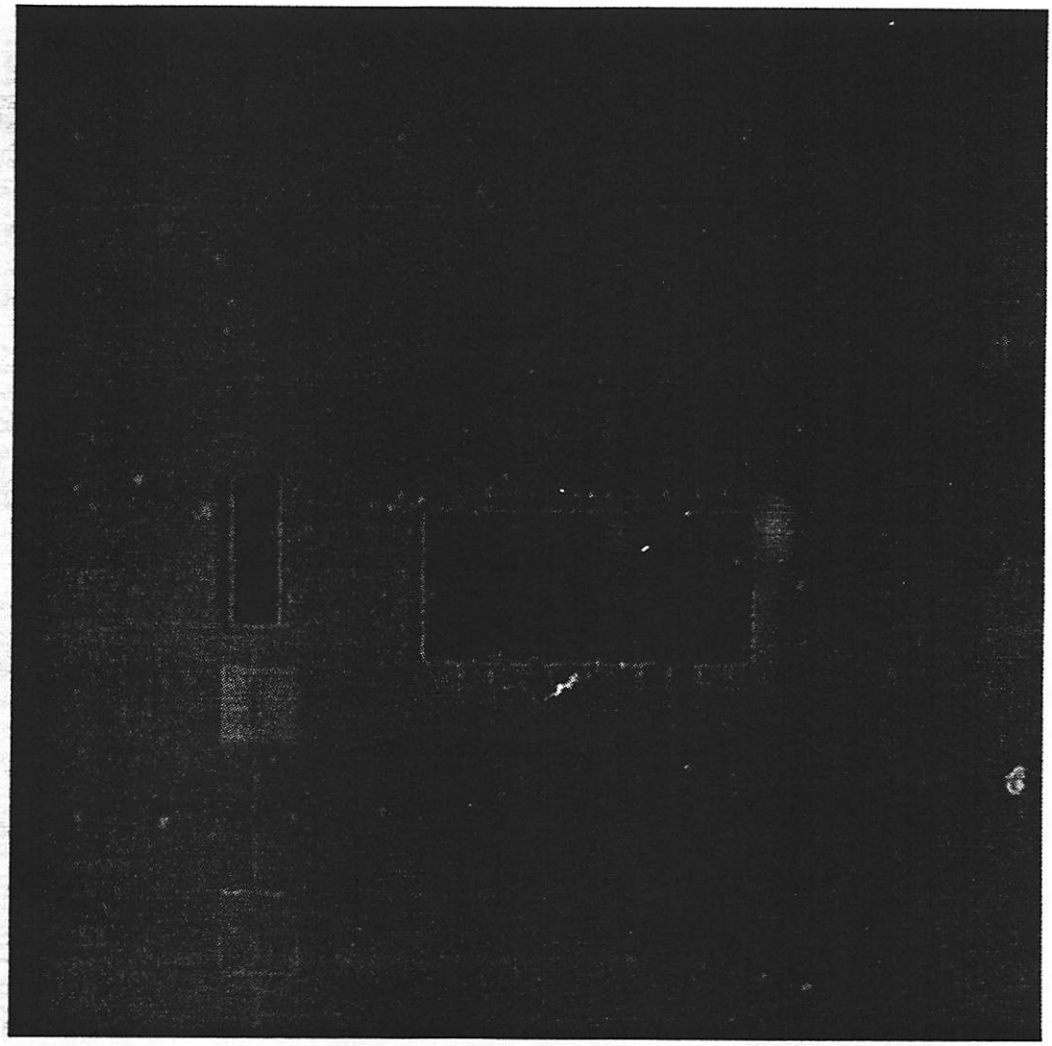

Figure 2.21 FIB image of a test aperture where two large rectangles are cut in the artifact using a coarse FIB to prepare for SEM cross-section inspection.

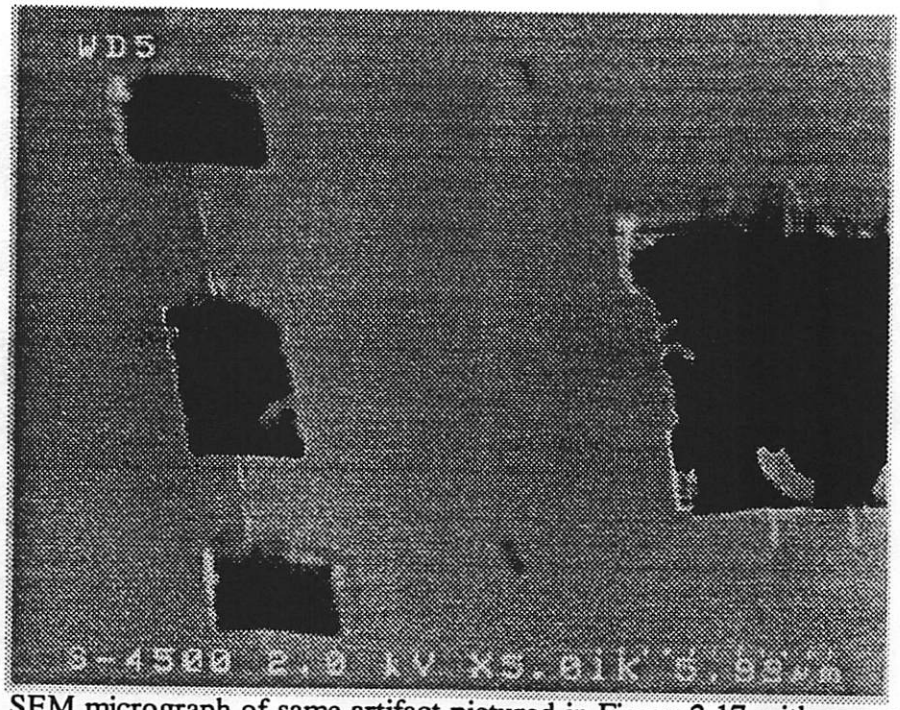

Figure 2.22 SEM micrograph of same artifact pictured in Figure 2.17 with several more FIB mills to relieve stress in the nitride membrane to achieve a more accurate image of the AIM slit cross-section. The stress in the large opening has relaxed while considerable stress remains in the long single slit on the left side of the figure.

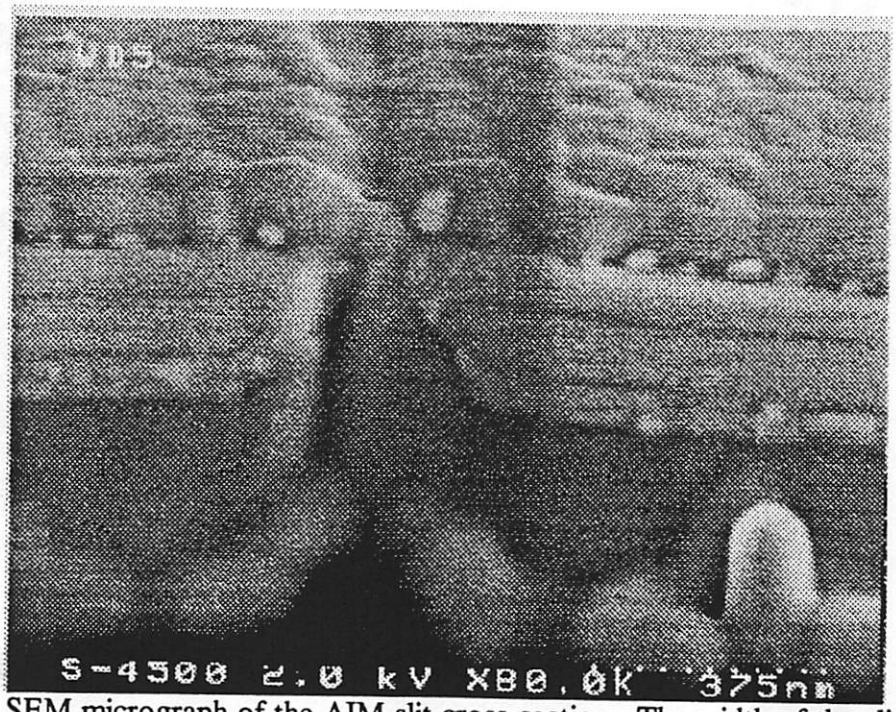

Figure 2.23 SEM micrograph of the AIM slit cross-section. The width of the slit aperture is approximately 90nm. The image provides good delineation of the three materials, Al, InSb, and Si_3N_4.

2.4.4 Final Response Function Characterization

With a clear picture of the physical profile of the aperture, this information is used to arrival at a more accurate simulation of the response function of the aperture as mentioned in section 2.4.2.4. Using the final aperture geometry from Figures 2.19b, TEMPEST run are carried out under the same conditions as previous simulations. Figure 2.24 shows the resulting response of the real aperture plotted along with the optimum aperture defined from earlier simulations. The only difference in the two responses is in the peak of the first diffracted order. The theoretical optimization of the fabrication process using TEMPEST simulations are successful in predicting the optimum aperture profile.

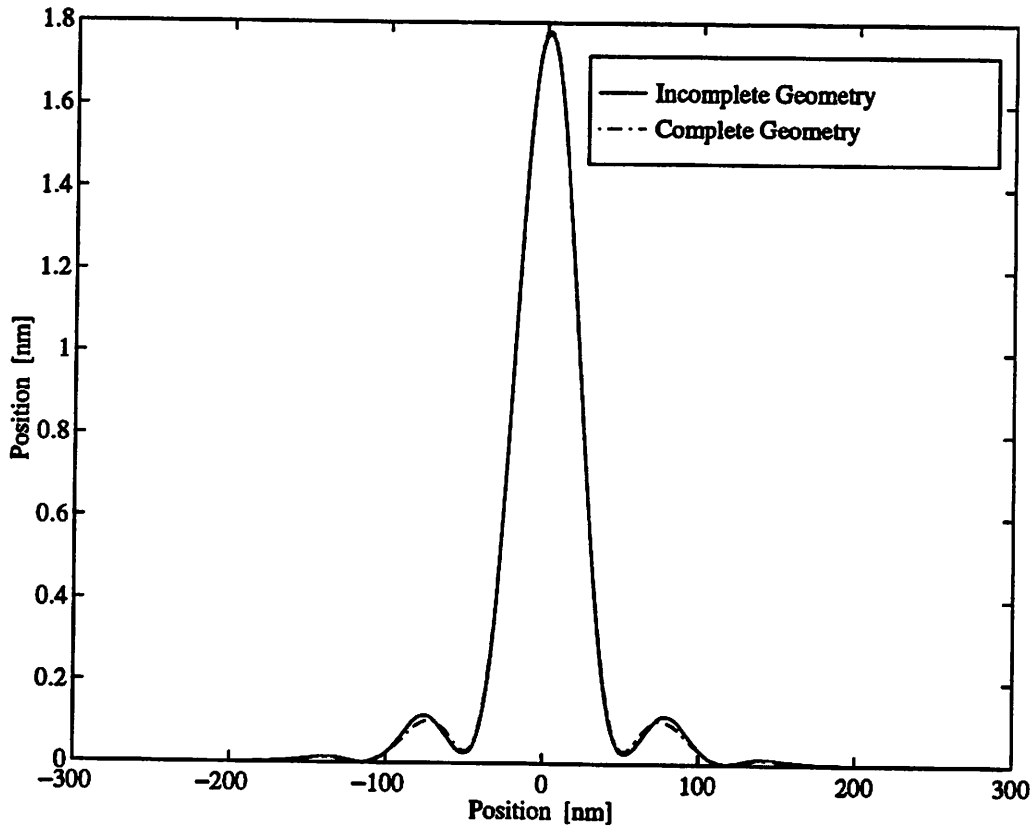

Figure 2.24 Simulated intensity at the bottom of the simulation domain from TEMPEST simulations using the complete geometry defined by Figure 2.19b as well as using the incomplete geometric model from the "optimum" aperture defined by initial simulations as in Figures 2.15 and 2.16.

2.5 Conclusion

Several absorber materials and fabrication techniques are investigated for the manufacture of sub-100nm scanning apertures for EUVL AIM. Several techniques are developed for the fabrication of scanning pinholes and slits using e-beam lithography. Alignment and etch issues are avoided by the use of FIB lithography for the patterning of the apertures. Several EUVL AIM artifacts are successfully fabricated and characterized with respect to both the artifact's physical profile and response to incident EUV radiation.

References

[1] A. Ray-Chaudhuri, K. Krenz, C. Fields, et. al., "Development of Extreme Ultraviolet Interferometry utilizing a laser plasma source", OSA Optical Society of America Conference Proceedings, May 1996.

[2] C. Fields, A. Ray-Chaudhuri, K. Krenz, et. al., "Initial Experiments on Direct Aerial Image Monitor in the Extreme Ultraviolet", Optical Society of America Conference Proceedings, Boston, MA, May 1996.

[3] C. Fields, "EUV Aperture Fabrication using Focused Ion Beam Lithography", Unpublished, May 1996.

[4] Fourier Optics, Goodman, Wiley Publish., 1968.

[5] H. Medeki, J. Bokor, K. Goldberg, E. Tejnil, "Phase-shifting Point Diffraction Interferometry of Lithographic Optics", OSA Optical Society of America Conference Proceedings, May, 1996.

[6] K. Goldberg, J. Bokor, E. Tejnil, "A Numerical Study of 3-D Pinhole Diffraction", Optical Society of America Conference Proceedings, Boston, MA, May 1996.

[7] A. Wong, A Neureuther, "Rigorous 3-D time-domain finite-difference electromagnetic simulation for pholithographic applications", IEEE Transactions on Semiconductor Manufacturing, 8, pp. 419-31, 1995.

[8] D. Tichenor, A. Chaudhuri, G. Kubiak, K. Nguyen, et. al., "Progress in the development of EUV imaging systems", Optical Society of America Conference Proceedings, May 1996.

[9] Intel Focused Ion Beam Lab, R. Livengood, T. Rinni, J. Giacobi, R. Rao.

[10] Broers, A. N., "Resolution limits for electron-beam lithography", *IBM Journal of Resist Development*, vol. 32, no 4, pp.502-513, July 1988.

[11] Wei C. and Ahmed H., "Fabrication of high aspect ratio silicon pillars of <10nm diameter", Appl. Phys. Lett.62 (12, pp. 1116-1120), 22 March 1993.

[12] Fischer P. B. and Chou S. Y., "Sub-50 nm high aspect-ratio silicon pillars, ridges, and trenches fabricated using ultrahigh resolution electron beam lithography and reactive ion etching", Appl. Phys. Lett.62 (12, pp. 1414-1416), 22 March 1993.

[13] Gentilli M., Grella L., Di Fabrizio E., Luciani L., Baciocchi M., Figliomeni M., Figliomeni M., Maggiora R., Cerrina F., and Mastrogiacomo L., "Development of an

electron-beam process for the fabrication of x-ray nanomasks", J. Vac. Sci. Technol. B 11(6, pp. 2938-2942), Nov/Dec 1993.

[14] Rosenfield M. G., Thomson R., Coane P. J., Kwietniak K. T., Keller J., Klaus D. P., Volant R. P., Blair C. R., Tremaine K. S., Newman T. H., and Hohn F. J., "Electron-beam lithography for advanced device prototyping: Process tool metrology", J. Vac. Sci. Technol. B 11(6), pp. 2615-2620, Nov/Dec 1993.

[15] Nakayama Y., Okazaki S., Saitou N., and Wakabayashi H., "Electron-beam cell projection lithography: A new high-throughput electron-beam direct-writing technology using a specially tailored Si aperture", J. Vac. Sci. Technol. B 8(6), pp. 1836-1840, Nov/Dec 1990.

[16] Fischer P. B., Dai K., Chen E., and Chou S. Y., "10nm Si pillars fabricated using electron-beam lithography, reactive ion etching, and HF etching", J. Vac. Sci. Technol. B 11(6), pp. 2524-2527, Nov/Dec 1993.

[17] Chen W., and Ahmed H., "Fabrication of sub-10 nm structures by lift-off and by etching after electron-beam exposure of poly(methylmethacrylate) resist on solid substrates", J. Vac. Sci. Technol. B 11(6), pp. 2519-2523, Nov/Dec 1993.

[18] Eisenmann H., Waas T., and Hartman H., "PROXECCO-Proximity effect correction by convolution", J. Vac. Sci. Technol. B 11(6), pp. 2741-2745, Nov/Dec 1993.

[19] Dobisz E. A., Marrian C. R. K., Salvino R.E., Ancona M.A., F.K. Perkins, and Turner N.H., "Reduction and elimination of proximity effects", J. Vac. Sci. Technol. B 11(6), pp. 2733-2740, Nov/Dec 1993.

[20] Bojko R. J., Hughes B.J., "Quantitative lithographic performance of proximity correction for electron-beam lithography", J. Vac. Sci. Technol. B 8(6), pp. 1909-1913, Nov/Dec 1990.

[21] Owen G., "Methods for proximity effect correction in electron lithography", J. Vac. Sci. Technol. B 8(6), pp. 1889-1892, Nov/Dec 1990.

[22] K.B. Nguyen, A.K. Wong, A.R. Neureuther, D.T. Attwood, *et al.*, "Aerial Images of EUV Projection Lithography Masks with defects in Reflective Coatings: Electromagnetic Simulation," Soft x-ray Projection Lithography (Monterey, CA, USA), OSA Proceedings, vol. 18, pp. 47-53, Optical Society of America, Washington, D.C., USA, 1993.

[23] H. Kinoshita, K. Kurihara, and H. Takenaka, "Soft x-ray Reduction Lithography Using Multilayer Mirrors," OSA Optical Society of America Conference Proceedings on Soft x-ray Projection Lithography, Vol. 30, No 11B, pp. 3048-3052, November 1991.

[23] M. Cai, Q, Wang, D.D. Allred, L.V. Knight, and A.Reyes-Mena, "Characterization of Annealed Mo/Si Soft X-ray Multilayers: Raman Spectroscopy and STM as tools in Understanding Structures and interfaces," OSA Optical Society of America Conference Proceedings on Soft X-ray Projection Lithography, Vol. 18, pp. 187-197, 1993.

[24] T.E. Everhart, "Fundamental Limits of Lithography," *Materials for Microlithography*, Am. Chem. Soc. Symp. Ser. 266 American Chemical Society, Washington, DC, 1984.

[25] A.R. Neureuther, C.G. Wilson, "Reduction in X-ray Lithography Shot Noise Exposure Limit be Dissolution Phenomena," J. Vac. Sci. Technol. B 6 (1), pp. 167-173, American Vacuum Society, Jan/Feb 1988.

[26] T. DeRose, H. Hoppe, T. Duchamp, J.A. McDonald, W. Stuetzle, "Fitting of surfaces to scattered data", Proceed. of SPIE Symp. on Curves and Surfaces in Computer Vision and Graphics III, Vol. 8130, pp. 212-20, 1992.

[27] F. Cheng and B.A. Barsky, "Interproximation: interpolation and approximation using cubic spline curves", Conf. on Computer Aided Design, Vol. 23, No. 10, pp. 700-5, 10 December, 1991.

[28] T.J. Peters, I.R. Greenshields, and S.M. Dorney, "Topological fidelity in surface reconstruction", SPIE Symp. on Curves and Surfaces in Computers Vision and Graphic III, Vol. 1830, pp. 221-5, 1992.

[29] S.K. Park, "Image gathering, interpolation and restoration: a fidelity analysis", Proc. of the SPIE symp. on Visual Information Processing, Orlando, FL, Vol. 1705, pp. 134-44, 20-22 April, 1992.

[30] R. Hazra and S.K. Park, "Small-kernel, constrained least-squares restoration of sampled image data", Proc. of the SPIE symp. on Visual Information Processing, Orlando, FL, 20-22 April, 1992, Vol. 1705, pp. 155-64.

[31] E. Abbe, "Beitrage zur Theorie des Mikroskops und der mikroskopischen ahrnehmung", Archiv f. Midroskopische Anat., Vol. 9, pp. 413-468, 1873.

Chapter 3

AIM System Design

3.1 Introduction

The 10X-I EUVL system at Sandia was originally designed as a testbed for printing patterns in photoresist only [1 2]. The wafer rests on by three stainless steel balls that define the image plane. A large mass placed on top of the wafer locks it to the camera in an attempt to reduce the impact of system vibration on the imaging performance. Locking the wafer to the camera ensures that camera vibrations couple to the wafer and the two vibrate together. There existed no scanning stage at the wafer on the original system design. Different field sites were exposed by physically pushing the wafer and weight together as they rested on top of the three stainless balls. There also existed no means by which to move or align the mask stage. Figure 3.1 shows the 10X-I EUVL projection lithography test bed.

Image monitoring and at-wavelength lateral shearing interferometry experiments required a new mask and wafer stage design. The first requirement for AIM experiments is angular rotation of one of the planes for image-to-artifact alignment. The second requirement is the capability of fine scanning motion in one or both of the planes. The wafer stage must be capable of movement in steps of 5nm relative to the projected aerial image (Chapter 1). This is accomplished by scanning the wafer plane artifact relative to the image or by scanning the image relative to the artifact with the latter relaxing the minimum step requirement to 50nm. The AIM and interferometry experiments share the

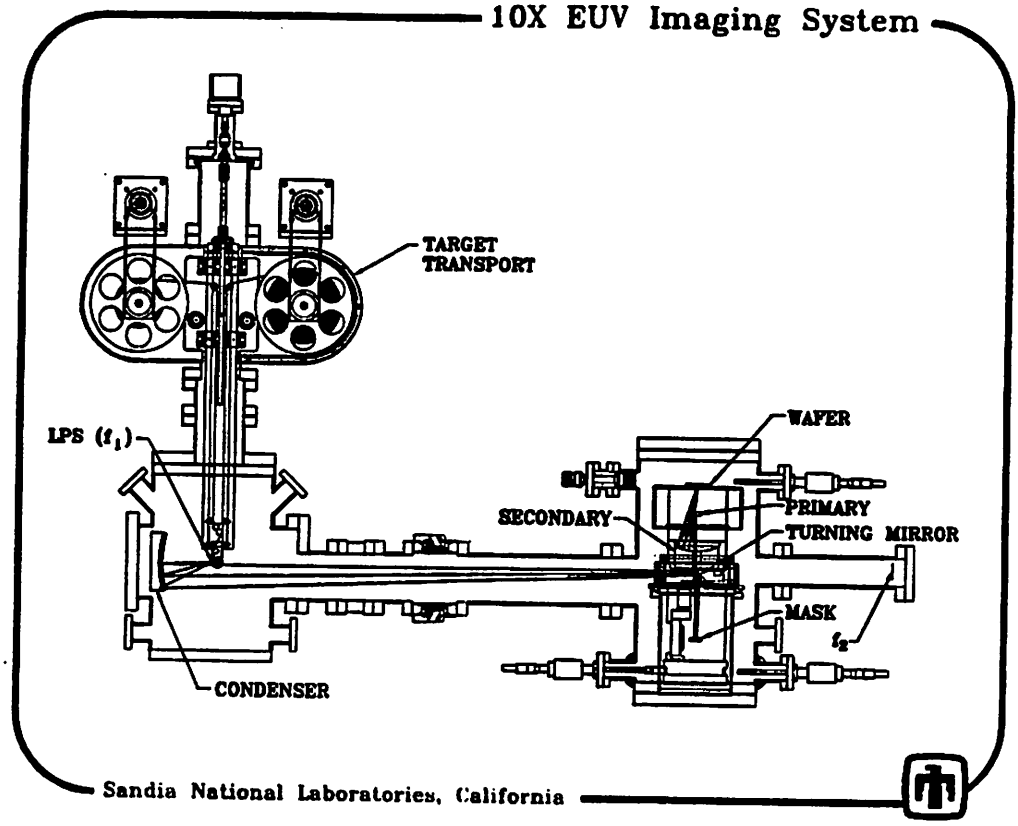

Figure 3.1 10X-I EUV imaging system cutview illustrating the target chamber, interconnecting vaccum housing, and wafer chamber. Courtesy of Dan Tichenor

requirement of theta alignment but the positioning requirements for the interferometery experiments are on placement accuracy not minimum step.

3.2 Mechanical Hardware Design

Scanning wafer and mask stages are designed and built by Sandia to meet the requirements of both experiments. Both the object and image planes stages have the capability of fine and coarse motions. Pico-motos provide coarse stage motion as described in Chapter 1. The fine motion of both stages is accomplished by piezo-electric stacks with capacitive position sensors in a closed loop feedback configuration. The

piezo-electric stacks purchased have a linear range of 15μm with a minimum step size of 1nm. This provides adequate scanning distance for both high resolution AIM scans and a 2π phase shift for lateral shearing interferometry using a 12μm pitch grating [3-4].

The mask stage is shown in Figure 3.2 installed in the wafer vacuum chamber.

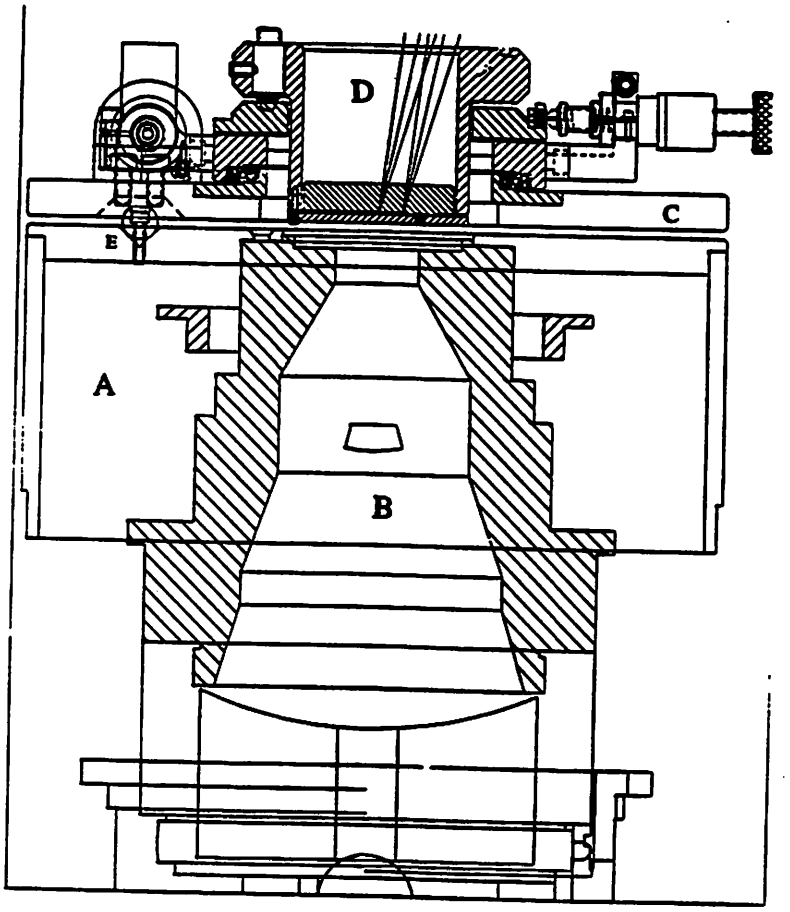

Figure 3.2 Cross-section view of wafer chamber with new mask stage installed. The wafer plane shown is the original design illustrating the previous method of wafer positioning involving a mechanical arm that pushes the wafer as it rests on the three SS balls that define the image plane. Courtesy of Sandia National Labs.

This figure illustrates the previous image plane system with the wafer mechanically pushed across the three balls that define the image plane. Figure 3.2a shows the mechanical motor that controls the Z-height of the mask plane to adjust the focal plane of the image.

Figure 3.3 shows a top-down view of the new mask stage. The mask, which consists of an optical flat with a Si-Mo multi-layer coating, is loaded in to position A of Figure 3.3. The mask pattern is typically defined by patterns in a gold absorber layer. The mask is held in position with a spring-loaded set screw (B in Figure 3.2). The theta motion is accomplished by a pico motor (C in Figure 3.2) used to push a lever arm to rotate the object plane.

Figure 3.4 shows the wafer plane stage. The three balls that previously had defined the image plane were removed. In their place is a cast aluminum "skirt" (labeled A in Figure 3.4) on top of the 10X reduction Schwarzchild camera (labeled B in Figure 3.4). The top of this skirt contains three larger balls that provide a kinematic mount for the wafer stage plate mounted on top. As well as the positioning motors, this plate (labeled C in Figure 3.4) contains the cross-roller bearing stages to provide stage motion. The wafer stage is designed with a large cutout in the center of the plate that allows for the insertion of a stainless cup (labeled D in Figure 3.4) into the stage. The cup is kinematically mounted in the wafer stage. The scanning motion is accomplished by pushing the cup together with the stage on the crossed-roller bearings across the projected aerial image. The wafer plane is defined by the top surface of a stainless plate mounted to the bottom of the cup. These mechanically polished plates provide less than 1μm of variation across the entire top surface that defines the image plane. The three adjustable height balls (labeled E in Figure 3.4) on the cup provide a kinematic mount to the wafer stage and also adjust wafer plane tilt. The scanning aperture described in chapter 2 is mounted, membrane side down, onto the center cut-out defined on the cup plate. The

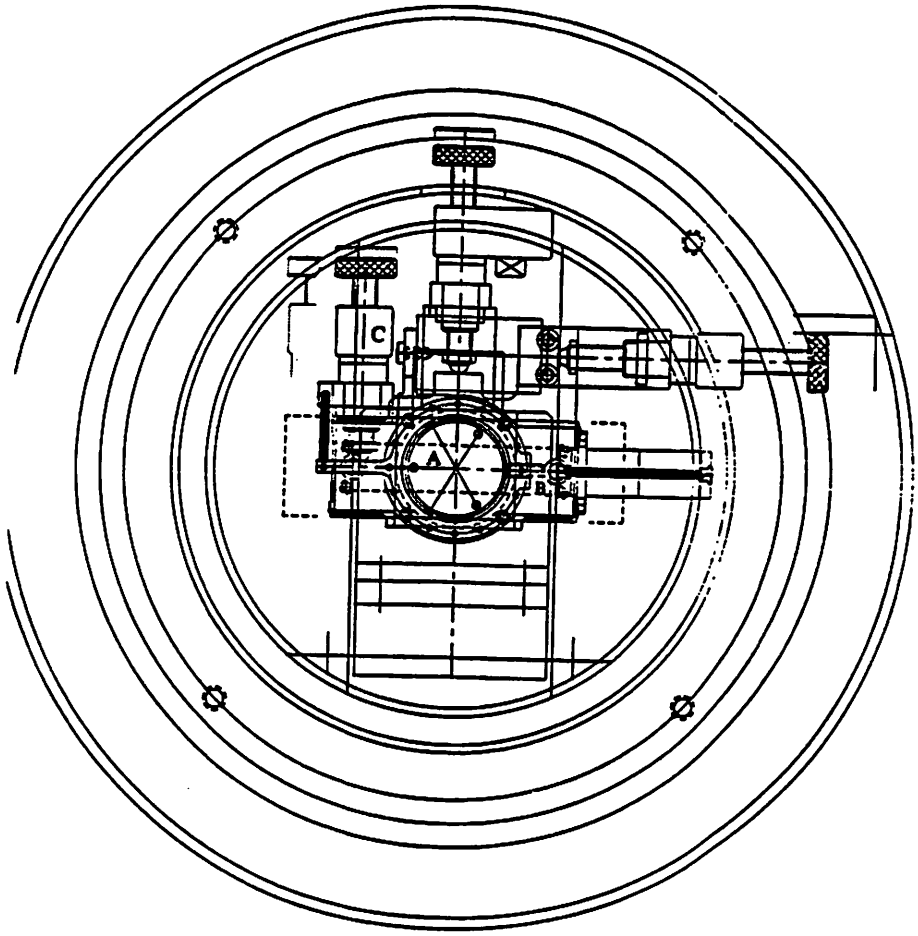

Figure 3.3 Top-down view of the mask stage illustrating the mounting of the multilayer mask and the pico-motors that control coarse stage motion. Theta is controlled by the left pico-motor. Courtesy of Sandia National Labs.

6mm circular cut-out in the center of the wafer plane plate is accomplished by electro-discharge machining techniques to prevent distortion of the planarity of these plates.

The modifications provide motion capabilities in the object plane in X, Y, Z, and Theta with fine motion capabilities in the X direction only. Mask movement in the Z direction controls the focal plane. In the image plane there exists coarse motion capabilities in X and Y with fine motion in the Y direction. The image plane stage is designed to allow 90 degree rotation for fine scans in the orthogonal direction. Both the plate on top of the skirt and the cup, relative to the plate, can be independently rotated 90

degrees relative to each other to provide versatility. Alternatively, fine scans in the orthogonal direction may be performed by scanning the object plane.

The final stage modification is the design of a photodiode cup and holder plate which insure that the photodiode is positioned close behind the scanning aperture. The limits are due to the diffraction of the incident beam as it passes through the aperture. To

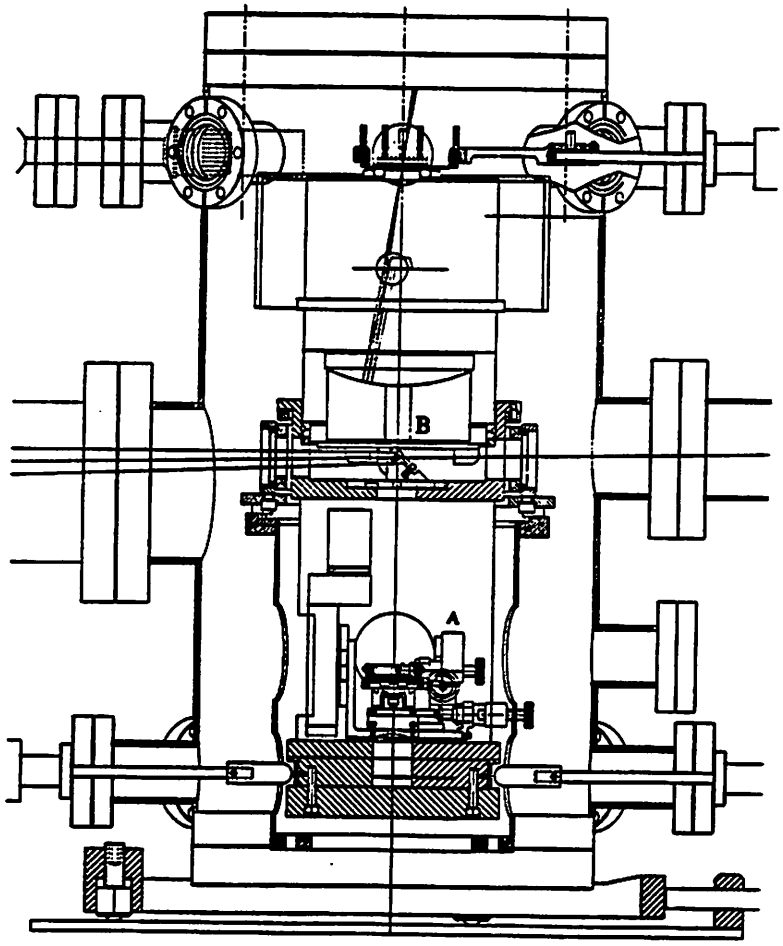

Figure 3.4 Cross-section view of 10X-I Schwarzchild camera and wafer stage. The wafer plane is defined by the top surface of the plate connected to the cup which is kinematically mounted on the movable wafer stage. The piezo stack that controls fine scans is to the right of the cup and normal to the page. One of the pico-motors is shown to the right of the image plane cup. The cup and plate that hold the diode are inserted into the image plane cup displayed here. Courtesy of Sandia National Labs.

maximize the available photon flux signal and signal to noise ratio (SNR), the specification is that the diode should capture all of the energy in the central lobe of the diffraction pattern. From the Fraunhofer diffraction theory the magnitude of the electric field in the far field is given as the Fourier transform of the aperture. For the 1-D case where the aperture is a top-hat function, the resulting diffraction pattern takes the form of the sinc function, the first null of which occurs at distance from the center: $\Delta x = (\lambda * z)/(2 * w)$, where λ is the wavelength, w is the half-width of the aperture and z is the distance from the aperture to the image plane (photodiode to aperture spacing distance). The full lateral length of the photodiode is 960μm, therefore the value $\Delta x = 480\mu m$. Then for an aperture half-width of w=50nm and $\lambda = 13.4nm$, we find that the diode must be placed at or closer than:

$$z = {}^{(2*\Delta x*w)}/_{\lambda} = 2 * 480\mu m * ({}^{50nm}/_{13.4nm}) = 3.58mm \qquad (1)$$

The aperture itself is on the front surface of a 500μm thick silicon wafer chip. The chip has 70nm of nitride layer along with approximately 200nm of InSb absorber. Furthermore, the height of the bonding wire for most of the photodiodes was approximately 200μm. Therefore, the total distance from the front of the aperture to closest possible physical position of the photodiode is equal to: 3.58mm - (0.5mm+0.2mm+70nm+200nm) = 2.61mm. This means that the diode must be at or closer than 2.6mm behind the back edge of the membrane chip. A similar result is found if the scanning aperture is a circularly symmetric pinhole. In this case the diffraction pattern will be the "Airy" pattern with half width of the pattern being equal to $(0.61*\lambda*z)/w$. For the case of the pinhole aperture, the diode must be placed within ~2.0mm.

A cup is designed and built to hold the diode in its TO-18 package. The diode plate mounts to the bottom of the cup and provides adjustment of the position of the plate and diode relative to the center of the image field. The diode, plate, and cup were designed to be inserted into the cup which holds the aperture chip. The alignment of the photodiode to the center of the diffraction pattern done on an optically with the aid of a short working distance telescope and a CCD camera, accounted for the non-telecentricity of the imaging system. The cup and plate bring the top surface of the diode within 1mm of the image plane. Metal sheet stock shims raise the diode cup to the appropriate height.

3.3 Signal Collection Electronics

A block diagram of the signal collection electronics is shown in Figure 3.5. The EUV photons that pass through the narrow scanning aperture impinge upon an EUV sensitive photodiode, are collected, and then amplified by the a charge sensitive amplifier (CSA). The output pulse of the pre-amplifier is input to a pulse shaper then gated-integrator (G/I) and sample and hold (S/H) circuitry before being sampled by the computer.

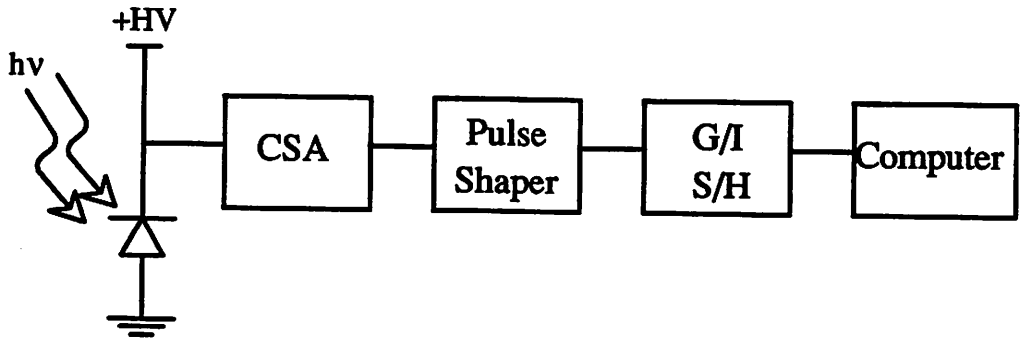

Figure 3.5 Block diagram of signal collection electronics train for EUVL AIM experiments.

As discussed in chapter 1, the photodiode operates in the photoamperic mode such that the photo-generated charge is integrated onto a feedback capacitance. Figure 3.6 shows the electrical connection of the detector, preamplifier, and bias network. The bias network consists of the two high-voltage (HV) capacitors in parallel with the diode

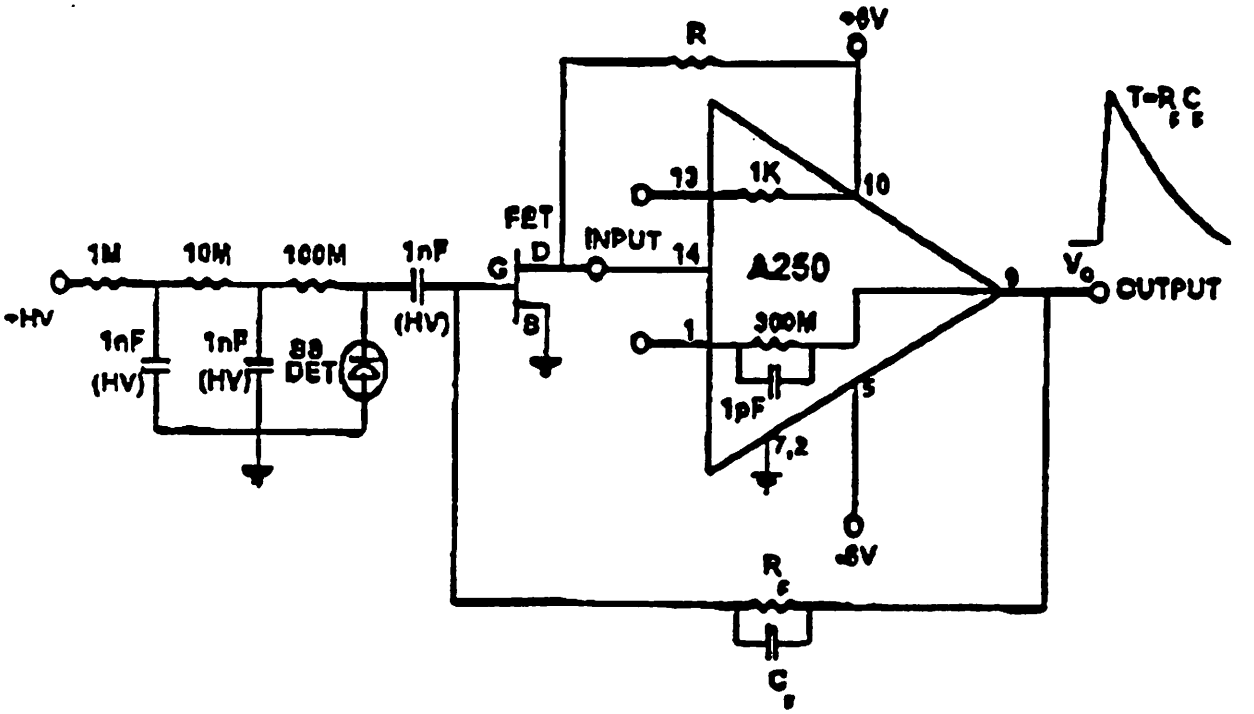

Figure 3.6 Electrical connection of photodiode and preamplifier, Reference [8].

detector together with the 1, 10, and 100MΩ resistors in series from the +HV supply. The signal is AC coupled through a 1nF HV capacitor to the gate of the input junction field effect transistor (JFET). The resistor R controls the drain current of the input JFET. No feedback capacitor (C_f) is used in the circuitry. Instead the terminals of the 1GΩ feedback resistor (R_f) provide a C_f of 0.25pF thus giving a pulse exponential decay time τ = R_fC_f of 250μsec which was experimentally verified. The gain of the amplifier stage is

defined by the value of C_f and is given by Gain = $1/C_f$ [Volts/picoCoulomb] (C_f in picoFarads) or 0.66 μV/electron. Two high-gain pre-amplifier boxes are constructed. The first utilizes the 0.25pF of the feedback resistor while the lower gain box uses an actual 1pF valued discreet capacitor with a 300MΩ resistor providing a pulse τ of 300μsec. The low-gain pre-amplifier box is used in experiments with higher flux to prevent saturation of the pre-amp which occurs at an output voltage of +3.0V.

Low-frequency noise is proportional to the ratio of detector and feedback capacitance (C_d/C_f) [5] where C_f is the feedback capacitor value used in the pre-amplifier stage and C_d is the capacitance of the photodiode. The detector capacitance is reduced by the application of a reverse bias voltage. The diode manufacturer quotes a zero-bias detector capacitance of 22pF [6], and the estimated detector capacitance for a 9V bias is 6pF, and 2pF for a 50V bias.

The diode (the AXUV-3EL from International Radiation Detector (IRD)) is built using the arsenic laser-annealed implant into a 1Ω–cm p-epi silicon layer [5], and thin oxide (8nm) described in section 1.3.3.1. These diodes have no doped dead-region and zero surface recombination resulting in near theoretical quantum efficiencies to EUV photons. Their cross-section and reported quantum efficiencies are shown in Figure 3.7 [6]. Since leakage current is directly proportional to the area of the diode, we selected a diode with a small area [$(0.96mm)^2$] to maximize the SNR. The dark current for this diode is 100pA with a shunt resistance value of 1GΩ.

The preamplifier, the A250 charge sensitive preamplifier from AMPTEK Inc. [8], permits the use of an external field effect transistor (FET) which allows the FET to be matched to the particular detector capacitance. This allows the selection of an ultra-low

noise FET since the majority of the noise contribution will be from the first stage of amplification, in this case the thermal noise of the input stage FET. The FET used for our circuitry is the 2SK147. The use of a 9V battery for the detector reverse bias results in an estimated detector capacitance of 6pF. Preamplifier output rise time in this configuration is 3nsec and the output noise is 0.5 keV full width half maximum (FWHM) in Si, or the equivalent noise charge (ECN from chapter 1) of 137 electrons RMS. Table 1 lists the specifications of the preamplifier.

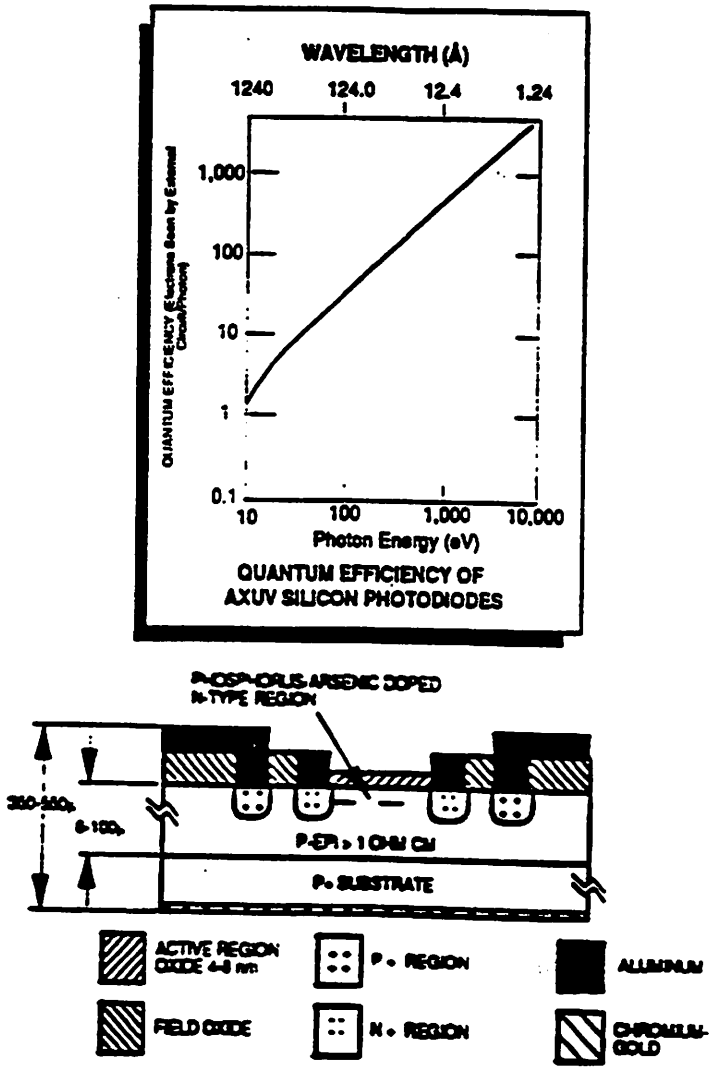

Figure 3.7 Quantum efficiency and cross-sectional illustration of the AXUV Silicon photodiode, Reference [6].

Sensitivity (w/ C_f=0.25pF)		0.64μV/electron
Noise at room temp.		100 electrons
Gain-BW product (f_T)		> 300MHz
τ_{rise} with 100pF load		4.5ns

Table 1. A-250 Charge Sensitive Preamplifier Specifications from AMPTEK. Reference [8].

The output of the pre-amplifier stage is connected through 10 feet of shielded coaxial cable to the input of a nuclear pulse amplifier (an EG&G ORTEC model 673 Spectroscopy Amplifier and Gated Integrator). The well documented [9 - 15] technique of pulse shaping for nuclear instrumentation takes the low level pulse from detectors or pre-amplifiers and transform it into an output pulse more suitable for measurement and analysis through amplification and filtering. Band-limiting the input pulse reduces low and high frequency noise. The pulse shaper used in these experiments is a gaussian shaper with a single differentiation followed by three integration stages. The shaping time constant of 2μsec accommodates the maximum adjustable integration time on the G/I which is set to 15μsec. The gain is set to 500X for the single slit scans and 20X for knife-edge scans to produce output pulses below the input threshold of the G/I (+2.0V).

The output pulse height, which holds the information contained in the original pulse, is maintained precisely. The detector and preamplifier determine the shape, magnitude, and noise content of the input signal to the main amplifier. Pulse rise time is determined by the detector characteristics, and the decay time by the resistance and capacitance appearing at the terminals of the detector. For the best possible SNR, the capacitance is kept as low as possible and resistance as high as possible. The resistance seen between the input and output terminal of the preamplifier for this experiment is 1GΩ and the feedback capacitance is 0.25pF providing a $^1/_e$ pulse decay time of 250μsec. Such

large values can be used since pulse-pile-up is not an issue as the pulse repetition time (PRT) of the laser is 50msec.

The output of the pulse shaper is applied to a gated-integrator (G/I) combined with sample-and-hold (S/H) circuitry (an SRS model 242 Gated Integrator and Boxcar Averager). The gain of the G/I is used to adjust the signal output voltage to a level appropriate for voltage sampling. The voltage level from the S/H is read into a computer with an analog-to-digital converter (ADC) board.

A significant amount time was spent in the reduction of circuit and system noise. The noise reduction measures that had the most impact are the following (listed in order of importance): Matching the capacitance of the detector to the capacitance of the input FET (choice of correct FET), the use of batteries as the power supply for the pre-amp stage and detector biasing, the use of short and well shielded signal cables the use of differential voltage measurements, ensuring that any high voltage lines are separated from the signal line, and pulse processing (band-limiting) the pre-amp output pulse. The SNR was also improved by wrapping the shielded signal cable from the photodiode around a metal torroid to provide a lossy inductor in the circuit path [16].

The electronic noise floor of the total signal collection electronic train is quantified by measuring the voltage levels under normal EUV system operation using a single 50μm X 0.1μm slit artifact. The measured SNR is 12 for single-shot operation compared to the 13 calculated in section 1.3. The measured SNR is 20 taking the average of 5 shots and 25 for 10-shot averaging with diminishing returns beyond 10 samples.

3.4 Software Design

The Labview software package from National Instruments is used for the development of the computer interface for the AIM experiments. It is a visual-based programming language similar to the Visual-BASIC or Visual-C programming languages which facilitate the design of "virtual instrumentation" in that several common functions such as graphs, displays, dials, indicators, etc... exist as pre-programmed modules. The Labview program automates data collection with all the associated timing issues, controls the motion of the pico-motors (analog output), and drives the Q/I piezo-electric stack (GPIB interface). The software capabilities allow for the complete automation of the AIM experiments. With the software it is also possible to automate the resist exposure process in a more user-friendly environment.

Initial versions of the software stepped the Q/I stage into position, fired a single shot of the laser, performed the data collection, and then again stepped the Q/I stack and repeated the entire sequence. The laser single-shot capability is accomplished by Labview software written to "spoil" the Q-switch of the solid state laser by controlling the timing of the Q-switch. To achieve laser emission the Q-switch sync pulse is sent at the moment of peak inversion in the laser. If this pulse is sent at a later time, there will be no photoemission, and the energy will be dissipated as heat in the laser rods. This technique results in poor laser performance with regard to shot-to-shot energy density uniformity. This laser is tuned for optimum performance at 20Hz and is not designed for single shot operation. The modified software simply opens the laser shutter at the beginning of the AIM scan and closes it again at the end. Contamination of the condenser due to

unmeasured laser shots is minimized since the PRT of the laser is 50msec and the settling time of the Q/I is 50μsec.

3.5 Detector Calibration/Normalization

The use of a reference detector minimizes the effect of pulse-to-pulse variations in EUV flux at the image plane. Sources of flux variance include laser source variations, target positioning, and laser-to-target alignment. The standard practice uses an identical detector to measure the incident source flux. The voltage measured with the image plane detector is divided by the voltage from the reference detector to reduce the impact of shot-to-shot variations in the measured image plane signal. The small image spot size of 10X-I precludes positioning of a reference detector at the image plane. There also exists no EUV beam splitter by which a portion of the beam could be diverted to impact the reference detector. The normalization detector (ND) used for these experiments is shown in Figure 3.1.

Problems exist with the use of the ND as a normalization detector. First, it is not an identical detector to the image plane silicon p-n junction detector. It is unclear from the outset if response of the ND is linear in this flux region. A second problem is the location of this detector. There exists an optical path difference of 58.9 cm between the ND and AIM detectors. There will be a reduction in the number EUV photons due to the relatively short attenuation length in Krypton gas ($^{\mu}/_{\rho}$ = 2345cm^2/g). The exponential attenuation of the photon flux will provide an added non-linearity to the normalization efforts. At an operting pressure of 100mTorr, 2.1% of the EUV flux is lost in 1cm and

72% of the signal is lost in the 58.9 cm from the ND to the AIM PD. Therefore, it is necessary to monitor pulse-to-pulse variations in the system pressure.

Both of the obstacles listed in the preceding paragraph are overcome by calibration of the AIM detector to the ND detector and system pressure. The calibration takes the form of taking many measurements of the two detector signals along with a correlated pressure reading while the object and image planes are held fixed. Variations are induced in the flux at the two planes by slightly opening and closing the condenser lens aperture stop during the calibration run. The pressure is also varied $^{+}/_{-}10\%$ by slight adjustment of the throttle-valve controller to simulate the magnitude of pressure variations seen during actual resist exposures. The resulting data is fit to a model using multi-variant regression which provides the significance of each of the model parameters (ND voltage and pressure). Although the non-linearity associated with pressure variations is exponential, a multi-variant linear regression analysis is justified since the exponential may be expressed in terms of a polynomial expansion.

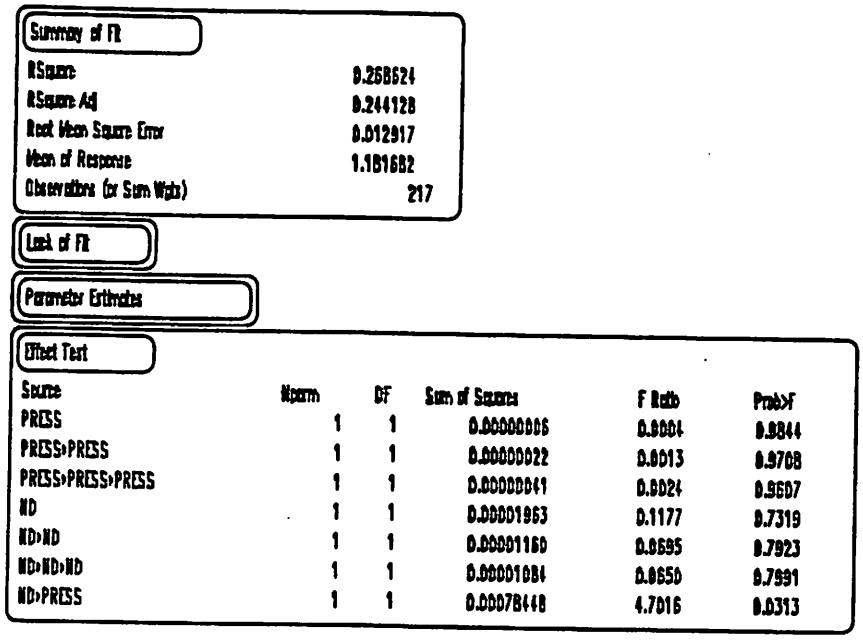

Summary of Fit

RSquare	0.268524
RSquare Adj	0.244128
Root Mean Square Error	0.012917
Mean of Response	1.181682
Observations (or Sum Wgts)	217

Lack of Fit

Parameter Estimates

Effect Test

Source	Nparm	DF	Sum of Squares	F Ratio	Prob>F
PRESS	1	1	0.00000005	0.0001	0.9944
PRESS*PRESS	1	1	0.00000022	0.0013	0.9708
PRESS*PRESS*PRESS	1	1	0.00000041	0.0024	0.9607
ND	1	1	0.00001963	0.1177	0.7319
ND*ND	1	1	0.00001160	0.0695	0.7923
ND*ND*ND	1	1	0.00001084	0.0650	0.7991
ND*PRESS	1	1	0.00078448	4.7016	0.0313

Figure 3.8 Linear regression model fit for AIM PD normalization with associated multiple analysis of variance (MANOVA)table.

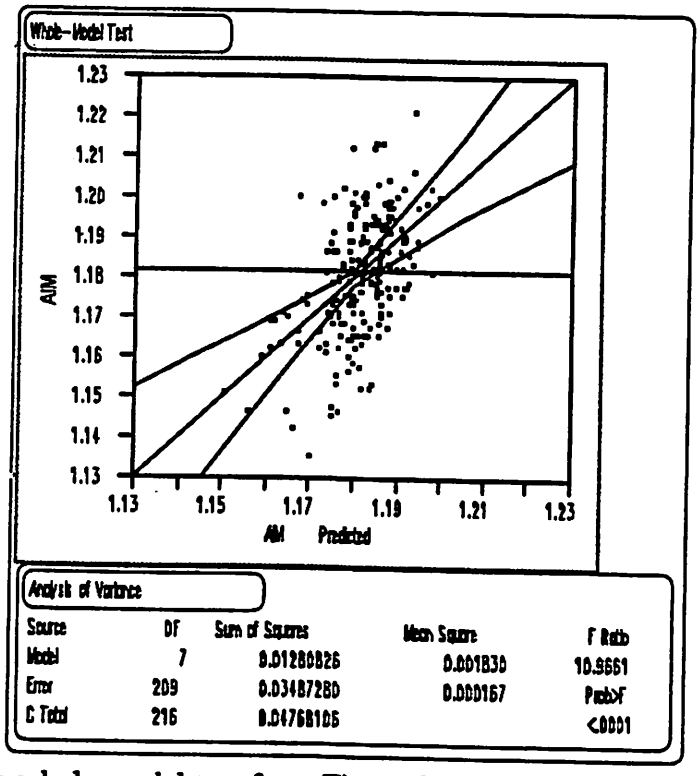

Analysis of Variance

Source	DF	Sum of Squares	Mean Square	F Ratio
Model	7	0.01280826	0.001830	10.9661
Error	209	0.03487280	0.000167	Prob>F
C Total	216	0.04768105		<.0001

Figure 3.9 Plot of the whole model test from Figure 3.8 illustrating the result of the model fit. The solid line represents the model fit while the dashed lines represent the 95% confidence interval curves, and the dots represent the raw data fitted to the model.

The technique employed is to fit a model involving all primary terms, higher order terms (to 3rd order), cross-correlation terms, and a DC offset by the use of a Multiple Analysis of Variance (MANOVA) table. Figure 3.8 shows such a model fit with the resulting parameter coefficient table along with the MANOVA analysis results. The average of the measurements, root mean squared (RMS) error, and total number of observations are listed in the top section of Figure 3.8 labeled Summary of Fit. Significant terms are determined by comparing the F-ratios in the Effect Test box of the MANOVA table that tabulates the degrees of freedom (DF) used to calculate the Sum of Squares, F-ratios, and significance of each term. An F-ratio of 2 means that a term has a 50% chance of being significant to the dependent variable. Larger F-ratio numbers indicate a higher probability of significance. From analysis of the F-ratios for the terms in the Effect Test portion of the figure, it can be seen that the terms involving ND have a higher F-ratio than terms involving the pressure and the cross-interaction term ND*PRESS is the most significant.

Figure 3.9 is a plot of the Whole-Model Test and the analysis of variance (ANOVA) table for the fit. The solid line in Figure 3.9 is the model fit, the dashed lines are the 95% confidence interval curves, and the dots represent the raw data plotted versus predicted values. The Analysis of Variance summary is listed below the model plot. The averaging provided by the large number of data points results in the high value of F-ratio (10.96).

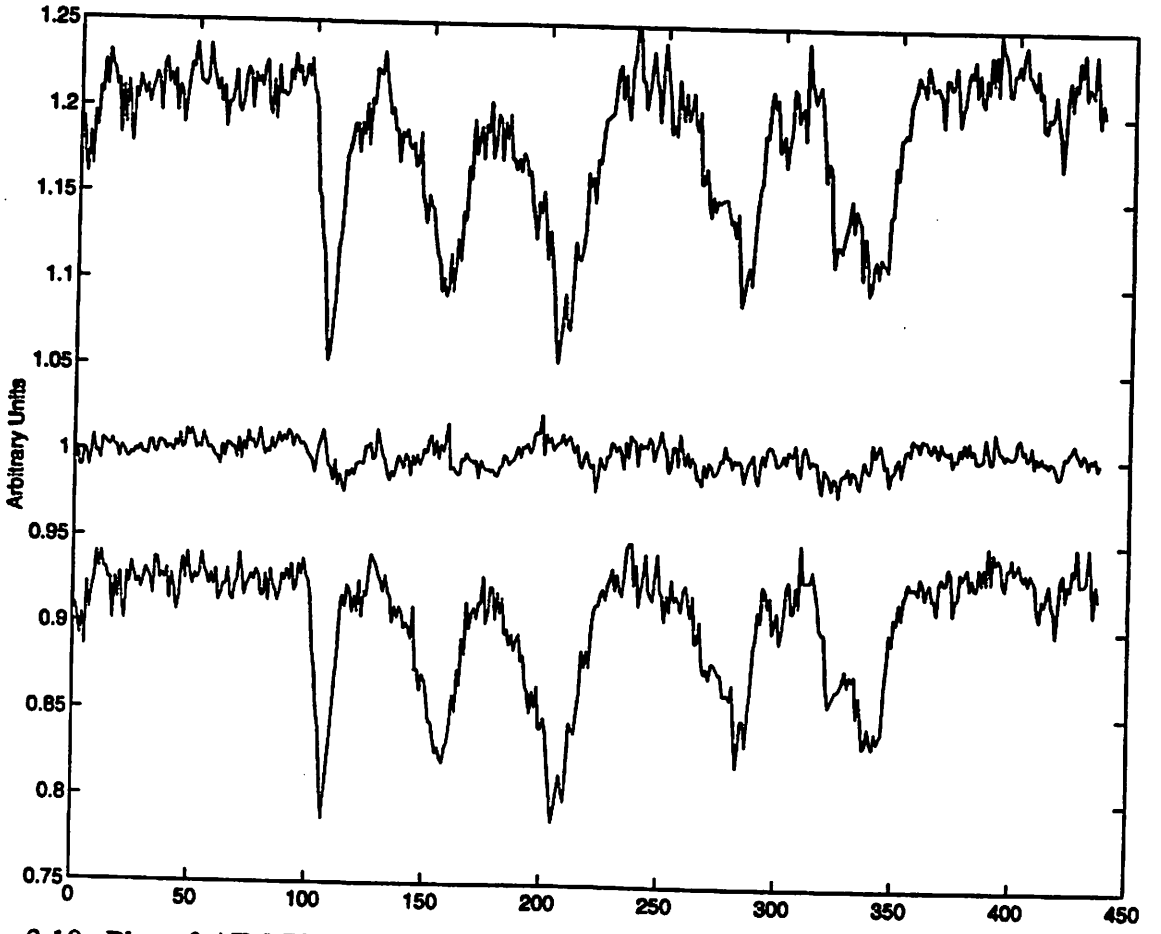

Figure 3.10 Plot of AIM PD and ND voltages illustrating the results of the normalization techniques. The data is taken by meauring successive voltage reading from the AIM system with all stage positions fixed.

Figure 3.10 shows the results of the normalization techniques. The top line is the raw AIM PD signal and the bottom line is a scaled version of the ND voltage signal. The flux variation from the condenser lens aperture stop is apparent in the signal dips. The middle line is the normalized AIM signal. Note that the large flux variations have been completely removed from the normalized data.

Although we achieved a measure of success modeling the non-linearities of the system, it is desirable to remove the variability associated with the fluctuating krypton pressure entirely. Pressure variations were removed by replacing the existing Roots-type

blower pump with a new Scroll-type pump. With the new pump, the system pressure varied by only 0.3% (3σ). New normalization runs resulted in the removal of the krypton pressure from the model. The F-ratio of pressure in the new data sets was less than 0.5 in all cases indicating that pressure is no longer a significant factor in predicting the EUV flux at the image plane. This fact permits fitting the normalization model using only DC and ND terms.

If the data in Figure 3.10 and similar experiments are separated into regions based upon the magnitude of the ND signal voltage levels and separate models fit to each region, it is found that there exist two separate operating regimes of the ND. In the low-flux region the output signal is nearly proportional to the square of the number of incident photons ($\gamma^{1.8}$). In the high-flux regime the response is more linear ($\gamma^{1.2}$). Under typical operating conditions, the available source flux collected by the condenser will put the ND in the nearly linear region and typically does not vary enough to dip into the square-law operating regime.

Several calibration runs resulted in a model for normal operating conditions, with no artificial variations of pressure or EUV flux. The model consisted of DC and ND terms only. Four different model fits to the data are tabulated below.

Model #	Model	F-Ratio
1.	$AIM = AIM_0 + C_1*ND + C_2*ND^2$	9236
2.	$AIM = C_1*ND + C_2*ND^2$	209322
3.	$AIM = AIM_0 + C_1*ND$	256145
4.	$AIM = C_1*ND$	372299

Table 2. Normalization Models and Measure of model fit (F-Ratio).

Model number 4, which is the simple linear model with no DC intercept term, is now the best fit to the experimental calibration data. The effect of the systematic DC offset is removed by routing the ND pulse through an identical G/I-S/H stage as the AIM PD signal which has provisions for zero-level adjustment.

3.6 Conclusion

Hardware built by Sandia staff facilitate both AIM experiments and interferometery experiments on the 10X-I EUVL test bed. Specifically, mask and wafer stages are built to allow fine (3nm minimum step) and coarse (25mm) positioning of the object and image planes in either axis (X, Y). The work of this thesis involves specifying the hardware requirements, as well as installation, test, and calibration. Additional work involves software designed using Labview visual-based data acquisition programming language, to allow the complete automation of AIM experiments including all aspects of the timing of the test bed operations, timing and control, and data collection.

Signal collection electronics are selected to provide compatibility with AIM experiments in the EUV including a small-active area EUV sensitive photodiode, an ultra-low noise preamplifier, and pulse shaping amplifiers. Careful design of the preamplifier box was found to be important to the successful amplification of the low-flux signals including avoiding contamination of the pre-amp components. Noticeable contamination effects include fingerprints which provide a noisy conduction path around the outside of the 1GΩ feedback resistor. Insulation to EMI is provided by a cast aluminum box. The measured SNR of the AIM system is 12 for single slit (50μm X 0.1μm) artifact measurements compared the the theoretically calculated value of 13.

References

[1] D. Tichenor, G. Kubiak, A. Chaudhuri, and R.Stulen, "Development of a projection lithography system", OSA Proceedings on Extreme Ultraviolet Lithography, Optical Society of America, Monterey, CA, pp. 128-32, 1993.

[2] D. Tichenor, G. Kubiak, A. Chaudhuri, and R.Stulen, "Development of a projection lithography system", OSA Proceedings on Extreme Ultraviolet Lithography, Optical Society of America, Monterey, CA, pp. 128-32, 1993.

[3] A. K. Ray-Chaudhuri, C. H. Fields, K. D. Krenz, W.G. Oldham, and R. H. Stulen, "Interferometry for Evaluation of Extreme Ultraviolet Optics," EIPBN Conf. Atlanta, GA 1996, JVST - B, Nov./Dec., 1996.

[4] A. K. Ray-Chaudhuri, K. D. Krenz, C. H. Fields, R. H. Stulen, and W.G. Oldham, "Development of Extreme Ultraviolet Interferometry for Laser Plasma Source Operation," OSA Proceedings on Extreme Ultraviolet Lithography, Optical Society of America, Boston, MA, pp. 128-32, 1996.

[3] F.S. Goulding, "Pulse-shaping in low-noise nuclear amplifiers", **Nuclear Instruments and Methods**, pp. 493-504, North-Holland Publishing Co., 1972.

[4] M. Nakamura, D.A. Landis, and G. Rai, "Low power shaper amplifier for the EOS TPC detector", IEEE Transactions on Nuclear Science, Vol. 38, No. 2, pp. 50-2, April, 1991.

[5] R. Korde, L.R. Canfield, "Silicon photodiodes with stable, near-theoretical quantum efficiency in the soft x-ray region", SPIE X-Ray Instrumentation, Vol. 1140, pp. 126 - 132, 1989.

[6] International Radiation Detector (IRD) technical specification sheet for the AXUV series soft-X-ray photodiodes, September, 1995.

[7] R.S. Muller, T.I. Kamins, **Device Electronics for Integrated Circuits**, John Wiley & Sons Publisher, 1977.

[8] AMPTEK Inc. A250 Charge sensitive pre-amplifier technical specification sheet, 1995.

[9] E. Barberis, N. Cartiglia, D.E. Dorfan, J. Rahn, et. al., "A fast shaping amplifier-comparator integrated circuit for silicon strip detectors", IEEE Transactions on Nuclear Science, Vol. 40, No. 4, pp. 740-3, August, 1993.

[10] N.P. Paschalidis, A.G. Andreou, E.T. Sarris, "A CMOS analog-digital integrated circuit for charged particle spectrum measurements", IEEE Transactions on Nuclear Science, Vol. 40, No. 4, pp. 1313-18, October, 1993.

[11] S. Gadomski, G. Hall, T. Hogh, P. Jalocha, et. al., "The deconvolution method of fast pulse shaping at hadron colliders", Nuclear Instruments & Methods in Physics Research, Sect. A., Vol. A320, pp. 217-27, 15 August, 1992.

[12] J.W. Zaninetti, C.A. Marques, "A pulse amplifier/shaper for use with radiation detectors", Revista Telegrafica Electronica, No. 908, pp. 732-8, July, 1989.

[13] IEEE standard test procedures for amplifiers and preamplifiers used with detectors of ionizing radiation, IEEE, NY, NY, 10 May, 1989.

[14] S. Desi, "A low noise figure nuclear spectroscopy amplifier", Nuclear Instruments & Methods in Physics Research, Sect. A., Vol. A305, No. 1, pp. 214-57, 10 July, 1991.

[15] H. Ikeda, N. Ujiie, K. Kawaguchi, Y. Akazawa, "Evaluation of a bipolar amplifier prototype for silicon strip readout", Nuclear Instruments & Methods in Physics Research, Sect. A, Vol. A300, No. 2, pp. 217-27, 15 January, 1991.

[16] E. Gatti, P.A. Rizzo, M. Sampietro, "Enhancements in pulse amplitude spectroscopy, decoupling detector and preamplifier by a series inductor", Nuclear Instruments & Methods in Physics Research, Sect. A., Vol. A297, No. 3, pp. 479-88, 10 December, 1990.

[17] Z. Djuric, J. Piotrowski, "Infrared photodetector with electromagnetic carrier depletion, Optical Engineering (ISSN 0091-3286), Vol.31, pp. 1955-60, September 1992.

[18] Y. Wang, N. Mansour, S. Nabil, "Theoretical study of a potential low-noise semimetal-based avalanche photodetector", IEEE Journal of Quantum Electronics (ISSN 0018-9197), Vol.28, pp. 507-13, February, 1992.

[19] M. Vidal, B. Puig, J.M. Buxo, "A bipolar photodetector compatible with standard CMOS technology", Solid-State Electronics (ISSN 0038-1101), Vol.34, pp. 809-14, August, 1991.

[20] J.P. Garcia, E.L. Dereniak, "Extrinsic silicon photodetector characterization", Applied Optics (ISSN 0003-6935), Vol.29, pp.559-69, 1 February, 1990.

[21] P. Blixt, A. Krotkus, M. Kull, "A differential photodetector employing photoconductivity, for subnanosecond laser beam position measurements", Journal

of Physics. E, Scientific Instruments, (ISSN 0022-3735), Vol.21, pp. 971-3, October, 1988.

[22] J.A. Modolo, G.W. Anderson, F.J. Kub, "Wafer level high-frequency measurements of photodetector characteristics", Applied Optics (ISSN 0003-6935), Vol.27, pp. 3059-61, 1 August, 1988.

[23] T.H. Chyba, L. Mandel, "Angular sensitivity of a vacuum photodiode, or does a photodetector always count absorbed photons?", Journal of the Optical Society of America B, Optical Physics (ISSN 0740-3224), Vol.5, pp. 1305-11, June, 1988.

[24] A. VanderLugt, "Use of decimated photodetector arrays in spectrum analysis", Applied Optics (ISSN 0003-6935), Vol.27, pp. 2061-70, 15 May, 1988.

[25] A. Kostenbauder, S.J.B. Yoo, A.E. Siegman, "A fast diffusion-driven photodetector: theory and experiment", IEEE Journal of Quantum Electronics (ISSN 0018-9197), Vol.24, pp. 240-4, February, 1988.

[26] V.A. Chumak, M. Bertolotti, A. Ferrari, "Position-sensitive photodetector based on hydrogenated amorphous silicon p-i-n junctions", Review of Scientific Instruments (ISSN 0034-6748), Vol.58, pp. 202-6, February, 1987.

[27] A. Longoni, G. Ripamonti, A. Grassi, "Photodetector array performances improved by low-cost microprocessor-based measurement techniques", Journal of Physics. E, Scientific Instruments, (ISSN 0022-3735), Vol.17, pp. 282-6, April, 1984.

[28] S.G. Chamberlain, P.Y. Lee, "A novel wide dynamic range silicon photodetector and linear imaging array", IEEE Journal of Solid-State Circuits (ISSN 0018-9200), Vol.19 pp. 41-8, February, 1984.

[29] Djuric, Zoran Piotrowski, Jozef, "Infrared photodetector with electromagnetic carrier depletion, Optical Engineering (ISSN 0091-3286), Vol. 31, pp. 1955-60 September, 1992.

[30] Wang, Yang; Mansour, Nabil; Salem, Ali, "Theoretical study of a potential low-noise semimetal-based avalanche photodetector", IEEE Journal of Quantum Electronics (ISSN 0018-9197), Vol. 28, pp. 507-13, February, 1992 .

[31] Vidal, M. Puig; Bafleur, M.; Buxo, J., "A bipolar photodetector compatible with standard CMOS technology Solid-State Electronics (ISSN 0038-1101), Vol. 34, pp.809-14, August, 1991.

[32] Garcia, J. P.; Dereniak, E. L., "Extrinsic silicon photodetector characterization", Applied Optics (ISSN 0003-6935), Vol. 29, pp. 559-69,1 February, 1990.

[33] Blixt, P.; Krotkus, A.; Kull, M., "A differential photodetector employing photoconductivity, for subnanosecond laser beam position measurements", Journal of Physics. E, Scientific Instruments, (ISSN 0022-3735), Vol. 21, pp. 971-3, October 1988.

[34] Modolo, John A.; Anderson, Gordon Wood; Kub,, Francis J., "Wafer level high-frequency measurements of photodetector characteristics", Applied Optics (ISSN 0003-6935), Vol.27, pp. 3059-61, 1 August, 1988.

[35] Chyba, T. H.; Mandel, L.," Angular sensitivity of a vacuum photodiode, or does a photodetector always count absorbed photons?", Journal of the Optical Society of America. B, Optical Physics (ISSN 0740-3224), Vol. 5, pp. 1305-11, June, 1988.

[36] VanderLugt, A., "Use of decimated photodetector arrays in spectrum analysis", Applied Optics (ISSN 0003-6935), Vol.27, pp. 2061-70, 15 May, 1988.

[37] Kostenbauder, Adnah; Yoo, S. J. B.; Siegman, A. E., "A fast diffusion-driven photodetector: theory and experiment", IEEE Journal of Quantum Electronics (ISSN 0018-9197), Vol. 24, pp. 240-4, February 1988.

[38] Chumak, V. A.; Bertolotti, M.; Ferrari, A., "Position-sensitive photodetector based on hydrogenated amorphous silicon p-i-n junctions", Review of Scientific Instruments (ISSN 0034-6748), Vol. 58, pp. 202-6, February , 1987.

[39] Longoni, A.; Ripamonti, G.; Grassi, A., "Photodetector array performances improved by low-cost microprocessor-based measurement techniques", Journal of Physics. E, Scientific Instruments, (ISSN 0022-3735), Vol. 17, pp. 282-6, April, 1984.

[40] Chamberlain, Savvas G.; Lee, Jim P. Y., "A novel wide dynamic range silicon photodetector and linear imaging array", IEEE Journal of Solid-State Circuits (ISSN 0018-9200), Vol. 19, pp. 41-8, February, 1984.

Chapter 4

EUVL System and Vibration Issues

4.1 Vibration Reduction Measures

There are several major sources of vibration on the current 10X-I EUVL system. The vacuum pump that rests on the floor couples vibration modes up through the laser table legs to the vacuum chamber. The system also has installed a large flywheel rotating at 20KRPM referred to as a "chopper" [1-4]. This chopper is part of the attempt to reduce ejecta from the solid metal target from depositing on the condenser lens. Significant increase in condenser lens lifetime was observed after the installation of this chopper. The wafer chamber was located on the same laser table as the target chamber so vibration from the chopper coupled through the table and also from the target chamber to the wafer chamber through the solid metal vacuum flange that connected the two.

Several measures are taken in an attempt to reduce the system vibration including separating the two chambers onto individual laser tables in an attempt to reduce the magnitude of the vibration from the target chamber and chopper to the wafer chamber through the table. The solid metal vacuum flange is also replaced by a flexible bellows to reduce the vibration from the target chamber to the wafer chamber through the vacuum housing.

Another vibration isolation measure is installation of a thick Sorbothane layer [12]. between the vacuum pump and the laboratory floor. A half-inch thick layer of Sorbothane and a thin piece of aluminum sheet stock is installed under each table leg. Sorbothane is thermoset, polyether based, polyurethane material designed for high energy absorption by

turning mechanical energy into heat. The 0.5 inch Sorbothane with durometer value of 70 is selected for loads between 1700-2500 lbs.

4.2 EUVL System Vibration Measurements

4.2.1 Transducer Measurements

To evaluate the effectiveness of these vibration suppression attempts, transducer measurements are taken at three locations on the system: On the vacuum table near the target chamber, on the second vacuum table near the wafer chamber, and at the wafer plane directly on top of the three stainless steel (SS) balls that defined the image plane. Two sets of measurements are taken at each location; one before and another after the improvements listed in section 4.1 are implemented. Initial vibration spectrum plots reveal that all significant vibration modes occurs at frequencies below 1.6kHz. The output transducer measurements in the spectrum plots are dbV_{rms}, which is dBm referenced to 1mV. To investigate the contribution of the mechanical pump and the chopper to system vibration, several transducer measurements were taken each location with each on and off. Figures 4.1-4.4 show the results of these measurements which plot the magnitude of the vibration frequency components versus frequency from 0 (DC) to 1.6kHz.

Early attempts were made to isolate the major sources of system vibration. Figures 4.1a and 4.1b are two vibration power spectrum plots, again taken on top of the image plane balls before and after, respectively, the vibration suppression measures of section 4.1. These measurements are taken with the vacuum pump on and the chopper off (i.e., stationary). A comparison of the plots reveals that several of the vibration modes

were reduced in magnitude including peaks at 360, 724, and 1068 Hz. There is a significant reduction in the vibration which is attributed to the chopper and to the efforts to isolate the wafer vacuum chamber from the rest of the system (i.e. the sorbothane under the pump and vacuum table legs and utilization of the lossy vacuum bellows and isolation mounts).

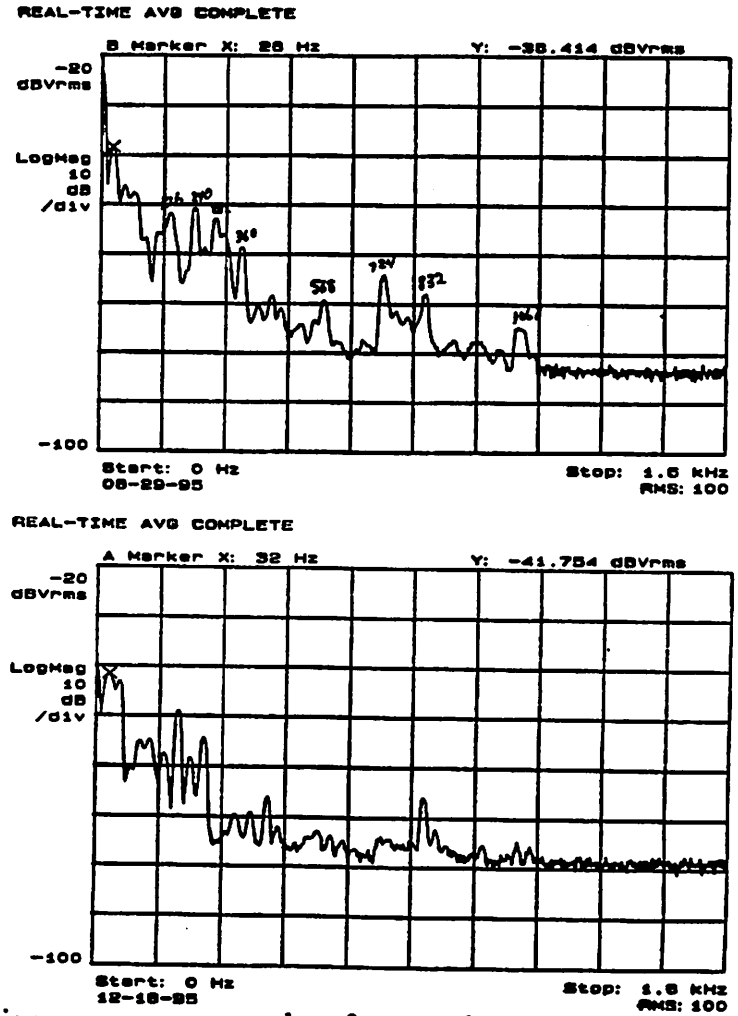

Figure 4.1 Vibration power spectrum data for transducer-head measurements taken on top of the three image plane balls with the vacuum pump on and the chopper off. The figures plot the log magnitude of the transducer-head measurement in $dB_{V_{rms}}$ versus frequency taken the average of 100 samples to improve the signal to noise. The two plots represent the vibration of the EUV system before (plot (a) dated 08-29-95) and after (plot (b) dated 12-18-95) the vibration suppression efforts outlined in section 4.1 including the separation of the system onto two tables and the insertion of sorbothane dampeners. The plots show the effectiveness of these efforts in suppressing vacuum pump vibration that couples to the image plane.

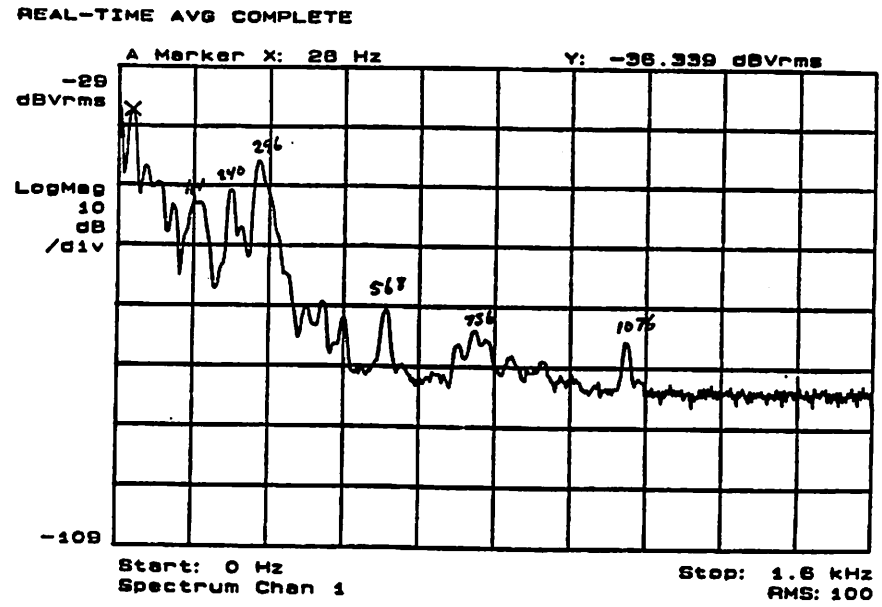

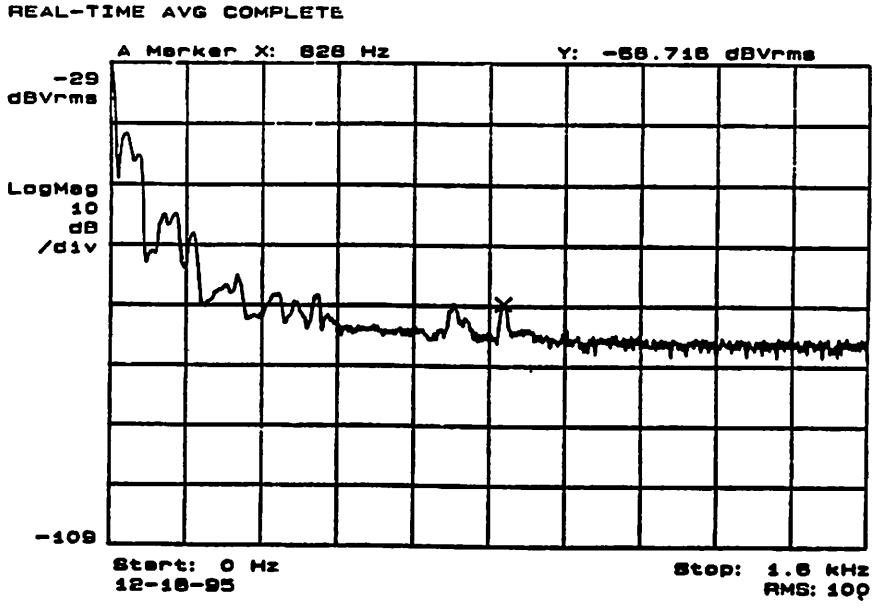

Figure 4.2 Vibration power spectrum data for transducer-head measurements taken on top of the three image plane balls with the vacuum pump and the chopper off. The figures plot the log magnitude of the transducer-head measurement in dB_{Vrms} versus frequency under the same measurement conditions as the previous measurements where the two plots represent the vibration of the EUV system before and after the vibration suppression efforts outlined in section 4.1. The plots show the effectiveness of these efforts in suppressing transient vibration that couples from the room and floor to the image plane.

Isolating the major contributors of the vibration we now look at random vibration from the floor that couple up the table legs to the wafer chamber and camera. Figures 4.2a and 4.2b are the results of transducer measurements once again taken on the three SS balls before and after, respectively, the vibration suppression measures. Both of these measurements are taken with both the chopper and vacuum pump off. The vibration measured now couples up from the ground or through the connection between the target and wafer chambers (previously a solid piece of stainless, currently a flexible bellows). The plots show reductions in vibration modes at 240, 246, 568, 765, and 1076Hz with the most significant reduction of 25dbV_{rms} at 296Hz.

To isolate and measure the impact of separating the single laser table into two, transducer measurements are taken on the table adjacent to the wafer vacuum chamber. This data provides information concerning the magnitude of chopper vibrations that couple to the wafer chamber through the table versus the coupling path through the direct vacuum connection between the chambers. Figures 4.3a and 4.3b show the resulting vibration spectrum plots of these measurement taken with both the pump and the chopper on, again before and after, respectively, the vibration suppression measures of the previous section. Several vibration modes are attributed to coupling through the old table. All vibration nodes at frequencies above 1kHz were suppressed entirely with a 25dbVrms suppression at 1240Hz. Several of the lower frequency modes are also reduced, namely: 988, 912, 704, 592, 340, and 72 Hz.

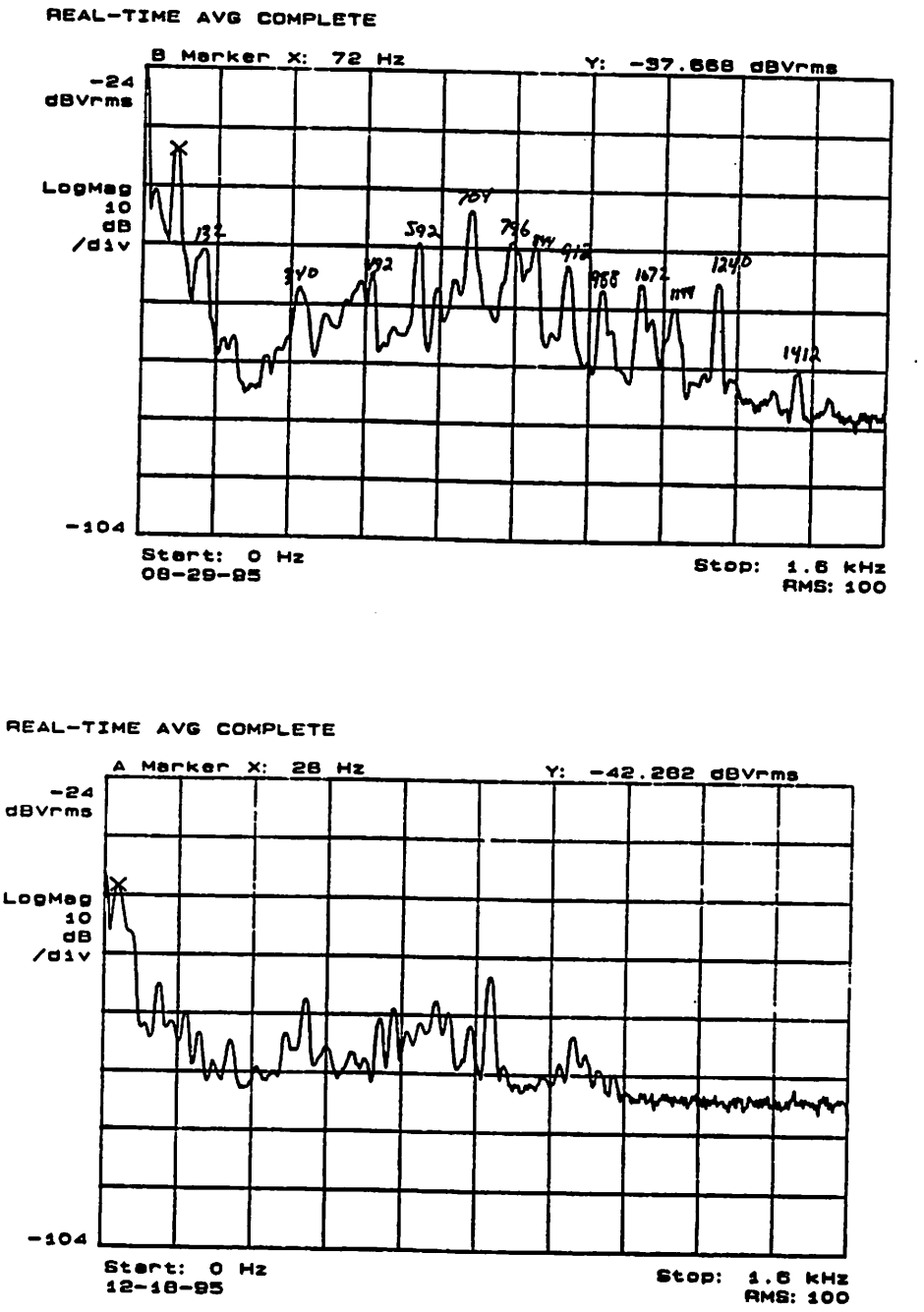

Figure 4.3 Vibration power spectrum data for transducer-head measurements taken on the wafer vacuum chamber table, adjacent to the vacuum chamber. The measurements are taken with the vacuum pump and the chopper on. The figures plot the log magnitude of the transducer-head measurement in dB_{Vrms} versus frequency under the same measurement conditions as the previous measurements where the two plots represent the vibration of the EUV system before and after the vibration suppression efforts outlined in section 4.1. The plots illustrate the effectiveness seperating the single laser table into two by directly measuring the vibration modes present on the table surface itself.

Figures 4.4a and 4.4b plot the spectrum of two measurements taken by placing the transducer head direction on the three stainless steel image plane balls before and after, respectively, the vibration suppression measures of section 4.1. These plots show the combined effect of all vibration dampening efforts. These measurements are taken before the new wafer and mask stages, described in chapter 3, are installed. Both measurements are taken under normal operating conditions with the pump and chopper running. These plots show the improvements from the separation into two tables with the vacuum bellows coupling and the Sorbothane introduction both under the table legs and under the vacuum pump. Many peaks are reduced, and several are removed entirely. The oscillation peak at 268Hz is reduced by nearly 30dbV_{rms} while the oscillation mode at 1072Hz is reduced 45dbV_{rms}. A comparison of Figure 4.4b with 4.1b show that a significant portion of the vibration is still attributed to the chopper flywheel.

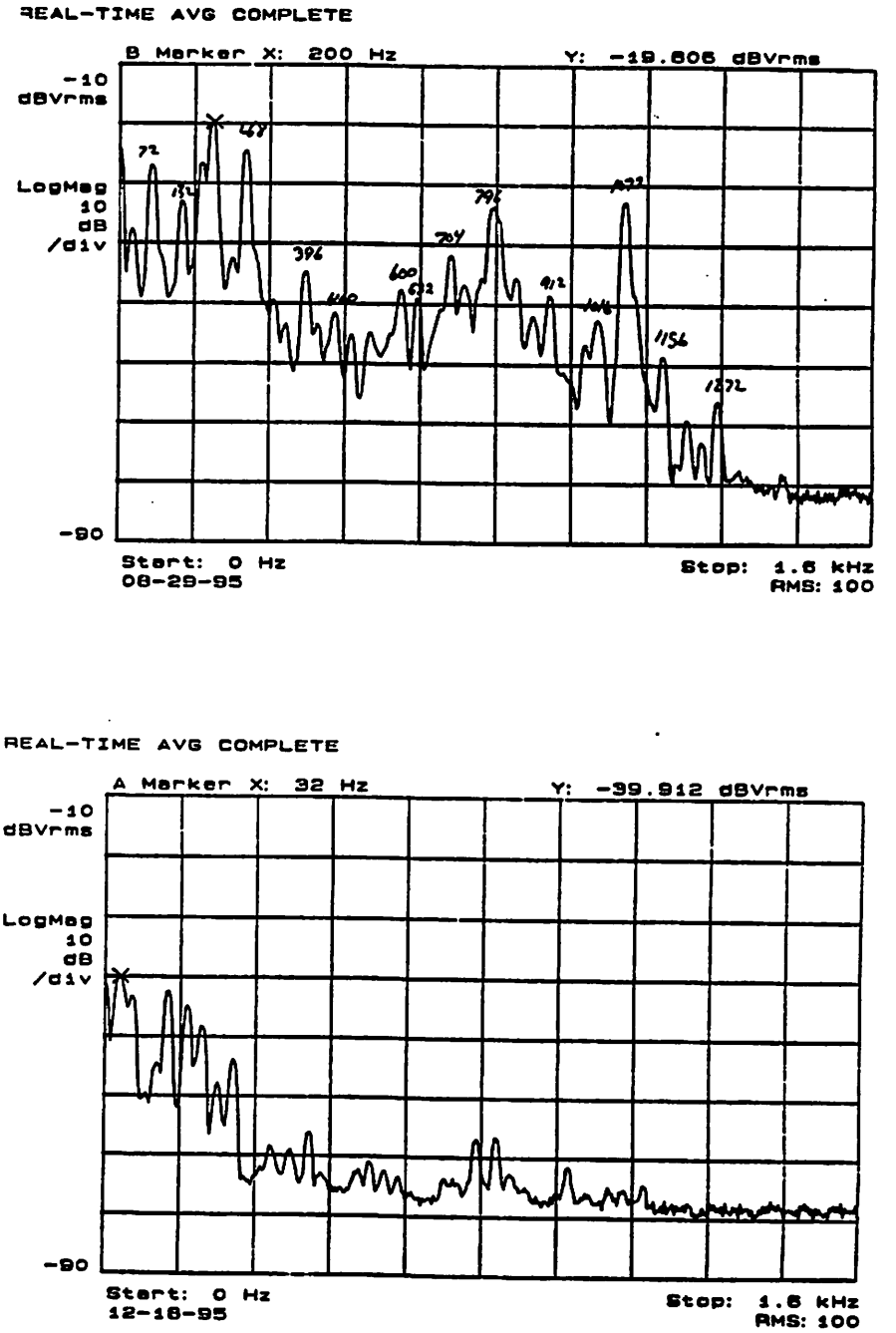

Figure 4.4 Vibration power spectrum data for transducer-head measurements taken on top of the three image plane balls with the vacuum pump and the chopper on. The figures plot the log magnitude of the transducer-head measurement in $dB_{V_{rms}}$ versus frequency under the same measurement conditions as the previous measurements where the two plots represent the vibration of the EUV system before and after the vibration suppression efforts outlined in section 4.1. The plots show the effectiveness of the efforts in suppressing all vibration source under normal operating conditions including both chopper and vacuum pump vibration.

4.2.2 Knife-edge Measurements

4.2.2.1 Knife-edge Fabrication

Knife-edges are commonly used for such optical experiments as Focaut Testing and modulation transfer function (MTF) measurement [5-10]. The knife-edges used for previous EUV imaging experiments are simply the edges of razor blades. The blades used in these experiments typically contain several microns of roughness along the edge of the blade that degrades the quality of the measurements. Another problem with the use of a razor blade is that due to its physical construction, it is difficult to position the edge at the image plane and requires moving the image plane to the plane of the razor which injects another source of error into the measurements.

In an attempt to overcome these obstacles, an optically sharp knife-edge has been fabricated using silicon processing technology. This new knife-edge facilitates aerial image measurements as well as total EUVL system performance measurements. The knife-edge is defined using the difference between the etch rates of the <100> and <110> planes of silicon. The specifics of the fabrication process are found in appendix B7 and are outlined here for reference.

The knife-edges in these experiments originate as $1mm^2$ (100) Silicon nitride membranes. After suitable masking, the membranes are etched through with a preferential etch which does not attack (111) Silicon planes, resulting in a knife-edge. Since silicon exhibits low attenuation of EUV photons, a final evaporation step is required to make this knife-edge useful for EUVL experiments. Here a 0.5% transmission thickness of InSb (80nm) is deposited by thermal evaporation onto the frontside of the wafer. Figure 4.5 is

a qualitative illustration of the Si MEMS knife-edge and its mounting on an image plane plate compared with that of the razor blade knife-edge.

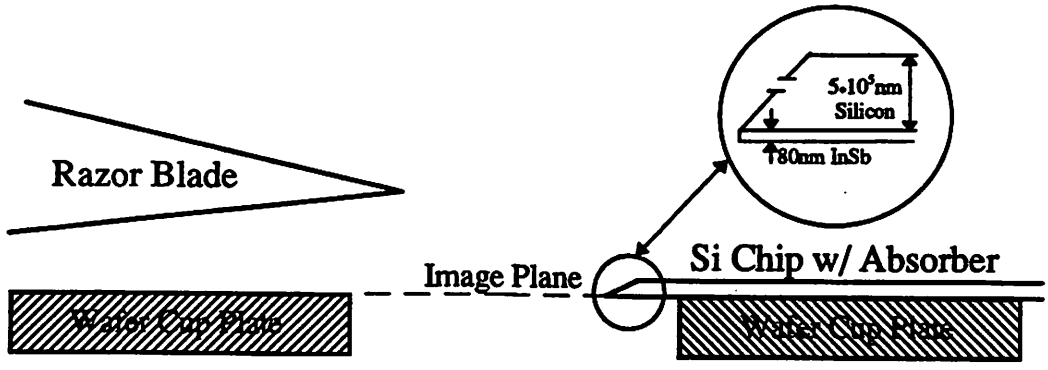

Figure 4.5 Qualitative illustration of razor blade and Si MEMS knife-edge and their relative image-plane cup plate mounting.

4.2.2.2 Knife-Edge Response Function

The response of this new EUV knife-edge may be evaluated analytically by analogy with the case of the diffraction theory of shadow exposures in optical lithography. Here we are imaging the edge of a dark half-plane by shadow-casting the aerial image at the wafer plane through the knife-edge across some distance (h) on the diode. Exhaustive studies of this case have been carried out theoretically for the case of partially coherent illumination beginning with Kirchoff's diffraction theory [5, 9, 28].

Simulations are conducted to investigate the response function of this new knife-edge, using the U.C. Berkeley simulation program TEMPEST. Figure 4.6 shows the results of the simulation to measure the response function of the full knife-edge with a top InSb absorber layer thickness of 80nm. This is a plot of the intensity produced by the incident plane wave interacting with the knife-edge. The intensity nodes, seen as bright streaks in the plot, are caused by the coherent interaction of the incident plane wave that passes unobstructed with the wave diffracted from the tip of the knife-edge.

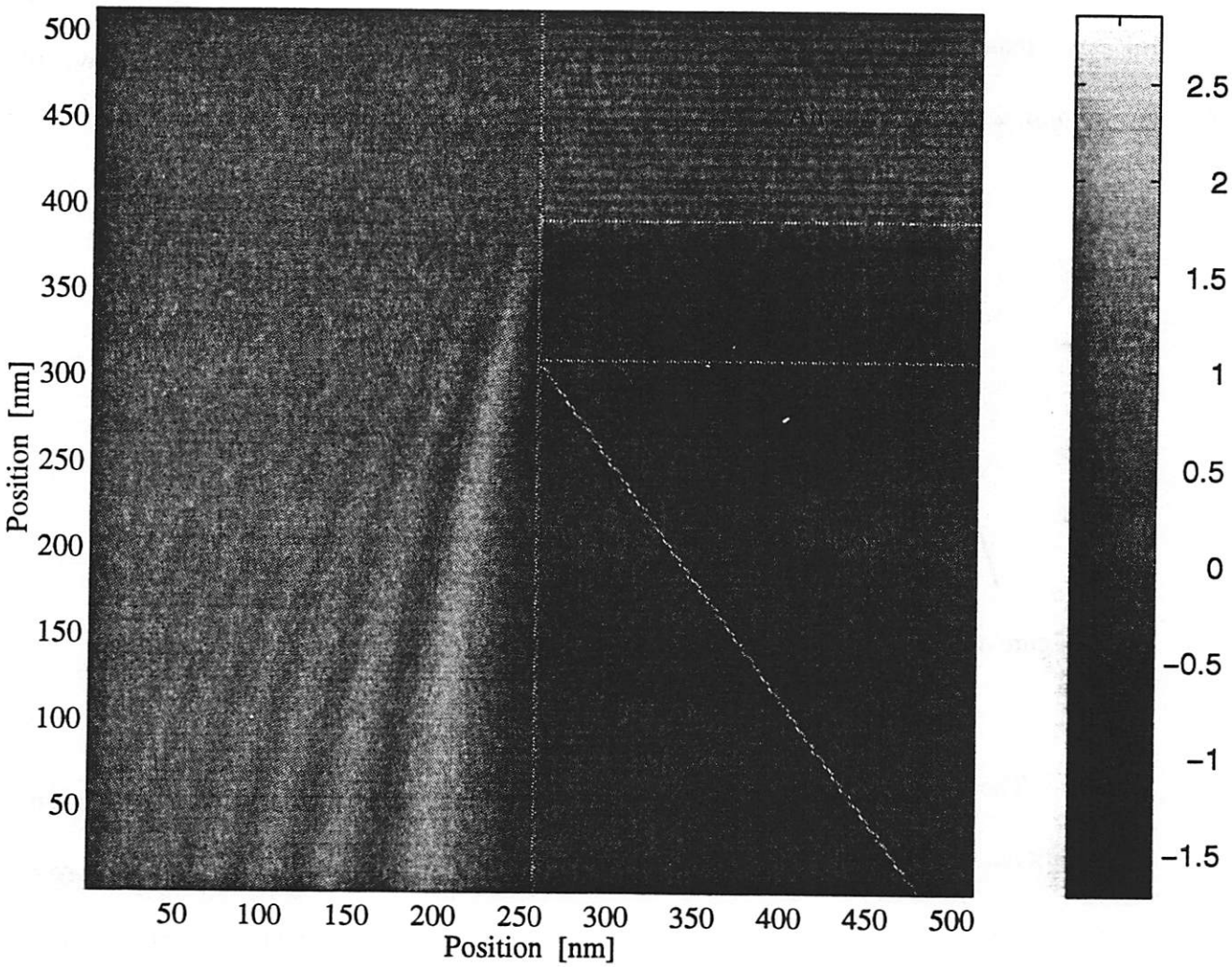

Figure 4.6 Simulated intensity plot of 13.4nm plane wave passing at normal incidence by optical knife-edge fabricated using MEMS processing and EUV absorber evaporation.

The 10X-I imaging system's non-telecentric objective presents the incident photons at the image plane at an angle of 12.1 degrees from the normal. The knife-edge is positioned such that the non-telecentricity of the system causes the incident rays to pass through a thinner amount of material as qualitatively illustrated by Figure 4.7. Mounting the knife-edge as in orientation 2 of Figure 4.7 presents a more idealized optically sharp edge than orientation 1. The simulations assume a normal incidence plane wave of 13.4nm wavelength with 0 bandwidth (coherent illumination).

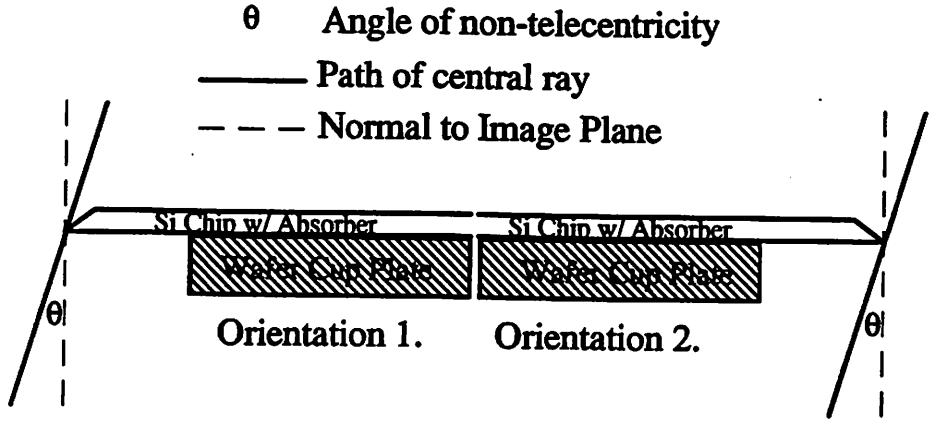

Figure 4.7 Qualitative illustration of Si MEMS knife-edges mounted in two differing orientations relative to the non-telecentric angle of the 10X-I camera.

The angle of the top absorber layer will vary slightly owing to evaporation conditions. Figure 4.8 shows the results of variation in the thickness of the absorber layer near the edge from 90 - 45 degrees. The figure shows a series of intensity plots at the bottom of the simulation domain for each case of top absorber layer angle near the edge. The simulations show that the main effect of variations in the top angle is to shift the position of the response curve. For each case simulated, the width of the transition region

(90%-10%) is less than 52nm. The average transition width is 52.17nm with a sample standard deviation of 3.7nm for 7 cases. A shift of this nature in the response of the knife-edge will produce no noticeable difference in the measured signal owing to relatively large size of the photodiode.

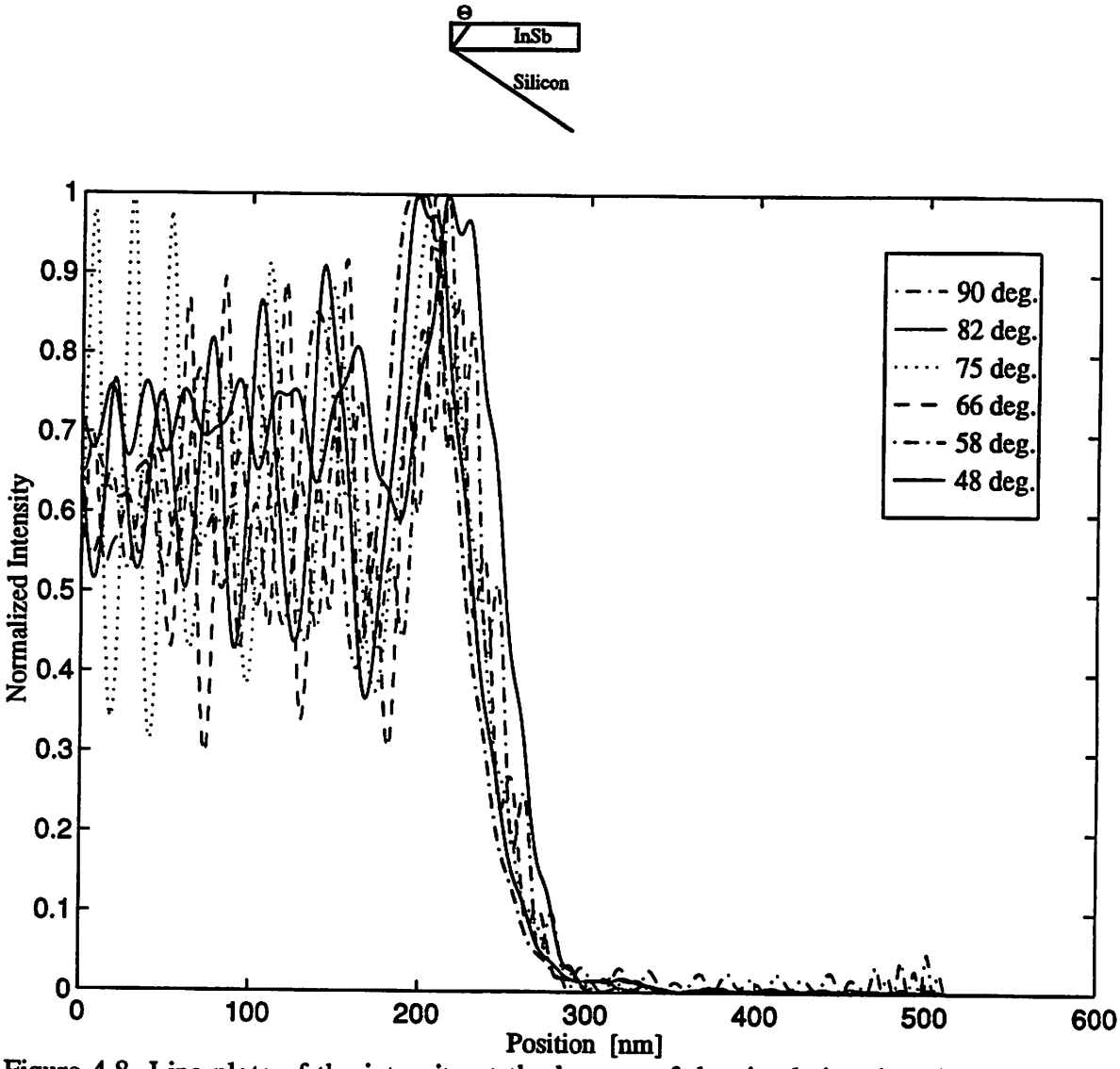

Figure 4.8 Line plots of the intensity at the bottom of the simulation domain for several cases where the angle of the top absorber layer is varied from 90 to 45 degrees.

Simulations of the absorber deposition onto the silicon knife-edge are conducted using the simulation tool SAMPLE as in section 2.4.2 for the case of the slit. The six curves plotted in Figure 4.9 show the final knife-edge profile after deposition from a hemi-spherical source where the angle is varied from 5 to 45 degrees. For the case of the large angle source (45degrees) the entire sidewalls of the silicon edges are coated while the small angle (5degrees) source results in nearly vertical absorber sidwalls. In all cases the absorber angle at the edge varies less than 45 degrees and is well characterized by the TEMPEST simulations.

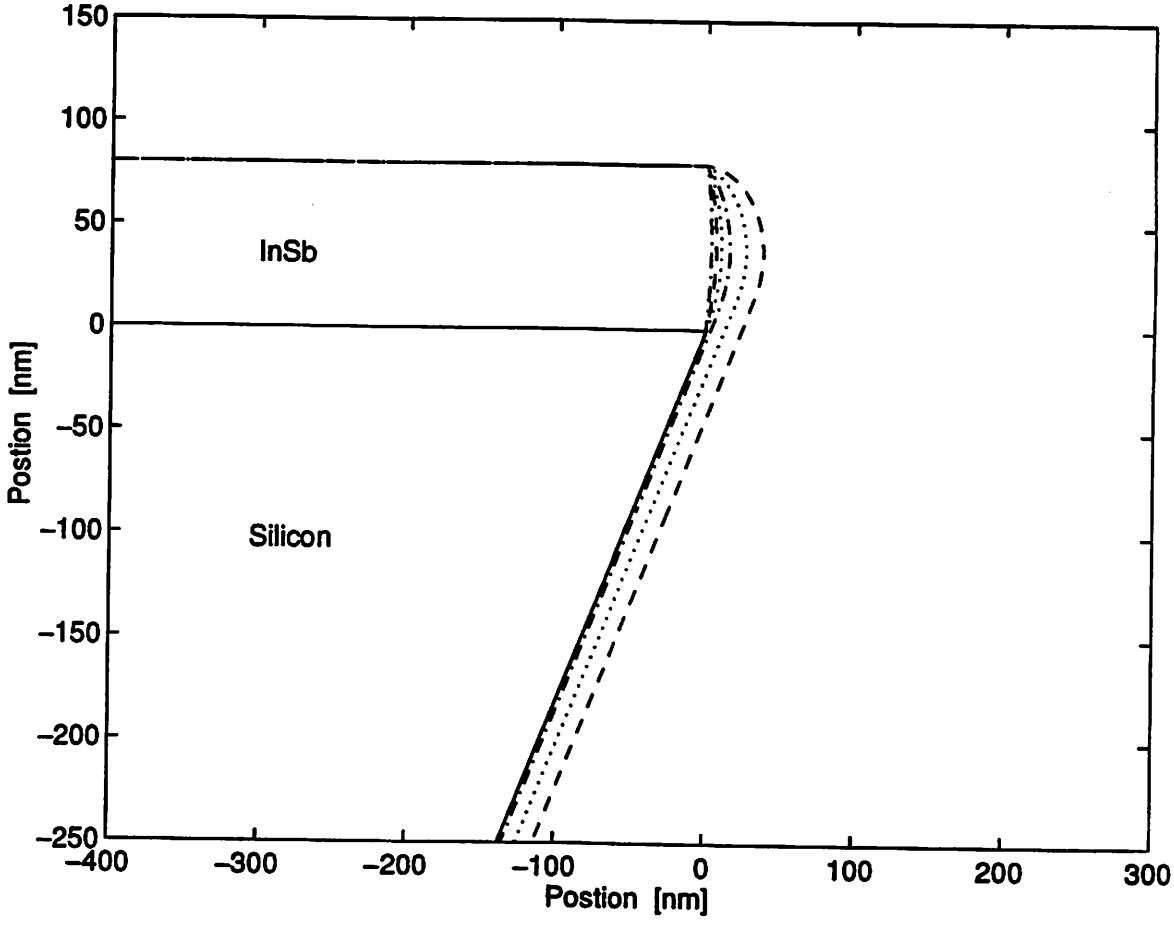

Figure 4.9 Knife-edge profiles consisting of a silicon edge defined by MEMS process, followed by absorber deposition from a hemi-spherical source where the source angle is varied from 5 to 45 degrees.

4.2.2.3 Vibration Measurements

The aerial image of a 2.5μm slit source is projected onto the knife-edge artifact placed at the image plane of the system. A scan across this image provides a measured signal intensity versus scan position that is the integral of the slit source aerial image. The ideal top-hat aerial image results in a normalized signal that is a ramp function with a constant slope of 0.4V/μm. The width of the linear region of the measured ramp signal is equal to width of the slit source: 2.5μm. A measurement of the stage and system vibration may be obtained by positioning the knife-edge in the middle of the scan and taking a series of successive intensity measurements. The only requirement of the sampling knife-edge, with respect to the vibration measurements, is that the transition width of the knife-edge be less than the width of the slit source such that signal variations due to vibration result in linear voltage signal variations. The previous section on simulation of the knife-edge response estimates the average transition region width to be 52.2nm.

The projected aerial image for these experiments is not an idealized top-hat function. To accurately model the experiments, three sets of simulations are carried out using the aerial image simulation program SPLAT [14]. The first series of simulations is for the purely diffraction limited case. A second series of simulations uses the raw pupil map data from the interferometery measurements of this camera at AT&T Bell Labs in Murray Hill, N.J. using visible light interferometry. The third set uses a set of 36-term Zernike Polynomials fit to the raw pupil map data from the visible light interferometry measurements. Figures 4.10a and 4.10b are mesh and contour plots of the raw pupil map data and the surface defined by the Zernike polynomials in waves (λ_{EUV}=13.4nm). These

two sets of data are better compared by viewing image maps of the data shown in Figures 4.11a and 4.11b. The 36 terms are insufficient to capture the higher frequency components, and therefore, the large $0.8\lambda_{EUV}$ peak seen in the plots of the raw data is lost in the fit.

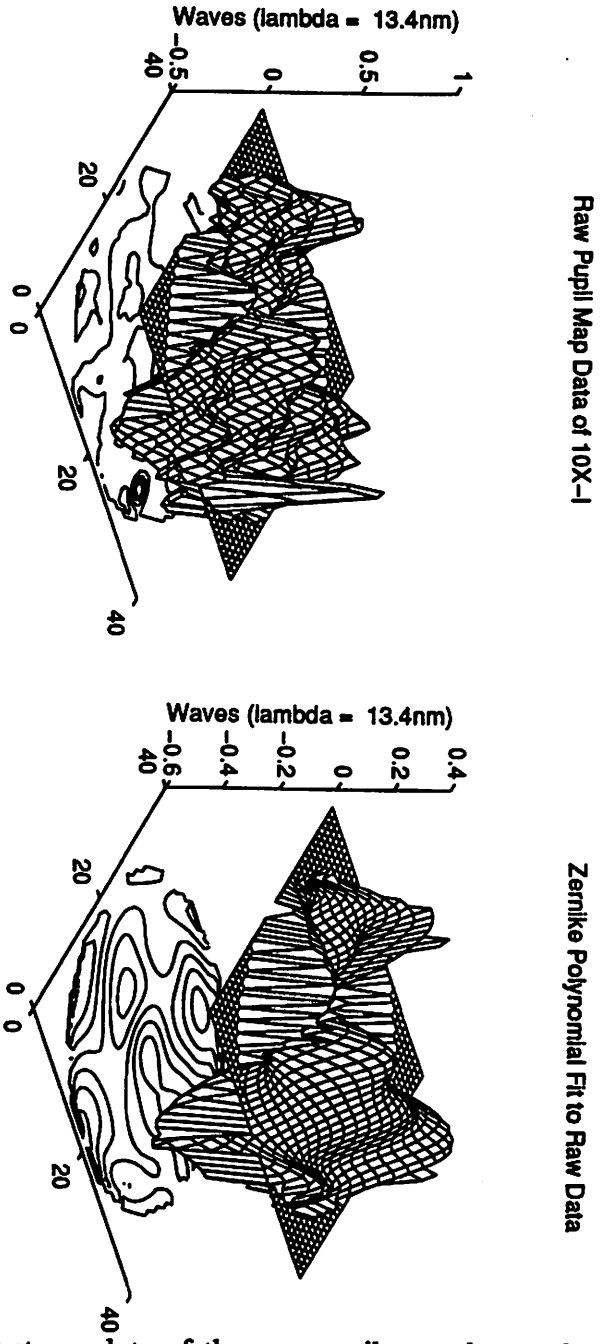

Figure 4.10 Mesh and contour plots of the raw pupil map data and a 36-term Zernike polynomial fit to the raw data.

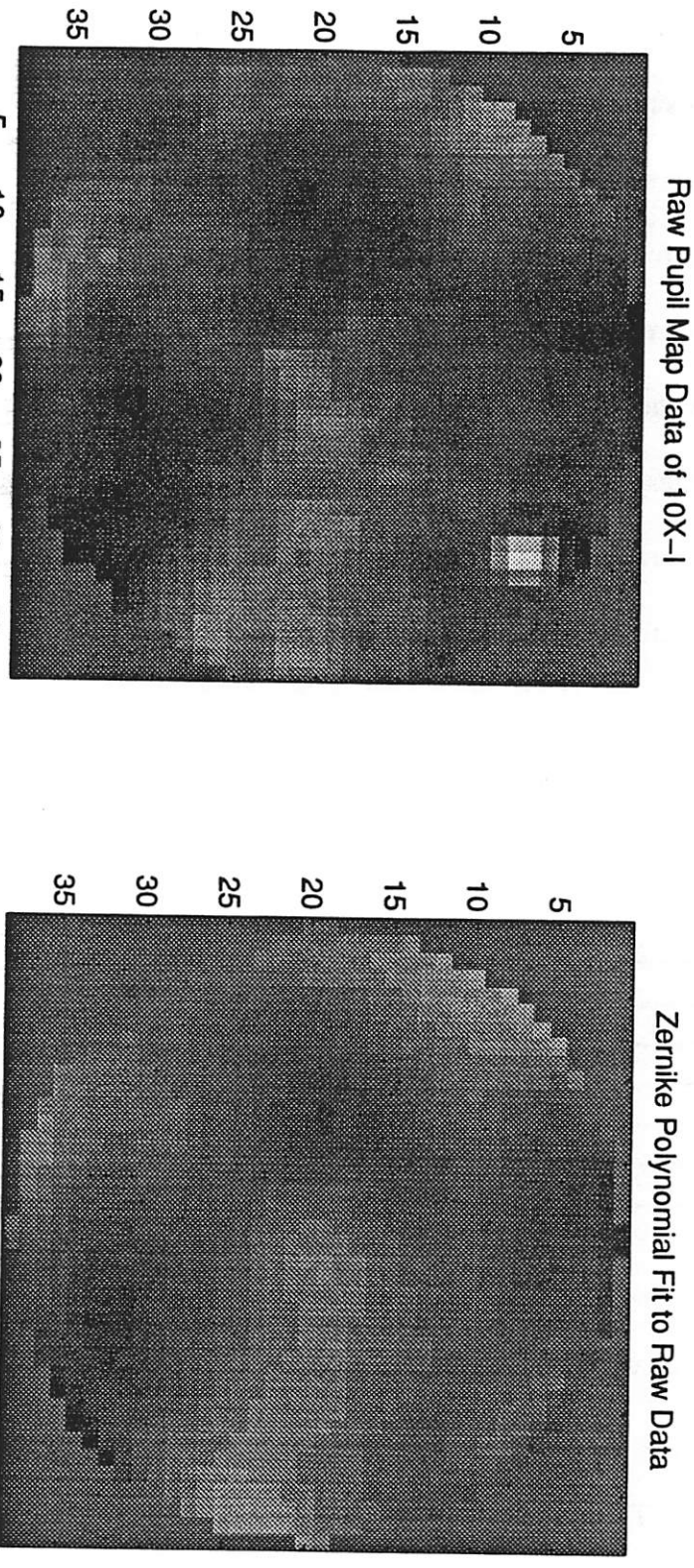

Figure 4.11 Intensity plots of the raw pupil map data and a 36-term Zernike polynomial fit to the raw data.

Figure 4.12 shows simulated aerial images of a 2.5μm slit source imaged with the 10X-I camera. The solid curve represents the purely diffraction-limited case. The dashed-dotted curve represents simulations using the raw pupil map data while the remaining curves are for the simulations done using the Zernike coefficients fitted to the raw data.

There are two methods to evaluate the effect of the knife-edge response. The first calculates the curves in Figure 4.13 by convolution of the knife-edge response with the aerial images. The second method first convolves the aerial image with the derivative of the response function and then integrates. Both of these methods are equivalent. Figure 4.13 points to negligible deviation from the fixed slope of 0.4V/μm in any of the images. The 52.2nm width of the knife-edge response function results in slight reduction in the idealized slope from 0.4V/μm to 0.39V/μm. Table 4.1 lists the slopes of the measured and simulated signals taking the response function into account.

Aerial Image		$Slope^{-1}$ [nm/mV]
Diff.-Limited		2.56
Raw Pupil Map		2.73
Zernike Fit (36 terms)		2.63
Zernike Fit (37 terms)		2.86
AIM Signal		2.70

Table 4.1 Slope of linear region of 2.5μm slit source knife-edge scan

To quantify the magnitude of the vibration, it is necessary to obtain a reference set of measurements that reflect the electronic noise of the AIM system, where vibration is not a factor. This reference set of data is obtained by positioning the wafer stage such that the entire 2.5μm slit source impinges upon the photodiode and is not obstructed by the knife-edge, far enough from the edge such that vibration causes no significant variation in

the detected signal. For future reference, we shall refer to this regime as "brite" while data taken with the knife-edge positioned at the mid-point of the scan shall be referred to as the "edge". The only qualification on the exact positioning of the "edge" measurements is that the artifact be positioned in the linear portion of the scan as mentioned previously. The measured knife-edge scan signal is simulated by plotting the integral the curves in Figure 4.12 which is shown in Figure 4.13.

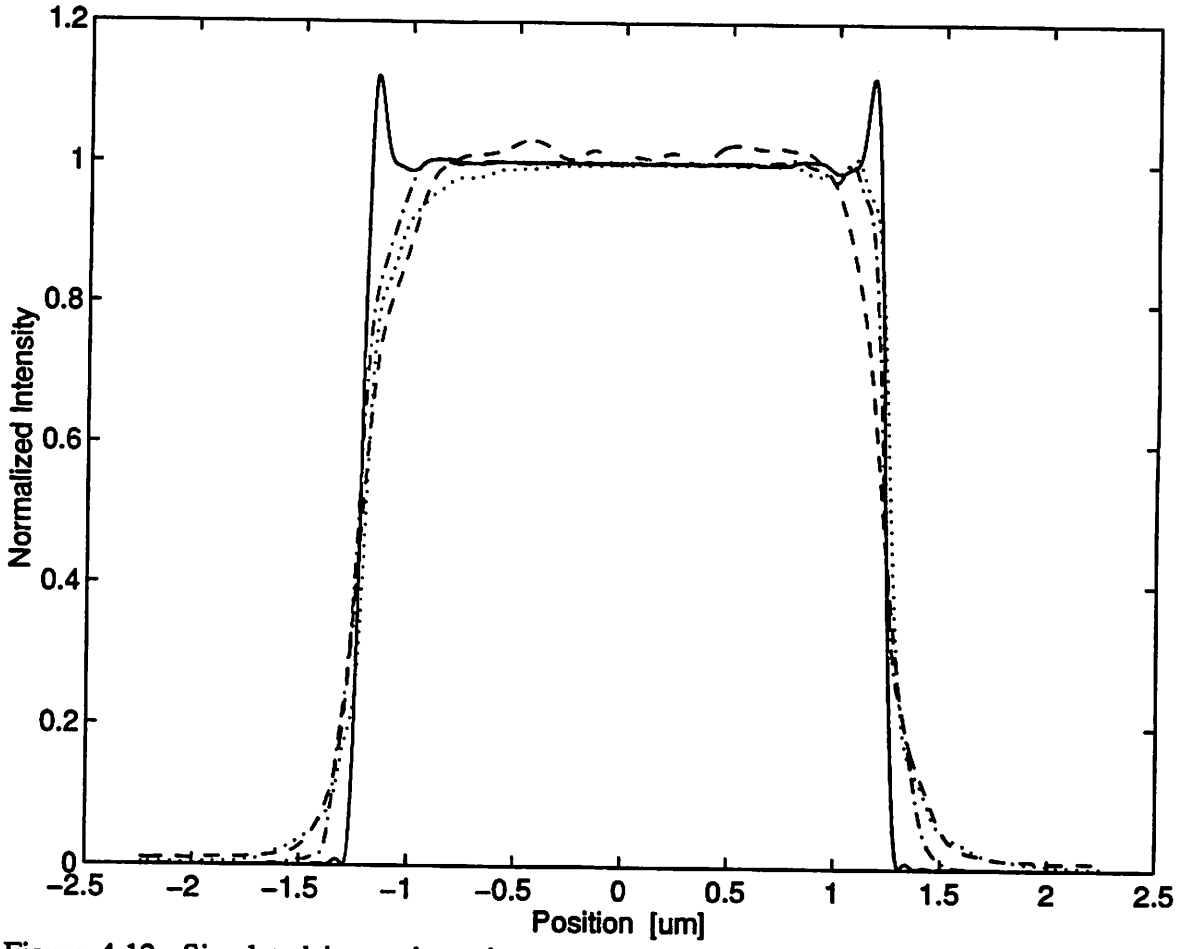

Figure 4.12 Simulated image intensity versus position for a 2.5μm line source imaged with the 10X-I EUVL system.

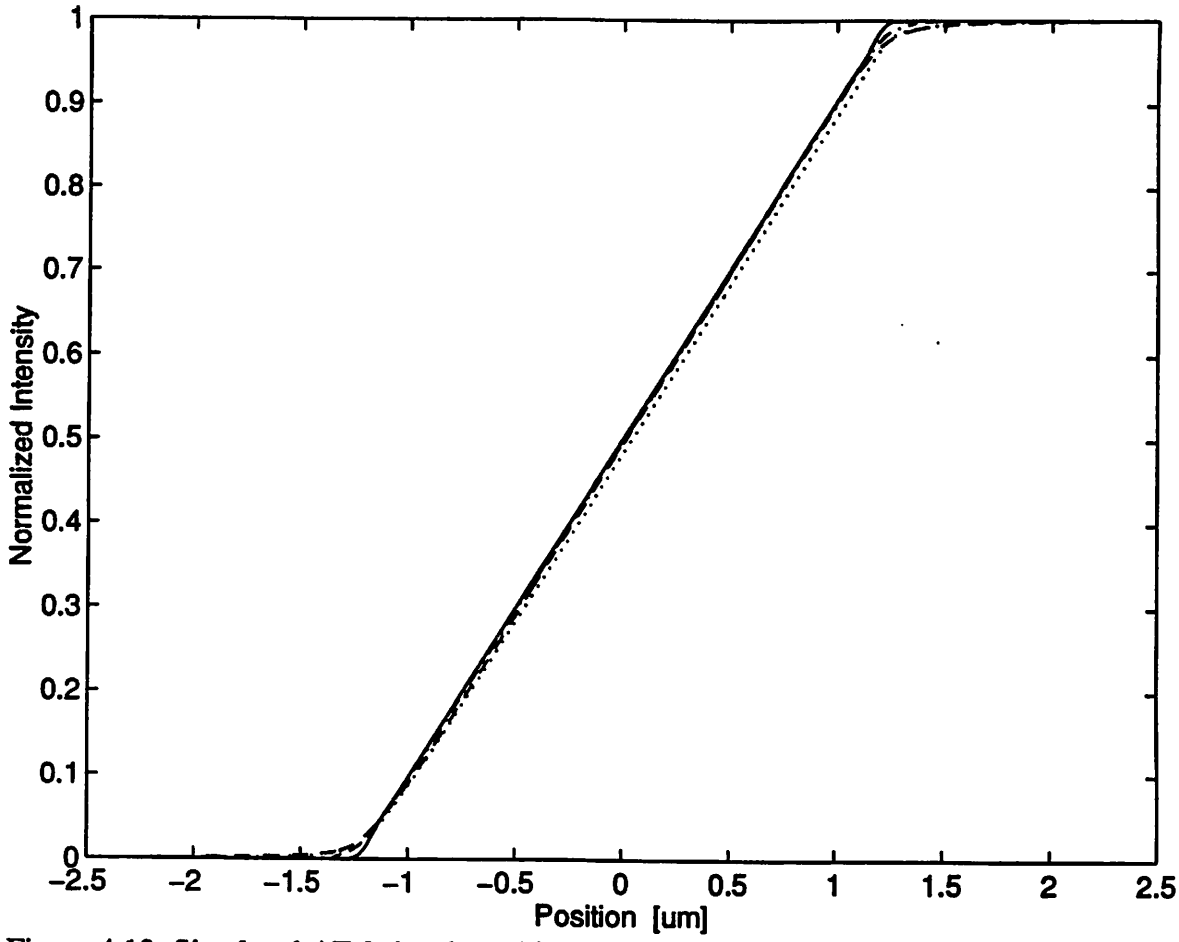

Figure 4.13 Simulated AIM signal resulting from knife-edge scans of a 2.5μm line source imaged with the 10X-I EUVL system.

Electronic noise in both of these regions produces a distribution of voltage reading around some average. The central limit theorem dictates that, assuming a sufficient number of samples are taken, the distribution will approach a standard normal distribution with a mean (μ) and a standard deviation (σ).

If no vibration exists in the system and we neglect shot noise, we would expect the two sets of data to be identical with respect to their variances (i.e., $\sigma^2_{brite} = \sigma^2_{edge}$). However, for systems with vibration, $\sigma^2_{edge} > \sigma^2_{brite}$. Assuming that these two test statistics are: (1) identically independent and (2) normally distributed (IIND), we may subtract them in quadrature and define a new test statistic σ^2_{vib} defined:

$$\sigma^2_{vib} = \sigma^2_{edge} - \sigma^2_{brite} \quad (1)$$

Since the two sets of data are taken under the same conditions with the same signal collection electronics and within a relatively short time span, they may be considered identical. Since they are taken at distinctly different times and wafer stage locations, they may be considered independent. This satisfies (1) of the IIND requirement.

To compute the magnitude of the vibration we first calculate σ_{vib} following equation 1. Since the vibration is a double-sided distribution, we then take $6*\sigma_{vib}$ to measure the full (99.5%) magnitude of the peak-peak swing. This variation in signal voltage maps to a variation in stage position. The 6σ variation is compared to both the measured scan voltage signal and the results from simulation to provide an upper and lower bound, respectively, of the vibration.

Satisfaction of the requirement of normal distribution is analyzed with the aid of the Spapiro-Wilk (S-W) test for normality [19]. This test compares the data to a standard normal distribution centered around the data mean and generates a test statistic, the W-number similar to the F-number which is the ratio of the mean-squared-error within the treatment to the overall mean-squared-error. If the p-value reported is less than 0.05 (or some other alpha), then it can be concluded that the distribution is not normal.

Vibration measurements consist of a series of data is taken both in the brite and on the edge for approximately 10 seconds. With a laser pulse frequency of 20Hz, this provides approximately 200 points in each data set. If the distribution is determined not to be normal, then more data points could be taken. Another method may be used if there exists an insufficient number of data points to achieve an alpha of less than say 0.05. It is

possible to use the Normal Quantile report to assess the extent of the vibration. It is possible to use the voltage difference between the 0.5% and 99.5% quantiles in the rms subtraction as in equation 1 to determine the $6\sigma_{vib}$ value of the vibration. The lack of normality in the distribution is also measured by comparing the computed value of $6*\sigma_{vib}$ with the 0.5-99.5% quantile value. One motivation for the choice of the latter method is the desire to save condenser lens life-time due to debris contamination.

The results of the analysis of the distribution of two normalized AIM voltage signals on the edge are shown in Figures 4.14and 4.15. Figure 4.14 represents a distribution that is very nearly normal while Figure 4.15 is an example of a distribution of questionable normality. The first section of each figure contains histogram plots of the normalized vibration data. A normal curve is superimposed on the data for a visual comparison of the normal fit to the data. The curve to the right of each histogram is a Normal Quantile plot. In this curve the raw data is represented by the dots with the 95% confidence intervals represented by the dashed lines. This plot shows the observed values against the approximated expected normal order statistics. If the data distribution is normal, the points on this plot follow a straight line. Different forms of curvature signal different kinds of departures from normality.

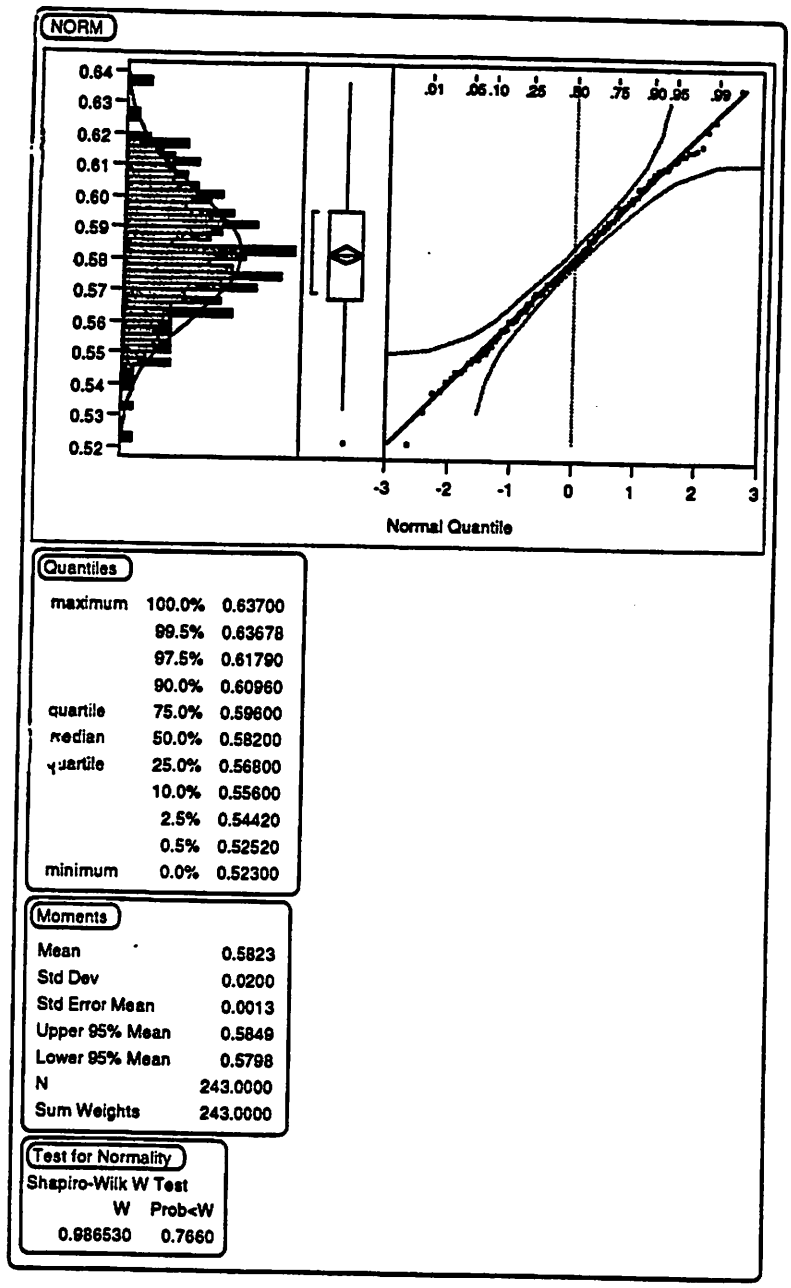

Figure 4.14 Statistical analysis of vibration measurement data for a vibration data that approximates a normal distribution. The top portion of the figure plots a histogram of the data with a normal distribution plotted by the solid line curve. A normal quantile plot is shown to the right of the histogram which is another visual technique for the evaluation of distribution normality. The individual quantile values are tabulated below the histogram plot. The moments of the distributions and the results of the Shapiro-Wilk test for normality are also tabulated in the figure.

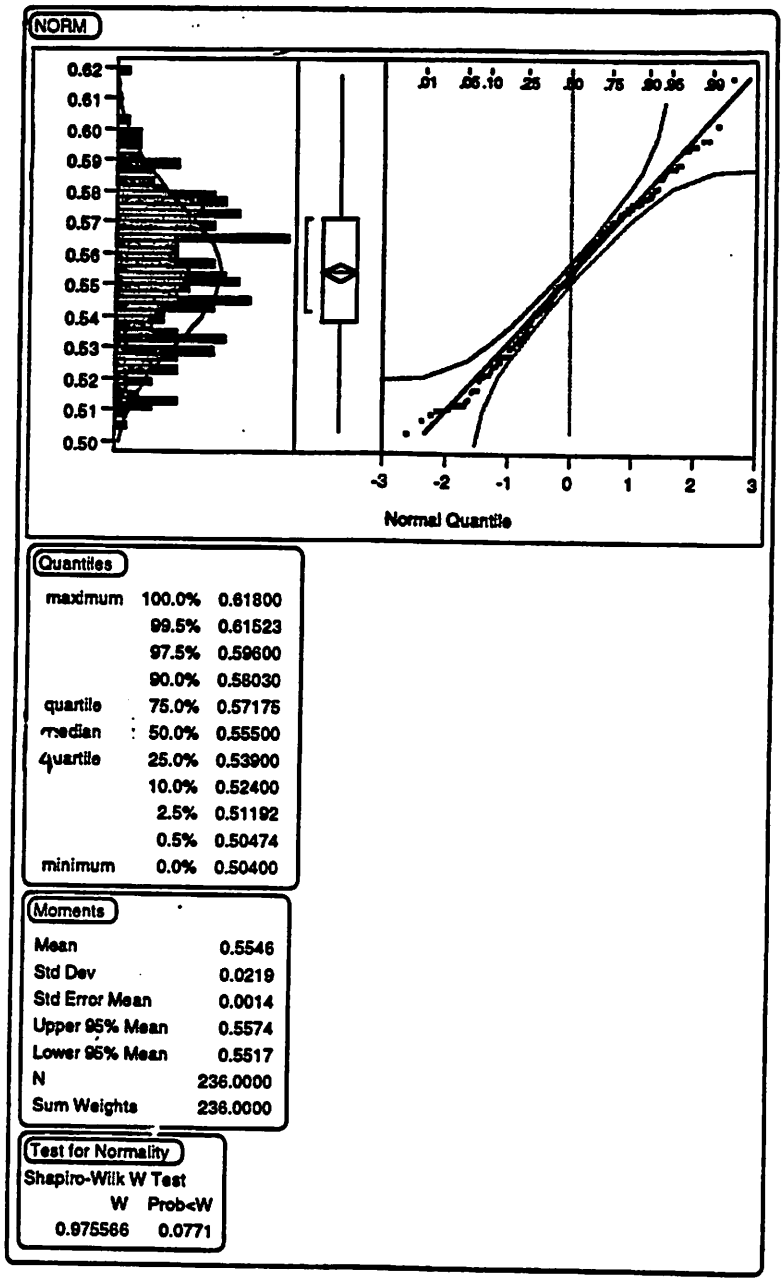

Figure 4.15 Statistical analysis of vibration measurement data for a vibration data that has a 7.7% chance of being normal. The top portion of the figure plots a histogram of the data with a normal distribution plotted by the solid line curve. A normal quantile plot is shown to the right of the histogram which is another visual technique for the evaluation of distribution normality. The individual quantile values are tabulated below the histogram plot. The moments of the distributions and the results of the Shapiro-Wilk test for normality are also tabulated in the figure.

The central section of each figure breaks down the distribution of the measured data into percentiles. The last section of each plot contains the results of the S-W test for normality. From Figure 4.14 the W-value is 0.986530, which tell us that this distribution has a 76.6% chance of being normal, while the W-value from Figure 4.15 is 0.975566 predicting only a 7.71% chance that this distribution is normal.

Table 4.2 offers a comparison of several distributions to determine when it is appropriate to use the 6σ value directly from the distribution, and when it is recommended to use the 99.5%-0.5% values from the quantile reports.

Orientientation / Location	6σ [mV]	99.5%-0.5% [mV]	W#	Prob < W [%]
X-dir. Brite	99.6	90.6	0.979	25.0
X-dir. Edge	120	112	0.987	76.6
Y-dir. Brite	94.8	82.7	0.982	44.7
Y-dir. Brite	131	110	0.976	7.7
Y-dir. Edge	116	107	0.985	66.6

Table 4.2 Normality report for two sets of knife-edge vibration measurement data.

The Shapiro-Wilk function asymptotically approaches a value of 1 so the distributions in table 4.2 with W-values closer to 1, more closely resemble a normal distribution and the 6σ values more closely compare with the 99.5% - 0.5% values from the quantile breakdown. A S-W probability of 7.7% in the above table leads to a 16% error in estimating the width of the distribution while a S-W probability of 76.6% leads to an estimation error of 6.7%.

A misalignment due to a rotational error further distorts the measured aerial image. An error in theta convolves the aerial image with a linear ramp function with a linear ramp width equal to: $400\mu m * \sin(\theta)$ where θ is the angle of misalignment. The 400μm stems

from the fact that the knife-edge used for these measurements is 1mm long on edge that completely contains the 400μm image field as seen in Figure 4.16.

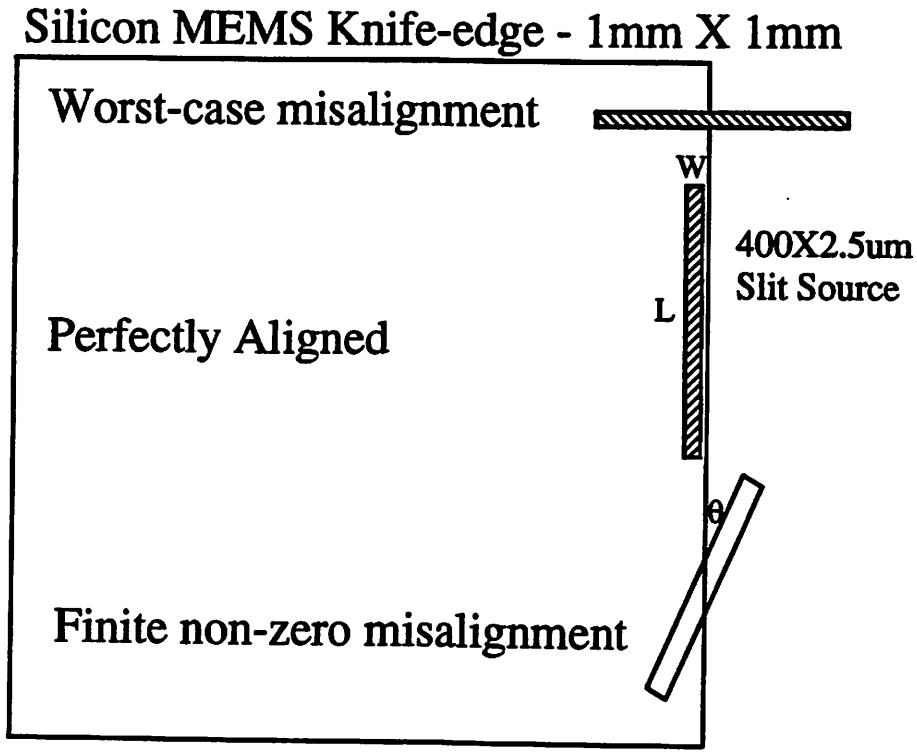

Figure 4.16 Illustration of Silicon knife-edge for three cases of slit-source misalignment

For some lateral translation (x_{vib}), the change in the area of aerial image as seen in Figure 4.16 will no longer be constant (x_{vib}*L), but the apparent length L will vary with the angle of mis-alignment (θ), i.e., L(θ). It can be shown that if the width of the aerial image of the slit is W then L(θ) is define:

$$L(\theta) = W + (L-W)\cdot\cos^2(\theta) \qquad (2)$$

The area change due to the vibration in the cases of no alignment error is $A_1=x_{vib}\cdot L$ and for the case of a rotational error the area becomes $A_2 = x_{vib} \cdot L(\theta)$. The percentage

reduction in the measured vibration signal is calculated as the ratio of the areas (A_2/A_1) which in this case simplifies to only the ratio of the two L's.

$$\frac{A_1}{A_2} = \frac{W + (L - W) \cdot \cos^2(\theta)}{L} \tag{3}$$

The $\cos^2$ term in equation 3 is a slowly varying function around zero degrees of misalignment. A vibration measurement that is misaligned 10 degrees will still capture 97% of the total vibration that is present and could have been measured with perfect alignment. For a theta error of 5 degrees or less, there will be less than a 1% loss of the measured magnitude of the vibration. The camera has 380nm of distortion in the Y-direction, which will manifest itself in these experiments in a similar manner to a theta mismatch.

Many vibration experiments are performed in the course of the aerial imaging experiments. The vibration data in table 4.3 quantifies the magnitude of the system vibration in both directions using the vibration signal slope of the AIM signal from table 4.1 (2.7 nm/mV). Angular alignment (theta in Figure 4.16) is accomplished by maximizing the signal slope of successive scans so the error in theta is determined by the minimum noticeable slope change.

	$6*\sigma_{edge}$ [mV]	$6*\sigma_{brite}$ [mV]	$6*\sigma_{vib}$ [mV]	Vibration [nm]
Y-Dir.	59	85	61	165
X-Dir.	44	40	18.3	49

Table 4.3 Knife-edge vibration details

For the data taken in the Y-direction, there is as much as a 2.0 degree error in theta which from the previous discussion could induce an error of only 0.1%. A major factor in the uncertainty of the correct determination of the 6σ value which for the Y-direction data, there existed a 5% difference in the 6σ values as determined earlier. This puts the value of the vibration in the Y-direction at: 153 ±3.8nm

For the data taken in the X-direction knife-edge vibration measurements, there was at most a 2.5 degree error in theta which would induce an error of only 0.1%. In the correct determination of the 6σ value there existed a 7% difference. Then the result for the vibration in the X-direction is: 46 ± 1.6nm.

These results are unacceptable and limit the accuracy of future AIM experiments as well as significantly affecting the printing of features in PR. Several steps are taken to reduce the magnitude of the stage and/or camera vibrations. The leaf-spring that holds the camera in place is tightened and mounts were designed to spring-load the wafer stage plate to the camera. The idea of spring-loading the stage is the same as when the large mass was put on top of the wafer on the three image plane balls. Adjustment of the leaf spring and spring-loading the stage reduces the range of the image/stage vibration to a level below the resolution of the current knife-edge measurement technique.

4.1.3 Single Slit Vibration Measurements

The vibration measurement technique detailed in the previous section provides a proof-of-principle and a coarse measure of the EUVL system vibration. The measurement accuracy is limited experimentally by the edge roughness and the finite width of the

available slit source mask and also by image field distortion. Higher resolution using this technique is achieved by the use of a more narrow slit source where the measured response asymptotically approaches the apparent line spread function (ALSF) of the camera as the slit source width approaches zero.

A mask hard-edge mask defined in a gold absorber is available for AIM experiments. High resolution measurements are possible by measuring the aerial image of this hard edge with a narrow scanning slit, as described in chapter 2, used as the artifact in the image plane. This technique overcomes the experimental limitations of the slit mask used in the previous technique. The slope of the signal edges provided by these AIs will be between 5-10V/μm. Even when convolved with the response function of the sampling slit, this experiment provides a very sensitive test to quantify vibration. Deconvolution with the response function is not necessary when the width of the transition region is larger than the sum of the width of the slit response function and peak-to-peak vibration.

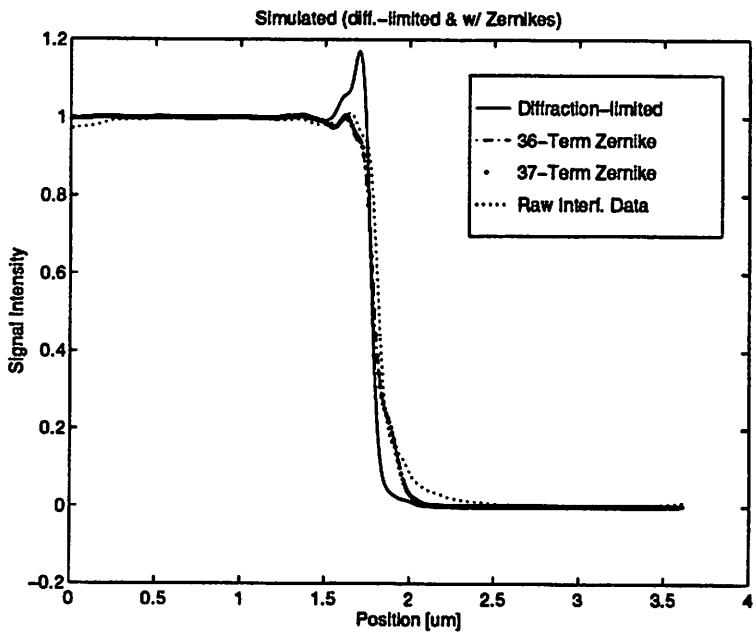

Figure 4.17 Image intensity versus position for step-function aerial images produced from the 10X-I EUVL system, simulated using SPLAT.

Figure 4.17 shows SPLAT aerial image simulations of an edge oriented in the X-direction. Again the results of three simulations are shown in the plot: The ideal diffraction-limited case, using the raw interferometer data, and using the fitted Zernike coefficients. All simulations shown here are for a partial coherence value (σ) of 0.5. Details of the imaging response of the system and its dependence on partial coherence are explored in chapter 5. The slopes of the images in the transition region are listed in table 4 for each of the cases studied. The simulated values are convolved with the slit response function detailed in chapter 2.

Aerial Image	Slope^{-1} [nm/mV]
Diffraction-Limited	0.9
Raw Pupil Map	2.12
Zernike Fit (36 terms)	2.05
Zernike Fit (37 terms)	2.15
AIM Signal	1.95

Table 4. Slope of linear region of hard edge

In estimating the vibration using this method, an error of about 10% is introduced by variations in the optical model. For this reason, the vibration measurements are calculated by comparison to the measured AIM signal. This leaves the correct estimation of σ_{vib} as the major source of error, typically introducing an error of around 5%. The results of two such vibration measurements are listed in table 5. These measurements are taken immediately prior to high resolution edge scans used in the AIM experiments of section 5.4. The theta rotation error in both directions is less than 0.1 degree.

Vibration is reduced by securing the wafer stage plate to the camera. The wafer stage plate is modified to allow for the introduction of spring-loaded mounts that provided

vibration dampening by locking the plate to the camera through a high-K spring. Another vibration suppression method that has a significant impact is tightening the leaf-springs that secure the camera to the wafer vacuum chamber. Vibration is reduced from an initial value $6\sigma_{vib}$ of 375nm to the current value of 17nm. Again a visual plot of the vibration data of these two extremes is very compelling. Figure 4.18 plots the normalized AIM voltage before and after all the implementation of the vibration dampening measures.

	σ_{edge} [mV]	σ_{brite} [mV]	σ_{vib} [mV]	$6*\sigma_{vib}$ [mV]	Vibration [nm]
X-Dir.	21.9	15.8	15.2	91	17.7
Y-Dir.	20.7	18.7	8.8	53	10.3

Table 5. Statistical detail of distribution of vibration data

The Q/I stacks vibrated when they were extended more than 3μm. Noise in the lines to and from the position sensor owing to poor vacuum feedthrough connectors cause the feedback drive control network to "chatter" trying to follow the position sensor noise. This effect is overcome by wrapping the sensor cables around toroids to provide a lossy inductor in the circuit as with the AIM PD pre-amp signal.

The normalization routine developed in chapter 3 also plays a role in the vibration measurements. By normalizing the measured AIM PD signal with the ND signal shot-to-shot variations in the signal are removed. Without the normalization routine, these variations are mistaken for vibration. Figure 4.18 shows a plot of a vibration signal measured on the edge. The solid line is the measured PD voltage and the dashed line is the ND voltage. The middle, dotted line is the normalized AIM signal. In this case, normalization prevents the false misinterpretation of 5nm of vibration in the analysis of the data from this vibration run.

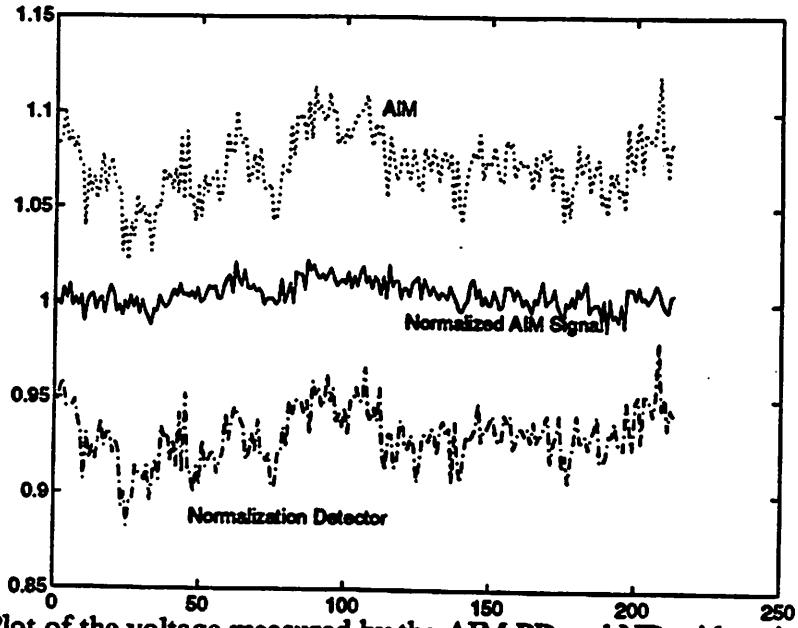

Figure 4.18 Plot of the voltage measured by the AIM PD and ND with a single slit artifact positioned on the edge of a step-function aerial image. The middle line represents the normalized signal voltage. The signal variations seen in both the AIM PD and ND signals owing to variations in the source flux are removed in the normalized curve. Without the normalization procedure (section 3.5), this variation would be mistaken for 5nm of vibration.

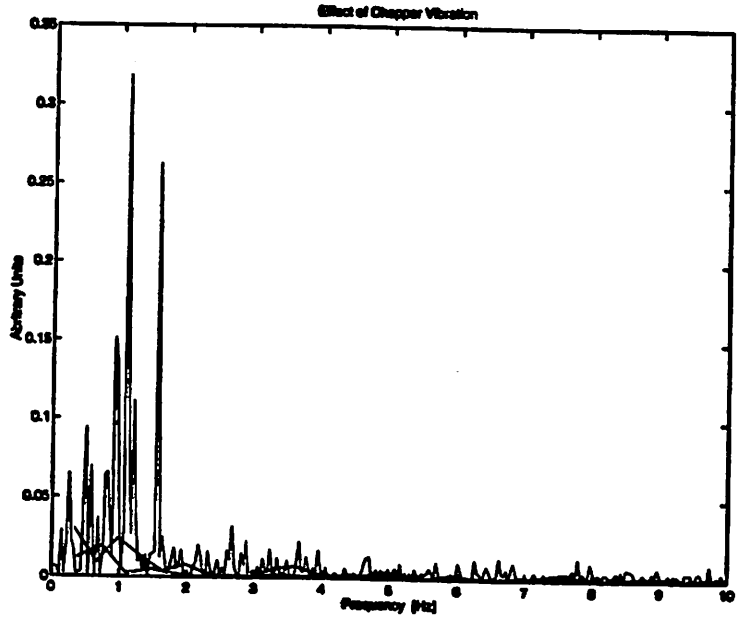

Figure 4.19 Power spectral density of three AIM vibration measurements with a single slit artifact positioned on the edge of a step-function aerial image. The frequency band of the PSD plot is limited by the vibration data sampling frequency (20Hz). Qualitative comparison of the data is possible and points to the chopper as the primary component of the vibration.

Spectral analysis of the vibration data could be compared to the vibration frequency peaks measured in the part 1 of this chapter. However, the vibration data in Figure 4.18 is a measure of the vibration sampled at 20Hz, limited by the operating frequency of the laser. It can be seen from Figures 4.1-4.4 that the majority of the vibration peaks occur at frequencies well above 20Hz. For this reason, any spectral analysis of the data is highly aliased and provides no information regarding the spectral content of the vibration. However, spectral analysis provides a reference for determining the major sources of the remaining vibration, as was done in section 4.1. Several such measurements are taken with the pump and chopper on and off. Figure 4.19 shows the power spectral density (PSD) of these vibration measurements. The solid line represents data taken under normal operating conditions. The dashed curve is the case where the vacuum pump is turned off during the measurements. The dotted line represents data taken with the chopper flywheel stationary. Since no further improvement is noted by turning off the pump, it can be seen from these curves that the chopper is still the major source of vibration for this system.

4.3 Optics Alignment

Alignment of the optical system is accomplished by imaging the plasma onto a scintillator placed at a surrogate pupil plane (letter B in Figure 3.2) with the camera removed from the system. The condenser lens is then adjusted in X and Y such as to center the phosphor image on a cross-hair on the scintillator. The Z position is adjusted by maximizing the brightness of the image on the phosphor. These adjustments are fairly

accurate due to the relatively bright image spot since the entire beam impinged on the phosphor.

Upon completion of this adjustment the turning mirror is installed and another surrogate plane alignment is done. This alignment consists of viewing another phosphor image, this time placed at the entrance pupil of the camera, before the camera is actually installed. The beam has now gone through two more bounces which reduces its magnitude by half (R ~ 0.7 / reflection). This leads to the potential for measurement inaccuracies due to the relatively low levels of the visible light emitting from the phosphor. Once the camera is installed no further adjustment to the condenser was possible for fear of disrupting the alignment since there was no longer any feedback available.

A mount is designed and built which allows the insertion of the EUV sensitive photodiode at the entrance pupil of the camera. A cross-section and top-down illustration of the mount are shown in Figure 4.20. The surrogate phosphor is removed and the EUV diode is installed in its place. The new modification permits the real-time alignment and optimization of the condenser lens where the feedback variable being optimized is the voltage signal monitored on a computerized "strip-chart".

The mount is designed to position the ~1mm^2 diode in the center of the pupil plane. The beam is centered in the pupil by optimizing the strip-chart voltage reading. This alignment technique is more robust and accurate than the previous scintillator alignment scheme and precludes the need for the first phosphor alignment entirely. This new technique is currently in use, not only for AIM experiments, but for all optical alignments done on the 10X-I system.

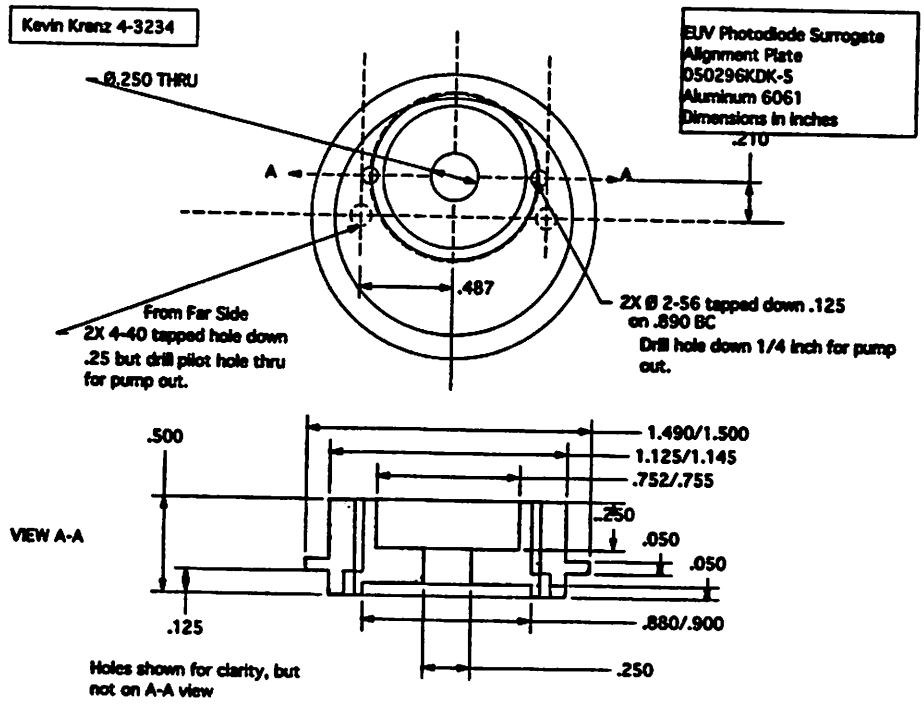

Figure 4.20 Engineering drawing of the EUV photodiode surrogate holder and alignment plate. Cross-section and top-down views of the mount are shown.

4.4 Condenser Lens Evaluation

The development of an *in-situ* detector and collection electronics provides the capability of evaluating the imaging performance of EUVL multi-layer condenser lenses. These lenses are typically evaluated by performing point-by-point reflectivity measurements. While these measurements provide meaningful information they do not measure the efficiency of the lens in collecting and focusing the EUV photons from the broad-band plasma radiation. Spherical aberrations in a condenser can cause the rays through the margin of the condenser to completely miss the pupil of the objective lens [9]. This will reduce the available flux at the image plane and therefore system throughput.

Using the photodiode surrogate plane mount described in section 4.3, a series of condenser lens evaluation experiments is conducted on the 10X-I test-bed that measure the EUV flux at the entrance pupil of the camera with a clear field mask placed at the object plane. The condenser lens is installed in the test-bed and the flux is measured at the pupil plane. The measurement consists of maximizing the photodiode signal through adjustments of the X, Y, and Z position of the condenser lens. As mentioned previously, adjustment of the Z position changes the focus of the condenser lens.

This technique allowed the characterization of five condenser mirrors from two vendors in a single day. The five multi-layer mirrors demonstrated a 4X difference in total EUV flux delivered to the objective lens entrance pupil.

4.5 Conclusion

A novel technique was developed for the fabrication of an optically sharp knife-edge using standard silicon MEMS process technology. This knife-edge was used to measure 10X-I system vibration. Initial measurements showed several hundred nanometers of vibration. These measurements were successful in identifying major sources of vibration, which were then reduced. Subsequent knife-edge measurements pointed to around 150nm of peak-peak vibration.

The final vibration experiments consisted of scanning a single narrow slit across an aerial image step-function. The peak-to-peak amplitude of the vibration was between 10 and 20nm depending upon orientation.

The *in-situ* detector system developed here has two other utilities pertaining to EUV system operation: *In-situ* optical alignment and condenser lens evaluation.

References

[1] D.A. Tichenor, A.K. Ray-Chaudhuri, G. D. Kubiak, S. J. Haney, K. W. Berger, R.P. Nissen, G.A Wilkerson, R.H. Stulen, P.H. Paul, R.W. Arling, T.E. Jewell, Edita Tejnil, et. al., "10X reduction imaging at 13.4nm," OSA Optical Society of America Conference Proceedings on Extreme Ultraviolet Lithography, Vol. 35, pp. 89-97, Monterey, CA, 1994.

[2] O.R. Wood, II, J.E. Bjorkholm, K.F. Dreyer, L. Fetter, M.D. Himel, R.R. Freeman, D.M. Tennant, J.E. Griffith, G.N. Taylor, W. K. Waskiewicz, D.L. White, D.L. Windt, A. A. MacDowell, B. La Fontaine, B.M. Lum, A.R. Neureuther, J.B. Kortright, E.M. Gullikson, and K.D. Nguyen, "Experiments and simulation of EUV lithographic resist patterning at wavelengths from 7 to 40nm," OSA Optical Society of America Conference Proceedings on Extreme Ultraviolet Lithography, Vol. 35, pp. 110-5, Monterey, CA, 1994.

[3] D.A. Tichenor, G. D. Kubiak, M.E. Malinowski, S. J. Haney, K. W. Berger, R.H. Stulen, L.A. Brown, O.R. Wood, II, J.E. Bjorkholm, D.M. Tennant, R.R. Freeman, T.E. Jewell, W. K. Waskiewicz, D.L. White, and D.L. Windt, "Soft X-ray projection imaging using a laser plasma source," OSA Optical Society of America Conference Proceedings on Soft X-Ray Projection Lithography, Vol. 12, pp.54-57, 1991.

[4] J.E. Bjorkholm, D. Tennant, D. Taylor, M. Himel, R.R. Freeman, W.K. Waskiewics, D.L. Windt, S Spector, A.K. Ray-Chaudhuri, R.H. Stulen, W. Ng, and F. Cerina, "At-Wavelength metrology of 13nm lithography imaging optics", Rev. Sci. Instrum., Vol. 66, No. 2, pp. 2241-3, Feb., 1995.

[5] M.N. Wernick and G.M. Morris, "Effect of spatial coherence on knife-edge measurements of detector modulation transfer function", Opplied Optics, Vol. 33, No. 25, pp. 5906-5913, 1 Sept., 1994.

[6] R. Mercier, F. Polack, P. Fournet, G. Tissot, and J.P. Marioge, "Control at 11.4nm of an XUV Schwarzschild objective", Rev. Sci. Instrum., Vol. 66, No. 2, pp. 2184-2186, Feb., 1995.

[7] A.P. Tzannes, J.M. Moones, "Measurement of the modulation trasfer function of infrared cameras", Optical Engineering, Vol. 34, No. 3, pp. 1808-17, June, 1995.

[8] D.E. Vandenberg, W.D. Humbel, A Wertheimer, "Quantitative evaluation of optical surfaces by means of an improved Foucault test approach", Optical Engineering, Vol. 32, No. 8, pp. 1951-3, Aug., 1993.

[9] W.J. Smith, **Modern Optical Engineering**, R.E. Fischer and W.J. Smith, Series Editors, McGraw-Hill Publish, 1990.

[10] Hisataka Takenaka, Tomoaki Kawamura, Yoshikazu Ishii, Tsuneyuki Haga, and Hiroo Kinoshita, "Evaluation of Mo-Based Multilayer EUV Mirrors," OSA Optical Society of America Conference Proceedings on Extreme Ultraviolet Lithography, Vol. 35, pp. 26-32 , Monterey, CA, 1994.

[11] D.P. Gaines, S.P. Vernon, G.E. sommargren, and D.R. Kania, "Coating Strategy for Enhancing Illumination Uniformity in a Lithographic Condenser," D.P. Gaines, S.P. Vernon, G.E. sommargren, and D.R. Kania, OSA Optical Society of America Conference Proceedings on Extreme Ultraviolet Lithography, Vol. 35, pp. 41-46, Monterey, CA, 1994.

[12] S.P. Vernon, M.J. Carey, D.P. Gaines, and F.J. Weber,"Multilayer Coating for the EUV Lithography Front-End Test Bed," OSA Optical Society of America Conference Proceedings on Extreme Ultraviolet Lithography, Vol. 35, pp. 33-40, Monterey, CA, 1994.

[13] T.D. Ngyuen, C. Kan-Malek, and J.H. Underwood, "Achievement of Low Stress in Mo/Si Multilayer Mirrors," OSA Optical Society of America Conference Proceedings on Extreme Ultraviolet Lithography, Vol. 35, pp. 56-60 , Monterey, CA, 1994.

[14] J.H. Underwood, E.M. Gullikson, W. Ng, A. Ray-Chaudhuri, and F. Cerrina, "Effect of contamination and Oxide Layers on Scattering and Reflectivity of Multilayer Mirrors," OSA Optical Society of America Conference Proceedings on Extreme Ultraviolet Lithography, Vol. 35, pp. 61-67, Monterey, CA, 1994.

[15] E.L. Church and P.Z. Takacs, "Specifying the Surface Finish of X-Ray Mirrors," OSA Optical Society of America Conference Proceedings on Soft X-Ray Projection Lithography, Vol. 18, pp. 105-107 1993.

[16] Z. Djuric, J. Piotrowski, "Infrared photodetector with electromagnetic carrier depletion, Optical Engineering (ISSN 0091-3286), Vol.31, pp.1955-60, September 1992.

[17] Y. Wang, N. Mansour, S. Nabil, "Theoretical study of a potential low-noise semimetal-based avalanche photodetector", IEEE Journal of Quantum Electronics (ISSN 0018-9197), Vol.28, pp.507-13, February, 1992.

[18] M. Vidal, B. Puig, J.M. Buxo, "A bipolar photodetector compatible with standard CMOS technology", Solid-State Electronics (ISSN 0038-1101), Vol.34, pp.809-14, August, 1991.

[19] J.P. Garcia, E.L. Dereniak, "Extrinsic silicon photodetector characterization", Applied Optics (ISSN 0003-6935), Vol.29, pp.559-69, 1 February, 1990.

[20] P. Blixt, A. Krotkus, M. Kull, "A differential photodetector employing photoconductivity, for subnanosecond laser beam position measurements", Journal of Physics. E, Scientific Instruments, (ISSN 0022-3735), Vol.21, pp.971-3, October, 1988.

[21] J.A. Modolo, G.W. Anderson, F.J. Kub, "Wafer level high-frequency measurements of photodetector characteristics", Applied Optics (ISSN 0003-6935), Vol.27, pp.3059-61, 1 August, 1988.

[22] T.H. Chyba, L. Mandel, "Angular sensitivity of a vacuum photodiode, or does a photodetector always count absorbed photons?", Journal of the Optical Society of America B, Optical Physics (ISSN 0740-3224), Vol.5, pp.1305-11, June, 1988.

[23] A. VanderLugt, "Use of decimated photodetector arrays in spectrum analysis", Applied Optics (ISSN 0003-6935), Vol.27, pp.2061-70, 15 May, 1988.

[24] A. Kostenbauder, S.J.B. Yoo, A.E. Siegman, "A fast diffusion-driven photodetector: theory and experiment", IEEE Journal of Quantum Electronics (ISSN 0018-9197), Vol.24, pp.240-4, February, 1988.

[25] V.A. Chumak, M. Bertolotti, A. Ferrari, "Position-sensitive photodetector based on hydrogenated amorphous silicon p-i-n junctions", Review of Scientific Instruments (ISSN 0034-6748), Vol.58, pp.202-6, February, 1987.

[26] A. Longoni, G. Ripamonti, A. Grassi, "Photodetector array performances improved by low-cost microprocessor-based measurement techniques", Journal of Physics. E, Scientific Instruments, (ISSN 0022-3735), Vol.17, pp.282-6, April, 1984.

[27] S.G. Chamberlain, P.Y. Lee, "A novel wide dynamic range silicon photodetector and linear imaging array", IEEE Journal of Solid-State Circuits (ISSN 0018-9200), Vol.19 pp.41-8, February, 1984.

[28] Valiev, **The Physics of Submicron Lithography**, Submicron Press, 1992.

Chapter 5

Mid-Spatial Frequency Scatter

5.1 Introduction

This chapter explores the use of AIM to characterize the impact of mid-spatial frequency scatter on the imaging performance of the 10X-I EUV projection lithography test bed. Scattered light, flare, is present in the images formed by all photolithography lenses, and results in a reduction of the lithographic process tolerances. It comes from diverse causes ranging from dust to high order aberrations and changes as materials degrade and contaminates accumulate. The magnitude of the flare also varies from lens to lens and with time. The impact of scattered light is typically evaluated by observation of images of opaque objects formed in positive photoresist [1]. Several studies have developed novel test structures and techniques to obtain more quantitative data from measurements of photoresist profiles [2-3].

Scatter is measured in positive photoresist by observing the image of an opaque object as the surrounding dose is increased and quantified by measuring the background dose required to cause complete loss of the image or the location of the receding edge with increasing dose. For the former case, if the dose in open surround is 20 times the dose to clear when the image of the opaque object clears, then the scattered light is equal to 1/20 = 5%. This method is prone to inaccuracies due to lateral development of images of opaque objects smaller than the PR thickness, which leads to an over estimation of the scatter.

5.1.1 Scatter in EUVL Systems

Scatter in EUVL systems presents several issues that are specific to EUV optics and differ from those of lithography carried out at traditional "optical" wavelengths (i.e. visible or excimer laser sources). EUVL scatter arises due to imperfections in the multi-layer coating [4-6], roughness of the substrates due to polishing, and contamination of the optics. Not only must the optical elements be fabricated with an unprecedentedly high figure accuracy, but they must also be coated with multi-layer mirrors which match accurately in wavelength and bandpass, do not distort the optical figure, and yet remain stable with unimpaired reflectivity in a production environment.

The wavelength dependence of scatter is well documented [1, 13]. For a point object, the total power P_S scattered out of the image point and into a circle of radius r is given by:

$$P_S = 16\pi^2 R_0 P_0 \frac{\sigma^2_{eff}}{\lambda^2} \qquad (1)$$

Where P_0 is the power incident on the lens from the source, R_0 is the reflectivity of an ideally smooth lens, and λ is the wavelength of the radiation. The radial term r is contained in the term σ_{eff} which is the effective root-mean-squared variation of the surface roughness defined by equation 2 where $f_2 = r/R\lambda$ and R represents the distance from the lens to the image. The scaling law for this equation ($P_s \sim \sigma^2_{eff}/\lambda^2$) suggests that nonspecular scattering will become a significant problem at shorter wavelengths. For the same σ_{eff}, scatter at 13.4nm will be 342 times that at the DUV wavelength of 248nm.

$$\sigma^2_{eff} = 2\pi \int_{f_1}^{f_2} f \cdot PSD(f)df \qquad (2)$$

Where PSD(f) is the power spectral density of the surface roughness. Since the nonspecular scattering is directly related to the PSD of the reflecting surface, the latter is the natural quantity to characterize the surface roughness of the EUVL optics. Figure 5.1 shows a schematic PSD plot where the spatial frequency variations are broken down into three distinct regimes.

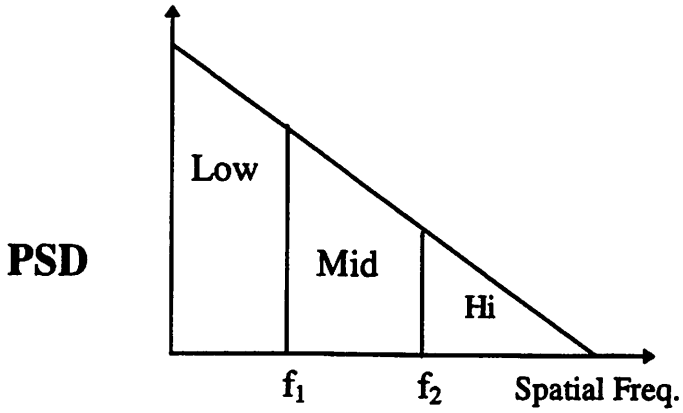

Figure 1. Example PSD of EUVL Optic illustrating the three region of spatial frequencies. Spatial frequencies above f_2, due to micro-roughness of the optic, scatter light out of the pupil and result in decreased throughput. Spatial frequencies below f_1 are the usual optical figure error. The mid-spatial frequency roughness between f_1 and f_2 scatters light into the image plane and reduces process latitude.

High spatial frequency variations are the result of micro-roughness due to substrate polishing. These spatial frequencies scatter the incident radiation into large angles such that most rays miss the exit pupil of the camera. The light scatter at these frequencies does not degrade the overall imaging performance of the system, but is seen as a loss of flux at the image plane which reduces the throughput of the system.

The low spatial frequencies are due to long-range variations in the optic, referred to as figure error, and scatter light into the imaging pupil which does affect the imaging performance of the system. These variations produce the standard aberrations such as the Seidel aberrations (Coma, Astigmatism, etc...), which are characterized by polynomial expansions including the classical Zernike polynomials.

The region between f_1 and f_2 of Figure 5.1 constitute the mid-spatial-frequency region. The spatial frequencies of interest here are between $1mm^{-1}$ and $1\mu m^{-1}$, which scatter light into the imaging plane and are not well characterized by the typical 36-term polynomial representation.

5.1.2 Effect of Partial Coherence

The effect of mirror aberrations and phase errors are contained in the point spread function (PSF) of the optic. Following the convention in Goodman [7] the PSF is defined as the Fraunhofer diffraction pattern of the exit pupil, given by:

$$h(u,v) = \frac{A}{\lambda \cdot z_i} \iint P(x,y) \exp[-j\frac{2\pi}{\lambda \cdot z_i}(ux+vy)]dxdy \qquad (3)$$

Where P(x,y) is amplitude transmittance function of the optic. Then from Eq. 3, it can be said that the PSF is the scaled Fourier transform of the amplitude transmittance function which is the pupil function of the camera.

Other techniques to characterize EUV wavefront errors utilize a synchrotron which provides a high degree of coherence from a very narrow bandwidth source [4, 8, 21]. For the purely coherent case, the image field amplitude is given by:

$$U_i(u,v) = \iint h(u-\xi, v-\eta) U_g(\xi,\eta) d\xi d\eta \tag{4}$$

For the general case, it can be said that for a diffraction-limited system, the image can be calculated as the convolution of the image predicted by geometrical optics $U_g(\xi,\eta)$ with the impulse response of the system $h(\xi,\eta)$ which is the Fraunhofer diffraction pattern of the exit pupil.

When the coherence area of the object is small compared with the resolution cell size, the illumination is said to be incoherent. Phrased another way; if θ_s is the angle subtended by the condenser lens and θ_p is the angle subtended by the entrance pupil of the imaging system, both as seen from the object, then an incoherent system is provided for $\theta_s >> \theta_p$ and conversely, coherent imaging is obtain for the case of $\theta_p >> \theta_s$. For the case of incoherent illumination, the image intensity is given by:

$$I_i(u,v) = \kappa \iint |h(u-\xi, v-\eta)|^2 I_g(\xi,\eta) d\xi d\eta \tag{5}$$

Then it can be said that for the case of completely incoherent illumination, the image intensity is equal to the convolution of the geometrical optics intensity I_g with the intensity impulse response which is the square modulus of the amplitude impulse response. Then for the coherent case we may say that the intensity is linear with the field magnitude while the incoherent case can be said to be linear in intensity.

Several theoretical methods have been applied to solve the problem of partial coherence in image analysis [9-11]. Special treatment is required for the case of scatter when imaging with partially coherent EUV illumination. The method detailed by Stearns [12] begins the calculation of scatter in real EUVL systems with the mutual intensity

following the nomenclature from Born and Wolf [13] where the mutual intensity functions at the object and image planes are $J_0(s_0,s_0')$ and $J_1(s_1,s_1')$ respectively. Assuming that the object is illuminated by quasi-monochromatic radiation of wavelength λ, and that R is the distance from the exit pupil to the image plane, then the Fourier transforms of the mutual intensity functions are related by:

$$J_1(s,s') = G(\lambda Rs)\cdot G^*(\lambda Rs')\cdot J_0(s,s') \tag{6}$$

Where G(s) is defined as the generalized pupil function containing both real and imaginary components defined by the equation:

$$G(s) = G_0(s)\cdot \exp[i\cdot\Phi(s)] \tag{7}$$

The imaginary term represents a pure phase shift which deforms the wavefront leaving the exit pupil, that is directly related to the structure of the rough mirror surfaces. For reference, Goodman [7] uses the nomenclature W(x,y) for this wavefront error term. Then by substituting (7) into (6) we obtain:

$$\langle J_1(s,s')\rangle = G_0(\lambda Rs)\cdot G_0^*(\lambda Rs')\cdot\langle \exp[i\cdot(\Phi(\lambda Rs)-\Phi^*(-\lambda Rs'))]\rangle\cdot J_0(s,s') \tag{8}$$

Stearns estimates the phase variations induced by roughness in the multilayer mirror at each interface. Details of the analysis of the multilayers are found in reference [12]. The intensity distribution is obtained by setting $s_1=s_1'$ in this equation 8 yielding:

$$\left\langle I_1(s_1)\right\rangle = I_1^{\,0}(s_1)\cdot\exp[-4k^2\sigma^2_{eff}] + I_1^{\,0}(s_1)\cdot\exp[-4k^2\sigma^2_{eff}]\cdot\frac{4\cdot k^2}{(\lambda\cdot R)^2}\,Peff\left(\frac{s_1}{\lambda\cdot R}\right) \tag{9}$$

Where the effective surface roughness variance and PSDs are defined as:

$$\sigma^2_{eff} \equiv \sum n^2_{zm}\cdot\sigma^2_m \tag{10}$$

$$P_{eff}\left(\frac{s_1}{\lambda \cdot R}\right) \equiv \sum_m \frac{n^2 z_M}{\alpha^2_m} \cdot P_m\left(\frac{s_1}{\alpha_m \cdot \lambda \cdot R}\right) \tag{11}$$

The term $I_1(s_1)$ represents the image intensity and $I_1^0(s_1)$ represents the image intensity that would exist without roughness. The term α represents the mapping of the spatial coordinates at the m_{th} surface to the exit pupil ($\alpha = s_m/s$).

Several assumptions are made by Stearns to this point. They are: (i) the traditional "small angle approximation" which says that the angle between the principal ray and any other ray that propagates through the system is small; $\sin^2\theta << 1$, (ii) for a point object, the pupil function is independent of the location of the point in the object field, the imaging system is "isoplanatic", (iii) the scattering is weak so that multiple scattering and shadowing effects can be neglected; the "Born approximation", (iv) the curvature and slope of the surface roughness are small, (v) the interfaces in the multi-layer coating are completely conformal, (vi) the "small roughness approximation", and (vii) the surface roughness distribution is Gaussian, stationary, and ergodic (the ensemble average can be replace by an average over the entire surface area).

If we assume a point object, then equation 9 can be expressed as the convolution of the PSF of the objective lens in the absence of scatter (PSF^0) with the PSF taking scatter into account (PSF^{SC}). All of the information about the imaging response of the objective is contained in the PSF^0 term including the effects of partial coherence, leaving the term PSF^{SC} independent of coherence. Assuming a point object, equation 9 becomes:

$$\langle I_1(s_1)\rangle = \delta(s_1) \otimes PSF^0(s_1) \otimes PSF^{sc}(s_1) \tag{12}$$

Where $\otimes$ denotes convolution.

Assumption number (vii) listed above leads to the simplification of collapsing all the coherence information into a single PSF^0 leaving the PSF^{SC} term independent of coherence effects. By taking an ensemble average, it is no longer possible to evaluate the coherent interaction of light from two points of known height on the optic. The effective surface roughness leads to a scatter model that is independent of axial orientation and location. That is to say that the scatter should be the same magnitude in both axes and independent of illumination coherence.

Taking the Fourier transform of equation 12, yields:

$$MTF(s) = MTF^0(s) * MTF^{sc}(s) \tag{13}$$

Then the term MTF^{SC} provides a quantitative measure of the effect of multi-layer optical scatter. The term MTF^0 is the nominal transfer function of the optical system without roughness using conventional ray tracing code and includes information concerning the figure of the optical surfaces. Stearns goes on to express equation 13 in terms of the variance of the roughness of the EUVL system as:

$$\sigma^2{}_m \leq \min\{\frac{1}{4k^2 M n^2{}_{zm}} \ln[\frac{MTF_0(s)}{MTF(s)}]\} \tag{14}$$

Where M is the number of reflections in the objective lens, and n_{zm} is the normal component of the incident field, which is equal to the sin of the angle of incidence on the m_{th} optic. For the 10X-I Schwarzschild objective, M=2 and assuming ~normal incidence for each of the two bounces, equation 14 is rewritten as:

$$\sigma^2{}_m = \min\{\frac{1}{4\left(\frac{2\cdot\pi}{13.4nm}\right)^2\cdot 2\cdot 1^2}\ln[\frac{MTF^\circ(s)}{MTF(s)}]\} = 0.5685\cdot\min\{\ln[\frac{MTF^\circ(s)}{MTF(s)}]\} \quad (15)$$

Equation 15 provides a very powerful and simple method of both specifying the requirements to optics manufacturers and estimating the surface roughness variance from measurement of the system MTF. By careful measurement of the MTF and comparison to the simulated MTF for the diffraction-limited case, taking figure into account, an estimate may be made of the surface roughness through direct measurement of the aerial image. These measurements will be compared to theory and to visible-light interferometry measurements of sample EUVL test optics.

5.2 Measurement Accuracy Issues

There are several factors which will act to reduce the fidelity of the measurements of the projected aerial image intensity. One major factor, the sampling aperture, has been addressed in previous sections. The physical profile of the sampling aperture is well known and its response simulated. Other issues such as vibration and angular misalignment also distort the measured signal. In the incoherent limit, the measured signal is the convolution of the actual aerial image convolved individually with each of these functions. Accurate representation of the illumination coherence is critical to the accurate prediction of the image intensity to be measured.

5.2.1 Vibration

The effect of vibration is estimated by the convolution of the aerial image with the positional distribution from vibration measurements. It is possible to use the actual measured distributions to represent the vibration function. To speed the calculations, it is desirable to fit an even-valued function to the sample distributions. Vibration tests in Chapter four reveal that the distribution of the vibration is nearly normal so the distribution is estimated to be Gaussian with $6\cdot\sigma$ value of 17nm.

In the absence of other confounding effects, the measured AIM signal will be the convolution of the vibration distribution with the true aerial image, in the coherent limit, given by:

$$V_{AIM} = AI \otimes VIB(x) \tag{16}$$

Where V_{AIM} is the measured PD voltage, VIB(x) is a Gaussian random variable that is stationary with time, and AI is the projected AI in the coherent limit.

5.2.2 Theta alignment

An error in theta (shown in figure 4.15) causes degradation of the AIM aperture response function. The misalignment has the effect of convolving the projected aerial image with a ramp function that has a minimum value of zero, a maximum value of 1, and slope of $1/\sin(\theta)$ where θ is the angle of the misalignment. The measurement accuracy of the angular alignment for these experiments is ± 0.091 degrees (3σ=0.018 degrees) for the 100μm long single slit experiments. Fine alignment is accomplished by measurement of

the slope of successive scans. For the knife-edge artifact which covers the entire image field, this accuracy equates to a 640nm ramp width.

The width of the ramp function for convolution is 160nm for the case of the 100μm long single slit artifact. This width is greater than the FWHM of the aperture response function calculated in chapter 2. The effect of theta misalignment is nearly an order of magnitude (160nm:17nm) larger than the width of the vibration distribution discussed above (5.2.1).

5.2.3 Aerial Image Sampling

The minimum demonstrably controllable step size of the Q/I stack is 3nm. To step across the entire throw of the stack would require 5000 steps. If 20 averages are taken at each measurement point, the scan will require 83.3 minutes = 1.39 hours to complete. Taking only 10 averages will reduce this time nearly in half, which is still too long. Experimental AIM SNR values depend on the number of sample averages where diminishing returns occur for more than 10 samples. There is between 10 and 20nm of vibration during the experiments which confirms the inefficiency of 3nm sampling steps illustrating the trade-off between information density and efficiency.

Fellgett and Linfoot [14-15] first applied Shannon's [16] theory of information sampling to the assessment of image quality. Huck and Park [17-18] extended the formulations to include performance characteristics of line-scan imaging systems by accounting for degradation caused by sampling and quantization.

Huck concluded that for optimum efficiency samples should be taken at intervals about 0.5 to 0.7 times the equivalent diameter of the PSF [18]. Narrower sampling

intervals improves information density if the radiance field consists mostly of spatial detail equal to or smaller than the PSF, while broader sampling intervals would generally reduce both information density and efficiency.

We are interested in interrogating aerial image intensity deviations with spatial frequencies on the order of $10\mu m^{-1}$ which corresponds to a 100nm step size. To assure accurate measurements and avoid aliasing, the maximum step size possible is 50nm. Taking this as an upper limit and 20nm as a lower limit imposed by vibration, a step size of 25nm is chosen for the edge-scans.

When a continuously variable function is represented by discrete steps there is always a quantization error. For realistic assumptions quantization noise variance σ_Δ^2 is given by [15-18]:

$$\sigma_\Delta^2 = \frac{\Delta^2}{12} \tag{20}$$

where Δ is the signal difference associated with the least significant bit of the ADC. These experiments used a Labview 2400-T ADC board and software for the conversion with a LSB of 1mV. The magnitude of the input to the ADC board is controlled by the gain setting of the S/H stage which provide inputs around $1V_{peak}$. Therefore, ADC quantization noise is not a concern for these experiments.

5.2.4 Illumination Coherence of 10X-I EUVL System

The degree of the coherence of the illumination on the 10X-I imaging system must be known to accurately interpret the results of the AIM measurements. Both

measurement and simulation play a role in estimating the coherence of the system. Simulation provides the dependence of imaging performance on the coherence and is carried out separately for each individual mask geometry. Measurement of the pupil fill provides a rough estimate of the degree of coherence.

There exists an entrance pupil stop which can be inserted to provide an objective with a fixed NA (selectable from 0.06, 0.07, & 0.08), and therefore fixed partial coherence σ. To maximize the image plane flux, this pupil stop is not in place during these experiments resulting in $\sigma \sim 0.55$.

To obtain a more accurate measure of the fill factor, far-field images of the pupil are taken with a CCD camera. A clear field mask was used at the object plane and the image field intensity is measured ~17cm behind the image plane with a EUV-sensitive CCD camera. Figure 5.2 shows an intensity plot of the EUV image. The pupil is assumed to be a circle with a diameter equal to the width of the camera entrance pupil (100pixels in figure 2). Figure 5.3 shows a line-out of the intensity data in figure 2 for row 50. The FWHM value of the plot is 48 pixels. This gives a $\sigma = 0.48$. If the e^{-1} value is used, the resulting $\sigma = 0.62$. For the case of e^{-2}, we have $\sigma = 0.87$. The fill function is not a simple geometrical transmittance function with only values of 1 and 0. Figure 5.4 is an mesh plot of the intensity data from figure 2.

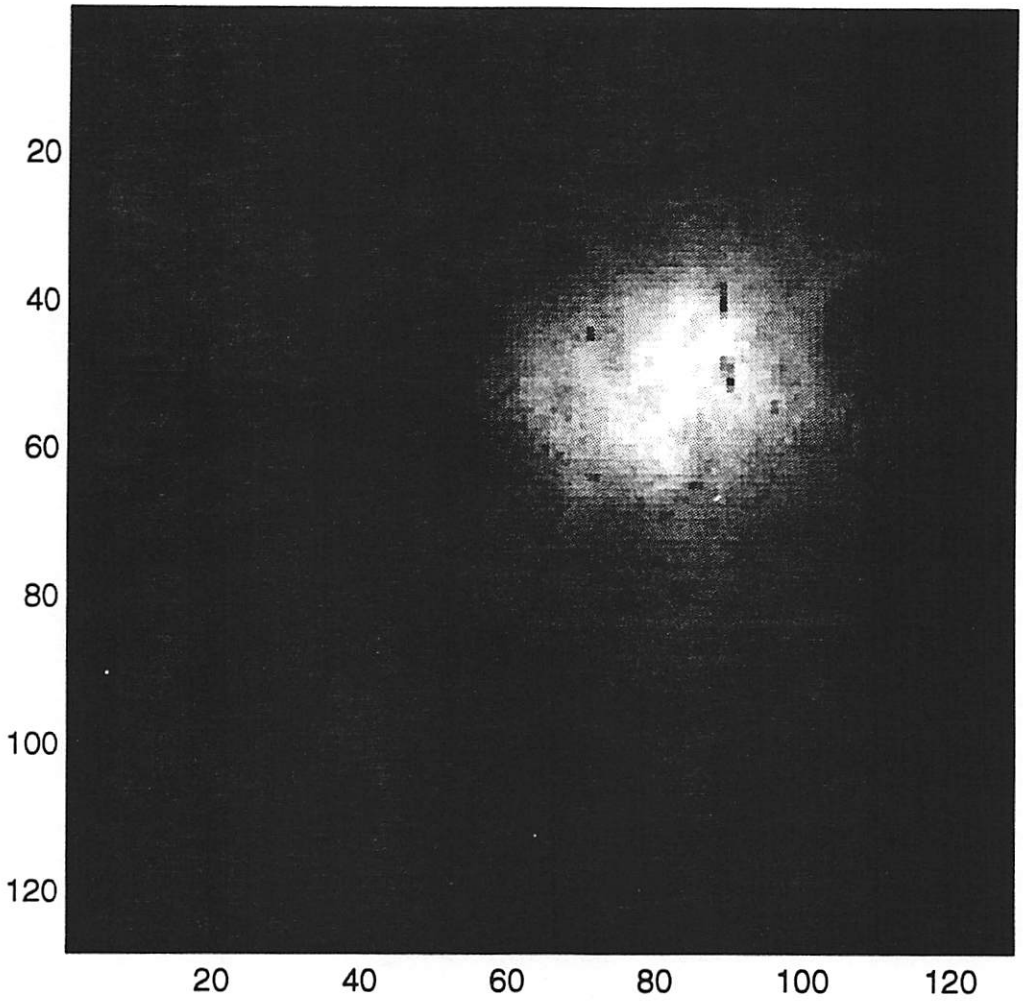

Figure 5.2 Intensity plot of the far-field intensity of the 10X-I pupil image measured with a CCD camera. A clear-field mask is placed at the object and the image is observed in the far field (~15cm behind the image plane). The subaperture width is 100 pixels in this plot.

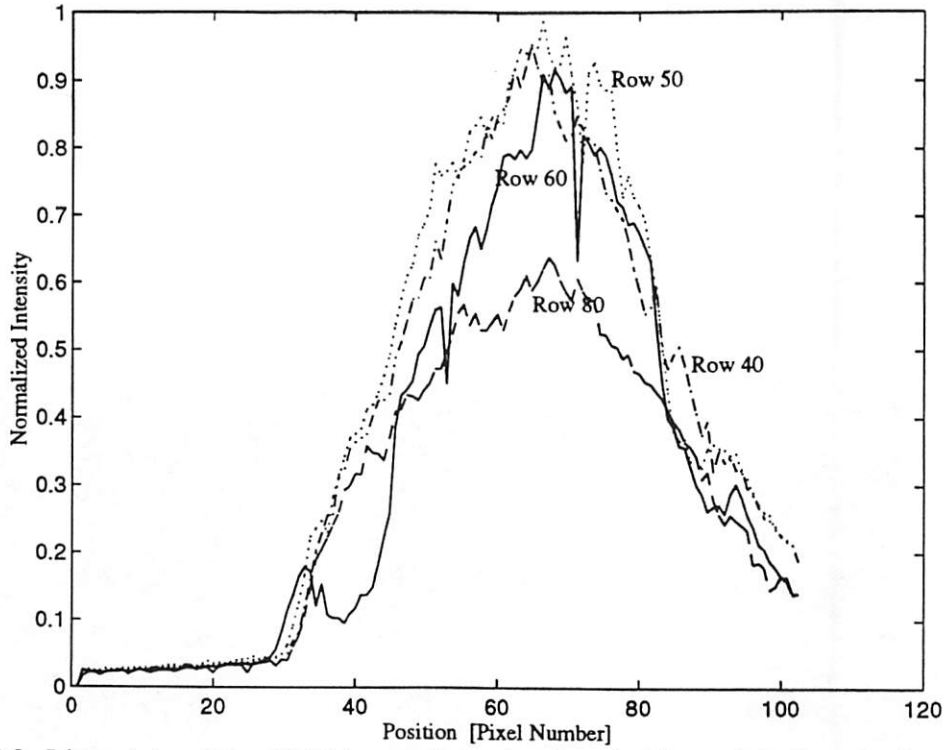

Figure 5.3 Line plots of the CCD image intensity data in Figure 5.2 for a horizontal line-out of rows 45, 50, 60, and 80. The FWHM of row 50 is 48 pixels which equates to a pupil-filling factor of 0.48.

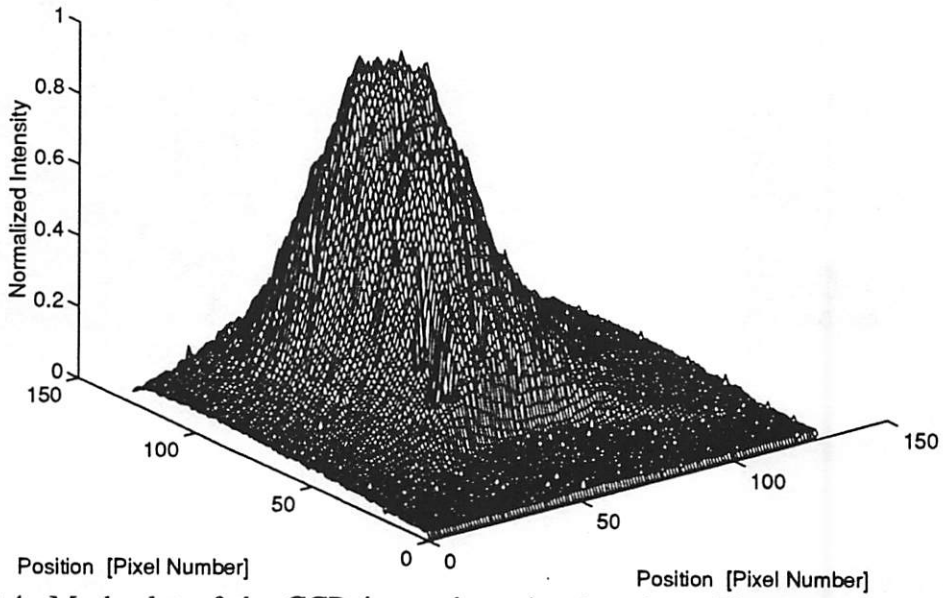

Figure 5.4 Mesh plot of the CCD image intensity data from Figure 5.2 illustrating the unique pupil function of the 10X-I camera.

Table 5.1 lists the partial coherence value s for the X and Y directions. The table lists line numbers which correspond to line-outs taken in that direction. The method used to calculate σ was to divide the pixel width of the intensity plot by the width of the pupil (100pixels). To give a feeling of the profile of the intensity distribution, three methods were used to determine the cutoff intensity for the calculation of the intensity width: (i) the FWHM value (50%) (ii) the e^{-1} value (iii) the e^{-2} value.

X-Direction		σ	
Line #	FWHM	e^{-1}	e^{-2}
30	0.03	0.20	0.77
40	0.41	0.50	0.83
50	0.48	0.50	0.88
60	0.48	0.62	0.87
70	0.30	0.52	0.87
80	0	0.11	0.82
Y-Direction			
Line #			
50	0	0.08	0.66
60	0.21	0.4	0.76
70	0.37	0.47	0.82
80	0.43	0.55	0.84
90	0.44	0.53	0.87
100	0.37	0.49	0.83
110	0	0.17	0.75

Table 5.1 Partial coherence values from far-field CCD intensity measurement of the 10X-I EUVL system. The table compares the measured coherence values using three cut-off intensity definitions.

The shaded values in the table indicate the line numbers with the two highest values of σ in that direction. The table indicates that the value of σ varies in the X-direction from 0.48 to 0.88 and in the Y-direction from 0.44 to 0.87 depending upon how the cutoff intensity value is defined. One method to quantify the effect of partial

coherence is to perform the plane wave decomposition method discussed in chapter 2 and then use the intensity profile to weight each of the separate planes. Rather than perform exhaustive simulation experiments, an estimation of σ is made from the data in table 5.1 ($\sigma_X = 0.6$ for the X-direction and $\sigma_Y = 0.55$ for the Y-direction).

5.3 Knife-edge Measurements of 2.5μm Slit Source

The imaging performance of the system is characterized by its modulation transfer function. Figure 5.5 shows a sample MTF for three cases of illumination coherence. The MTF is defined as the modulus of the optical transfer function (OTF) given in equation 21 which is the ratio of the frequency content of the image spectrum to the frequency spectrum of the object. The MTF plots the measured image intensity contrast produced from a sinusoidal grating object as a function of the spatial frequency of the grating. The measured image contrast is defined by equation 22, where I_{max} and I_{min} denote the maximum and minimum intensities, respectively, of the measured image. The MTF has value unity at DC and zero at the cutoff frequency of the coherent system (ρ_0) given in equation 23.

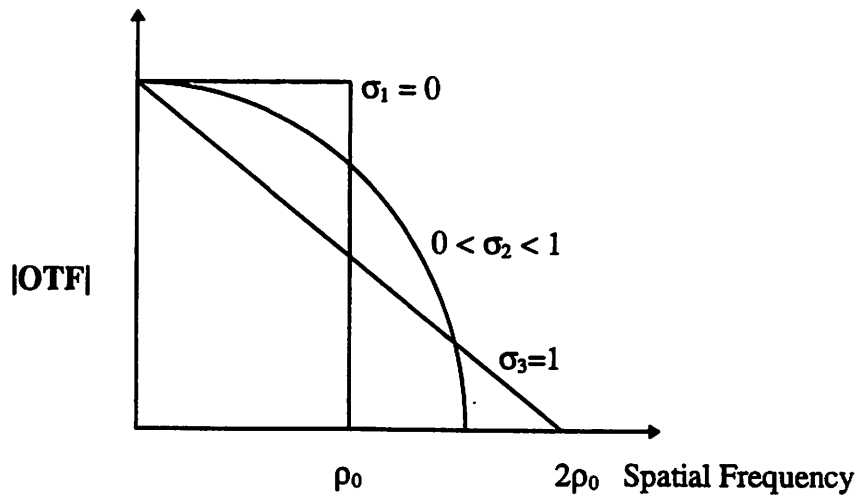

Figure 5. Modulus of OTF vs. spatial frequency and illumination coherence

$$OTF = MTF \cdot e^{jk\Phi(x)} \tag{21}$$

$$C \equiv \frac{I_{max} - I_{min}}{I_{max} + I_{min}} \tag{22}$$

$$\rho_0 = \frac{w}{\lambda \cdot z_i} \tag{23}$$

5.3.1 MTF determination

A classical experiment for measuring the system one-dimensional (1-D) MTF is to measure the aerial image intensity while scanning a knife-edge across the image of a slit source [9-11, 20-24]. The measured signal is the integral of the aerial image and for an infinitely narrow slit source, the aerial image intensity represents the line spread function (LSF) of the system. The MTF is calculated as the modulus of the Fourier transform of the LSF.

The measured signal is the edge-spread function (ESF) which is the cross correlation between the LSF image and the scanning knife-edge response (calculated in chapter 4). The ESF can be expressed as:

$$ESF(u) = N\int LSF(u_0)e(u_0 - u)du_0 = LSF(u) \otimes e(u) \tag{24}$$

where N is a normalization factor chosen so that ESF(x) = 1 for large, positive values of x (when the detector is fully illuminated). The term e(u) represents the edge function from section 4.2.2.2. Then the LSF is calculated through numerical differentiation of the ESF.

$$LSF = \frac{d}{dx}\{ESF\} \tag{25}$$

where $^{d}/_{dx}$ represents a numerical differentiation, x denotes the scanning step. Then using this equation, we may calculate the MTF as:

$$MTF(\omega) = \left| \frac{\mathcal{F}\{LSF(x)\}}{H_1(\omega)} \right| \tag{26}$$

in which $\mathcal{F}\{\ \}$ denotes the discrete Fourier transform, $H_1(\omega)$ represents the one-dimensional incoherent transfer function of the imaging system and ω is the spatial-frequency increment. Note that in practice, it is often desirable to increase the number of samples by padding the data sequence {LSF(x)} with zeros on both sides prior to implementation of equation 26. When a fast Fourier transform is used to compute Eq. 26, the padding step produces finer sampling of the MTF(ω) by decreasing $\Delta\omega$.

Goodman developed a nomenclature for the spread and transfer functions in the presence of varying spatial coherence [7]. The definition of the MTF above assumes incoherent illumination while the transfer function when imaging with fully coherent illumination is defined as the coherent transfer function (CTF). For the usual case of imaging with partially coherent light, the transfer function is referred to as the apparent transfer function (ATF) [7]. For simplicity we will use the term LSF for all cases remembering that the 10X-I images with partially coherent light.

5.3.2 Effect of Partial Coherence

The effect of illumination spatial coherence on the measurement of the imaging system MTF by the manner outlined above is the subject of much study [9-12, 20-24]. Figure 5.6 plots image intensity of a hard edge versus position for various values of

coherence from Wernick [9]. Starting from the equations which relate mutual intensities, Wernick computes the theoretical impact of illumination coherence on the error in the measurement of the true system MTF. Figure 5.7 is several plots of apparent MTFs as a function of illumination coherence (S-parameter). The separate curves for each plot are for different values of $\lambda \cdot k'$ for a detector array where k' is a term related to the pixel size. The S-parameter is similar to that defined earlier as the ratio of angles subtended from object such that purely incoherent illumination exists when S approaches infinity. Note that the apparent MTF differs significantly from the true MTF for values of S as high as 0.8.

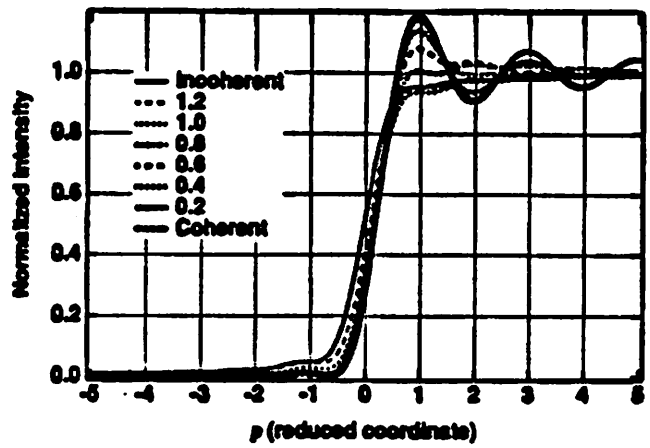

Figure 5.6 Plots of edge intensity versus position for several values of illumination coherence, Reference [9].

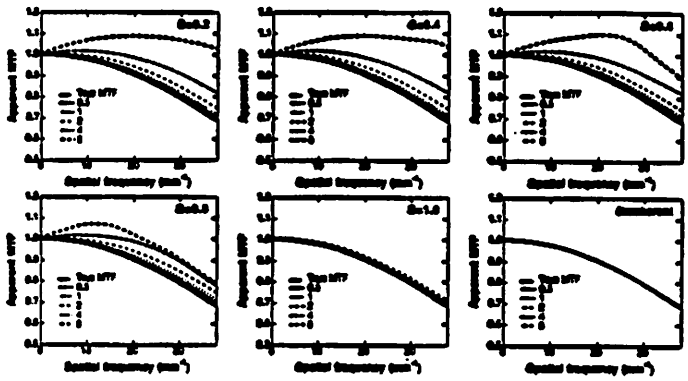

Figure 5.7 Plots of apparent MTF versus spatial frequency for several values of objective lens NA and illumination coherence (given by the S-parameter with S~1 for incoherent illumination), Reference [9].

Simulations are carried out to investigate the effect of coherence for the case of our 2.5μm EUV slit source image using the SPLAT simulation conditions listed in table 5.2. Figure 5.8 shows simulated aerial images of the slit source for six values of σ from 0.3 to 0.8 using the input parameters from the 10X-I objective and the 36-term Zernike polynomial fit to the pupil map data illustrated in Figure 4.9b. Figure 5.8a plots the simulated intensity versus position for the six cases of illumination coherence while Figure 5.8b plots the convolution of the image data from Figure 5.8a the knife-edge response function from Figure 4.8. Figure 5.8a shows a flat-top response with no ringing at the feature edge resulting in simulated AIM signals with a constant slope.

Wavelength		13.4nm
Numerical Aperture		0.08
Magnification		10
Partial Coherence (X, Y)		0.55, 0.6

Table 5.3 SPLAT simulation conditions used for simulations in chapters 4 and 5.

Simulations are also carried out using the raw pupil map data from Figure 4.9a as the input to the AI simulator SPLAT. Figure 5.9a shows the image intensity versus position for the same six cases of illumination coherence figure 8 (σ = 0.3-0.8) while Figure 5.9b shows the simulated AIM signal by convolving the data in Figure 5.9a with the knife-edge response from chapter 4. The intensity plot shows an asymmetric edge peak which is highly dependent upon illumination coherence resulting in simulated scan data in Figure 5.9b with varying slopes.

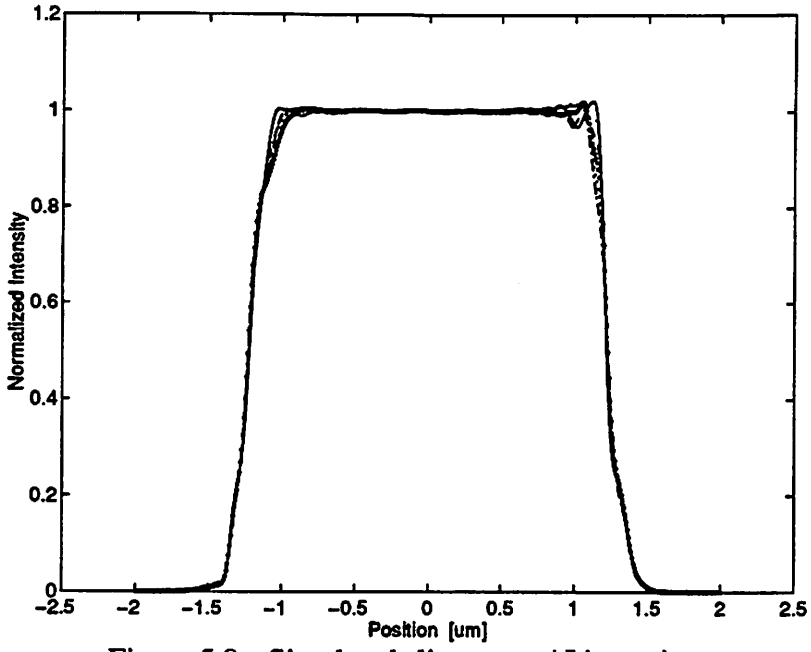

Figure 5.8a Simulated slit source AI intensity.

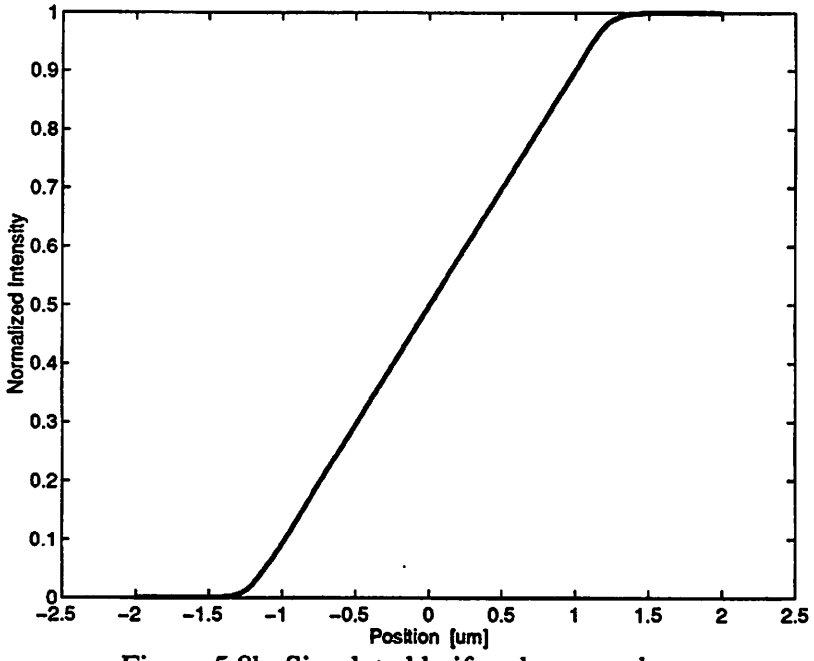

Figure 5.8b Simulated knife-edge scan data.

Figure 5.8 Simulated aerial image of a 2.5μm line source produced by the 10X-I EUVL system and the simulated knife-edge scan data produced by convolution of the data in figure (a) with the knife-edge response function calculated in chapter 4. The SPLAT simulations use a 36-term Zernike polynomial fit to the raw pupil map data from visible light interferometry measurements and model illumination coherence from $\sigma = 0.3$ to 0.8.

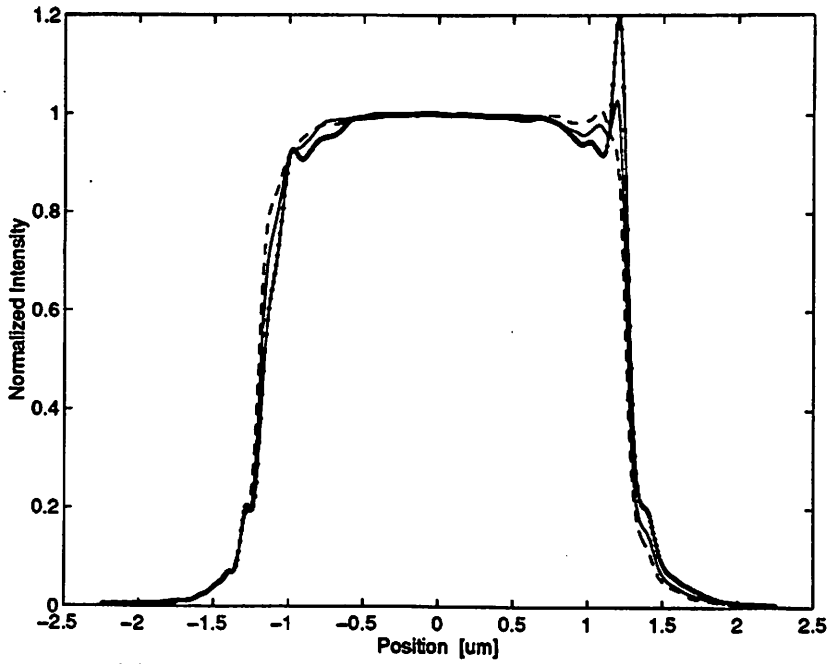

Figure 5.9a Simulated slit source AI intensity.

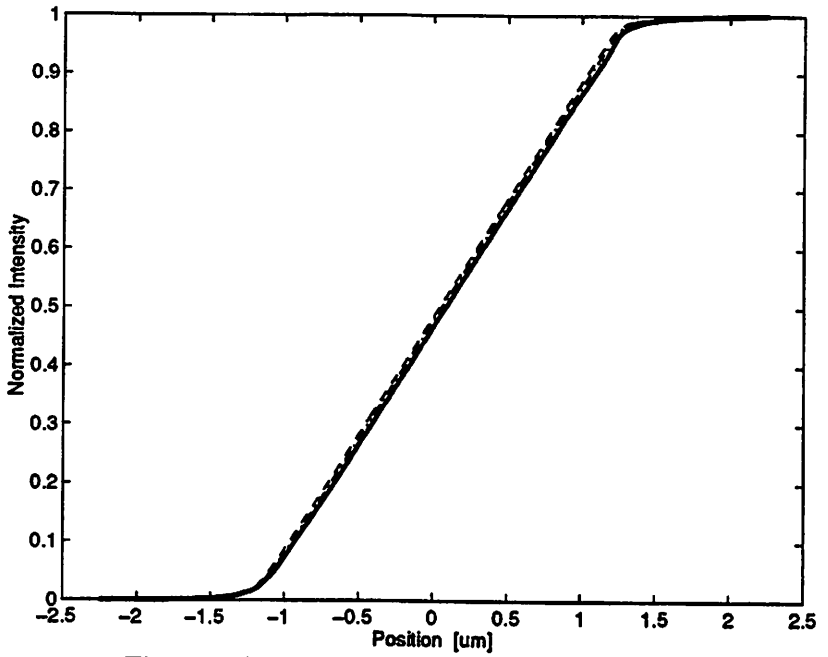

Figure 5.9b Simulated knife-edge scan data.

Figure 5.9 Simulated aerial image of a 2.5μm line source produced by the 10X-I EUVL system and the simulated knife-edge scan data produced by convolution of the data in figure (a) with the knife-edge response function calculated in chapter 4. Simulations use the raw pupil map data from visible light interferometry measurements and model illumination coherence from $\sigma = 0.3$ to 0.8.

5.3.3 Experimental Results

Figure 5.10 shows a plot of a single edge scan measured at the plane of best focus. The raw data is represented by the dots while the solid line represents the data after a triangle smoothing operation. Several such scans were performed through focus with a step size of 100nm and taking the average of 5 shots. The measured light intensity is reduced by an order of magnitude approximately 4μm from the edge.

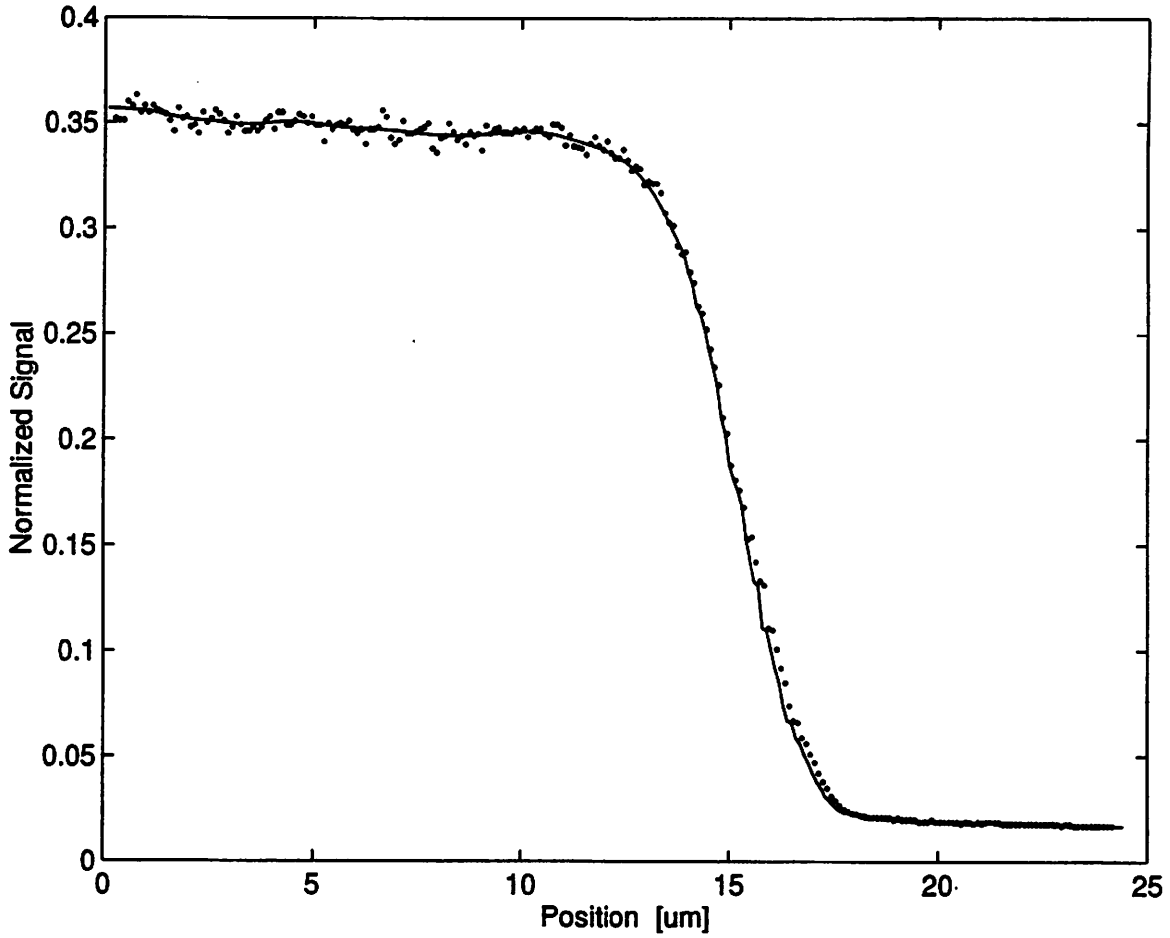

Figure 5.10 Measured knife-edge scan of a 2.5μm line source imaged by the 10X-I EUVL system at the plane of best focus. The raw data is represented by the dots and the solid line is the raw data after a band-limiting filter is applied to the data.

Figure 5.11 plots a long-range scan (500μm) knife-edge scan of the 2.5μm slit source aerial image. The wafer stage is stepped by actuating the pico-motors which decreases the SNR slightly. One sample is taken in intervals of 1μm resulting in a total scan time of 25 seconds. The aerial image intensity results shown in this plot correspond with similar experiments carried out in Europe at CERN [20]. The CERN optic displays near twice the magnitude of mid-range scatter (16% 300μm from the edge compared to 8% for the 10X-I).

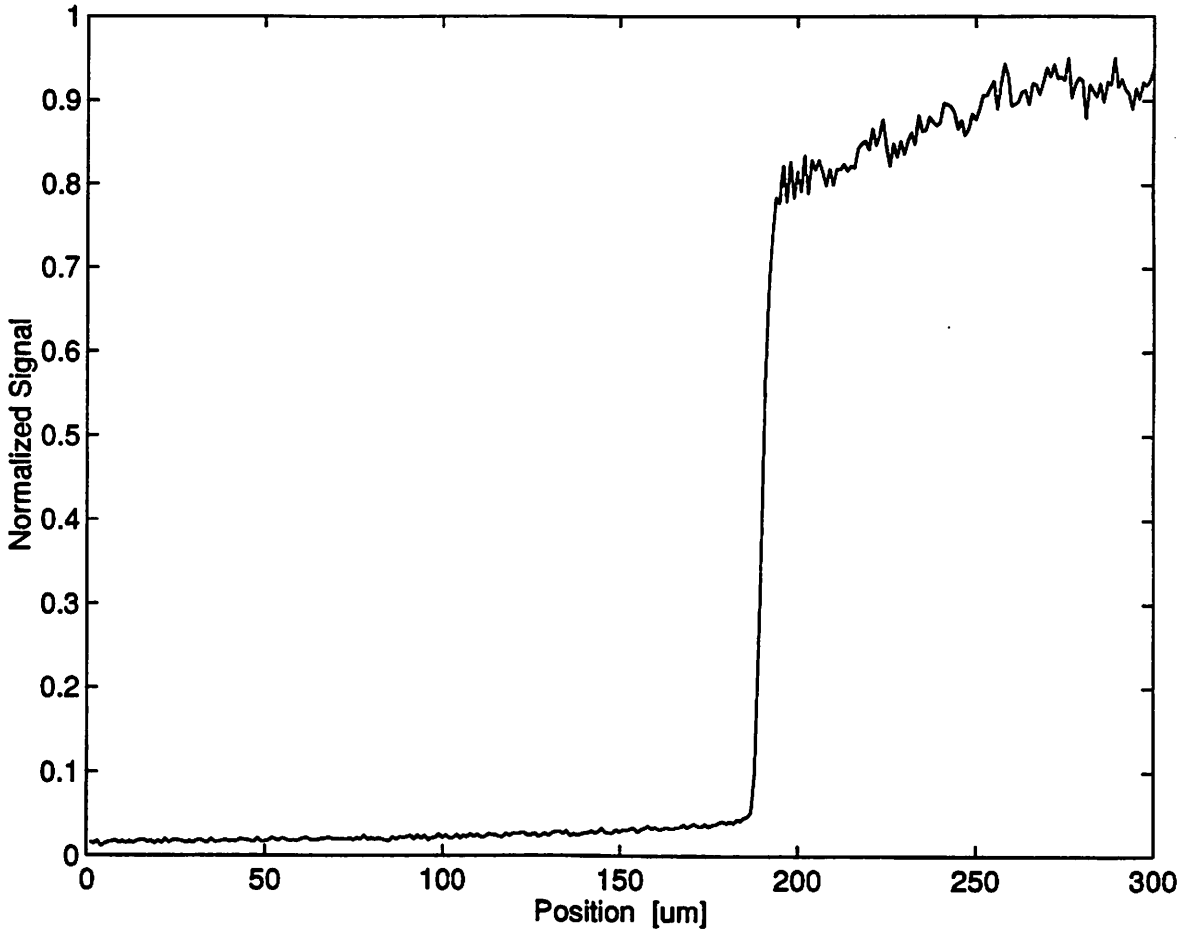

Figure 5.11 Long-range knife-edge scan of a 2.5μm line source imaged by the 10X-I EUVL system at the plane of best focus. The plot shows a non-zero intensity value 200μm from the line source.

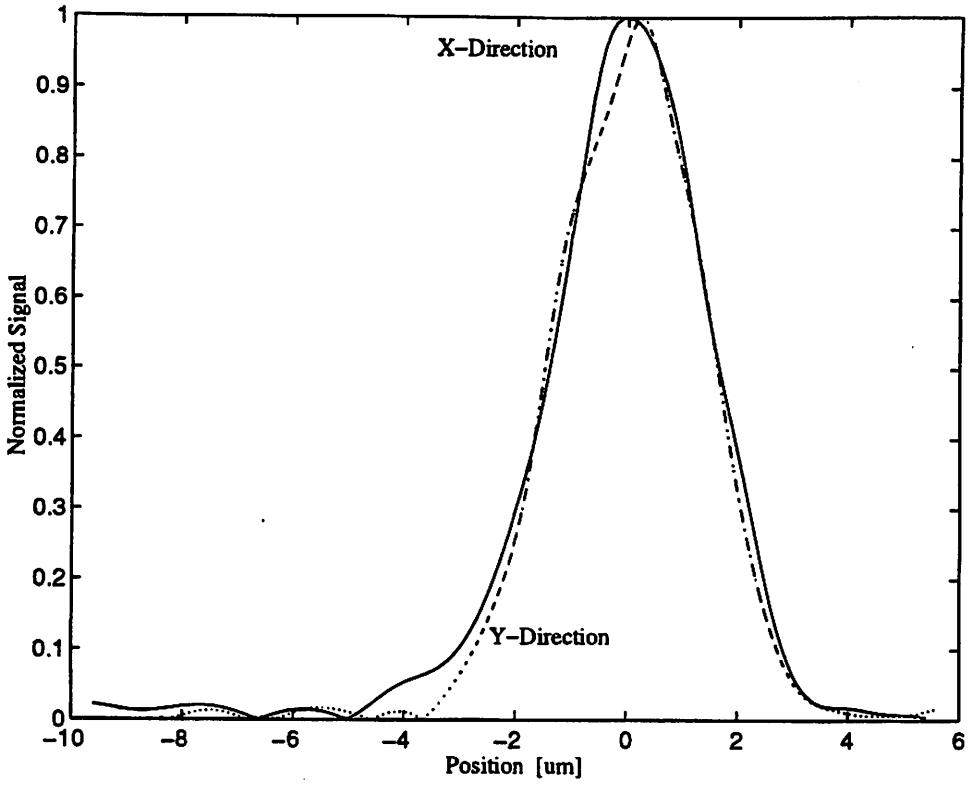

Figure 5.12 Measured aerial image calculated as the derivative of knife-edge scans of the projected line source aerial image in both the X and Y-directions.

5.3.4 Conclusion

These initial test results demonstrate the feasibility of performing direct aerial image measurements to characterize the optics of an extreme ultraviolet projection lithography camera operating at 13.4nm. Figure 5.13 shows three intensities plotted versus position, the simulated intensity using the raw pupil map data from interferometry, the measured AIM scan data and the simulated AI convolved with total artifact response including theta mis-alignment, mask edge roughness, vibration, and the theta rotation error function. The FWHM value of the measured aerial images was 3.5μm; 2.5μm of which is the geometric width of the image. Diffraction as measured in the simulations accounts for 0.25μm of the width, the mask edge roughness adds 0.1μm to the width, and the error in

angular alignment can account for 0.64μm of the width. The AIM data shows good correlation with the simulated and convolved AI at the center of the distribution but shows higher intensity at the edges of the AI. The raw pupil map simulation does not model the light scattered into these higher angles as seen in the figure which predicts an AI with zero background intensity.

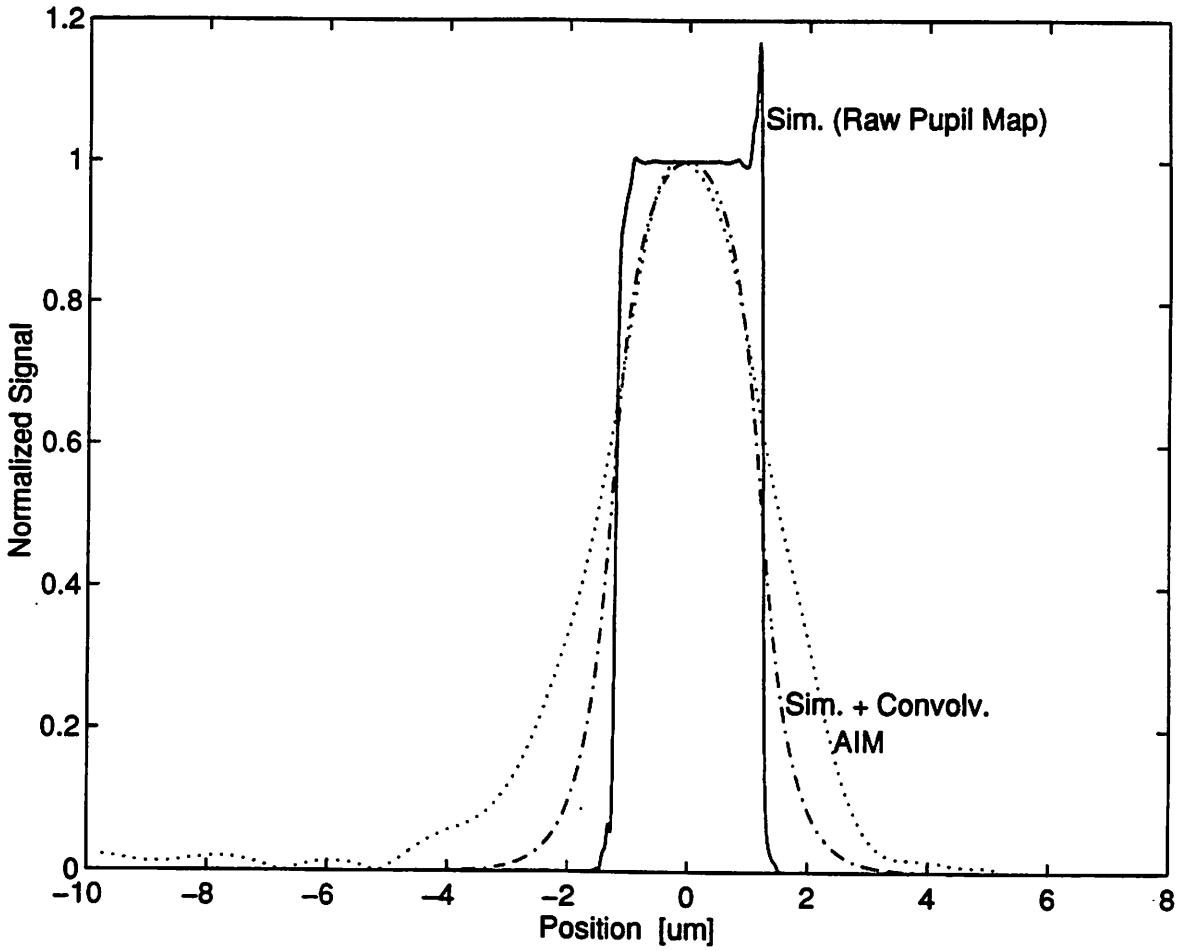

Figure 5.13 Measured and simulated AI intensity versus position for a 2.5μm slit source object imaged on the 10X-I EUVL system. The SPLAT simulations use the raw pupil map data from visible light interferometry. Also plotted is the simulated AI convolved with the complete experimental artifact response including theta misalignment, mask roughness, vibration, and knife-edge response.

5.4 Semi-infinite Plane Scatter Measurements

Higher resolution measurements are obtained by the evaluation of step function aerial image interrogated with a single narrow slit artifact. Such experiments are carried out using a 100μm X 0.09μm slit providing excellent rotational alignment. However, there is an issue with respect to distortion both in the slit and from the finite size of the well corrected field. The field distortion discussed in the preceding section is only a concern in one axis. Figure 5.14 is a distortion map of the one half of the image plane of the 10X-I EUVL system. The plot shows virtually no distortion in the X-direction. Therefore, the edge scans are performed in this direction to prevent measurement uncertainty due to distortion.

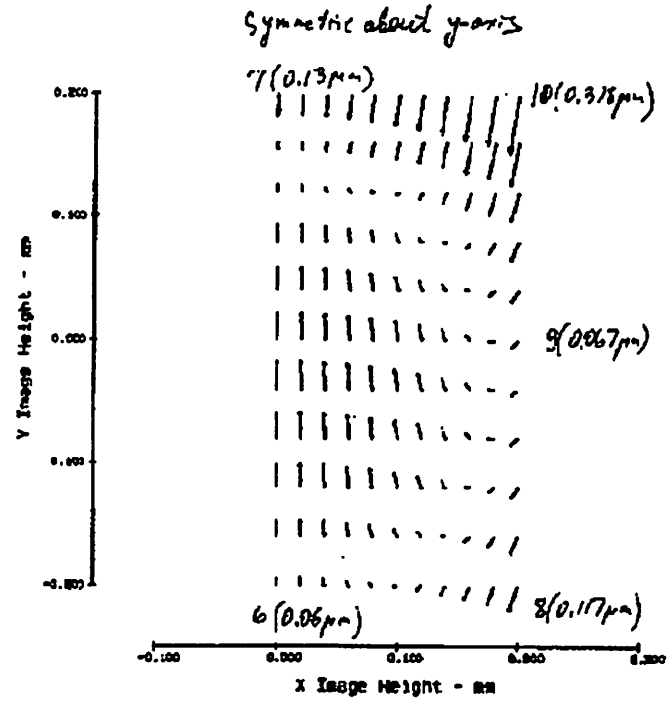

Figure 5.14 Calculated image distortion map of the 10X-I EUVL Schwarzchild camera based on the design data (one half of the image field is displayed). The map does not include figure or assembly errors. Courtesy of Tanya Jewel.

5.4.1 Experimental Procedure

AIM scans are performed of a semi-infinite plane aerial image. The artifact is a 100μm long single slit as described in chapter 2. The mask consists of an EUVL multi-layer mirror coated on one half with a thick gold absorber layer which presents a hard edge intensity pattern in one direction. The condenser is slightly defocused, providing Kohler illumination and reducing the effect of mask stage vibration (see chapter 4).

Figure 5.15 shows seven edge scans taken in focus steps of 1μm. There is no noticeable change in edge slope for this magnitude of focal plane excursion. Figure 5.16 plots the numerical derivative of the optimal focal plane scan data in Figure 5.15 which represents the measured apparent LSF of the 10X-I camera convolved with the artifact response.

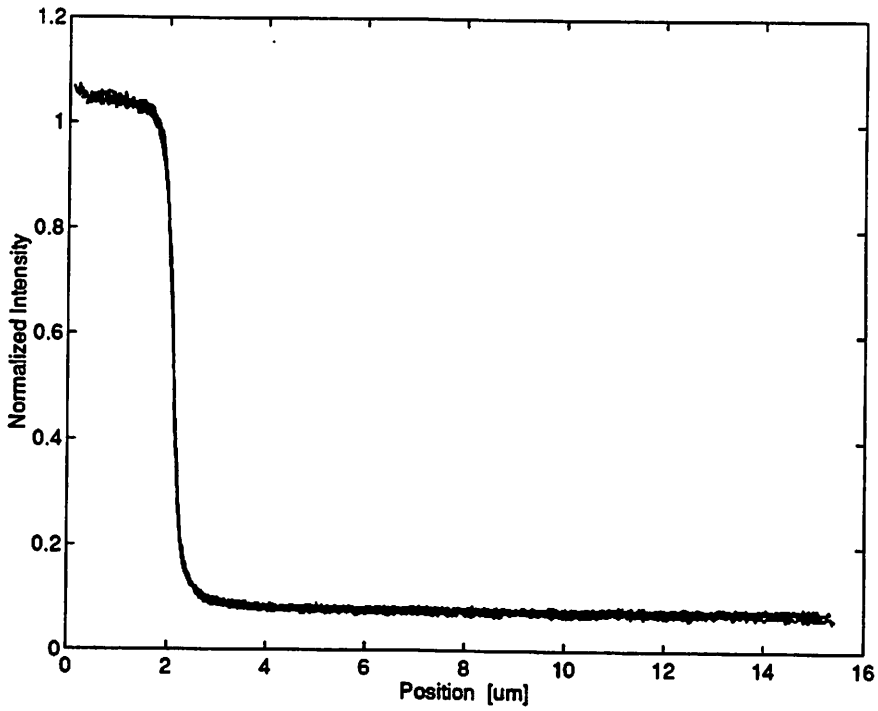

Figure 5.15 AIM slit-artifact scan of a step-function aerial image on the 10X-I EUVL system. Each curve represents a scan through a different focal plane. Six focal plane scans are shown in the figure.

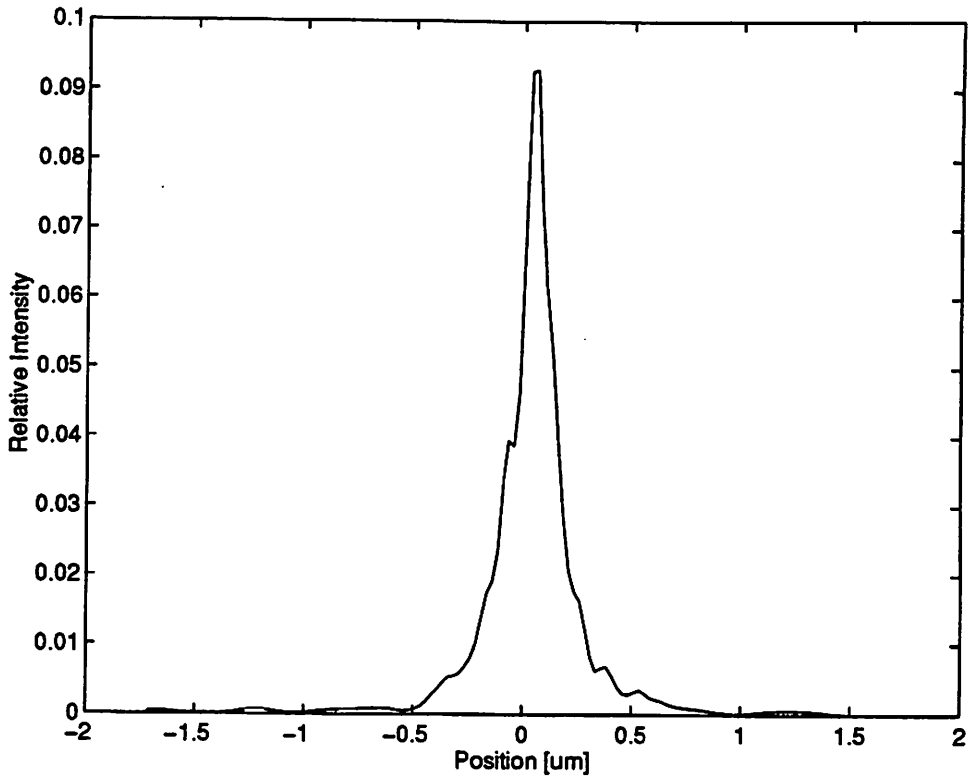

Figure 5.16 The numerical derivative of the optimum focal plane scan data in Figure 5.15 which represents the apparent LSF convolved with the AIM experimental response function.

These data are used to measure σ_{rms} by comparison with the LSF or MTF expected from a camera without scatter using equation 15. Therefore there are two methods to incorporate the effects of the experimental response function, which reflects the aperture response function, vibration, and theta mis-alignment as discussed in section 5.2. The first is to deconvolve the measured AI by the combined experimental response function. This technique requires frequency-band limiting the spectrum of the inputs prior to deconvolution to prevent frequency-band aliasing. A second technique is to "work-down" to the measured value by convolving the LSF^0 from simulation, without scatter, with the experimental response function. This latter method is preferred since it eliminates frequency-band aliasing.

To determine an accurate measure of the expected LSF^0, and ultimately the apparent MTF^0 of the system, simulations are conducted to evaluate the impact of illumination coherence on the imaging of a step-function object. Figure 5.17a plots intensity versus position for a hard-edge object simulated using SPLAT. The figure plots six aerial image intensities from varying partial coherence from $\sigma = 0.3$ to 0.8 simulated using the raw pupil map data of the 10X-I camera. Figure 5.17b is the calculated MTF of intensity data in (a). There is a only about a 6% difference in the MTF curves at the lowest spatial frequency ($0.25\mu m^{-1}$) while as much as a 200% between 4-5 μm^{-1}. There is only about a 10% difference between the $\sigma = 0.4$ - 0.6 curves which represents the approximate coherence of the 10X-I system.

This simulation experiment is also carried out using the 36-term Zernike polynomial fit to the raw pupil map data. Figure 5.18a plots the simulated intensity versus position for the same values of partial coherence ($\sigma = 0.3$ - 0.8). There is noticeably less difference between each of the curves in this figure than each of the separate intensity curves in Figure 5.17a. Figure 5.8b plots the simulated apparent MTF calculated from the ESF data in Figure 5.18a. The apparent MTF data in Figure 5.18b is a less sensitive function of illumination coherence than data in Figure 5.17b which uses the raw pupil map data directly in the simulation.

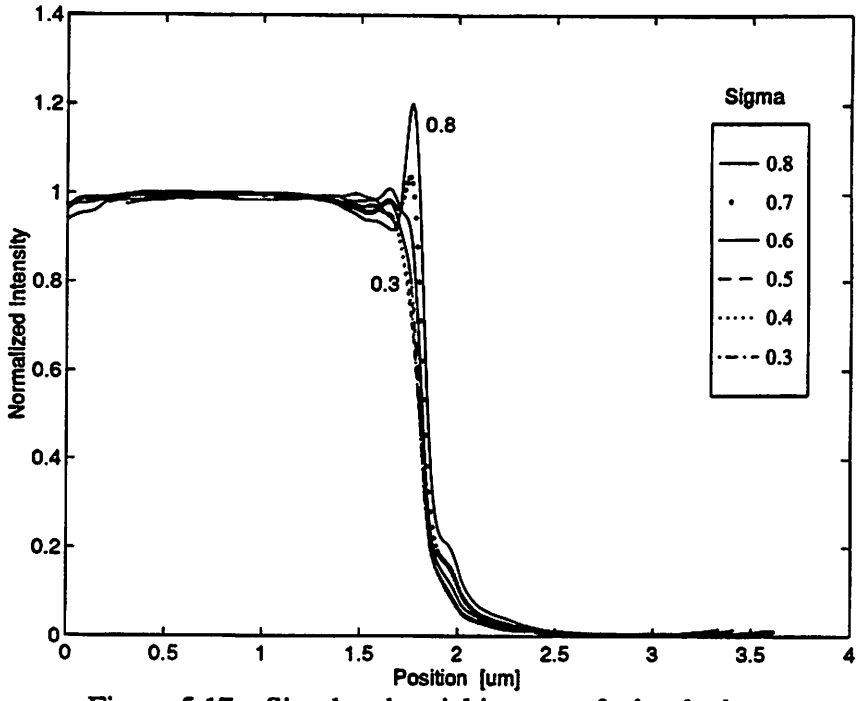

Figure 5.17a Simulated aerial images of a hard edge.

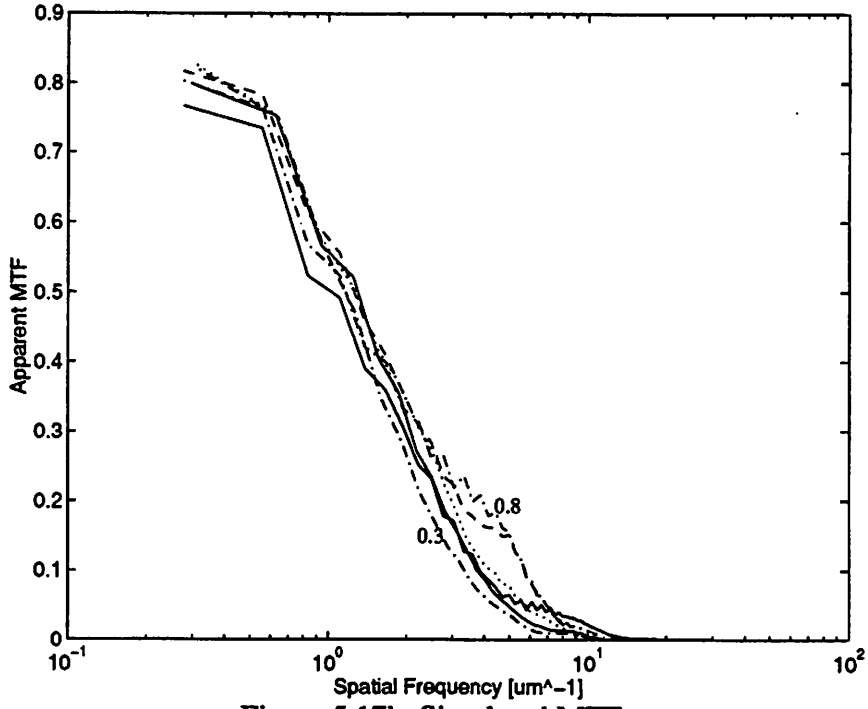

Figure 5.17b Simulated MTF.

Figure 5.17 Simulated image intensity versus position for six values of illumination coherence for the 10X-I EUVL system using the raw pupil map from visible light interferometric measurements. Also plotted are apparent MTFs corresponding to the data in figure (a) calculated as the modulus of the Fourier transform of the derivative of the image plotted in figure (a).

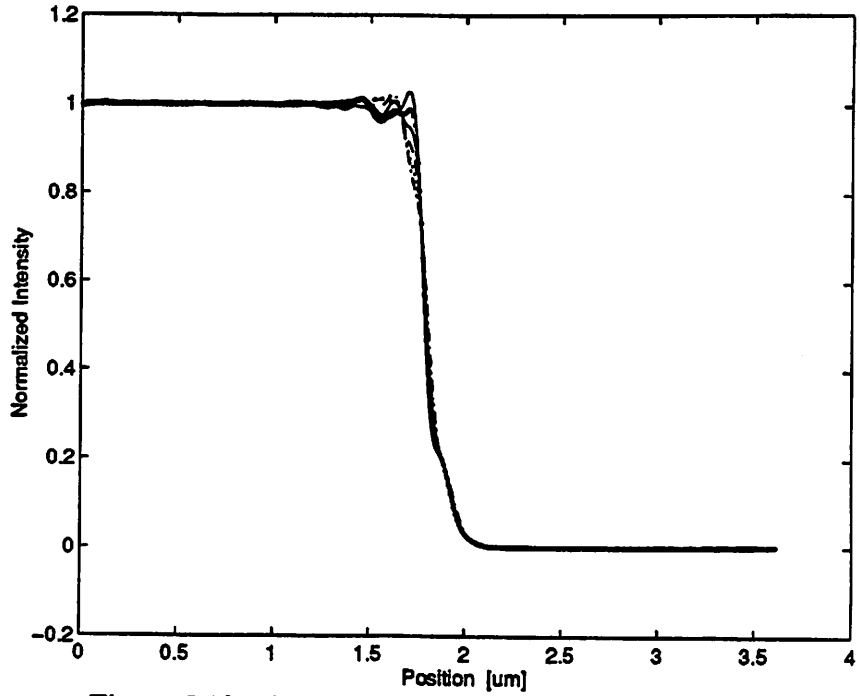

Figure 5.18a Simulated aerial images of a hard edge.

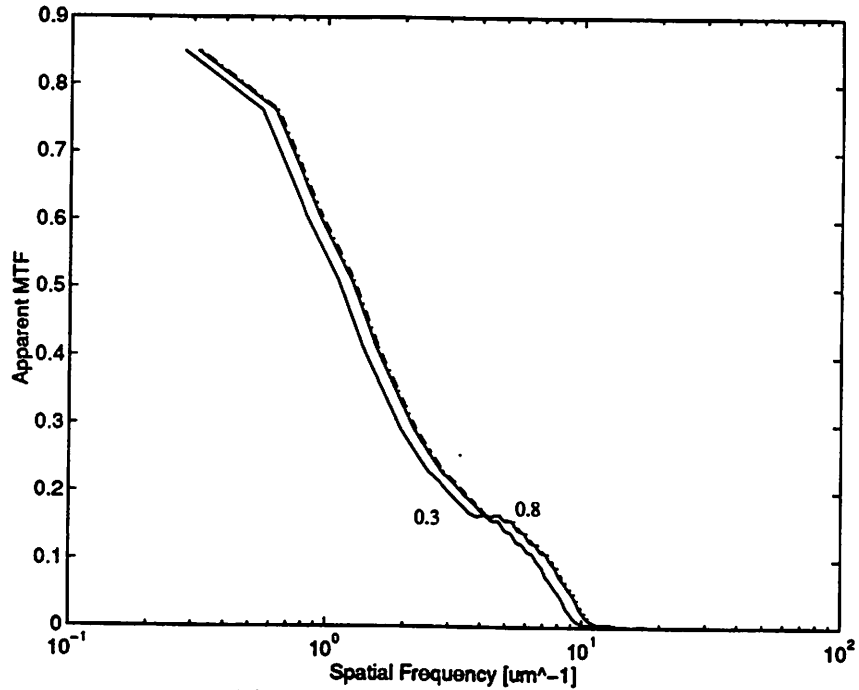

Figure 5.18b Simulated MTF.

Figure 5.18 Simulated image intensity versus position for six values of illumination coherence for the 10X-I EUVL system using the 36-term Zernike polynomial fit to the raw pupil map from visible light interferometric measurements. Also plotted are apparent MTFs corresponding to the data in figure (a) calculated as the modulus of the Fourier transform of the derivative of the image plotted in figure (a).

The aerial images simulated using the raw pupil map data are used for the calculation of σ_{rms}. A direct comparison of the two apparent MTFs used in the calculation is made in Figure 5.19 which plots the apparent MTF calculated from the AIM measurement and from simulation using a partial coherence of $\sigma = 0.6$ from table 5.3 for an edge in the Y-direction. The simulated edge is convolved with the AIM experimental response function which includes the response of the aperture, system vibration, and theta mis-alignment. The MTF is then calculated for both images as the modulus squared of the Fourier transform of the derivative of the ESF as discussed earlier.

If we assume that the difference in the two curves in Figure 5.19 originates from surface scattering, we can calculate σ_{rms} following equation 15. It is plotted versus spatial frequency in Figure 5.20. The calculated values plotted in Figure 5.20 have a maximum value of 1.3nm around the spatial frequency of $4\mu m^{-1}$ and represent the combined effective roughness of both mirrors that comprise the 10X-I Schwarzchild.

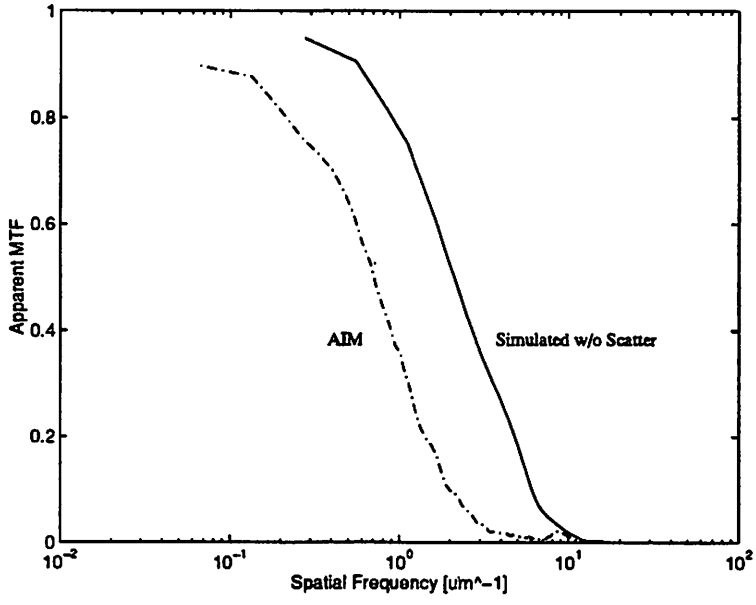

Figure 5.19 Apparent MTFs from direct AIM and SPLAT simulation using the raw pupil map data of the 10X-I camera and a partial coherence of $\sigma = 0.6$.

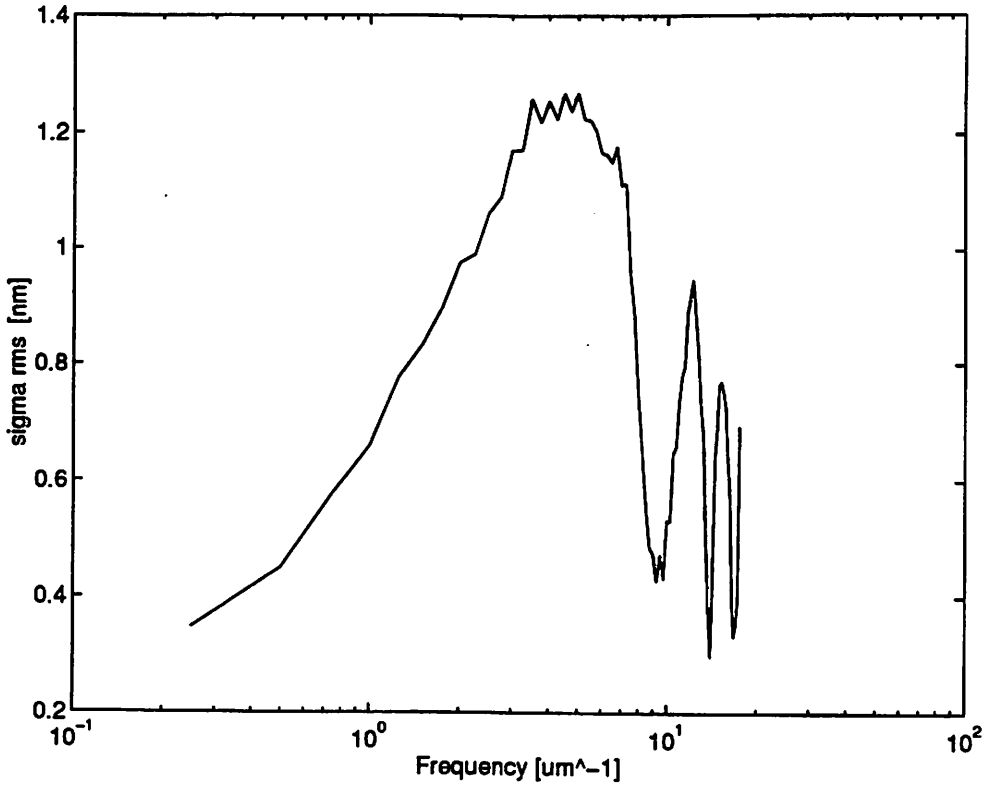

Figure 5.20 EUVL multi-layer mirror surface roughness in nanometers versus spatial frequency calculated using the apparent MTF data from Figure 5.19 using equation 5.15.

5.4.3 PSD from sample optics

The value of the multi-layer roughness calculated in the previous section may be compared to independent measurements using equations 5-2 and 5-10. These equations relate the roughness variance of each reflective surface of an imaging system to the total combined effective roughness variance where $n_{ZM} \approx 1$ for both reflections of the 10X-I camera. Independent measurements of σ_m are required for each of the multi-layer mirrors that comprise the Schwarzchild objective lens. The magnitude of this roughness for current high-quality EUVL optics is on the order of nanometers which is in the range of AFM measurement. Spatial frequencies between $10mm^{-1}$ and $10um^{-1}$ have been

characterized with the use of a Zygo NewView-100 white-light interferometric miscroscope [46].

The use of the 10X-I camera precludes its disassembly for surface roughness measurements using the techniques above. The Schwarzschild objective of the 10X-I is comprised of a primary mirror from one vendor and a secondary mirror from a different vendor. Two primary mirrors were obtained, one from each of the vendors mentioned above. The assumption here is that each vendor produces primary and secondary substrates with similar quality as a result of the same polishing procedure.

The surface profiles of these sample optics were measured with a visible light interferometer at Lawrence Livermore National Labs [47]. Figure 5.21 plots the measured PSDs of both multi-layer optics where each optics is measured at two separate locations. The interferometer measures the two-dimensional PSD of the surface and the data is reduced to a one-dimensional plot. The instrument response of the interferometer produces a 0.3nm rms error in the spatial frequency range of the measurement. The instrument response is evaluated by removing the peaks of the surface measurement then fitting a second-order polynomial to the resulting PSD. The instrument response has been removed from the PSD data shown in figure 5.21.

Since no PSD information is available from the AIM measurements for a comparison using equation 5-11, we must obtain a measure of the surface roughness from the interferometry PSD data. Each curve in Figures 5.21 is integrated following equation 5-2 to obtain the roughness as a function of spatial frequency plotted in Figure 5.22 along with the measured values of surface roughness from AIM measurement.

The average values of sigma for each mirror are calculated and combined according to equation 5-10. The resulting effective roughness from this calculation is plotted with averages of each mirror and values from AIM in Figure 5.23. The combined roughess from quadrature total is dominated by the roughness of optic 1 in this case. The rms value of the roughness from the quadrature total is 0.4nm over the spatial frequency range of interferometer measurement ($4 \cdot 10^{-6} nm^{-1}$ to $4 \cdot 10^{-4} nm^{-1}$). The rms value of the camera roughness from AIM is 0.7nm in the spatial frequency range from $2 \cdot 10^{-4} nm^{-1}$ to $1 \cdot 10^{-2} nm^{-1}$.

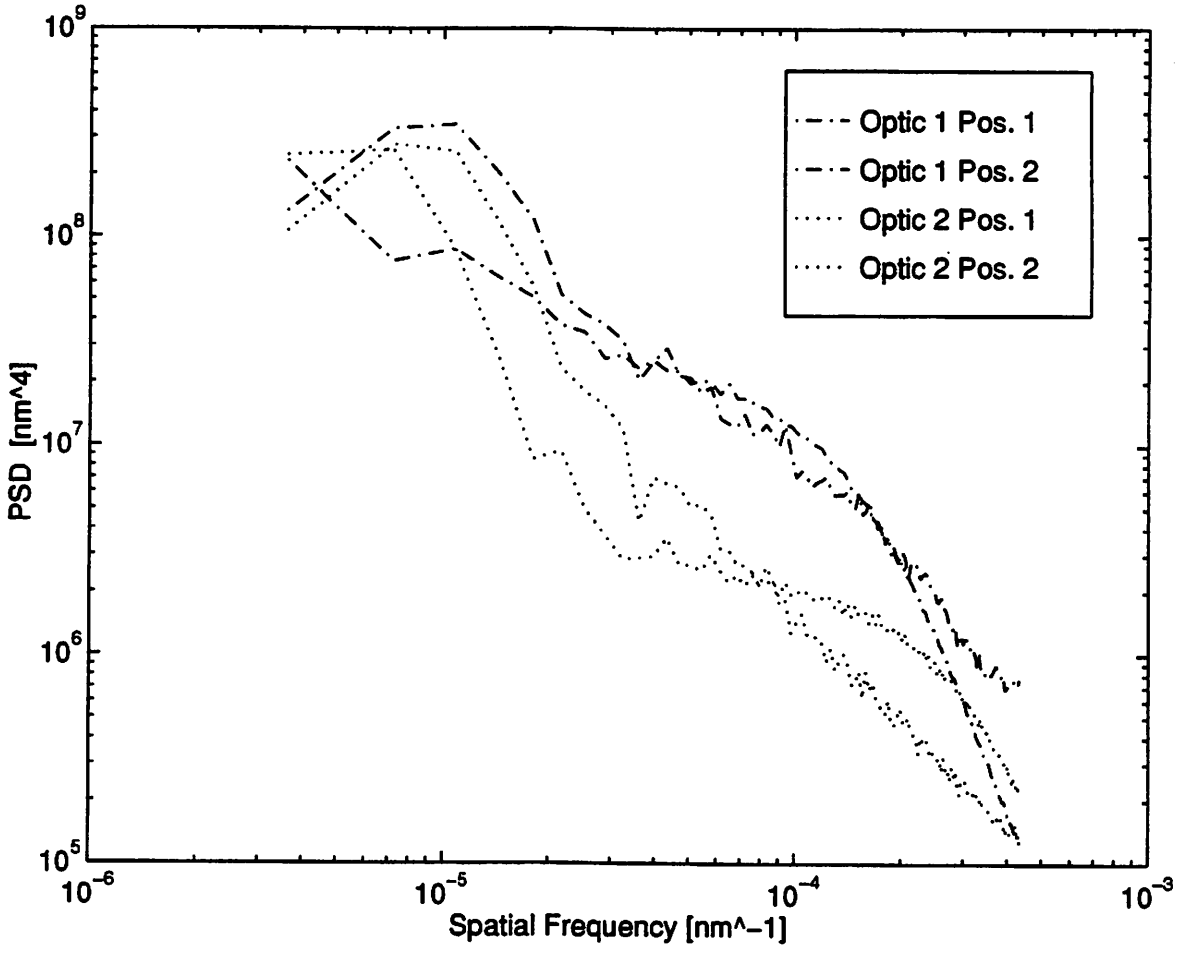

Figure 5.21 Two-dimensional PSD plot of two EUVL multi-layer primary mirrors measured at two locations on each mirror using visible light interferometry at LLNL.

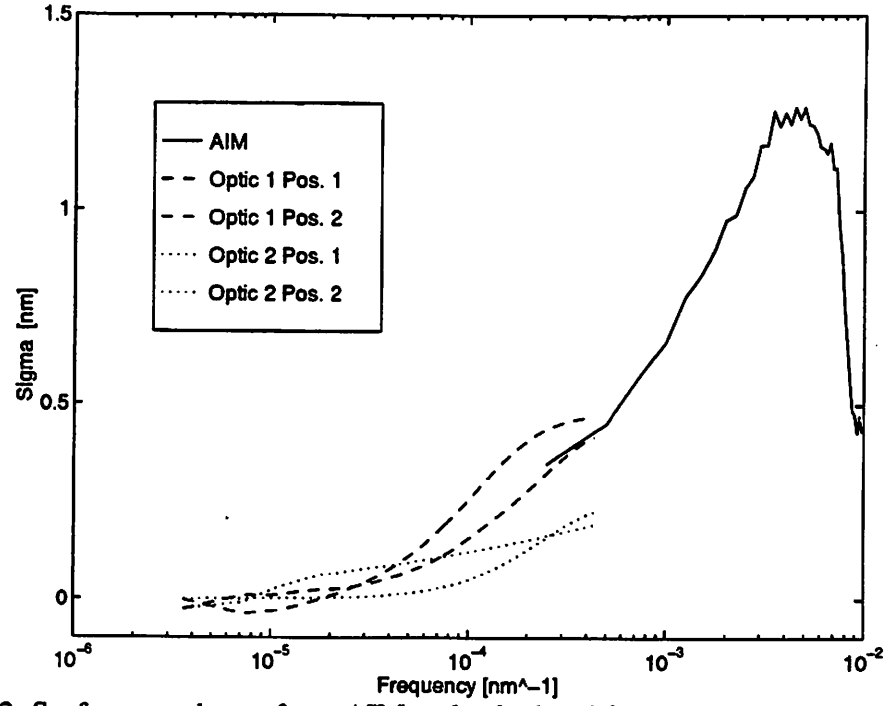

Figure 5.22 Surface roughness from AIM and calculated from the PSD data in figure 5.23 following equation 5-2.

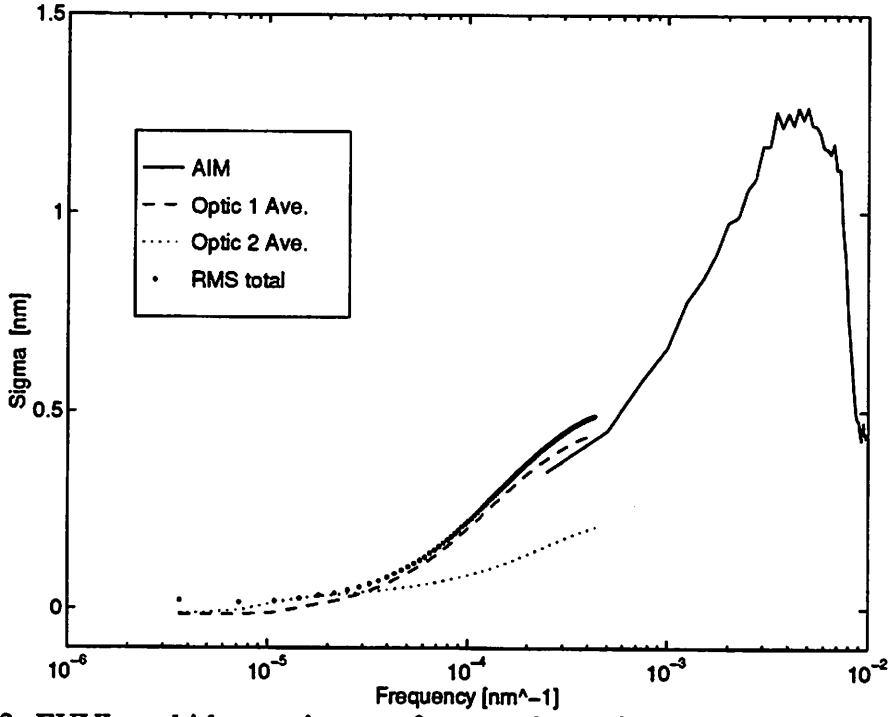

Figure 5.23 EUVL multi-layer mirror surface roughness from AIM and simulation using equation 5.15 (solid line) and the roughness values maximums from PSD measurements of sample mirrors using white-light interferometry [46].

5.5 Depth of Focus Study

Scatter in optical systems decreases the lithographic process window. Depth of focus experiments are conducted to evaluate the impact of scatter on the DOF process window. AIM scans of 0.5μm L/S are done using a single 50μm long slit artifact. A plot of the contrast of the AIM signal (equation 3) vs. focus plane provides a measure of the focal process latitude produced by the imaging system. Scatter acts both to reduce the peak contrast of the aerial image and also to reduce the width of the process window.

Figure 5.24 plots of several AIM scans versus position through focus for the 0.5μm L/S test pattern. The curves with higher contrast are closer to optimal focus while, the low contrast curves represent measurements one either side of the best focal plane. Figure 5.25 is a plot of the contrast of the measured image intensities vs. focus. The depth of focus is 10μm based on 80% image contrast.

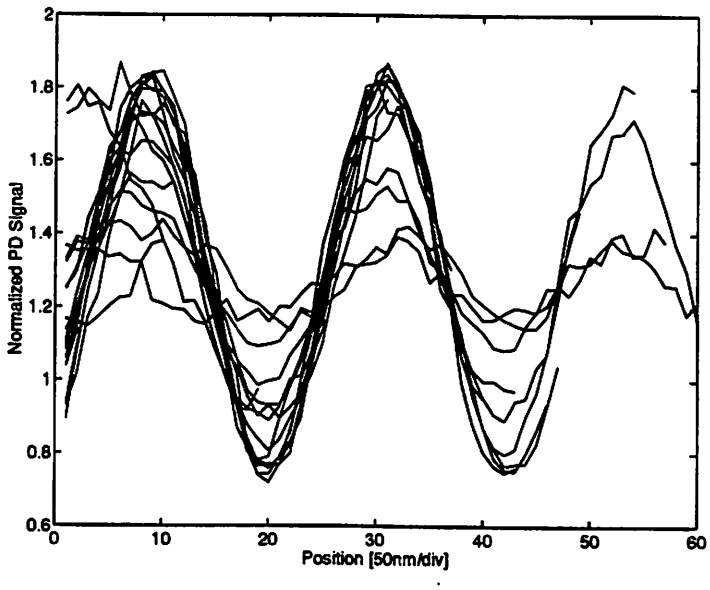

Figure 5.24 Measured image intensity versus position for AIM slit-artifact scans through focus of 0.5μm L/S imaged on the 10X-I EUVL system.

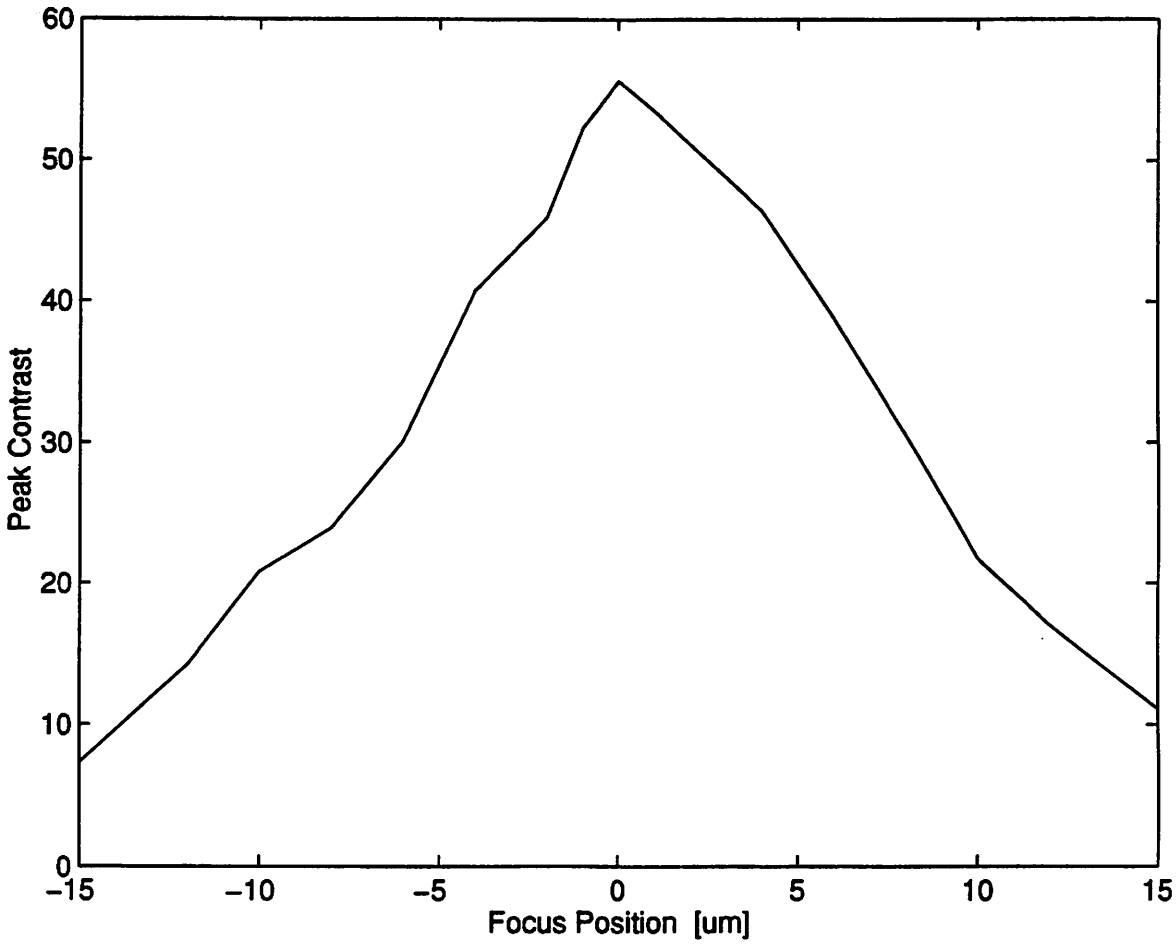

Figure 5.25 Measured image contrast versus focus position from the data in Figure 5.24.

Simulations of imaging 0.5μm L/S patterns are conducted using the raw pupil data and the 36-term Zernike polynomial representation of the pupil map data for DOF comparison to the measured data. The depth of focus is calculated by convolving the simulated aerial images with the AIM experimental response. Figure 5.26 plots the simulated DOF for both cases along with the measured DOF for this case. Both simulated cases predict a higher value of maximum peak contrast than is measured with AIM. This is expected from earlier simulations and AIM measurements since simulations do not accurately predict the effect of mid-spatial frequency scatter.

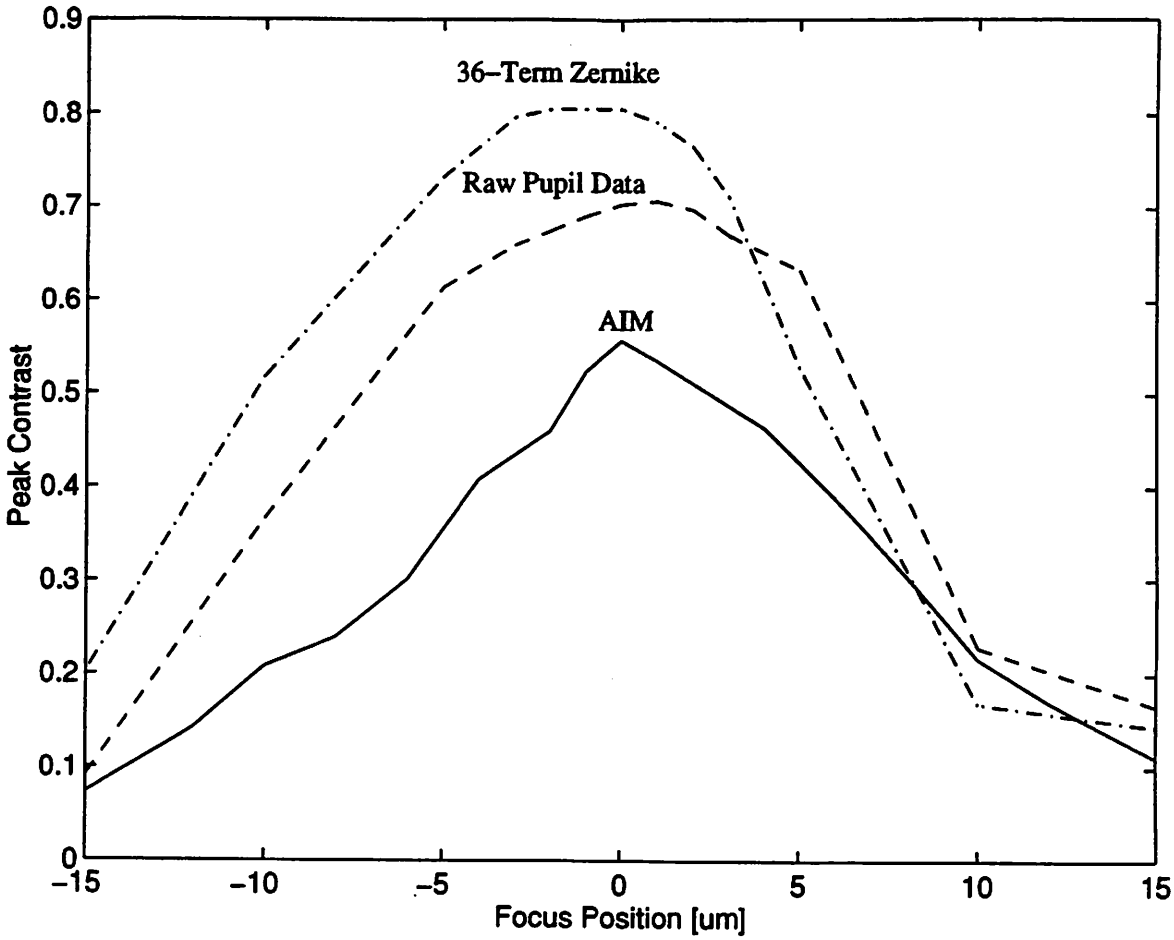

Figure 5.26 Measured and simulated image contrast versus position for AIs of 0.5μm L/S imaged on the 10X-I EUVL system.

5.6 Conclusion

The effect of mid-spatial frequency scatter on the imaging performance of the 10X-I EUVL system is evaluated using simulation and AIM. The measurements provide qualitative agreement with simulation. Knife-edge scans of a line source image show a DC base-line intensity of 8% of the clear-field intensity up to 200μm from the edge of the image.

More quantitative measurements of the imaging degradation are obtained by a slit-artifact scan of a step-function aerial image. AIM measurements and simulation are used to quantify the MTF degradation and estimate the effective EUVL multi-layer optic surface roughness. The value of σ_{rms} is between 0.4nm and 1.3nm between the spatial frequency region between $0.3\mu m^{-1}$ and $4\mu m^{-1}$, respectively.

Depth of focus experiments are carried out involving the measurement of the contrast through focus of 0.5mm L/S. The peak measured contrast of 56% with a working depth of focus of $\pm 5\mu m$ based upon 80% of peak image contrast.

References

[1] J.P. Kirk, "Scattered light in photolithographic lenses", SPIE Proceeding, Vol. 2197, pp. 566-72, 1994.

[2] A.R. Neureuther, K.K.H. Toh, J.E. Fleischman, D. Yu, G. Misium, B. Huynh, G. Uathavikul, and W. G. Oldham, "Exploratory Test Structures for Image Evaluation in Optical Projection Printing," SPIE Proceeding on Laser Microlithography II (1989), Vol. 1088 pp.83-87.

[3] W.G. Oldham, W. Arden, H. Binder, and C.H. Ting, "Contrast Studies in High-Performance Projection Optics," IEEE Trans. Elec. Devices, Nov. 1983, pp. 1474-1479.

[4] Hisataka Takenaka, Tomoaki Kawamura, Yoshikazu Ishii, Tsuneyuki Haga, and Hiroo Kinoshita, "Evaluation of Mo-Based Multilayer EUV Mirrors," OSA Optical Society of America Conference Proceedings on Extreme Ultraviolet Lithography, Vol. 35, pp. 26-32 , Monterey, CA, 1994.

[5] D.P. Gaines, S.P. Vernon, G.E. sommargren, and D.R. Kania, "Coating Strategy for Enhancing Illumination Uniformity in a Lithographic Condenser," D.P. Gaines, S.P. Vernon, G.E. sommargren, and D.R. Kania, OSA Optical Society of America Conference Proceedings on Extreme Ultraviolet Lithography, Vol. 35, pp. 41-46, Monterey, CA, 1994.

[6] S.P. Vernon, M.J. Carey, D.P. Gaines, and F.J. Weber,"Multilayer Coating for the EUV Lithograph Front-End Test Bed," OSA Optical Society of America Conference Proceedings on Extreme Ultraviolet Lithography, Vol. 35, pp. 33-40 , Monterey, CA, 1994.

[7] Goodman, **Statistical Optics**, Wiley Press, 1981.

[8] Z. Tan, A. A. MacDowell, B. La Fontaine, J. Russo, J.E. Bjorkholm, D. Tennant, D. Taylor, M. Himel, O.R. Wood, II, R.R. Freeman, W.K. Waskiewicz, D.L. Windt, D. White, S. Spector, A.K. Ray-Chaudhuri, and R.H. Stulen, "At-Wavelength Metrology of EUV Cameras using Lateral-Shearing Interferometry," OSA Optical Society of America Conference Proceedings on Extreme Ultraviolet Lithography, Vol. 35, pp. 151-160, Monterey, CA, 1994.

[9] M.N. Wernick, G.M. Morris, "Effect of spatial coherence on knife-edge measuremements of detector modulation function", Applied Optics, Vo. 33., No. 25, 1 September, 1994, pp. 5906-13.

[10] K.A. Valiev, **The Physics of Submicron Lithography**, Plenum Press, 1992.

[11] S.A. Akhmanov and R.V. Khokhlov, *Problems in Nonlines Optics*, Moscow (1964).

[12] D.G. Stearns, "Image Degradation due to scatter in a distributed optical system: A theoretical treatment" , unpublished.

[13] Born and Wolf, **Physics of Optics**, Wiley Press, 1980.

[14] Fellgett, P.B., and E.H. Linfoot, Philos. Trans. R. Soc. London 247, 269 (1995).

[15] Linfoot, Eh., J. Opt. Soc. Am. 45, 909 (1995).

[16] Shannon, C., Bell Syst. Tech. J. 27, 379 (1948).

[17] Huck, F.O. and S.K. Park, Appl. Opt. 14, 2508 (1975).

[18] Huck, F.O., N. Halyo, and S.K. Park, Appl. Opt. 19, 2174 (1980).

[19] B. La Fontaine, D.L. White, A.A. MacDowell, Z. Tan, D.M. Tennant, and O.R. Wood, II, "Extreme Ultraviolet Moire Interferometry," OSA Optical Society of America Conference Proceedings on Extreme Ultraviolet Lithography, Vol. 35, pp. 167-170, Monterey, CA, 1994.

[20] R. Mercier, F. Polack, P. Fournet, G. Tissot, and J.P. Marioge, "Control at 11.4nm of an XUV Schwarzschild objective", Rev. Sci. Instrum., Vol. 66, No.2 , pp. 2184-6, February, 1995.

[21] A.K. Ray-Chaudhuri, R.H. Stulen, W. Ng, F. Cerrina, S. Spector, Z. Tan, J. Bjorkholm, and D. Tennant, "EUV Metrology of Multilayer Optics," OSA Optical Society of America Conference Proceedings on Extreme Ultraviolet Lithography, Vol. 35, pp. 161-166, Monterey, CA, 1994.

[22] A.P. Tzannes and J.M. Mooney, "Measurement of the modulation transfer function of infrared cameras", Optical Engineering, Vol. 84, No. 3, pp. 1808-17, June 1995.

[23] D.E. Vandenberg, W.D. Humbel, and A. Wertheimer, "Quantitative evaluation of optical surfaces by means of an improved Foucault test approach", Optical Engineering, Vol. 32, No. 8, pp. 1951-4, August 1993.

[24] Z.Tan, J. Bjorkholm, A. Ray-Chaudhuri, F. Cerrina, et. al., "At-wavelength metrology of 13nm lithography imaging optics", Review of Scienctific Instrumentation, Vol. 66, No.2, pp. 2241-3, February, 1995.

[25] K.A. Goldberg, R. Beguiristain, J. Bokor, H. Medecki, K. Jackson, D.T. Attwood, G.E. Sommargren, J.P. Spallas, and R. Hostetler, "Point-Diffraction Interferometry at EUV Wavelengths," OSA Optical Society of America Conference Proceedings on Extreme Ultraviolet Lithography, Vol. 35, pp. 134-141, Monterey, CA, 1994.

[26] A.K. Ray-Chaudhuri, W. Ng, F. Cerrina, S. Spector, Z. Tan, J. Bjorkholm, D. Tennant, and R.H. Stulen, "EUV Metrology of Multi-layer Optics," OSA Optical Society of America Conference Proceedings on Soft X-Ray Projection Lithography, Vol. 18, 1993.

[27] B. La Fontaine, A.A. MacDowell, Z. Tan, G.N. Taylor, D.L. White, D.M. Tennant, and O.R. Wood, II, "Real-Time, Sub-Micron Fluorescence Imaging of Extreme Ultraviolet Aerial Images," OSA Optical Society of America Conference Proceedings on Extreme Ultraviolet Lithography, Vol. 35, pp. 177-181, Monterey, CA, 1994.

[28] T.D. Ngyuen, C. Kan-Malek, and J.H. Underwood, "Achievement of Low Stress in Mo/Si Multilayer Mirrors," OSA Optical Society of America Conference Proceedings on Extreme Ultraviolet Lithography, Vol. 35, pp. 56-60 , Monterey, CA, 1994.

[29] J.H. Underwood, E.M. Gullikson, W. Ng, A. Ray-Chaudhuri, and F. Cerrina, "Effect of contamination and Oxide Layers on Scattering and Reflectivity of Multilayer Mirrors," OSA Optical Society of America Conference Proceedings on Extreme Ultraviolet Lithography, Vol. 35, pp. 61-67, Monterey, CA, 1994.

[30] E.L. Church and P.Z. Takacs, "Speifying the Surface Finish of X-Ray Mirrors," OSA Optical Society of America Conference Proceedings on Soft X-Ray Projection Lithography, Vol. 18, pp. 105-107 1993.

[31] K.B. Nguyen, A.K. Wong, A.R. Neureuther, D.T. Attwood, et al., "Aerial Images of EUV Projection Lithography Masks with defects in Reflective Coatings: Electromagnetic Simulation," Soft X-Ray Projection Lithography (Monterey, CA, USA), OSA Proceedings, vol. 18, pp 47-53, (Optical Society of America,. Washington, D.C., USA, 1993).

[32] H. Kinoshita, K. Kurihara, and H. Takenaka, "Soft X-Ray Reduction Lithography Using Multilayer Mirrors," OSA Optical Society of America Conference Proceedings on Soft X-Ray Projection Lithography, Vol 30, No 11B, November 1991, pp3048-3052.

[33] M. Cai, Q, Wang, D.D. Allred, L.V. Knight, and A.Reyes-Mena, "Characterization of Annealed Mo/Si Sorft X-Ray Multilayers: Raman Spectroscopy and STM as tools in Understanding Structures and interfaces," OSA Optical Society of

America Conference Proceedings on Soft X-Ray Projection Lithography, 1993 Vol. 18, pp. 187-197.

[34] T.E. Everhart, "Fundamental Limits of Lithography," Materials for Microlithography, American Chemical Society Sympmosium, Series #266, American Chemical Society, Washington, DC, 1984.

[35] A.R. Neureuther, C.G. Wilson, "Reduction in X-Ray Lithography Shot Noise Exposure Limit be Dissolution Phenomena," J. Vac. Sci. Technol. B 6 (1), pp167-173, (American Vacuum Society), Jan/Feb 1988.

[36] R.D. Watson, R.H. Stulen, "Analysis of Thermally Induced Distortion of Optics for Soft X-Ray Projection Lithography," OSA Proceedings on Soft X-Ray Projection Lithography, 1991, Vol. 12, pp.37-41.

[37] R. Shaw, "Quality criteria for quantized images", SPIE Proceed. on Image Processing, Analysis, Measurement, and Quality, Vol. 901, pp. 139-43, 1988.

[38] A.H. Robinson, "Multidimensional Fourier transforms and image processing with finite scanning apertures", Appl. Opt. 12, 2344-52, 1973.

[39] F.O. Huck, S.K. Park, D.E. Speray, and N. Halyo, "Information density and efficiency of two-dimensional (2-D) sampled imagery", SPIE Proceed. on Image Quality, Vol. 901, pp. 36-42, 1981.

[40] R.J. Arguello, H.B. Kessler, and H.R. Sellner, "Effect of sampling, optical transfer function shape, and anisotropy on subjective image quality", SPIE Proceed. on Image Quality, Vol. 310, pp. 24-33, 1981.

[41] T. DeRose, H. Hoppe, T. Duchamp, J.A. McDonald, W. Stuetzle, "Fitting of surfaces to scattered data", Proceed. of SPIE Symp. on Curves and Surfaces in Computer Vision and Graphics III, Vol. 8130, pp. 212-20, 1992.

[42] F. Cheng and B.A. Barsky, "Interproximation: interpolation and approximation using cubic spline curves", Conf. on Computer Aided Design, Vol. 23, No. 10, pp. 700-5, 10 December, 1991.

[43] T.J. Peters, I.R. Greenshields, and S.M. Dorney, "Topological fidelity in surface reconstruction", SPIE Symp. on Curves and Surfaces in Computers Vision and Graphic III, Vol. 1830, pp. 221-5, 1992.

[44] S.K. Park, "Image gathering, interpolation and restoration: a fidelity analysis", Proc. of the SPIE symp. on Visual Information Processing, Orlando, FL, 20-22 April, 1992, Vol. 1705, pp. 134-44.

[45] R. Hazra and S.K. Park, "Small-kernel, constrained least-squares restoration of sampled image data", Proc. of the SPIE symp. on Visual Information Processing, Orlando, FL, 20-22 April, 1992, Vol. 1705, pp. 155-64.

[46] D.P. Gaines, et.al., "Surface characterization of optics for EUV lithography", OSA TOPS on Extreme Ultraviolet Lithograph, Vol. 4, pp.103-6, 1996.

[47] D.P. Gaines, H.C. Chapman, New-View 100 visible light interferometer, Lawrence Livermore National Laboratory, Livermore, CA.

Chapter 6

Conclusions and Future Work

6.1 Conclusions

By direct measurement of the aerial image intensity at the image plane, it is possible to accomplish several tasks in a more accurate and timely fashion than is possible with convention methods involving photoresist. Finding the plane of best focus is an example of one of the utilities of AIM carried out in this thesis. The standard technique for finding the focal plane as described in chapter 1, involves exposing numerous sites on a PR coated wafer. Due to the low flux levels of the 10X-I system, this process could take the better part of a day. AIM provides the result in less than 30 minutes.

6.1.1 System Characterization

Alignment of the optical system is another utility of direct AIM for advanced EUVL systems. As described in chapter 4, the *in-situ* detector provided by the AIM setup is used for the real-time alignment of both the condenser and objective lens of the 10X-I EUV lithography system. This new technique provides visual computerized feedback allowing more quantitative optical alignment than earlier scintillator-based techniques (see chapter 4). The use of the *in-situ* detector further provides the capability of at-wavelength evaluation of spherical multi-layer condenser lenses.

System vibration is measured by two separate techniques involving the direct measurement of image intensity. Several hardware changes are made to the 10X-I system

to reduce this vibration and are detailed in chapters 3 and 4. However, the modified system including the new spring-mounted stages and associated hardware showed 350nm of lateral image vibration in the worst case direction.

At this point, several stage hardware modifications were implemented which include (listed in order of impact on vibration reduction): tightening of all hardware, tightening of the leaf-spring which secures the camera inside the vacuum can, spring-mounting the wafer stage to the camera, and insertion of a lossy inductor (toroid) on the Q/I capacative position sensor cables. The result of these efforts was a measured worst case system vibration of 17 ± 3 nm. This level of vibration suppression was reproduced numerous times and after several mask changes which involved complete removal off both mask and wafer stages as well as the camera.

6.1.2 EUV Multi-layer Optics Characterization

6.1.2.1 Knife-Edge Scans of Slit Source AI

Three distinct methods of aerial image monitoring are implemented on the 10X-I EUVL system at Sandia NL. The first set of experiments scans a knife-edge at the image plane across a 2.5μm slit source aerial image. The results provide qualitative agreement with theory and simulation [1-2]. Several factors limit the accuracy of the results in these experiments. First, the slit is too wide to provide an accurate measure of the LSF of the system. For this imaging system partial coherence confounds the determination of the LSF as discussed in chapter 5.

Other issues affecting the accuracy of these measurements include the fact that the slit mask used has a peak-to-peak roughness of 0.8μm which further distorts the measured

image. Another factor is that this camera has 0.38μm of distortion in the Y-direction, and since the slit image and scanning knife-edge traverse the entire field, the full magnitude of this distortion is seen in the measured aerial image.

6.1.2.2 Slit Scans of Step Function AI

A more accurate measure of the system LSF is obtained for quantitative evaluation of the impact of mid-spatial frequency scatter [3] by scanning a single narrow slit artifact over a step function AI. The signal provides a measure of the LSF when differentiated [4-5]. The system MTF is then calculated as the modulus of the Fourier transform of the system LSF. This spatial frequency dependent MTF(f) is used together with simulation to estimate an effective imaging system multi-layer surface roughness variance σ^2_{rms} following theoretical calculations [6]. The measured value of σ_{rms} was between 0.4nm and 1.3nm for the spatial frequencies between $0.1\mu m^{-1}$ and $25\mu m^{-1}$ respectively with an rms value of 0.7nm. Lower spatial frequencies were analyzed by visible light interferometry measurements of two representative primary mirrors. These measurements displayed an effective rms roughness value of 0.4nm between the spatial frequency range of $4*10^{-6}nm^{-1}$ to $4*10^{-4}nm^{-1}$.

6.1.2.3 Slit Scans of 0.5μm L/S AI

The final set of image monitoring experiments is a depth of focus study that involves scanning a single narrow slit artifact across the AI of 0.5μm equal line and spaces. The measured peak contrast of the AI is 57% which is in agreement with simulation and PR measurement. The depth of focus is ±5μm based on 80% of the peak contrast.

6.2 AIM Scanning Aperture

In chapter 2, several viable options for the fabrication of sub-100nm apertures are presented. FIB lithography is selected for the fabrication of the AIM apertures used in these experiments for its simplicity and the ability to customize the aperture profiles by subsequent evaporations. Indium Antimonide is chosen as the photon absorber material as a compromise between its high extinction coefficient at EUVL wavelengths and ease of deposition. The final aperture profile is tailored using the results of E-M simulations carried out to optimize the response of these EUV AIM apertures (see chapter 2).

This method proved very successful and yielded numerous single slit and slit array apertures which are still in use on the 10X-I EUVL system. This work produced nearly perfect EUV apertures which are planned for future AIM experiments as well as interferometry experiments to be conducted at another site [2]. Figure 1 is a FIB image of a PDI aperture fabricated using this technique. The aperture consists of a 5μm X 5μm square aperture and two minimum feature pinholes. The pinholes in this figure are circa 0.12μm in diameter. Subsequent absorber deposition following the process in chapter 2 is then used to produce the final PDI aperture. Experimental use of these apertures provides some insight into how they might be improved to be more durable and effective.

6.2.1 Scanning Aperture Fabrication

In the thin nitride process used for these experiments, the nitride thickness was around 700 Angstroms. The nitride films of this thickness exhibit many pinhole defects. It would be interesting to investigate the factors affecting the nitride process in an attempt to produce more defect-free films of this thickness.

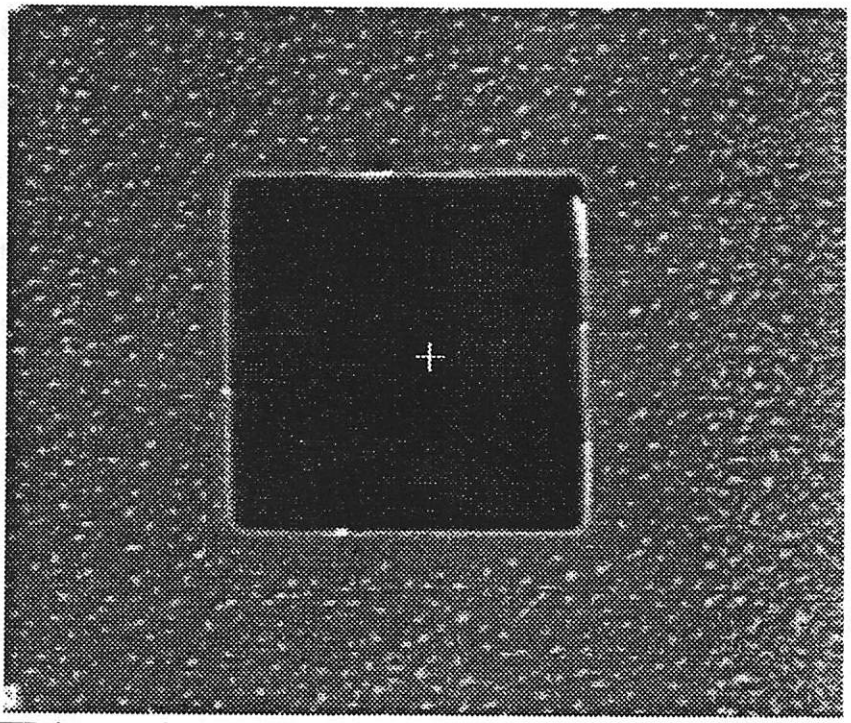

Figure 6.1 FIB image of a PDI aperture consisting of a 5μm X 5μm square aperture and two 0.12μm pinholes.

The absorber film of indium Antimonide was chosen as a compromise between high EUV photon absorption and ease of fabrication with existing VLSI process technology. After initial experiments were conducted, it was noticed that the InSb absorber apertures that were not stored in a moisture-free environment suffered from oxidation. This process distorted the profile of the slit aperture as it consumed the Indium during the oxidation. For apertures left in a standard room environment for more than a week, sufficient oxide film formed to completely close the 90nm aperture slits formed by the process described in chapter 2. The absorption coefficient of Silicon Dioxide is: $\mu_{SiO2} = 8.6\mu m^{-1}$. Even a 1000A film of SiO_2 across the aperture would result in loss of 58% of the available EUV flux.

Another material with slightly better EUV photon absorption than InSb is Nickel with an absorption coefficient of $\mu_{Ni} = 72\mu m^{-1}$ compared to $\mu_{InSb} = 65.6\mu m^{-1}$. Nickel films formed by e-beam evaporation or sputter deposition are less susceptible to oxidation. Initial experiments with sputter deposition of Ni films resulted in destruction of the Si_3N_4 membranes. Care must be taken when mounting membrane chips in preparation for sputter deposition including mounting the chips on some sort of riser which lifts them off of the chuck to allow the pump to pull vacuum equally from both sides of the membranes.

The AIM apertures used in these experiments followed the fabrication procedure in appendix B where the final step of the process is a top-layer deposition. The apertures may also be defined by depositing the complete front and back-side absorber layers prior to the FIB mill step. Apertures were successfully fabricated using this technique but cross-section profiles were not analyzed by SEM inspection nor simulated using TEMPEST. It is possible that these apertures yield equally adequate profiles and could place the critical FIB step at the end of the fabrication process.

Another possible area of research is the dry etching In and InSb films in Chlorine and Fluorine-based plasmas. Direct pattern transfer into these thin absorber films would present alternatives for e-beam lithography-based fabrication approaches. Initial calculations suggest that these film would etch in Cl-based plasmas with the same basic mechanisms as RIE of Aluminum films. However, there is a question of vacuum etch chamber contamination due to the high vapor pressure of Indium and Antimony.

6.2.2 Aperture Response Simulation

The TEMPEST simulations done in this thesis assumed normal incidence plane wave radiation. The 10X-I EUVL testbed produces EUV radiation at 12.1 degrees incidence with a numerical aperture of 0.08. It is possible to more accurately simulate the response of the scanning aperture slits if these conditions are taken into account. As of the time of the this thesis, the capability for accurately simulating waves at non-normal incidence does not exist in TEMPEST.

6.3 AIM for Future EUVL Systems

The ultimate goal of this research is to develop a rapid method of system characterization that is applicable to the next generation of production lithography systems. The next logical step in the progression of AIM at EUV wavelengths is the implementation on the next generation proto-type EUVL stepper, the 10X-II. The wafer stage of the 10X-II EUVL system utilizes a magnetically levitated stage which provides sufficient step resolution and stability for EUV AIM experiments.

The wafer chuck mounted on this stage has provisions for the installation of an artifact/photodiode mount identical to that on current GCA ALS and XLS model steppers. This mount is designed to hold a circular artifact and has room to install a photodiode closely behind the artifact. This mount is used for image quality measurements and for finding the plane of best focus on GCA steppers as described in chapter 1. This greatly simplifies the modification of 10X-II for AIM experiments. An AIM artifact must be fabricated on a circular substrate or one of the existing artifact chips cut to fit the mount. The IRD diode is smaller than the Hamamatsu diode originally designed for the mount by

GCA. The only obstacle left is the positioning of the preamplifier. As long as sufficient steps are taken to insulate against the effects of EMI (see chapters 3 and 4), the pre-amplifier can be place several inches away from the detector.

Currently the 10X-II uses a global and local alignment scheme that involves chevron alignment marks. Any AIM artifact designed for use on the 10X-II should include these alignment marks to allow the use of the current alignment scheme as well as AIM. Incorporation of the chevrons can be accomplished by etching the patterns into the silicon nitride some fixed distance from the aperture slit or pinhole, sufficiently far enough to be on the substrate and off of the membrane as illustrated in figure 2.

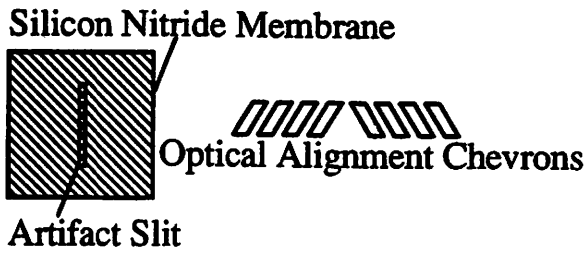

Figure 2. Illustration of potential 10X-II artifact incorporating AIM and chevrons.

A new alignment scheme could incorporate both of these alignment (chevrons and slit(s)) patterns at the image plane for alignment and registration. Optical alignment using the chevrons proceeds as normal, then the stage is stepped over to the AIM artifact for the final alignment. This can accomplished by projecting the aerial image of equal L/S patterns of a minimum feature size onto a single slit AIM artifact. The wafer stage is then quickly scanned through at least one complete period of the features and the contrast is measured. As discussed previously, maximizing the contrast of subsequent scans at different focus position provides the plane of best focus.

For global and local alignment a single minimum feature line could be projected onto the single slit artifact. Scanning the artifact across this image would result in a measured signal that peaks when the slit is aligned with the image. An alignment technique is possible using the chevrons for the coarse alignment and the AIM artifact for final fine alignment. This could involve stepping the stage from the chevrons to the AIM or one could image designing a mask that has both pattern which project an image which matches that spacing of these two alignment marks.

AIM has the potential to play an even larger role on the "α-system" which will be designed as a pseudo-production EUV stepper. The task of finding the optimal focal plane can be completely automated using the AIM technology. Alignment with accuracy of around 5nm could be accomplished with the AIM technique and some signal processing using standard statistical methods.

6.5 Conclusion

This manuscript has detailed the use of direct aerial image measurements to characterized current and projected future generations of lithography steppers. AIM began with earlier attempts to evaluate projection lithography systems and took the concept the final step by the complete removal of photoresist from the characterization process. The AIM experiments in this thesis represent the first successful tests of an assembled EUV lithographic system by direct measurement of the projected aerial images. AIM was used to quantify EUVL system vibration and its impact on imaging performance. System vibration was markedly reduced in the process of these experiments. The impact of mid-spatial frequency scatter on the imaging performance of EUV multi-layer mirrors

was analyzed using AIM and compared to simulation. These measurements lead to an estimation of the variance of the camera roughness from the measured and simulated system MTFs.

References

[1] C. H. Fields, A. K. Ray-Chaudhuri, K. D. Krenz, W.G. Oldham, and R. H. Stulen, "Direct Aerial Image Measurements to Characterize an Extreme Ultraviolet Projection Lithography System," EIPBN Conf. Atlanta, GA 1996, JVST - B, Nov./Dec., 1996.

[2] C. H. Fields, A. K. Ray-Chaudhuri, K. D. Krenz, W.G. Oldham, and R. H. Stulen, "Initial Experiments on Direct Aerial Image Measurement in the Extreme Ultraviolet," OSA Proceedings on Extreme Ultraviolet Lithography, (Optical Society of America, Boston, MA, 1996, pp. 124-8.

[3] A. K. Ray-Chaudhuri, C. H. Fields, K. D. Krenz, W.G. Oldham, and R. H. Stulen, "Interferometry for Evaluation of Extreme Ultraviolet Optics," EIPBN Conf. Atlanta, GA 1996, JVST - B, Nov./Dec., 1996.

[4] A. K. Ray-Chaudhuri, K. D. Krenz, C. H. Fields, R. H. Stulen, and W.G. Oldham, "Development of Extreme Ultraviolet Interferometry for Laser Plasma Source Operation," OSA Proceedings on Extreme Ultraviolet Lithography, Optical Society of America, Boston, MA, 1996, pp. 128-32.

[5] K.A. Goldberg, R. Beguiristain, J. Bokor, H. Medecki, K. Jackson, D.T. Attwood, G.E. Sommargren, J.P. Spallas, and R. Hostetler, "Point-Diffraction Interferometry at EUV Wavelengths," OSA Optical Society of America Conference Proceedings on Extreme Ultraviolet Lithography, Vol. 35, pp. 134-141, Monterey, CA, 1994.

[6] D.G. Stearns, D. Gaines, D. Sweeny, "Image Degradation due to scatter in a distributed optical system: A theoretical treatment" , To be published in the Journal of Applied Physics.

Appendix A:

A.1 Experimental Methodology

This section explores the results of a 3^5 full factorial experiment to analyze the factors that affect the ultimate resolution achievable through electron-beam (e-beam) lithography. The exposure tool used for this experiment is a Jeol-6400 Scanning Electron Microscope (SEM) modified to perform e-beam lithography. The five variables investigated are electron energy expressed in kV, exposure dose in $\mu C/cm^2$, photoresist thickness, line spacing pitch, and drawn linewidth. The first four of these five variables are run at three levels. A matrix of doses is run over a wide range to permit feature of different sizes and pitch to all clear at some dose. Linewidth measurements are taken at three doses around the critical dose for the correct linewidth development.

Constraints of time and effort would preclude exposing 3^5=243 different wafers. Due to the nature of e-beam lithography it is possible to automate the variation of exposure dose, linewidth, and pitch. The only constraint is the time required to measure the PR CD. The results of the measurements are analyzed using regression. The significance of each parameter and cross-interactions is analyzed and a model fit to significant terms.

This experiment is designed to study both types of proximity effects: Intra-proximity and inter-proximity. The major factor affecting the intra-proximity effect is the choice of electron beam writing energy and exposure dose. In this experiment, three different energies (20, 30, and 40kV) as well as three dose levels are studied. Inter-

proximity effects are seen as CD variations between closely spaced patterns. To characterize this variation, three different line spacing pitches are investigated.

It is important in any experiment to preserve the initial assumption that the results are identically independent and normally distributed (IIND). Care is taken during the processing; i.e. exposure, development, Au coating, and measurement, to insure that the samples are identical. To further insure the second condition of our IIND assumption, all lithography process steps are repeated under identical conditions for the different resist thickness samples. This is accomplished by writing three chips during the same vacuum chamber pump-down cycle.

A.2 Implementation

Three wafers are coated with different thickness' of 950K molarity PMMA. The thickness of each wafer is measured on a Nanospec ellipsometer in four locations on the periphery of the wafer as well as the center. The average values of the thickness were measured to be 1670, 2233, and 3023A with standard deviations of 17.8, 21.8, and 9.7A respectively. Each wafer is then cleaved into 10mm chips that are used for the e-beam exposure.

A test matrix pattern is designed for this experiment using CAD software. The test pattern consist of 10μm long lines drawn at five different linewidth dimensions: 200nm, 150nm, 100nm, 75nm, and 50nm. Although this variable is at five levels, the last two smallest features are near the resolution limit of the system and not expected to clear. Each linewidth dimension is drawn at an equal line space (L/S) pitch and then repeated at one-half that spatial frequency (1/2 pitch), and again at one-fourth the spatial frequency of

the original (1/4 pitch). The equal L/S pattern consisted of 8 equally spaced lines while the 1/2 pitch pattern consisted of 4 lines and the 1/4 pitch pattern contained only two lines drawn at a given dimension.

The final test pattern written consists of the above test pattern repeated 12 times (two columns, 6 rows) at varying dose. The field size of the pattern is 95μm. This pattern is repeated twice at each kV setting on each of the three chips for a total of 24 different dose settings per kV per chip. This test pattern is used to expose each of the three wafer chips described above.

Beam setup and shape optimization is critical to the effective patterning of fine features. Therefore, to insure identical/independent portion of our IIND condition, it is necessary that all exposures are done under the same settings. All three chips are loaded on the same sample holder and exposed during a single system pump-down. Changing the beam energy affects the shape of the electron column and therefore it is necessary to re-optimize the beam between changes in kV. All the patterns for a given kV and dose range are written on each of the three chips before the electron energy is set to a new value.

All three sample are developed at the same time under the identical conditions. The development is done for 60 seconds in a 3:1 mixture of Isopropyl Alcohol (IPA):Methyl Isobutyl Ketone (MIBK). The development is immediately followed by a 20 seconds rinse with IPA and then a final rinse for an additional 20 seconds with DI water. Following development, all three samples are coated with approximately 100A of Gold to aid in the linewidth measurements. The samples are then measured on the same SEM in which they are exposed. Exposure dose steps of $20\mu C/cm^2$ result in a measurement error

of at most $10\mu C/cm^2$ which is at most a 1% error and at best an error of 0.2% from the resulting data set.

A.3 Results and Discussion

Model Fit:

Very few 50nm and 75nm lines clear (or remained for the case of equal L/S patterns), only a few patterns at the highest kV setting. Therefore the data on these two drawn linewidths is not analyzed so the variable of drawn line will be studied at three levels. This fact is discussed later as relates to the results of the analysis. Neglecting this data, a total of 195 linewidth measurements are taken.

The dose to clear each feature varies greatly for different combinations of the other four variables. This results in measured linewidth data that is no longer perfectly orthogonal. There are not always three separate doses that result in measurable patterns that clear and remain in tact for every combination of variables. However, the data can still be analyzed with the use of linear regression.

Using statistical analysis software (JMP), a model is fit to the measured linewidth data using linear regression consisting the 5 first-order terms. Table A.1 details the fit of the model. Parameter estimates are given as well as the significance of each effect. It is clear that linear regression results in an excellent model fit to the data. The t and F-ratios point to drawn linewidth as the most significant parameter modeled, with an F-ratio of 373.95. It is expected that the most important factor in determining the dimension of the resulting line is the originally drawn dimension. Ideally, a plot of drawn vs. measured

linewidth has a slope of one. From table A.1 we see that the coefficient of this term is 1.16. This is attributed to intra-proximity effects since each line in this experiment is drawn with multiple electron beam passes per single drawn line. The backscattered electron exposures are cumulative for each pass so larger lines require more beam passes and tend to be overexposed, resulting in "blooming" of the lines.

Response: MeasLW

Summary of Fit

Rsquare	0.682403
Root Mean Square Error	0.029272
Mean of Response	0.162154
Observations (or Sum Wgts)	195

Parameter Estimates

Term	Estimate	Std Error	t Ratio	Prob>|t|
Intercept	0.0270409	0.0144	1.88	0.0620
kV	-0.005397	0.00051	-10.56	0.0000
tresist	-0.00003	0	-5.87	0.0000
DrawnLW	1.1602101	0.06	19.34	0.0000
Pitch	0.0355368	0.00963	3.69	0.0003
Dose	0.0006061	0.00005	11.61	0.0000

Effect Test

Source	Nparm	DF	Sum of Squares	F Ratio	Prob>F
kV	1	1	0.09562502	111.6031	0.0000
tresist	1	1	0.02956206	34.5016	0.0000
DrawnLW	1	1	0.32041484	373.9533	0.0000
Pitch	1	1	0.01166108	13.6095	0.0003
Dose	1	1	0.11557207	134.8831	0.0000

Table A.1 Linear regression model fit to experimental e-beam lithography data.

The second most significant variable is exposure dose with an F-ratio of 134.88. The exposure dose determines the total number of electrons deposited into the resist. Electron energy is the next most important variable with an F-ratio of 111.60. At higher electron energies, electrons are more likely to penetrate through the resist and stop in the silicon substrate. These electrons do not provide exposure dose to the resist and therefore do not aid in the scissoring action in the positive photoresist. Finally we see that resist thickness is much less significant but still almost three times as important as linewidth pitch.

Figure A.1 shows a plot of the whole-model test drawn along with the 95% confidence limit curves, the Analysis of Variance (ANOVA) table for the model, and finally a plot of the residuals of the model. The model has an F-ratio of 81.22.

Clear groupings of this data are present, seen as horizontal lines on the whole-model test and as diagonal lines on the plot of the residuals. This is explained by the fact that during the measurement, the linewidth measurements were discretized into steps of 25nm due to the resolution limits of the SEM. The lines in the whole-model test are also in increments of 25nm.

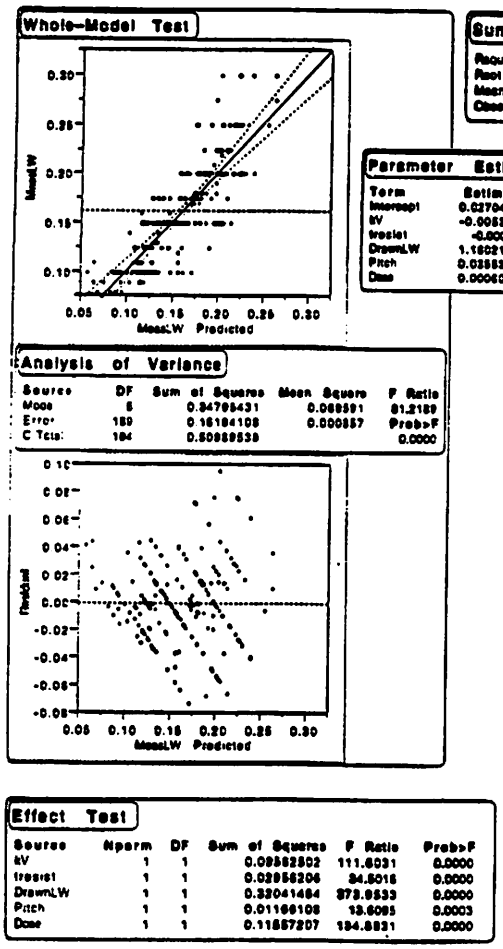

Figure A.1 Whole-model test of regression model fit with associated analysis of variance table. Also listed in the figure are estimates of the parameter coefficients with tests of their respective effect.

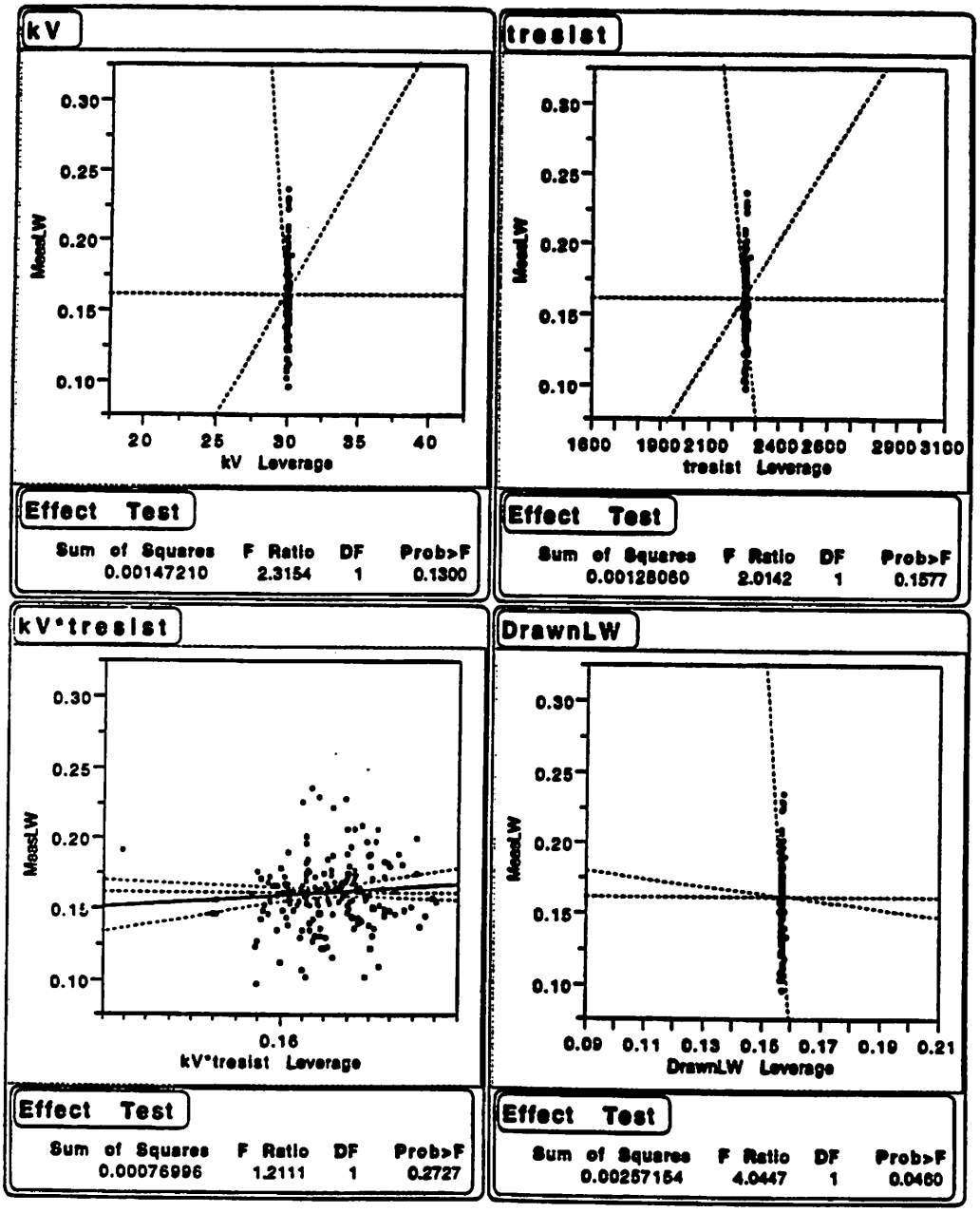

Figure A.2 Leverage plot of four of the five parameter effects investigated in this experiment. The dots represent the experimental data while the dashed lines are the 95% confidence interval curves of the effect. A steep slope indicates strong significance and if the 95% interval curves contain the horizontal line (the mean value), then the parameter can be said to be not statistically significant.

Figure A.2 plots the linear regression model and the data vs. 4 of the 5 the experimental variables. The plot of linewidth vs. kV shows a decrease in developed CD as the energy is increased. This provides a measure of the combined intra and inter-proximity effects. As the electron energy is increased, there is less scatter in the resist and substrate which leads to a more narrow energy deposition profile. The plot vs. the leverage of resist thickness shows a slight negative slope, indicating the minor effect of this variable. Extrapolating the linear fit, it would require an extra 600nm of resist to equal the same leverage as increasing the writing energy by only 10kV. The plot of measured vs. drawn linewidth shows a positive slope of almost one, as mentioned earlier. The plot of the model vs. line pitch provides a measure of the inter-proximity effect. This plot demonstrates the tendency for closely spaced lines to blur together which is the result of the summation of the forward and backward scattered electron from the each of the nearby lines. This leads to overexposure and widens CDs upon development. Figure A.3 plots the model fit and data vs. dose. The steep slope of the line confirms our earlier analysis that exposure dose is the most significant factor, aside from drawn linewidth.

Table A.2 lists the correlation coefficients for second order interactions between the main effects. The highest correlation is between exposure dose and the other variables; confirming the conclusion that dose is the most significant effect besides drawn LW. Investigation into 3rd, 4th, and 5th order effects reveal no significant linear cross-interactions. Further analysis using models involving non-linear models is recommended.

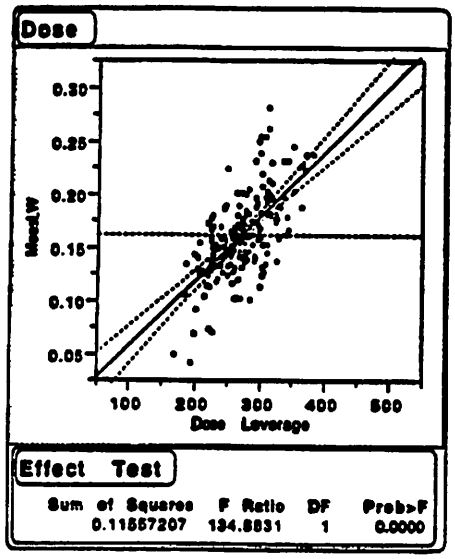

Figure A.3 Leverage plot of exposure dose. The steep slope and tight confidence curves indicate strong statistically significance with a relatively small distribution variance.

Correlations

Variable	kV	tresist	DrawnLW	Pitch	Dose
kV	1.0000	-0.0179	-0.0226	0.0277	0.6968
tresist	-0.0179	1.0000	0.0653	0.0185	0.3431
DrawnLW	-0.0226	0.0653	1.0000	0.1814	-0.2746
Pitch	0.0277	0.0185	0.1814	1.0000	-0.3881
Dose	0.6968	0.3431	-0.2746	-0.3881	1.0000

Table A.2 List of cross-correlation coefficients that represent the effect of cross-term interaction on the resulting resist profiles.

At the outset of this experiment it is suspected that both exposure dose and electron energy play a key role in determining developed feature sizes. However, it was not obvious which plays the larger role. Now it is clear that exposure dose carries more weight in the final outcome. Prior to this experiment, it was also incorrectly thought, by

me anyway, that the thickness of the PMMA layer was critical to achieve ultimate resolution. It is now apparent that varying the thickness of the photoresist layer would not have as much affect on the proximity effects and the developed linewidth as varying the energy of the electron source. It can be seen from the data that CD distortion resulting from proximity effects can be reduced by the use of a higher kV source.

A.4 Conclusion

The main factors affecting the resulting linewidths in electron-beam lithography are analyzed using linear regression. Regression is used to fit a model to measured linewidth data from a 3^5 factorial experiment. This model contains the five variables of exposure dose, electron energy, line pitch, resist thickness and drawn linewidth. The results of the analysis point to exposure dose as the most important factor, after drawn linewidth, in determining the developed CD.

From the analysis we obtain a measure of both the inter and intra-proximity effects. Electron beam writing energy is found to be nearly as significant as dose and plays the major role in reducing proximity effects by reducing the forward-scattered electron distribution width. Although line pitch plays an important role in determining the magnitude of the inter-proximity effects, it is found that it is possible to overcome this effect by the proper choice of exposure dose. Current research is under way to find efficient methods for the calculation of dose corrections to compensate for proximity effects [9,10,11,12]. The thickness of the photoresist layer (PMMA) has comparatively little effect with respect to proximity effects and therefore the resulting developed linewidths. The latter two are interesting results and were not anticipated.

References:

[1] Broers, A. N., "Resolution limits for electron-beam lithography", *IBM Journal of Resist Development*, Vol. 32, no. 4, pp.502-513, July 1988.

[2] Wei C. and Ahmed H., "Fabrication of high aspect ratio silicon pillars of <10nm diameter", Appl. Phys. Lett.62 (12), pp. 1116-1120,March 1993.

[3] Fischer P. B. and Chou S. Y., "Sub-50 nm high aspect-ratio silicon pillars, ridges, and trenches fabricated using ultrahigh resolution electron beam lithography and reactive ion etching", Appl. Phys. Lett.62 (12), pp. 1414-1416, 22 March 1993.

[4] Gentilli M., Grella L., Di Fabrizio E., Luciani L., Baciocchi M., Figliomeni M., Figliomeni M., Maggiora R., Cerrina F., and Mastrogiacomo L., "Development of an elctron-beam process for the fabrication of x-ray nanomasks", J. Vac. Sci. Technol. B 11(6), pp2938-2942, Nov/Dec 1993.

[5] Rosenfield M. G., Thomson R., Coane P. J., Kwietniak K. T., Keller J., Klaus D. P., Volant R. P., Blair C. R., Tremaine K. S., Newman T. H., and Hohn F. J., "Electron-beam lithography for advanced device prototyping: Process tool metrology", J. Vac. Sci. Technol. B 11(6), pp.2615-2620, Nov/Dec 1993.

[6] Nakayama Y., Okazaki S., Saitou N., and Wakabayashi H., "Electron-beam cell projection lithography: A new high-throughput electron-beam direct-writing technology using a specially tailored Si aperture", J. Vac. Sci. Technol. B 8(6), pp.1836-1840, Nov/Dec 1990.

[7] Fischer P. B., Dai K., Chen E., and Chou S. Y., "10nm Si pillars fabricated using electron-beam lithography, reactive ion etching, and HF etching", J. Vac. Sci. Technol. B 11(6), pp.2524-2527, Nov/Dec 1993.

[8] Chen W., and Ahmed H., "Fabrication of sub-10 nm structures by lift-off and by etching after electron-beam exposure of poly(methylmethacrylate) resist on solid substrates", J. Vac. Sci. Technol. B 11(6), pp.2519-2523, Nov/Dec 1993.

[9] Eisenmann H., Waas T., and Hartman H., "PROXECCO-Proximity effect correction by convolution", J. Vac. Sci. Technol. B 11(6), pp.2741-2745, Nov/Dec 1993.

[10] Dobisz E. A., Marrian C. R. K., Salvino R.E., Ancona M.A.,F.K. Perkins, and Turner N.H., "Reduction and elimination of proximity effects", J. Vac. Sci. Technol. B 11(6), pp2733-2740, Nov/Dec 1993.

[11] Bojko R. J., Hughes B.J., "Quantitative lithographic performance of proximity correction for electron-beam lithography", J. Vac. Sci. Technol. B 8(6), pp1909-1913, Nov/Dec 1990.

[12] Owen G., "Methods for proximity effect correction in electron lithography", J. Vac. Sci. Technol. B 8(6), pp.1889-1892., Nov/Dec, 1990.

Appendix B - Silicon Processing Details

B.1 - Super Hard Bake Photoresist

1. Spin on OCG-825 photoresist (PR) to desired thickness.
2. Prebake at 90 deg. C for 1min.
3. Hardbake is accomplished in VWR-120 oven. Load wafers into oven with initial temperature 120 deg. C.
4. After wafers are loaded into oven, increase setpoint to 300deg. C.
5. Allow wafers to hardbake for 1 hour.
6. Reset temperature setpoint to 120 deg. C.

B2 - Silicon Nitride Membrane Process

1. If starting with new, clean wafers, proceed onto step #2. Otherwise, clean the wafers in the Pirahna bath in SINK8 for 5-10 minutes followed by a three-tank DI rinse.
2. Grow a low-stress silicon nitride film of the desired thickness in TYLAN18 using the standard low-stress nitride recipe in the tylan computer.
3. Clean wafers in the Pirahna bath in SINK8 for 5-10 minutes followed by a three-tank DI rinse.
4. Bake out wafers in VWR-120 oven at 120 deg. C for 1 hour.
5. Apply HMDS to wafers in the VAPOR PRIME.
6. Spin-on OCG-825 PR onto the backside of the wafers on SVG coater track (track 1; program 2). This will result in a PR thickness of 1.3μm.

7. Pattern square windows onto the backside of the wafer using any of the photolithography tools (e.g. GCA 10X reduction stepper). Orient the boxes such that they are parallel to the major flat of the wafer. Keep in mind that that anisotropic etch of the silicon will result in a constant angle of 54.74 degrees from the normal. This will result in a lateral enchroachment of about 700μm for a 500μm thick wafer substrate (i.e. if the length of the box on the backside of the wafer is 800μm, then the length of the final membrane square on the frontside will be about 100μm).

8. Post Exposure Bake (PEB) on hotplate at 120deg. for 1 minute or use track 2 program 9.

9. Develop the PR on SVGDEV. Use premixed 934 developer. Consult program list on the wall near the stepper as these change often.

10. Optically inspect PR patterns for size and orientation.

11. Descum the wafer in TECHNICS-C for 2 minutes using an oxygen plasma operating at 50W.

12. Hardbake the wafers for 1 hour in the VWR-120 oven at 120deg. C.

13. Etch nitride in LAM1 using program THNSTD Recip.1 which has an etch rate (ER) of 952A/min.

14. Strip the PR in the PRS-2000 bath in SINK5 for 15-30 minutes followed by DI rinse.

15. Repeat the Pirahna clean detailed in step #1

16. Dip the wafers in HF (also at SINK8) for 10sec. to remove the native oxide, which will impede the subsequent silicon etch, followed by a three tank DI rinse.

17. Etch the silicon by placing the wafers in the heated (80deg. C) KOH bath at SINK6. The etch mixture ratio is 2:1 H2O:KOH (e.g. 3liters of H2O:1500mg of KOH pellets). At T=80deg. C this mixture will produce an etch rate of 1mm/min, or about 4hours and 20minutes for a typical 500μm thick silicon wafer. The etch is a 400:1 preferential etch in the <100> crystal plane.

18. Perform a three tank DI rinse.

B.3 - Double Lift-Off Process

1. Perform silicon nitride membrane process detailed in appendix B2.

2. Perform SHBPR process detailed in appendix B1.

3. Spin-on 2000A of PMMA PR (495k molarity 4% concentration at 4000rpm).

4. Bake at 170deg. C for >2hours.

5. Cleave the wafer into 10-15mm sample chips.

6. Perform the electron-beam exposure using the Jeol 2400 SEM.

7. Develop PMMA in 3:1 mixture of IPA:MIBK for 70sec. followed by ipa rinse for 20 seconds then a final DI rinse for an additional 20seconds and blow dry with N_2.

8. Evaporate 200A of Aluminum onto the chip in the Veeco (V401).

9. Lift off the PMMA by placing the chip into a heated (90deg. C) bath of acetone for 10 minutes followed by an acetone rinse for 20seconds then a DI rinse for 20seconds and blow dry with N_2.

10. Perform an O_2 descum in the TECHNICS-C plasma etcher for 2.8minutes. The O2 plasma should be operated at 50W with a base pressure of 230mT.

11. Evaporate 1200A of InSb onto the chip in the Veeco (V401).

12. Lift-off the SHBPR using PRS-2000. The temperature of the bath should be 90deg. C and ultrasonic agitation will be required to remove the metal "caps" on top of the PR pillars.

13. Perform an O2 ash in the TECHNICS-C plasma etcher to remove any remaining PR. This process is the same as detailed in step 10 with the exception that the operating power will now be 300W.

14. If a thicker metal absorber layer is required, simply increase the film thickness in steps 2 and 11 proportionally.

B.4 - Al-Ge Hard Mask Process

1. Perform silicon nitride membrane process detailed in appendix B2.

2. Evaporate 100A of Titanium onto wafer using the Veeco (V401) as glue layer to improve the adhesion of the film to be deposited in step #3.

3. Evaporate 3000A of Germanium onto wafer using the Veeco (V401).

4. Evaporate 500A of Aluminum onto wafer using the Veeco (V401).

5. Spin 2000A of PMMA PR onto wafer as in B3 - step #3.

6. Bake at 170deg. C for >2hours.

7. Cleave the wafer into 10-15mm sample chips.

8. Perform the electron-beam exposure using the Jeol 2400 SEM.

9. Develop PMMA in 3:1 mixture of IPA:MIBK for 70sec. followed by ipa rinse for 20 seconds then a final DI rinse for an additional 20seconds and blow dry with N_2.

10. Etch the Aluminum film in LAM3. Following the standard recipe in the LAM computer results in an etch rate of 2000A/min. Therefore a main etch time 20 seconds is required to etch the 500A film with a 30% overetch.

11. Etch the Germanium film in TEGAL using the Aluminum layer as a hard mask for the etch. Perform the etch for 60 seconds which will etch the 3000A film with a 33% overetch. For Ge etch process details, see appendix B5.

B.5 - Germanium Dry Etch Process

1. The Ge etch is performed in the TEGAL dry etcher. The operating parameters are as follows:

2. SF6 gas flow rate: 20.0 sccm

3. Base Pressure setting: 100mT

4. Power: 50W

5. These settings will result in an etch rate of 4000A/min.

B.6 - Optical "FIB Pre-test" Process

1. Perform steps 1 - 15 of process module B2.

2. Spin 8000A of APEX-E PR onto the frontside of the wafer using SVG-COAT (3000rpm).

3. Using the UltraTech micro-stepper, expose the PR using a mask made up of pinhole arrays varying in size from 0.5μm to 0.1μm.

4. Develop the PR in a 3:2 mixture of DI:MF-312 for 50seconds followed by a DI rinse for 20 seconds then blow dry with N_2.

5. Etch the pinhole patterns into the nitride layer with LAM1 for 3minutes using the LAM etch program: THNSTD.

6. Perform steps 16 - 18 of process module B2.

7. Evaporate absorber metal (InSb or Ge) using the Veeco (V401) to desired thickness.

B.7 - "Knife-Edge" Fabrication Process

1. Perform silicon nitride membrane process detailed in appendix B2.

2. Etch the oxide from the nitride by dipping in 10:1 HF for approximately 1minute.

3. Turn on the hot phosphoric acid bath (right heated bath of sink7) by pushing the green TEMP CONTROL button on the right half of the sink. Set the controller to the desired temperature (150 deg. C). Wait for the temperature to stabilize. Acid will reach a rolling boil.

4. Immerse wafers in hot phosphoric acid. The time required to etch the film will vary because small amounts of water are added to the bath as the level goes down, thus diluting the acid. For a 1000A film, check the wafers after an hour. The endpoint of the wet etch will be apparent through a visual inspection of the wafers.

5. Perform the three tank DI rinse.

6. Evaporate 800A of InSb onto the front side of the wafer. (700A provides a transmission of 1% for 13.4nm radiation).

7. Optically inspect the wafer to find a defect-free membrane edge for use as the knife-edge.